Mechanics of Complex Hydraulic Fractures in the Earth's Crust

A Thesis
Presented to
The Academic Faculty

by

Youngjong Sim

In Partial Fulfillment
of the Requirements for the Degree
Doctor of Philosophy in the
School of Civil and Environmental Engineering

Georgia Institute of Technology
August 2004

Mechanics of Complex Hydraulic Fractures in the Earth's Crust

Approved by:

Dr. Leonid N. Germanovich, Advisor

Dr. Robert P. Lowell

Dr. Paul W. Mayne

Dr. Alexander M. Puzrin

Dr. Glenn J. Rix

Dr. Peter E. Van Dyke

Dr. Wenyue Xu

August 20. 2004

ACKNOWLEDGMENTS

I thank the U.S. National Science Foundation (Grant OCE-0221974) for providing the financial support for this work.

I would like to extend my sincere gratitude to Dr. Leonid N. Germanovich for giving me the opportunity to pursue my doctoral research. This study would not have been possible without his continuous support and guidance.

I would like to express my thanks and appreciation to Dr. Robert P. Lowell for his helpful comments, and multiple useful discussions concerning this thesis. I also would like to thank Dr. Paul W. Mayne, Alexander M. Puzrin, Dr. Glenn J. Rix, Dr., Dr. Peter E. Van Dyke, and Dr. Wenyue Xu for serving on my thesis committee. Their insightful suggestions and helpful discussions have greatly improved this thesis. Much gratitude also goes to Dr. Peter E. Van Dyke for taking time to review my thesis, and for helping preparation for the defense presentation.

I thank the faculty and the students of the geosystems program for providing pleasant work environment, and all of the members of the high performance computing group for providing the computing facilities.

I also thank Dr. Jan M. Vermilye for providing the field data for the calculations, and her helpful comments during the research that is described in Chapter III. My sincere appreciation is also extended to Mr. Kasemchart Sriwalai. His sincere guidance to the numerical part of Chapter III enabled me to recognize the power of high performance computing. I also thank Mr. Matthew Evans for reviewing the first version of this thesis.

I thank the past and present students of the Rock and Fracture Mechanics Group at Georgia Tech, Dr. Dmitriy Astakhov, Mrs. Hong Chang, Dr. Rajesh Chanpura, Mr. Jongwon Choi, Robert Hurt, Mr. Pierre Ramondenc, Mr. Chanin Ruangthaveekoon, and Mrs. Ruiting Wu for their cooperation during my Ph.D. study.

I thank the former and present Korean students of the Geosystems at Georgia Tech, Dr. Jinyoung Park, Dr. Seokwon Lee, Dr. Jongsub Lee, Dr. Gyechun Cho, Duwhan Kim, Jonghee Kim, Sungsoo Yoon, Hyunki Kim, Jooyong Lee, Taesup Yun, and Sihyun Kim for their help and friendship. I can't fail thank my friends, Youlboong Sung, Chanhee Park, and Joonam Park for their friendship and coffee time to refresh my head.

Most of all, I thank my parents, Sangmyung Sim and Youngbai Kim, my brothers, Youngje and Seunghan, the family of my wife, my wife, Eunju Joung, and my two cute daughters, Jaehee and Seohee, whose endless love, support, and encouragement gave me the strength and power to complete this thesis.

TABLE OF CONTENTS

LIST OF TABLES

LIST OF FIGURES

SUMMARY

Hydraulic fracturing is an important and abundant process in both industrial applications and natural environments. The formation of hydraulic fractures includes nucleation, growth, and termination in numerous rock types and stress regimes, at scales ranging from microns to many kilometers. As a result, the fractures show complicated geometries, which reflect the complexity of the underlying physical mechanisms. Fracture segmentation, commonly observed at all scales and in all materials, contributes to this complexity in many ways. In particular, the mechanical interaction of fracture segments as well as the interaction of a fracture with other fractures, the Earth's surface, and pre-existing geological discontinuities strongly affect almost all hydraulic fracturing processes.

For more than five decades, hydraulic fracturing techniques have been widely used to enhance oil and gas production. Recent observations based on geological evidence, laboratory tests, and mineback experiments confirm that complex multisegmented hydraulic fractures are common phenomena. However, current hydraulic fracture models presume a single fracture, or neglect the interaction between the fracture segments. This is despite the fact that the interaction dramatically changes the simulated dimensions of the hydraulic fractures and their net pressures.

The current work is the first systematic quantitative study of the effects of the mechanical interaction in and between complex hydraulic fractures at different spatial scales. A mathematical model, based on the boundary collocation method, has been developed. The model has been employed for a typical field case, a highly segmented

vein. This vein is well-mapped, and therefore, represents a well constrained case. The computed apertures are compared to the measured apertures. By using the simplest constitutive model, based on an ideal elastic material, and including the effect of interaction between the segments, it was possible to obtain an excellent match at all considered scales. In addition, the concept of the effective fracture, as currently accepted in the literature, has been tested for a simple simulation of fractures with closely spaced and interacting segments. In the studied field case, the effective fracture model provided rather robust and accurate results. It is shown, however, that in general, due to the complex interplay between the parameters of segmentation, this concept may not always be applicable and may lead to unbounded inaccuracy.

Unfortunately, in most cases, very little (if any) directly measured data on fracture and material properties is available. An important example of such a weakly constrained case involving hydraulic fracturing is diking beneath the seafloor at mid-oceanic ridges. In this study, it is shown that the conventional scenario of a dike propagating from the center of a pressurized magma chamber to the ocean floor is not consistent with conventional fracture mechanics due to the fact that the chamber has the shape of a thin lens. Even at such a large scale (i.e., a kilometer or more), the mechanical principles of elastic interaction appear to be applicable. The dikes that initiate from the subsurface magma lens, and the magma lens itself, are considered as mechanically interacting fractures in an elastic half-space bounded by the seafloor. Since diking is likely to generate a region of high permeability near its margin, in addition to heat, the ongoing hydrothermal activity becomes localized. Our modeling suggests the probable positions of the propagating dikes. Consequently, comparing the observed locations of

hydrothermal sites with respect to that of the magma chamber could be useful for constraining the mechanisms of the evolution of magma lenses.

Hence, the mechanical interaction is likely to have a pronounced effect on the behavior of complex natural and industrial hydraulic fractures, and needs to be included into the modeling efforts.

CHAPTER I

INTRODUCTION

1.1 Motivation

During the last few decades, hydraulic fracturing has been a widely used technology for oil and gas recovery [e.g., *Veatch et al*., 1983a, 1983b; *Economides and Nolte*, 2000], geothermal heat extraction [e.g., *Nemat-Nasser*,1983; *Murphy*, 1983], in-situ stress measurement [e.g., *Haimson*, 1978; *Hayashi et al*., 1997; *Shin et al*., 2001], waste disposal [e.g., *Keck et al*., 1996; *Withers et al*., 1996], coal degasification in advance of mining [e.g., *Diamond and Oyler*, 1987; *Palmer and Sparks*, 1991], and remediation of contaminated water [e.g., *Hocking and Wells*, 2002; *Murdoch and Slack*, 2002]. Obtaining proper results by hydraulic fracturing (in the petroleum engineering in particular) depends highly on the geometric configuration of the fracture and the stress regime in the subsurface. This is why hydraulic fracturing has been a subject of active research to clarify the mechanisms of fluid-rock (or sediment) interaction. The geometry of the hydraulic fractures is affected by mechanical, thermal, and chemical conditions of the surrounding host rock. This can result in complicated structures deep in the subsurface or near the surface. Therefore, understanding the fracturing processes by fluid injection is of practically great importance for maximizing its effectiveness.

In nature, hydraulic fractures also appear in a variety of forms, such as sheet intrusions (i.e., sills and dikes), veins, and even joints (refer to below). In many aspects, the mechanical behavior of natural hydraulic fractures is analogous to that of fracture

propagation in industrial hydraulic fracturing since natural hydraulic fractures are created in the host rock by opening mode (referred to as dilatant, tensile, or extensional mode by different authors) driven by the internal pressure of fluids (e.g., magma, water, gas, or an aqueous solution), remote stress (e.g., tectonic stress), or a combination of both.

These natural opening mode fractures are frequently found in the earth's crust. The formation of these fractures includes nucleation, dilation, propagation and termination in a variety of rock types and stress regimes at scales ranging from microns to many kilometers. As a result, the fractures show complicated geometrical features such as multiple segments.

Segmentation is indeed one of the most often encountered features contributing to the complexity of hydraulic fractures. Recent observations based on geological evidence, laboratory experiments, and mineback observations confirm that the occurrence of multisegmented hydraulic fractures (MHF) is a common phenomenon. However, current hydraulic fracture models presume a single fracture or neglect interaction between multiple fractures that dramatically changes hydraulic fracturing parameters such as fracture aperture, length, and net pressure [*Astakhov*, 2000]. In an attempt to gain insight into the causes of MHF, the next three sections focus on observations of MHF in nature, laboratory experiments, and industrial observations.

1.2 Natural multisegmented hydraulic fractures

1.2.1 Sheet intrusions

Sheet intrusions, such as vertical dikes and horizontal sills, are related to the magma fluid. If the magma fluid pressure is sufficiently high to overcome the in-situ compressive stress and rock strength, it splits the host rock [e.g., *Anderson*, 1938; *Hubbert and Willis*, 1957]. It is also possible that magma sometimes can simply be emplaced in the pre-existing fracture [*Currie and Ferguson*, 1970].

On the basis of observations of the geometric features of sheet intrusions, segmentations with consecutive overlapping are common phenomena for many types of rock. Figure 1.1 shows overlapping segments ranging from a few centimeters to several hundred meters in a vertical dike. Figure 1.1a shows granitoid dike segments propagating through the Glen Mountain gabbro at the scale of a few centimeter scale in Wichita Mountains, Oklahoma [*Germanovich et al*., 1997a]. Figure 1.1b shows pegmatite dike segments through older granite at the scale of a few meters in East Quarry of Stone Mountain, Georgia, respectively.

Figure 1.1c shows a part of northeastern minette dike segments found near Ship Rock in New Mexico [*Pollard*, 1978]. The dike has an outcrop length of 2,900 m and maximum aperture of 7.2 m, and is composed of 35 distinct segments [*Delaney and Pollard*, 1981]. It is generally known that the single parent dike begins to break into several segments when it encounters a region in which the direction of least principal stress is rotated about the axis of propagation direction as illustrated in Figure 1.2 [*Delaney and Pollard*, 1981]. For this reason, the segments show oblique-segmented

geometric features relative to the parent dike, which is called *en echelon* (Figure 1.1c). On the basis of observations of the length of overlapping, large overlapping can be probably more often observed at the smaller scale [*Germanovich et al*., 1997a].

Hydraulic fractures are often segmented when the direction of propagation is parallel to the bedding planes (i.e., the fracture is perpendicular to the bedding planes). Figure 1.3a shows the cross section of eleven dikes exposed in a well-stratified sedimentary rock in the Ardon Formation, Makhtesh Ramon, Israel [*Baer*, 1991]. Individual segments have apertures of 0.5 to 3 m and length of 1 to 20 m. *Baer* [1991] stated that the fracture could be segmented because of host rock stratification, that causes different in-situ stresses and shear moduli between adjacent layers. Based on the segment boundary as well as fingers on the dike wall, as shown in Figure 1.3b, he found that the propagation direction of the dike is parallel to the bedding plane. He also stated that the stress concentration at the dike tip is affected by adjacent segments, stratification of the host rock, and slippage of the bedding plane.

The segmentation of sheet intrusions usually originates from characteristics of the inhomogeneous rock and the stress regime (e.g., change of principal stress direction). *Hoek* [1994] suggested a general classification of segmented igneous dikes based on the direction of extension and homogeneity of the host rock (Figure 1.4).

1.2.2 Veins

Veins are composed of one or more minerals that precipitated from the hydrothermal solution that flows through a rock by diffusion, advection, or hydraulic fracturing [*Fisher and Brantley*, 1992; *Bons*, 2000]. Although the formation of veins is

not clearly understood, it is likely to be highly dependent upon the subsurface structures such as voids, fractures, and faults. Various types of veins are found in nature. Figure 1.5 shows overlapping calcite veins in carbonaceous shale having fracture-like sets with side splays where the interaction between two veins is expected to change the stress field around the tips [*Bons*, 2000]. *En echelon* veins are found in rocks as well. Figure 1.6 shows two types of *en echelon* vein arrays. One array is oblique to the principal vein and the other is parallel to the principal vein. From the study by *Pollard* [1982] and *Olson and Pollard* [1991], sigmoid echelon vein formation (Figure 1.5) is attributed to the change in the stress field around the tip due to mechanical interaction between adjacent segments. Observations by *Beach* [1980] include a single vein with a zigzag trace (Figure 1.7).

1.2.3 Joints

Joints, the most common brittle structure in the Earth's crust [*Pollard and Aydin*, 1988], can be formed by remote extension or hydraulic fracturing [*Secor*, 1965]. Multiple joints are also commonly found in nature. Figure 1.8 shows the map view of three echelon joint traces on the bedding surface of Dakota sandstone with a distinct trace pattern. Joint sets A and B have a curving path that overlap, while those in the joint set in the lower part of the figure are relatively straight. *Olson and Pollard* [1989] suggested that these differences result from a different state of principal stresses that leads to local stress change due to mechanical interaction.

The study of a planar joint surface is another method to observe fracture patterns in joints if the cross section is not available. The fracture surface of the echelon types

shows stepwise features that link discrete segments with gradual or abrupt initiation of breakdown from a single joint (Figure 1.9). Figure 1.10 shows an idealized block diagram illustrating echelon crack formation initiating from the parent crack.

Figure 1.11a shows the surface of the non-planar parallel joint set in layered sedimentary rocks. Figure 1.11b is a schematic drawing illustrating the initiation point and propagation direction of a joint. The pre-existing joint in the upper layer (siltstone) is horizontal and the joint in the lower layer (shale) is segmented, initiating from its boundary. *Helgeson and Aydin* [1991] stated that if a relatively thick shale is jointed by the introduction of additional energy into the system, the new joints initiate at the vertical extent of a pre-existing joint in siltstone and usually propagate at a small angle relative to the joint in siltstone.

Figure 1.12a shows a well-exposed set of parallel joints in the dolomite layers of Argot stream, central Dead Sea basin. The significant mechanical interaction during formation can be expected because the spacing of the joints is relatively small compared to their thickness. In addition, a detailed investigation reveals that multi-level branching from a single joint in the main dolomite layer (bottom of Figure 1.12a) is present, indicating dynamic fracturing [*Sagy et al*., 2001]. Figure 1.12b shows two orthogonal joint sets with a relatively large spacing in the limestone layers of the Central Formation, Chimney Rock, Utah [*Bai and Pollard*, 2000].

1.2.4 Segmentation of mid-oceanic ridges

Detailed geological observations reveal that the mid-oceanic ridges are segmented by discontinuities, such as transform faults and overlapping spreading centers in the East

Pacific Rise (EPR) [e.g., *Macdonald and Fox*, 1983; *Langmuir et al*., 1986; *Sempere and Macdonald*, 1986b; *Lonsdale*, 1989; *Macdonald et al*., 1991] as well as in the Mid-Atlantic Ridge (MAR) [e.g., *Weiland et al*., 1996]. Figure 1.13 shows the EPR that is discontinuous at the orthogonal transform fault. At a smaller scale, echelon types of numerous segments, called overlapping spreading centers, are found by magnifying the circles in Figure 1.13. They indicate that the mid-oceanic ridges have a hierarchical segmentation [*Macdonald et al*., 1991]. Figure 1.14 and Table 1.1 show this feature as found in mid-ocean ridges. The transform fault corresponds to the first-order discontinuity that can be found at fast- and slow-spreading ridges. Overlapping spreading centers (Figure 1.14a) and oblique shear zones (Figure 1.14b) are second-order discontinuities for fast-and slow-spreading ridges, respectively. In a few papers, these overlapping spreading centers have been modeled by fractures in the sea floor [e.g., *Pollard and Aydin*, 1984; *Sempere and Macdonald*, 1986a; *Macdonald et al*., 1991]. These third- and fourth-order discontinuities for ridges are summarized in Table 1.1.

Table 1.1 Hierarchical characteristics of mid-oceanic ridge segmentation [*Macdonald et al*., 1991]. Contents inside parenthesis are for a slow spreading ridge.

Order	Discontinuity	Segment length (km)	Offset (km)
1	transform fault large propagating rifts	600±300 (400±200)	> 30
2	overlapping spreading centers (oblique shear zones, rift valley jogs)	140±90 (50±30)	2 to 30
3	overlapping spreading centers (intervolcano gaps)	50±30 (15±10)	0.5 to 2
4	devals, offsets of axial caldera (intervolcano gaps)	14±8 (7±5)	< 1

1.3 Multisegmented hydraulic fractures in laboratory experiments

Laboratory experiments of hydraulic fracturing have provided insight into the mechanisms of propagating hydraulic fractures with well-controlled parameters. Since the contributions from the field scale are still limited, many laboratory experiments have been performed to understand complicated hydraulic fracturing behavior, in particular near a wellbore.

Numerous papers have been devoted to laboratory experiments of hydraulic fracturing, investigating the dimensions of hydraulic fractures, and identifying the mechanisms of fracture growth. Examples include hydraulic fractures in a relatively homogeneous material [*Hubbert and Willis*, 1957; *Medlin and Massé*, 1984], in layered formations [*Hubbert and Willis*, 1957; *Daneshy*, 1978; *Van Eekelen*, 1982; *Teufel and Clark*, 1984], in a horizontal wellbore or a wellbore deviated from a preferred fracture plane [*Veeken et al.*, 1989; *Hallam and Last*, 1991; *Weijers et al*., 1994; *Abass et al*., 1996], and in particulate materials [*Murdohk*, 1992, 1993a; *Panah and Yanagisawa*, 1989; *Dijk et al*., 2003; *Chang et al*., 2003], interacting with pre-existing fractures [*Lamont and Jessen*, 1963; *Anderson*, 1981; *Hanson et al*., 1981; *Blanton*, 1982, *Blair et al*., 1990], and propagating under hydrostatic conditions [*Takada*, 1990]. This section focuses on observations of multisegmented hydraulic fractures in laboratory experiments that simulate various field conditions.

1.3.1 Multisegmented hydraulic fractures in homogeneous materials

The results of many experiments have clearly shown the existence of multisegmented hydraulic fractures. *Hubbert and Willis* [1957] found that hydraulic fractures propagate in the plane that is normal to the least compressive stress (Figure 1.15). In this historic experiment, a gelatin material was used for the solid with a simulated wellbore. A hydraulic fracture with a height of 22 cm was formed by injecting slurry of a Plaster of Páris as a fracturing fluid into a pre-stressed sample. Although the authors did not focus on fracture segmentation and viewed their hydraulic fracture (Figure 1.15) as a single wing, fracture segmentation and overlapping with an offset in the fracture front can be observed even in this rather homogeneous material (Figure 1.15). In practice, it is anticipated that MHF can be already produced near a wellbore (refer to section 1.3.3 below) and continue to grow to the far-field as well (i.e., it reshapes, with some coalescence) with further stimulation. In *Hubbert and Willis*'s [1957] experiment, the formation of MHF may be attributed to the generic characteristics of unstable fracture growth [*Germanovich et al*., 1997a] or mode III mechanisms of fracture segmentation [*Pollard et al*., 1982; *Cooke and Pollard*, 1996].

To find nonlinear effects in hydraulic fracture propagation, *de Pater et al*. [1994] conducted experiments in a homogeneous sandstone with varying injection rate and confining stress. After performing these experiments, the sample blocks were cut into thin sections parallel to the borehole. Figure 1.16a shows the microscope image displaying multiple fractures predominantly through the rock matrix.

Dudley et al. [1995] conducted an extensive laboratory investigation of hydraulic fracturing to identify various fracture mechanisms that may also affect and control the

growth of large-scale hydraulic fractures in the field. The observed patterns of hydraulic fracture growth in sandstone specimens are fracture branching, bridging of the fracture faces, and formation of microfractures in the vicinity of the main fracture surface (Figure 1.16b).

Takada [1990] conducted an experimental study on the propagation of liquid-filled fractures in gelatin under hydrostatic conditions. He stated that when the total injection volume exceeds a critical value, segmentation of an isolated fracture begins to occur because of an enlarged irregular surface at the upper end of the fracture (Figure 1.17). Consequently, increased excess pressure makes fracture propagation locally unstable, inducing the rotation of principal stress, dynamic branching, and viscous fingering at the upper end.

1.3.2 Hydraulic fracture propagation in heterogeneous materials

It is expected that multiple segments are more likely to form in experiments in heterogeneous materials than in homogeneous media. The interfaces and discontinuities, such as joints, fissures, faults, and bedding planes, that are the most common features in natural rocks, affect hydraulic fracture growth in conjunction with tectonic stress. *Anderson* [1981] and *Hanson et al*. [1981] have performed laboratory experiments to study the effects of frictional properties of unbonded interfaces on the growth of hydraulic fractures in rocks. They found that a sudden change in the frictional properties of an interface can cause lateral offset at the interface. For example, Figure 1.18a shows the result of an experiment conducted by *Hanson et al*. [1981] to identify the effect of low friction on the hydraulic fracture growth across an unbonded interface. The three-

block limestone has been stacked in a press. An internal pressure was applied to force the fractures to propagate across the interfaces. The upper interface has lower frictional properties than the lower one. As a result, hydraulic fracture propagated across the upper interface with a lateral offset, while it propagated directly through the lower interface. This result shows that frictional properties at the interface affect the geometry of fracture growth. Figure 1.18b also shows the continuous and discontinuous fracture crossing of the unbonded frictional interface in the anchoring cement [*Renshaw and Pollard*, 1995].

Blanton [1982] also performed a hydraulic fracturing laboratory experiments in both Devonian shale and hydrostone. He concluded that the growth of hydraulic fractures is strongly influenced by natural fractures. Hence, in most cases the hydraulic fracture were either diverted or arrested by the pre-existing fractures.

Therefore, the above mentioned hydraulic fracturing experiments on heterogeneous materials suggest that diversion and offset may often occur. Indeed, symmetrical and single planar fractures are rarely expected in naturally fractured environments (e.g., petroleum reservoirs).

1.3.3 Segmentation by mixed mode loading

In conventional fracture mechanics, fracture propagation depends on three mode types (Figure 1.19). Generally, mode I (i.e., opening mode) is responsible for the fracture growth (Figure 1.19a), mode II (i.e., in-plane shear) is responsible for the fracture direction (Figure 1.19b), and mode III (i.e., anti-plane shear) is responsible for the fracture segmentation (Figure 1.19c). In reality, fractures usually propagate with all three modes combined. In particular, the formation of MHF is often associated with mode III.

One example was discussed in section 1.2. The rotation of the least principal stress, as shown in Figure 1.2, corresponds to the occurrence of mode III loading.

Figure 1.20 illustrates the procedure of a laboratory experiment of hydraulic fracturing to create segmentation in an acrylic cylinder. First, fluid is injected into the hole (Figure 1.20a) to create a horizontal fracture (Figure 1.20b). Then, additional fluid is injected while the specimen is loaded in torsion (Figure 1.20c), resulting in fracture segmentation (Figure 1.20d). Figure 1.21 shows the injection pressure response during the fracture segmentation process. For a single radial fracture, the injection pressure is expected to decrease after the fracture propagates [*Economides and Nolte*, 2000]. However, in this experiment, the injection pressure increases.

Knauss [1970] also observed the initial stage of crack segmentation in a brittle material by anti-plane shear (Figure 1.22).

Hydraulic fracture stimulations of horizontal or deviated wellbores indicate an increased likelihood of MHF, compared to vertical wellbores. This is because the direction of the wellbore may easily deviate from the maximum principal stress direction. This causes pronounced anti-plane shear during fracture propagation. Many laboratory experiments have shown that if a horizontal wellbore or deviated wellbore direction does not coincide with the preferred fracture plane, the geometry of hydraulic fracturing is tortuous and non-planar. This results in a loss of well productivity [e.g., *Veeken et al*., 1989; *Hallam and Last*, 1991]. These phenomena were observed by *Abass et al*. [1996], who conducted an experimental study on a prismatic gypsum cement block with dimensions of 6×6×10 in (15.2×15.2×25.4 cm) and varied angles between the borehole and maximum horizontal stress. They observed that the non-planar fractures (e.g.,

multiple fractures, re-oriented fractures, and T-shaped fractures) were created if the wellbore orientation was not parallel to the direction of the maximum horizontal stress. For example, when the orientation angle is 60° relative to the maximum horizontal stress, the fracture surface shows pronounced steps initiated from the wellbore (Figure 1.23). This results in multiple fractures directed away from the wellbore.

1.4 Industrial multisegmented hydraulic fractures

Direct observations from mineback experiments and overcored hydraulic fractures in the field also reveal that hydraulic fractures rarely, if ever, propagate as a single planar feature. Hydraulic fracturing is commonly conducted at the field scale for degasification from coal beds in advance of mining. Hence, it is possible to make a detailed mapping of exposed hydraulic fractures in a coal seam by mining operations. The overcored samples cutting through hydraulic fracture sections are also good sources to observe hydraulic fracturing behavior. Accordingly, some researchers have investigated hydraulic fracturing behavior through mineback experiments [*Diamond and Oyler*, 1987; *Palmer and Sparks*, 1991; *Jeffrey et al*., 1994, 1995; *Jeffrey*, 1996; *Jeffrey and Settari*, 1998; *Warpinski*, 1985; *Warpinski and Teufel*, 1987] while others studied overcored fracturing samples [*Warpinski et al*., 1993a, 1993b; *Fast et al*., 1994].

1.4.1 Mineback experiments

Warpinski [1985] measured the aperture and pressure in a propagating hydraulic fracture at the Department of Energy (DOE) Nevada test site in an existing tunnel

complex. He concluded that the pressure drop along the fracture is caused by the tortuosity of the fracture path, the roughness of the fracture surfaces, multiple fractures, and sharp curvature in the flow path resulting from geologic discontinuities. Multiple fracture strands were observed, regardless of rock type and stress regime.

Diamond and Oyler [1987] mined and observed the areas in coalbeds and surrounding strata affected by 22 stimulation treatments. Multiple vertical fractures were found in 12 areas, and multiple horizontal fractures in 7 out of 22 areas. Figure 1.24 shows that *en echelon* vertical fractures are filled with sand and extend from the roof down into the coalbed near the borehole.

Palmer and Sparks [1991] observed the height and width of hydraulic fractures in Black Warrior basin coalbeds in Alabama. They used downhole visual logging to better understand fracturing behavior. Multiple fractures in the coal seam and fracture offset at interfaces between coal and rock were found. Figure 1.25 shows one of the propped fractures in the coal seam and surrounding rock strata through downhole visual logging. Although the boundary between coal and rock could not be clearly identified (Figure 1.25), the authors expected that the widest mid-fracture would be generated in a coal seam because coal is soft and weak, compared to the host rock.

1.4.2 Overcored samples

Direct observations from cored hydraulic fracture, also confirm that multiple fractures are an overwhelming occurrence rather than an exception. *Warpinski et al*. [1993a] investigated cored hydraulic fractures obtained from the highly anisotropic reservoir in the Piceance basin near Rifle, Colorado. This core includes two fracture

intervals containing multiple fractures as illustrated in Figure 1.26. The first primary interval (HF-1) contains 30 multiple fractures spread out over 4 ft of core. The secondary interval (HF-2), offset by 60 ft horizontally and 17 ft vertically from the primary fracture interval, contains 8 multiple fractures over 3 ft. Some fractures are terminated or initiated with multiple fractures at the bedding plane of both intervals. The authors also emphasized that for more complex the reservoirs, the fracturing becomes more complex.

The inclined cored sample (235 ft) shown in Figure 1.27 was used to investigate hydraulic fractures of Opal-A diatomite at Lost Hills Field, California [*Fast et al*., 1994]. Seven propped fractures and two non-propped fractures were found. The additional fracture identified at 2,707 ft was found by a microresistivity log test without coring. Three propped fractures identified at 2,265.5, 2,266.5, and 2,267.0 ft were branched from the same well, based on the evidence that they have the same proppant material. The author inferred that the two non-propped fractures at 2,252.7 and 2,289.7 ft are natural fractures or fractures generated by water injection in a nearby well. The other fractures are created after near well treatment.

1.5 Modeling multisegmented hydraulic fractures

In this section we consider the Perkins-Kern-Nordgren (PKN) model that has been widely employed in hydraulic fracturing treatment and design [*Gidley et al*., 1989; *Economides and Nolte*, 2000]. After reviewing the conventional PKN model for a single hydraulic fracture (section 1.5.1), we describe the PKN model for MHF by *Germanovich et al.*, [1997b, 1998a]. The advantage of considering the PKN model is that in addition to

being practically important, it also provides most of the results in the closed mathematical form. This, in turn, allows to clearly analyze the importance of studying hydraulic fracturing segmentation.

1.5.1 Conventional PKN model

The conventional PKN model is based on a single vertical fracture with constant height H (Figure 1.28), perhaps, due to higher horizontal stress above and below the pay zone. The fracture is at a state of plane strain and the fluid pressure inside the fracture is constant in each vertical cross section perpendicular to the propagation direction. It is assumed that there is no fracture toughness, so that the resistance to the fracture propagation is due to the frictional losses in the fracturing fluid.

Following *Nordgren* [1972], the continuity equation for the volume of the fracture with an incompressible fluid can be expressed as

$$\frac{\partial q}{\partial x} + \frac{\partial A}{\partial t} = 0 \qquad (0 < x < L(t), \quad t > 0) \tag{1.1}$$

where q is the flow rate inside the fracture, A is the cross-sectional area of the fracture, $L(t)$ is the fracture length at time t. For simplicity, the case of no fluid leakoff is considered here. The flow rate for laminar flow of a Newtonian viscous fluid in an elliptical cross section can be expressed as

$$q = -\frac{\pi W^3 H}{64\eta}\frac{d\Delta p}{dx} \tag{1.2}$$

where Δp is the net pressure, η is the dynamic viscosity of the fracturing fluid,

$$W = \frac{(1-\nu)H}{G}\Delta p \tag{1.3}$$

is the maximum fracture aperture at a given vertical cross section, G is the shear modulus of the rock. Accordingly, the elliptic cross sectional area of the fracture is

$$A = \frac{\pi}{4}WH \tag{1.4}$$

Expressions (1.1) – (1.4) represent a set of four equations with four unknowns (q, A, W, and Δp). This set is typically solved with the following four boundary and initial conditions [e.g., *Kemp*, 1990]:

1. The flow rate q_{in} is constant at the wellbore:

$$q(0,t) = q_{in} \tag{1.5}$$

2. The fracture is initially closed:

$$W(x,0) = 0 \tag{1.6}$$

3. The fracture is closed at the tip:

$$W(L(t),t) = 0 \qquad (t > 0) \tag{1.7}$$

4. The velocity of the fracturing fluid at the tip is equal to that of fracture propagation:

$$\frac{dL}{dt} = \frac{q}{A} \qquad (x \to L(t) - 0, \quad t > 0) \tag{1.8}$$

Conditions (1.5) – (1.8) assure that the set of equations (1.1) – (1.4) has a unique solution [*Kemp*, 1990]. In particular, the closed-form solution for the fracture length, aperture, and net pressure are given by

$$L(t) = Q^{\frac{3}{5}}\left(5K\frac{t}{\lambda}\right)^{\frac{4}{5}} \tag{1.9}$$

$$W(\xi,t) = \left(QL(t)\right)^{\frac{1}{4}}\psi(\xi) \qquad (0 \le \xi \le 1) \tag{1.10}$$

$$\Delta p(\xi,t) = \frac{G}{(1-\nu)H}W(\xi,t) \tag{1.11}$$

where $\lambda \approx 3.531$ is a transcendental constant, $\xi = x/L$ is the dimensionless coordinate, and

$$K = \frac{G}{64(1-\nu)\eta H}, \quad Q = \frac{256(1-\nu)\eta}{\pi G}q_{in} \tag{1.11a}$$

Function $\psi(\xi)$ was first obtained by *Kemp* [1990]. After a small correction [*Germanovich et al*., 1998a] it can be written as

$$\psi(\xi) = \left[(1-\xi)^{\frac{4}{3}}\frac{152165744640}{189101759857}\left(1-\frac{1}{24}(1-\xi)+\frac{67}{32256}(1-\xi)^2-\frac{163}{2322432}(1-\xi)^3 + \frac{709537}{811550638080}(1-\xi)^4\right)\right]^{\frac{1}{4}}$$

$$(0 \le \xi \le 1) \tag{1.12}$$

These are the main parameters used in the hydraulic fracturing design.

1.5.2 PKN model for multisegmented hydraulic fractures

The first PKN model for MHF was derived by *Germanovich et al*. [1997b, 1998a] and studied in detail by *Astakhov* [2000]. In this model, a single PKN model is extended to the case of MHF with *N* segments by incorporating the effect of segment interaction to evaluate the aperture of the interacting segments. The vertical cross section of MHF

consists of N single PKN "models" to represent the geometry of the MHF (Figure 1.29). The nth segment has a height of h_n while H is the total height of the MHF. It is assumed that (1) the total fluid flow pumped into the fracture is redistributed into the segments, so that the flow in each segment is determined as a part of the solution, and (2) there is a good pressure communication between the segments, that is, the fluid pressures are equal in each vertical cross section of each segment.

The total flow of the fracturing fluid and the fracture cross sectional area are

$$q = \sum_{n=1}^{N} q_n \tag{1.13}$$

$$A = \sum_{n=1}^{N} A_n \tag{1.14}$$

where

$$q_n = -\frac{2c_n}{3\eta}\left(\frac{d\Delta p}{dx}\right)\int_{-h_n/2}^{h_n/2}\left(\frac{W_n(z)}{2}\right)^3 dz\,, \tag{1.15}$$

and

$$A_n = \int_{-h_n/2}^{h_n/2} W_n(z)dz \tag{1.16}$$

are the flow rate inside the nth segment and the area of the nth interacting segment, respectively.

Instead of equations (1.1) – (1.4), describing a non-segmented PKN fracture, we now have:

$$\frac{dq}{dx} + \frac{dA}{dt} = 0 \tag{1.17}$$

$$q = -\frac{\pi W_{eff}^3 H}{64\eta_{eff}} \frac{d\Delta p}{dx} \tag{1.18}$$

$$W_{eff} = \frac{(1-\nu)H}{G_{eff}} \Delta p \tag{1.19}$$

$$A = \frac{\pi}{4} W_{eff} H \tag{1.20}$$

where the effective parameters of MHF (marked by "*eff*") are given in Table 1.2. The boundary conditions (1.5) – (1.8) remain the same in the case of MHF:

$$q(0,t) = q_{in}, \quad W_{eff}(x,0) = 0, \quad W_{eff}(L(t),t) = 0, \quad \frac{dL}{dt} = \frac{q}{A} \quad (x \to L(t) - 0) \tag{1.21}$$

Since equations (1.1) – (1.4) and (1.9) – (1.12) coincide in form, the solution of (1.17) – (1.20) can immediately be written from (1.9) – (1.11) by replacing the corresponding symbols:

$$L(t) = Q_{eff}^{\frac{3}{5}} \left(5K_{eff} \frac{t}{\lambda} \right)^{\frac{4}{5}} \tag{1.22}$$

$$W_{eff}(\xi,t) = \left(Q_{eff} L_{eff}(t)\right)^{\frac{1}{4}} \psi(\xi) \tag{1.23}$$

$$\Delta p(\xi,t) = \frac{G_{eff}}{(1-\nu)H} W_{eff}(\xi,t) \tag{1.24}$$

The effective parameters Q_{eff} and K_{eff} are also given in Table 1.2. Note that in Table 1.2, W^{max} is the maximum aperture in the MHF under consideration, and $W_0^{\max}$ is the aperture (in the center) of a single fracture of size H loaded by the same pressure Δp as the MHF.

As can be seen from Table 1.2, the dimensionless coefficients b_1, b_2, and β depend on the interaction of the segments. To quantify the effect of interaction, the parameters obtained above are compared with those of a single fracture (of the same total height H) and the non-interacting model, in the case of MHF with N = 19 and 81 segments (Figures 1.30 and 1.31). The overlap and offset are assumed to be $a = 0.1h$ and $b = 0.2h$, respectively (Figure 1.29). It can be seen that the net pressure can be overestimated by an order of magnitude if the interaction is ignored (Figures 1.30 and 1.31). If the number of segments increases, the error becomes more significant. This result indicates that the effect of interaction needs to be taken into account.

Table 1.2 Summary of formulae for multisegmented hydraulic fractures in the case of no leakoff.

Parameter	Formula
Maximum aperture, $W^{\max}(\xi, t)$	$W^{\max}(\xi,t) = W_{eff}(\xi,t)\dfrac{\beta}{b_1}$
Effective viscosity, η_{eff}	$\eta_{eff} = \dfrac{b_1^3}{b_2}\eta$
Effective shear modulus, G_{eff}	$G_{eff} = \dfrac{1}{b_1}G$
Effective parameter, K_{eff}	$K_{eff} = \dfrac{G_{eff}}{64(1-\nu)\eta_{eff}H} = \dfrac{G}{64(1-\nu)\eta H}\dfrac{b_2}{b_1^4} = K\dfrac{b_2}{b_1^4}$
Effective parameter, Q_{eff}	$Q_{eff} = \dfrac{256(1-\nu)\eta_{eff}}{\pi G_{eff}}q_{in} = \dfrac{256(1-\nu)\eta}{\pi G}q_{in}\dfrac{b_1^4}{b_2} = Q\dfrac{b_1^4}{b_2}$
Normalized cross sectional area of MHF, b_1	$b_1 = \dfrac{A}{A_0} = \dfrac{2}{\pi}\sum_{n=1}^{N}\dfrac{h_n}{H}\int_{-1}^{1} w_n(\zeta)d\zeta$
Normalized total fluid flow through MHF, b_2	$b_2 = \dfrac{q}{q_0} = \dfrac{8}{3\pi}\sum_{n=1}^{N}\dfrac{h_n}{H}\int_{-1}^{1} w_n(\zeta)^3 d\zeta$
Normalized maximum aperture of MHF, β	$\beta = \dfrac{W^{\max}}{W_0^{\max}}$
Dimensionless aperture, $w_n(z)$	$w_n(z) = \dfrac{W_n(z)}{W_0^{\max}}$
Dimensionless coordinates	$\xi = \dfrac{x}{L},\ \zeta = \dfrac{z}{h_n/2}$
Area of a single fracture with height of H, A_0	$A_0 = \dfrac{\pi}{4}HW_0^{\max}$
Total fluid flow through a single MHF of height H, q_0	$q_0 = -\dfrac{\pi(W_0^{\max})^3 H}{64\eta}\dfrac{d\Delta p}{dx}$

1.5.3 Importance of hydraulic fracturing segmentation

In hydraulic fracturing treatment (Figure 1.32a), fractures created by fluid pumping are invisible since they are located in the subsurface strata and connected to the surface only by a narrow wellbore. The pressure response versus time is the main measurable parameter at the borehole or ground surface during pumping (Figure 1.32b). From this pressure curve, the created fracture geometry needs to be inferred. This is a basic, fundamental issue in the hydraulic fracturing treatment [e.g., *Economides and Nolte*, 2000].

Figure 1.33 illustrates the standard concept of inferring the fracture geometry from the pressure curve. The initial pressure decrease at stage 1 indicates radial fracture shape. The pressure increase at stage 2 suggests PKN type of fracture propagation between the pay zones. The gradual pressure increase at stage 3 is interpreted as further fracture propagation mostly as a PKN fracture, but also somewhat beyond the pay zone. An example based on the field data in Figure 1.34 suggests that the generated fracture geometries are of radial and PKN types during the pumping of the fluid.

The uncertainties associated with this type of analysis can be shown using the laboratory experiments shown in Figure 1.20. Observing pressure curve in Figure 1.21 and following the conventional pressure analysis (Figure 1.33), one should infer fracture geometry close to the PKN type (stage 3 in Figure 1.33). In actuality, however, the fracture was almost radial but segmented (Figure 1.20d). In this experiment, the segmentation constrained the fluid flow inside the fracture diminishing the pressure decrease that should have been otherwise observed for radial geometry (Figure 1.33).

Therefore, by ignoring the segmentation, it is likely that an incorrect fracture geometry is inferred from the pressure curve.

The existence of the MHF is a critical issue that needs to be considered for more reliable design [e.g., *Lehman and Brumley*, 1997; *Mahrer*, 1999], because there are discrepancies between field data and conventional simulations. Observed symptoms attributed to hydraulic fracture segmentation include elevated net pressure, shortening propped length, reduced individual fracture width with increased potential for screenouts, increased leakoff, and less reliable fracture confinement within the pay zone [*Medlin and Fitch*, 1983; *Davidson et al*., 1993; *Stadulis*, 1995; *Hainey and Weng*, 1995; *Wright et al*., 1995; *Lehman and Brumley*, 1997; *Germanovich et al*., 1998a; *Mahrer*, 1999; *Sato et al*., 1999; *Economides and Nolte*, 2000].

1.6 Goal and structure of thesis

Hydraulic fracturing is an important and abundant process in both industrial applications and natural environments. The formation of hydraulic fractures includes nucleation, growth, and termination in numerous rock types and stress regimes, at scales ranging from microns to many kilometers. As a result, the fractures show complicated geometries, which reflects the complexity of the underlying physical mechanisms. Fracture segmentation, commonly observed at all scales and in all materials, contributes to this complexity in many ways. In particular, the mechanical interaction of fracture segments as well as the interaction of a fracture with other fractures, the Earth's surface,

and pre-existing geological discontinuities strongly affect almost all hydraulic fracturing processes.

The main goal of this thesis is to understand the effects of mechanical interaction in and between complex natural and industrial hydraulic fractures at different spatial scales. For this purpose, mathematical models are developed to quantify the elastic interaction of these features.

A typical field case of a highly segmented vein is studied. For this well-mapped and, therefore, well constrained example, we test whether the simplest constitutive model, based on an ideal elastic material, captures the complex behavior of multisegmented fractures.

In most cases, very little, if any, direct measured data on fracture and material properties is available. In such situations, the system needs to be constrained by the available indirect data. Consequently, using the simplest model (i.e., based on elastic theory) is often the most straightforward option to conduct a sufficiently detailed parametric analysis.

An important example of such a weakly constrained case involving hydraulic fracturing is diking beneath the seafloor at mid-oceanic ridges. In this case, the common scenario of a dike propagating from the center of the pressurized magma chamber to the ocean floor is not consistent with conventional fracture mechanics due to the fact that the chamber has the shape of a thin lens. Even at this large scale (i.e., a kilometer or more), the mechanical principle of elastic interaction has a good potential to describe the observations. The dikes that initiate from the subsurface magma chamber, and the magma

chamber itself, can be considered as mechanically interacting segments in an elastic half-space bounded by the seafloor.

The detailed structure of this thesis is as follows:

Chapter I, *Introduction*, describes the topic of the research, provides literature review, and formulates the goal of this study.

Chapter II, *Mathematical Modeling of Multisegmented Hydraulic Fractures*, provides essential tools to evaluate the elastic interaction between the fracture segments. The boundary collocation method is employed for this purpose. The parallelized numerical code based on the boundary collocation method is developed for multiple interacting fractures. Displacements and displacement discontinuities are compared with available and obtained analytical solutions to verify the developed numerical code. It is shown that the required number of collocation points can be decreased by an order of magnitude without loosing the accuracy of calculations. This made the problems considered in the subsequent chapters treatable.

Chapter III, *Modeling Natural Multisegmented Hydraulic Fractures*, discusses the calibration of the net pressure by computing the apertures of highly segmented natural calcite veins in the field. The effect of elastic interaction between the segments is considered using the developed numerical code at three different spatial scales: microscale, mesoscale, and macroscale. For comparison, the case of non-interaction is also considered. For simplified approach, a concept of the effective fracture (with the same overall size or length as the real fracture) has been tested.

Chapter IV, *Diking Processes at Mid-Oceanic Ridges*, studies dike propagation from a magma chamber beneath the seafloor. Based on the thin melt lens model of an

axial magma chamber, two mechanisms of dike evolution from the magma lens (pressurization and depressurization of the magma chamber) are simulated to understand the relationships among the hydrothermal system, dike emplacement, and magma replenishment. To accomplish this, the developed model quantifies the mechanical interaction of magma lenses and dikes with the seafloor. The obtained results show that the dike-seafloor interaction is a key mechanism affecting dike propagation at mid-oceanic ridge environments.

Chapter V, *Conclusions and Recommendations for Future Work*, summarizes the results obtained in the previous chapters and presents recommendations for future work.

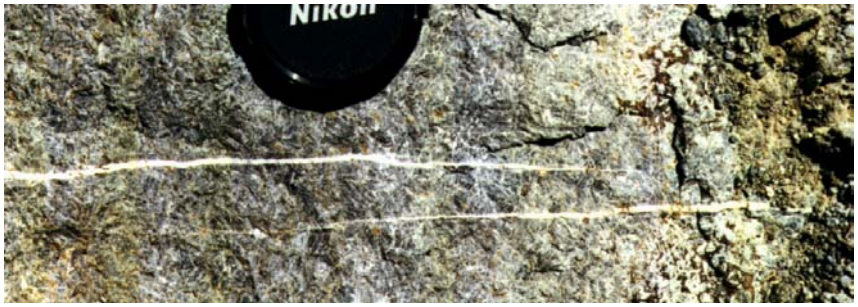

(a)

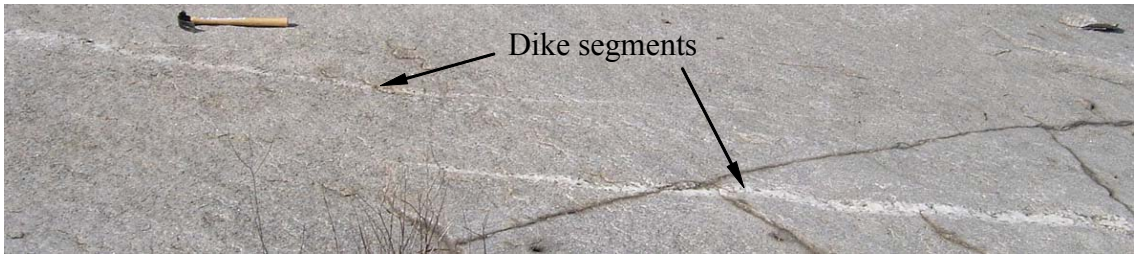

(b)

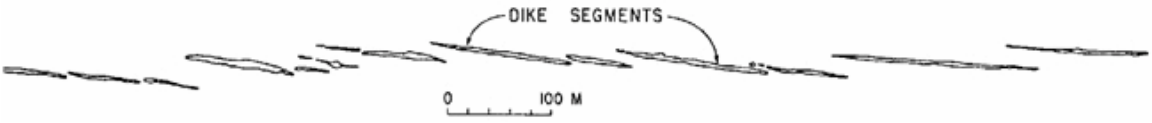

(c)

Figure 1.1 Segmentation with overlapping in a dike at various scales: (a) granitoid dike segments propagating through the Glen Mountain Gabbro at a scale of centimeter in Wichita Mountains, Oklahoma [*Germanovich et al*., 1997a]; (b) Pegmatite dike segments through older granite at a scale of several meter in East Quarry of Stone Mountain, Georgia; and (c) Minette dike segments at a scale of several kilometer near Ship Rock, New Mexico [*Pollard*, 1978].

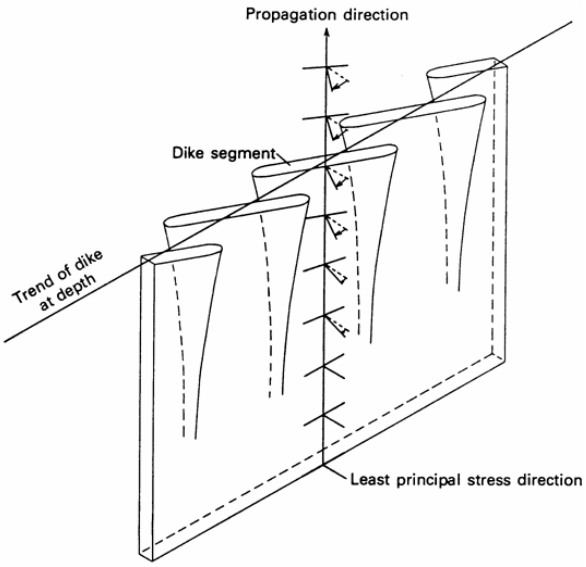

Figure 1.2 Formation of segmented dike due to rotation of the least compressive stress direction [*Delaney and Pollard*, 1981].

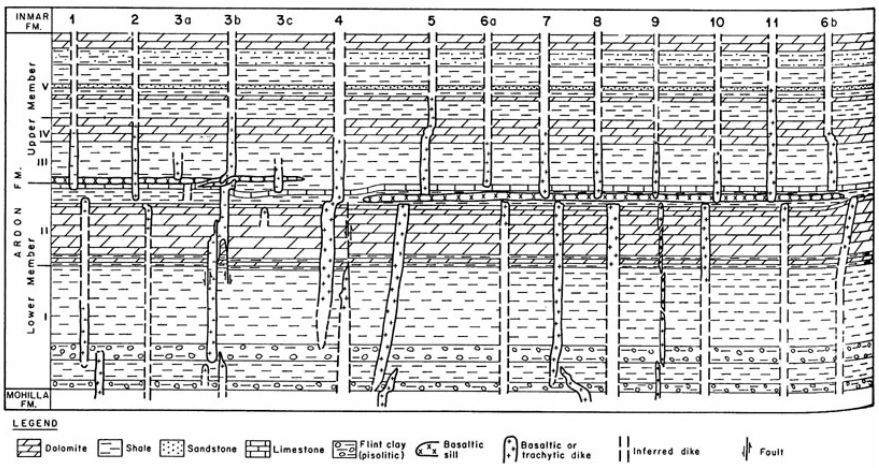

(a)

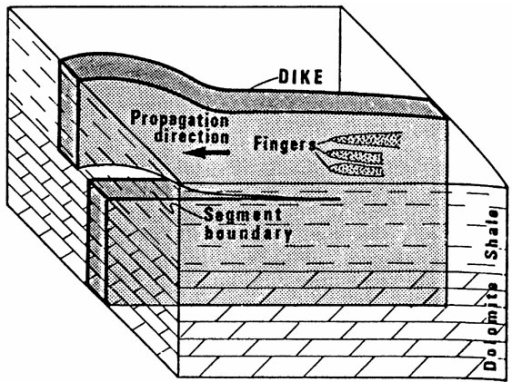

(b)

Figure 1.3 Dikes exposed in the Ardon Formation, Makhtesh Ramon, Israel [*Baer*, 1991]: (a) cross section of eleven dikes, and (b) mechanism of segmentation and direction of propagation parallel to the bedding plane.

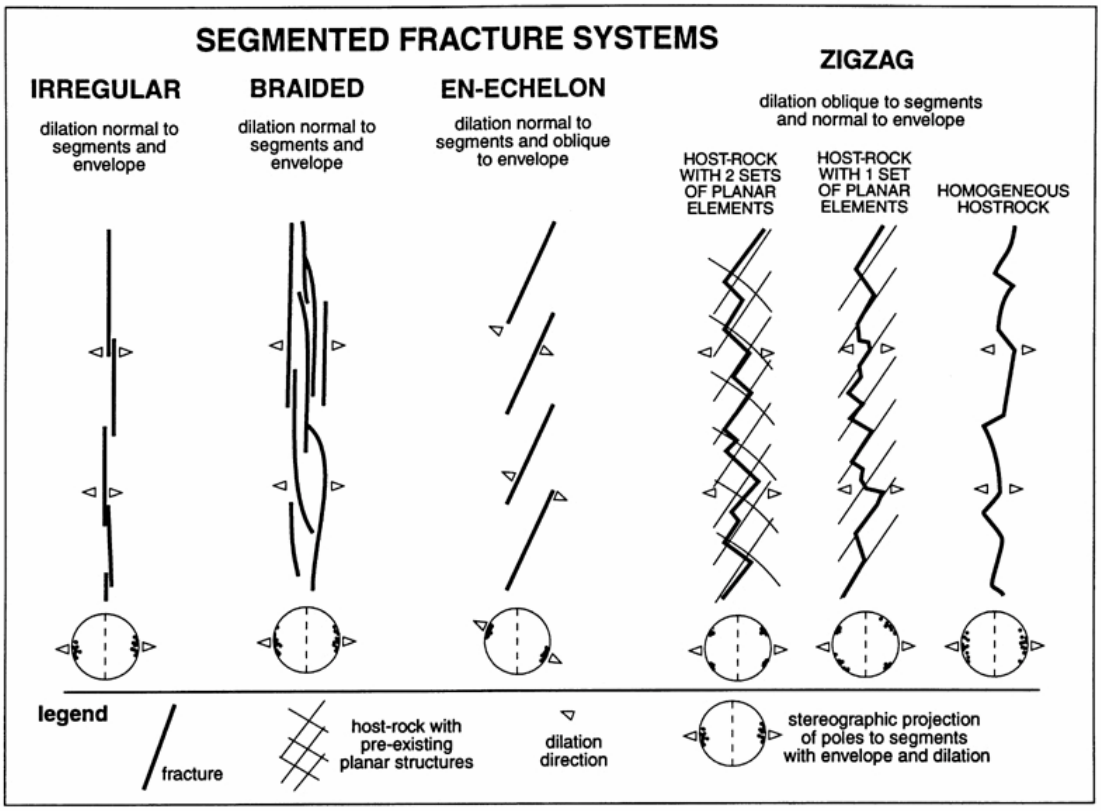

Figure 1.4 Classification of segmented igneous dikes [*Hoek*, 1994].

Figure 1.5 Overlapping calcite veins in Tapley Hill Formation, Opaminda Creek, Arkaroola, South Australia [*Bons*, 2000].

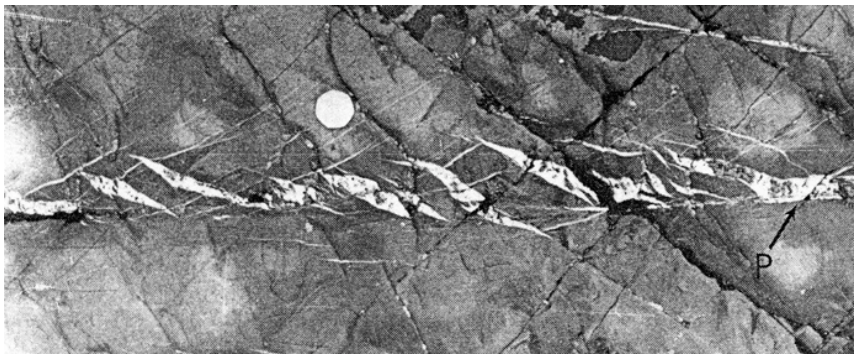

(a)

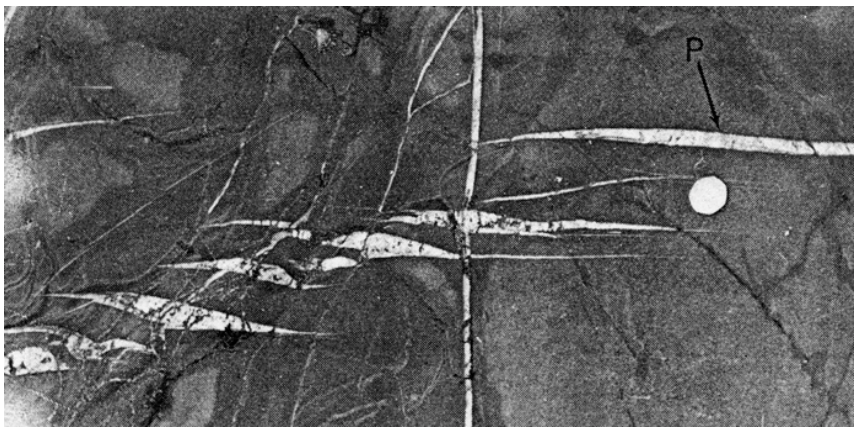

(b)

Figure 1.6 Two types of echelon veins in Millook Haven, S.W. England [*Beach*, 1977]: (a) echelon array oblique to the principal vein, and (b) echelon array parallel to the principal vein. "P" indicates principal vein.

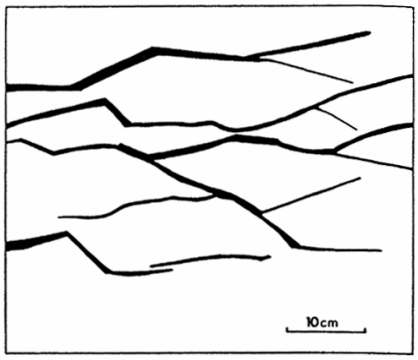

Figure 1.7 Irregular zigzag Geometric forms in a vein from Carboniferous flych, Millook Haven, N. Cornwall, England [*Beach*, 1980].

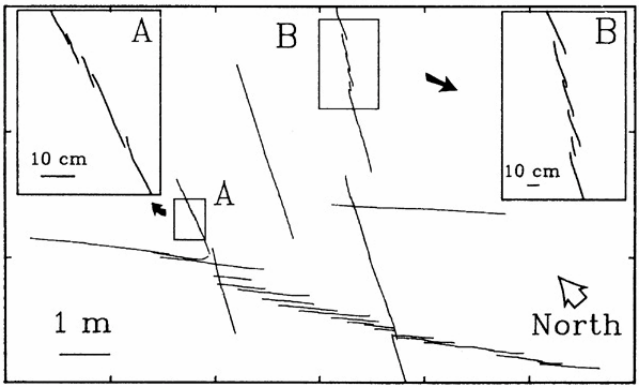

Figure 1.8 Map view of three joint traces in Dakota sandstone, Coal cliffs, central Utah [*Olson and Pollard*, 1989].

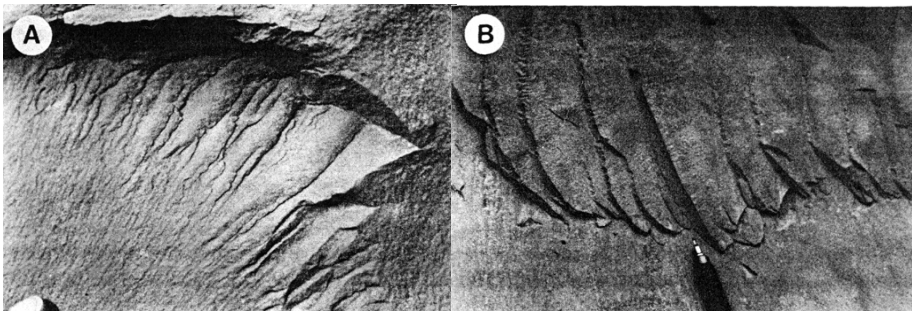

Figure 1.9 Echelon fracture surface [*Pollard and Aydin*, 1988]: (a) gradual initiation of breakdown in sandstone, and (b) abrupt initiation of breakdown in limestone.

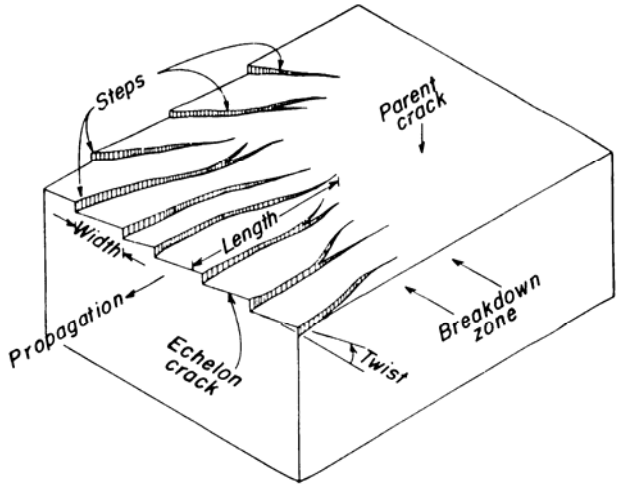

Figure 1.10 Abrupt initiation of breakdown in limestone [*Pollard et al*., 1982].

(a)

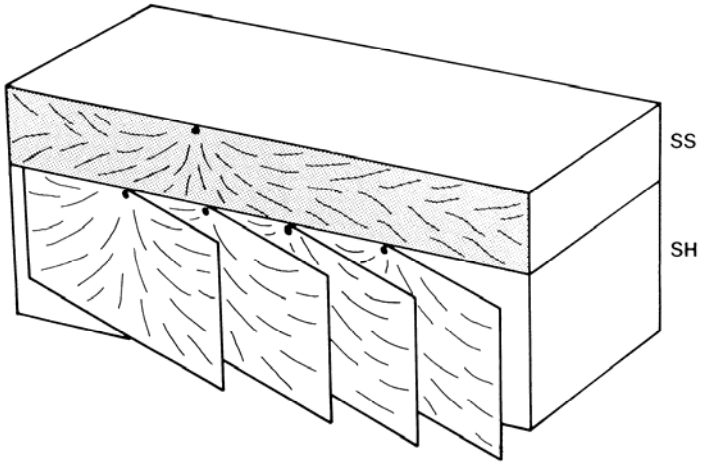

(b)

Figure 1.11 Non-planar parallel joint set in layered sedimentary rocks from the Appalachian Plateau near Finger Lakes, central New York: (a) photo of non-planar parallel joint set [Courtesy of *Carter*], and (b) schematic drawing of a joint surface with initiation point [*Helgeson and Aydin*, 1991].

(a)

(b)

Figure 1.12 Multiple joint set: (a) parallel joints set in the dolomite layer of Argot stream, central Dead Sea basin [*Sagy et al*., 2001], and (b) two orthogonal joint sets in the limestone layers of the Central Formation, Chimney Rock, Utah [*Bai and Pollard*, 2000].

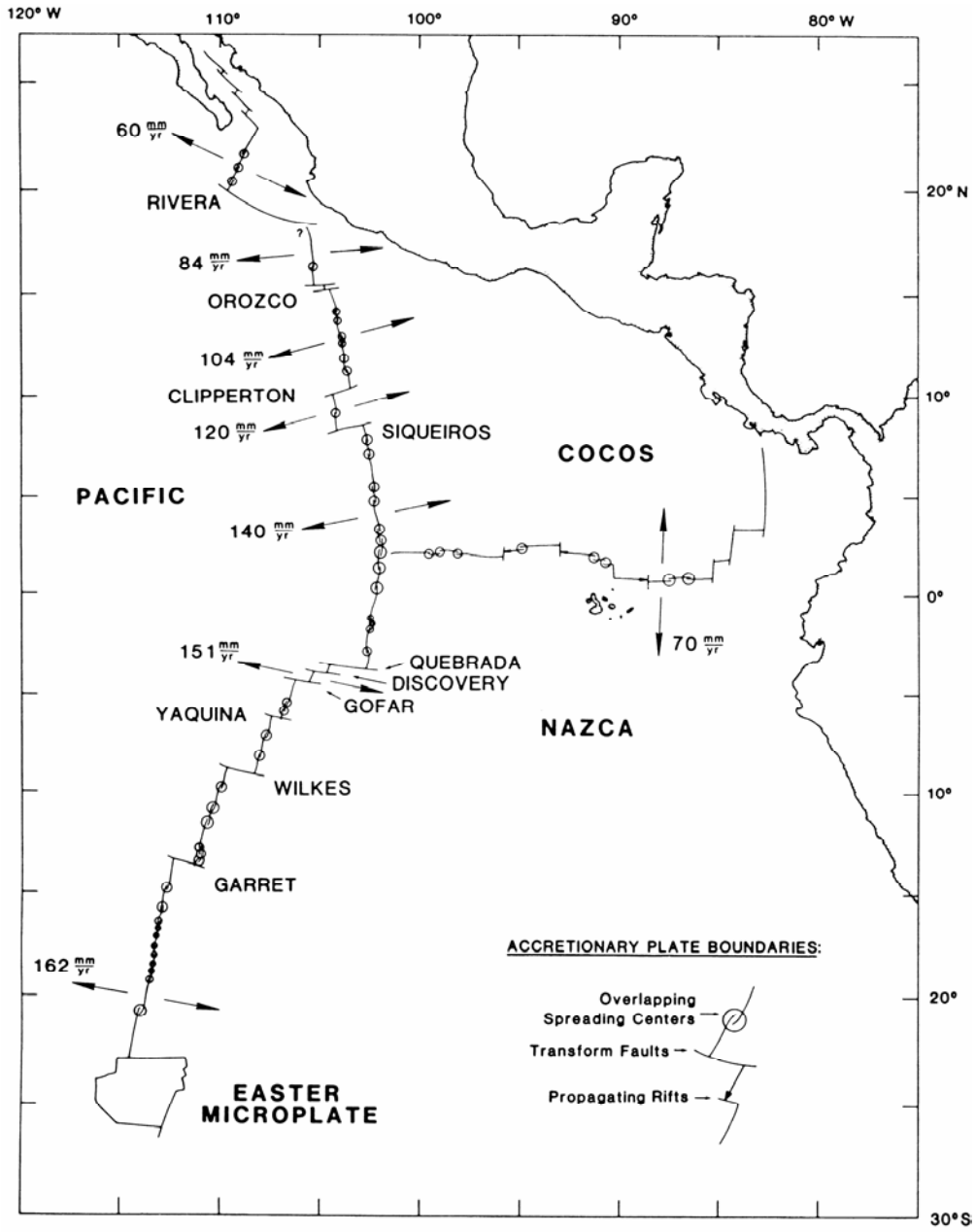

Figure 1.13 Segmentation of the East Pacific Rise and overlapping spreading centers [*Macdonald et al*., 1986].

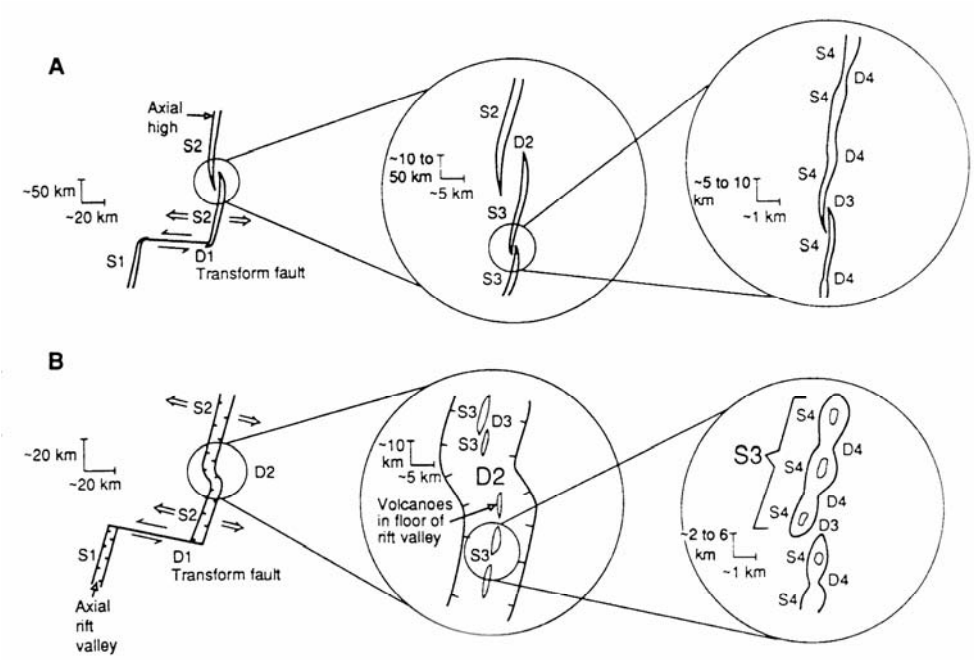

Figure 1.14 Ridge segmentation at different scales [*Macdonald et al*., 1991]: (a) fast spreading ridges, and (b) slow spreading ridges. S1, S2, S3, and S4 indicate ridge segments of order 1, 2, 3, and 4 and D1, D2, D3, and D4 indicate ridge axis discontinuities of order 1, 2, 3, and 4.

Figure 1.15 Vertical fracture formed in a gelatin material [*Hubbert and Willis*, 1957].

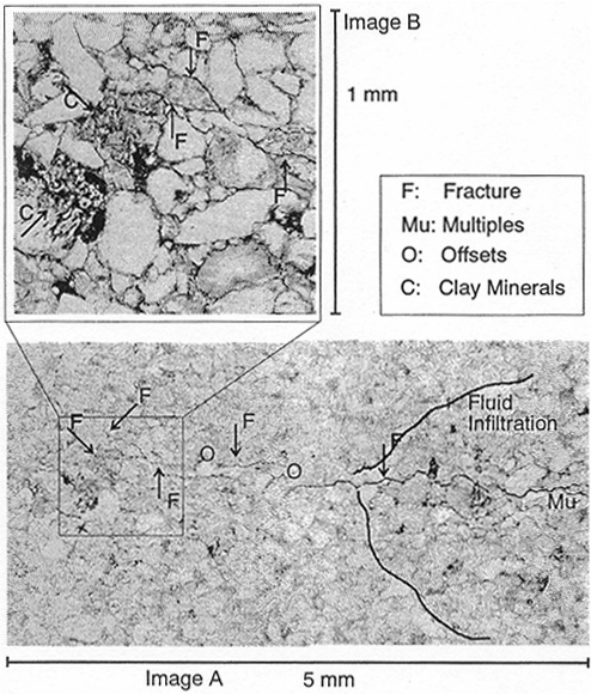

(a)

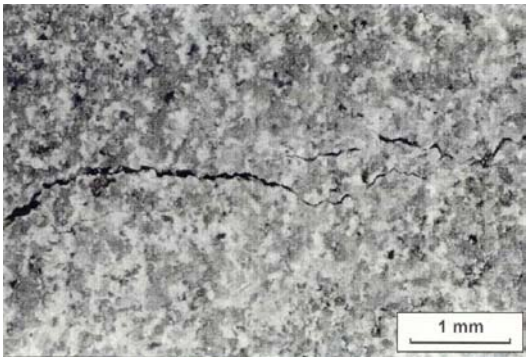

(b)

Figure 1.16 Multiple fractures in a homogeneous rock: (a) multiple fractures in sandstone [*de Pater et al*., 1994], and (b) hydraulic fracture branching in sandstone [*Dudley et al*., 1995].

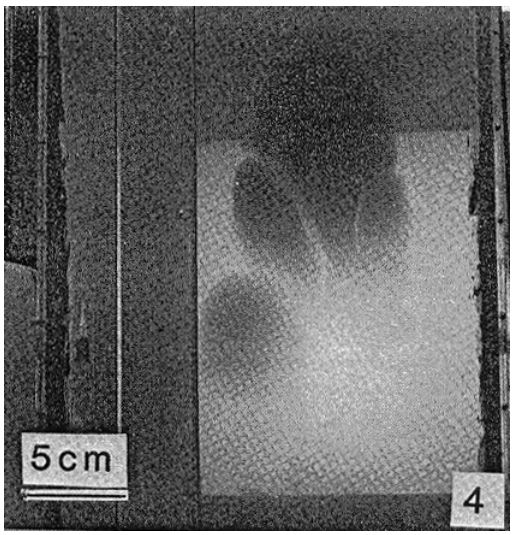

Figure 1.17 Segmentation of the liquid-filled crack in gelatin [*Takada*, 1990].

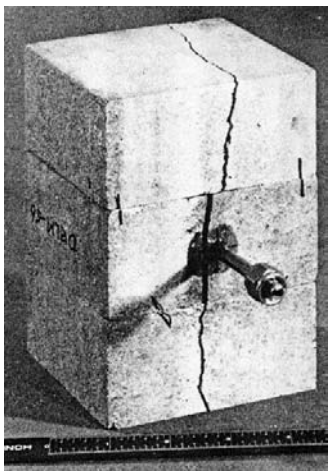

(a)

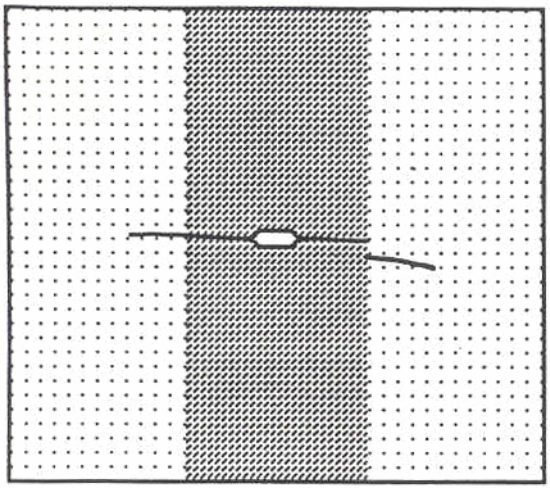

(b)

Figure 1.18 Fracture offset across the frictional interface: (a) effect of low friction region on hydraulic fracture growth across an unbonded interface of limestone [*Hanson et al*., 1981], and (b) continuous and discontinuous fracture crossing of the frictional interface of the anchoring cement [*Renshaw and Pollard*, 1995].

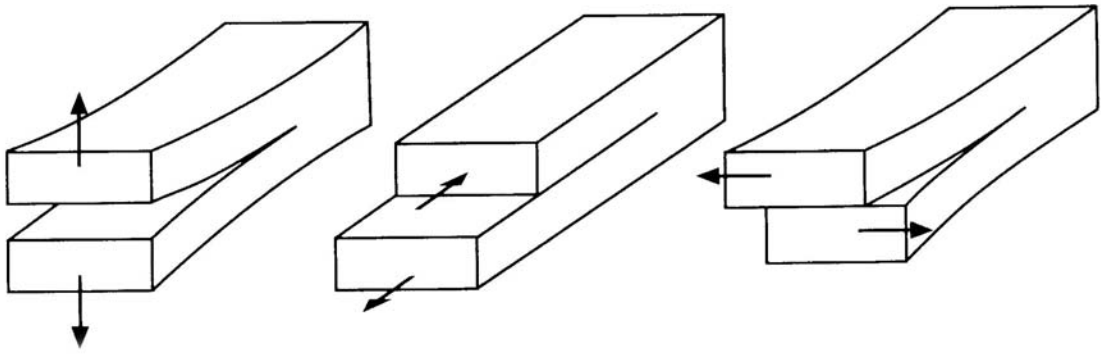

Figure 1.19 Three modes of fracture: (a) mode I, (b) mode II, and (c) mode III [*Lawn*, 1993].

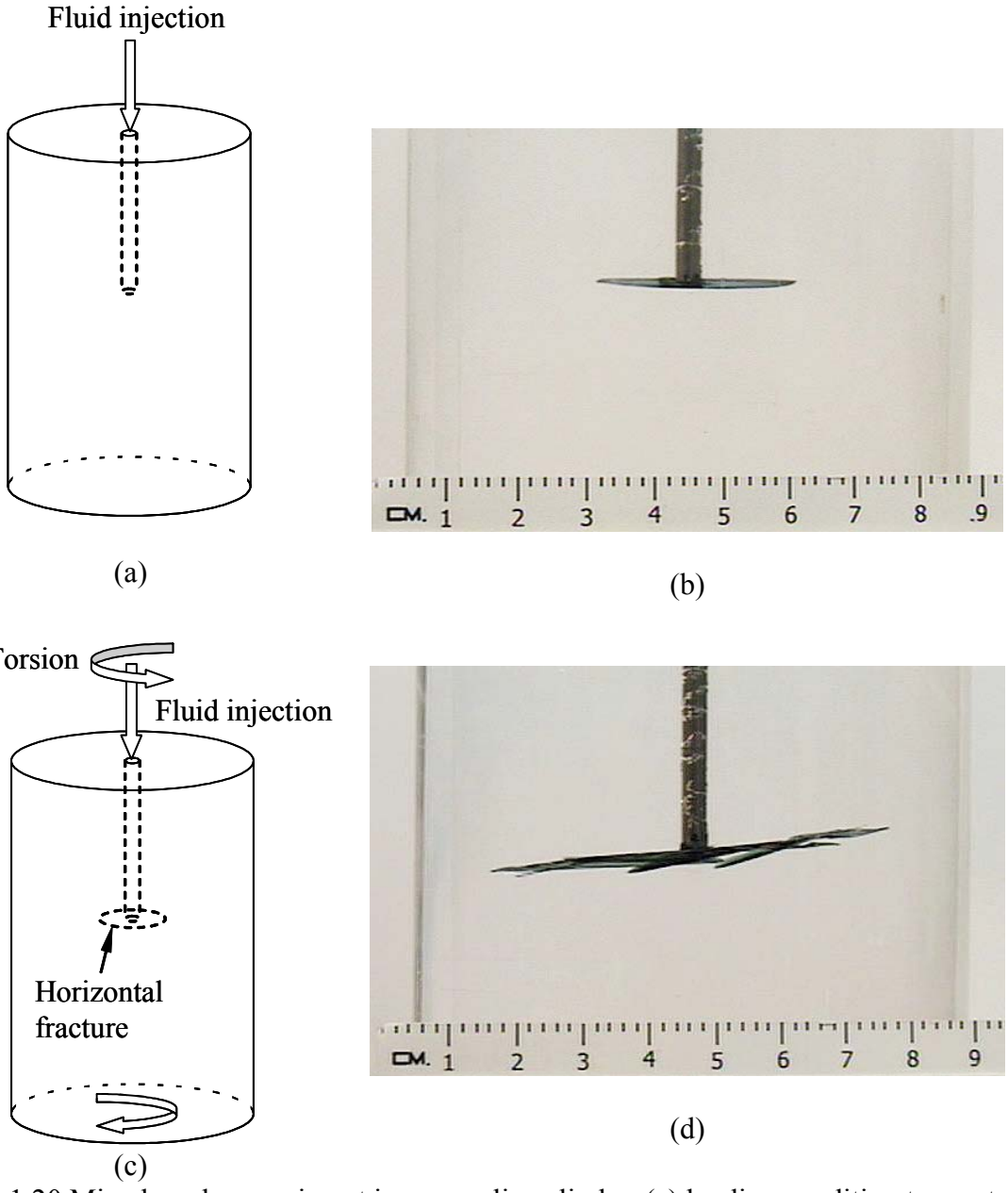

Figure 1.20 Mixed mode experiment in an acrylic cylinder: (a) loading condition to create a fracture (b) initial horizontal fracture, [*Wu and Germanovich*, 2003], (c) loading condition to create segmentation, and (d) segmentation from horizontal fracture [*Wu and Germanovich*, 2003].

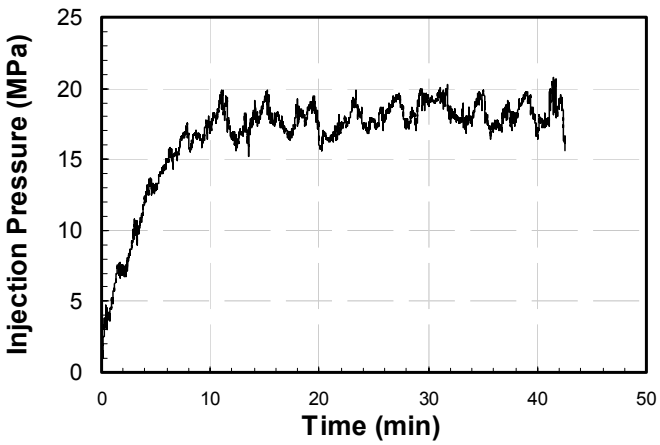

Figure 1.21 Pressure versus time during the segmentation [*Wu and Germanovich*, 2003].

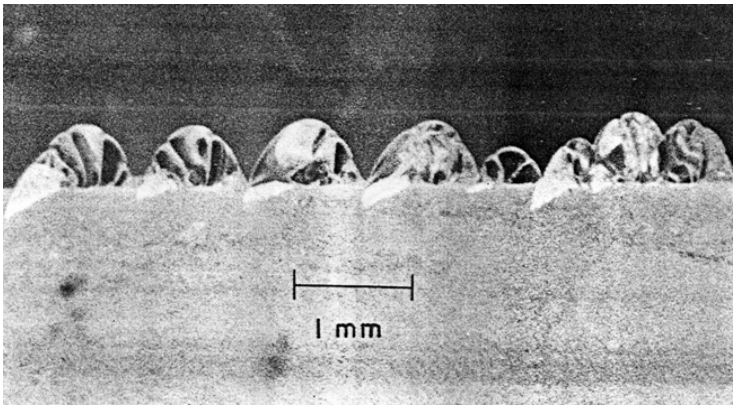

Figure 1.22 Crack segmentation in anti-plane shear [*Knauss*, 1970]

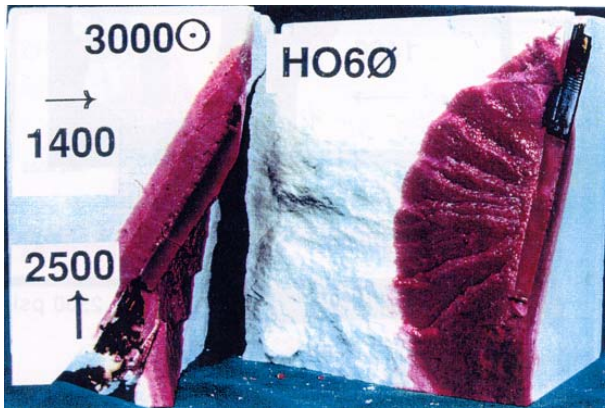

Figure 1.23 Fracture surface with steps at wellbore inclined at 60° with respect to the least principal stress [*Abass et al.*, 1996]. The numbers shown indicate confining principal stress in pounds per square inch (psi).

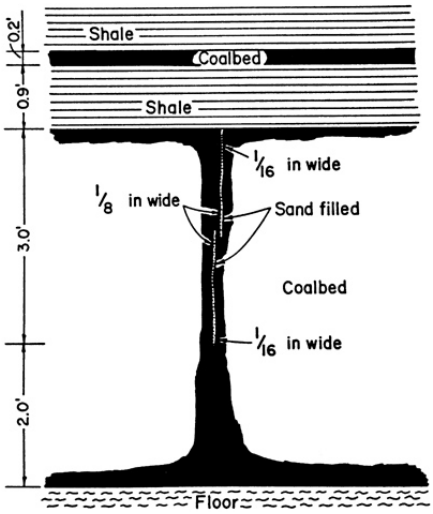

Figure 1.24 *En echelon* vertical fractures filled with sand near wellbore EM-8, Pittsburg coalbed, Pennsylvania [*Diamond and Oyler*, 1987].

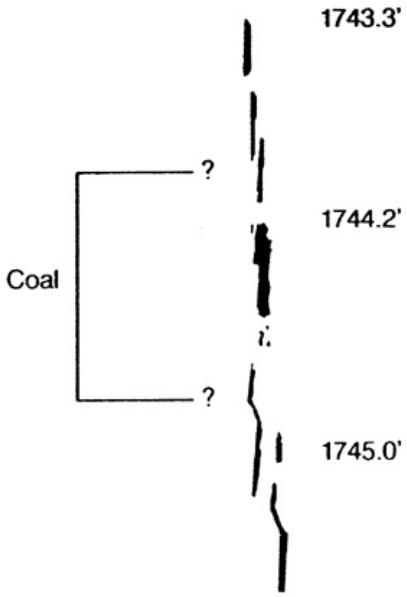

Figure 1.25 Multiple fractures in a coal seam and surrounding strata [*Palmer and Sparks*, 1991].

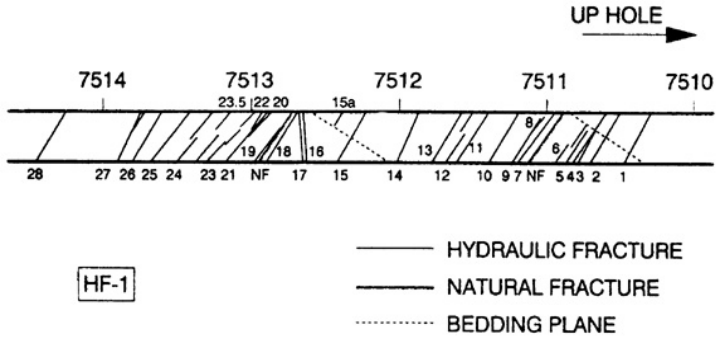

(a)

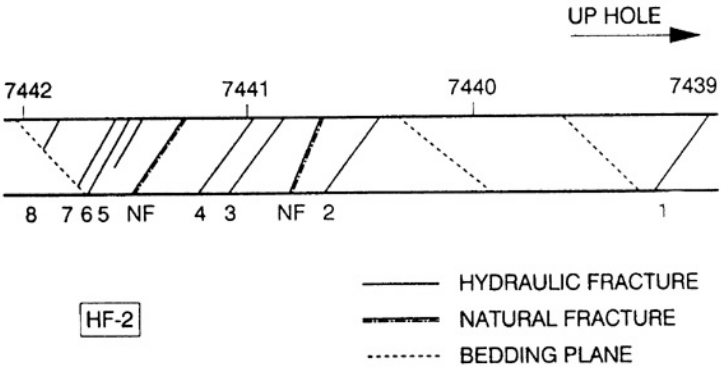

(b)

Figure 1.26 Cored hydraulic fractures obtained from the highly anisotropic reservoir in the Piceance basin near Rifle, Colorado [*Warpinski et al*., 1993a]: (a) primary fracture interval, HF-1, and (b) secondary fracture interval, HF-2.

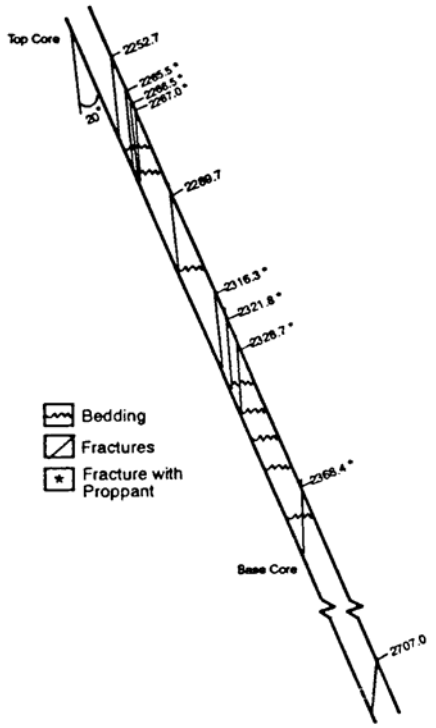

Figure 1.27 Cored hydraulic fractures in Opal-A diatomite at Lost Hills Field, California [*Fast et al*., 1994].

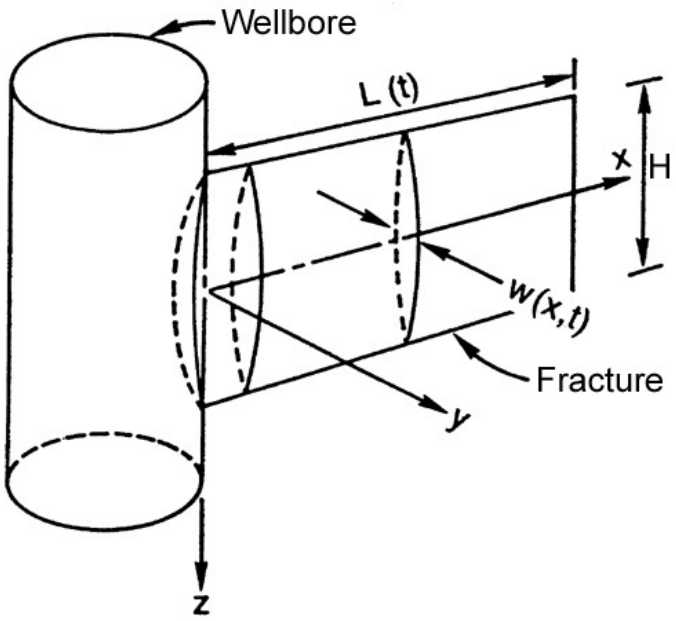

Figure 1.28 Single PKN model [*Nordgren*, 1972].

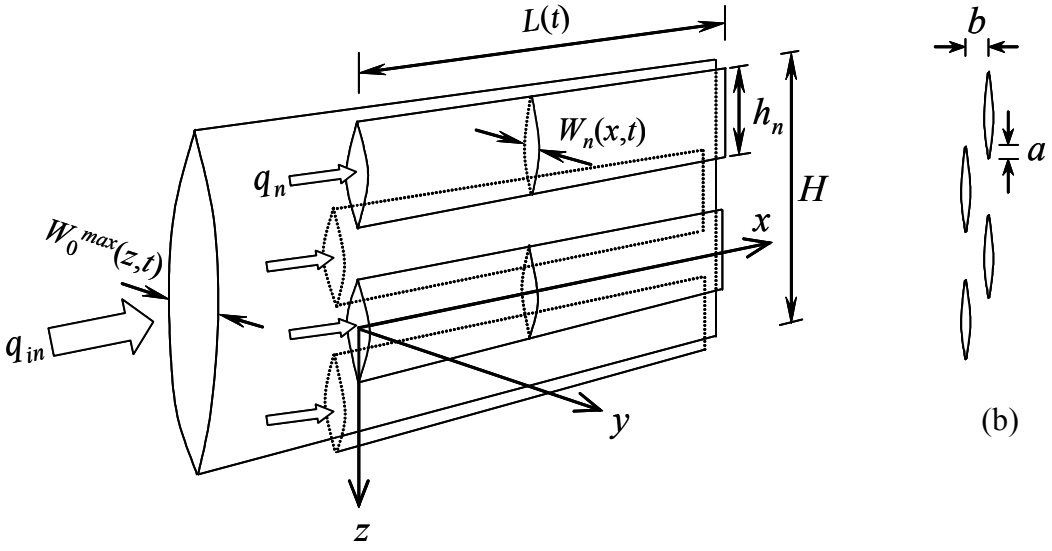

(a) (b)

Figure 1.29 A PKN model of multisegmented hydraulic fractures: (a) multisegmented hydraulic fractures and a single fracture of the same height, and (b) vertical cross section of multisegmented hydraulic fractures.

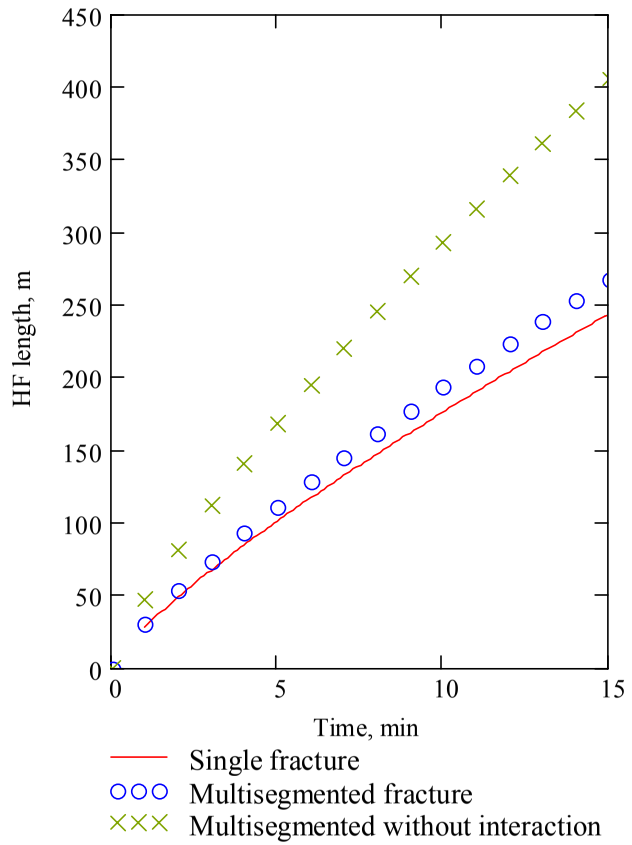

(a)

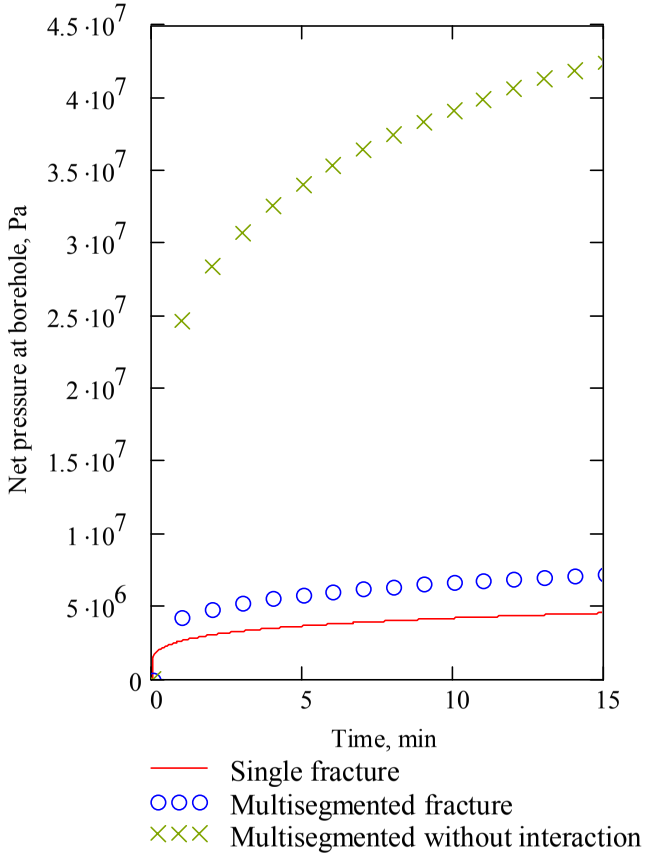

(b)

Figure 1.30 Comparison of hydraulic fracturing parameters with other methods (N = 19) [*Astakhov*, 2000]: (a) hydraulic fracture length, and (b) net pressure at the borehole.

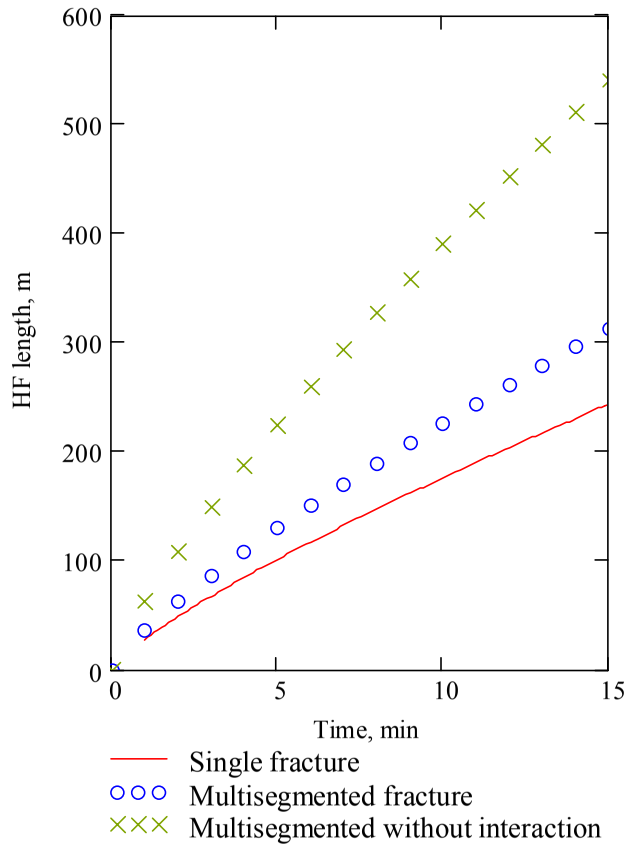

(a)

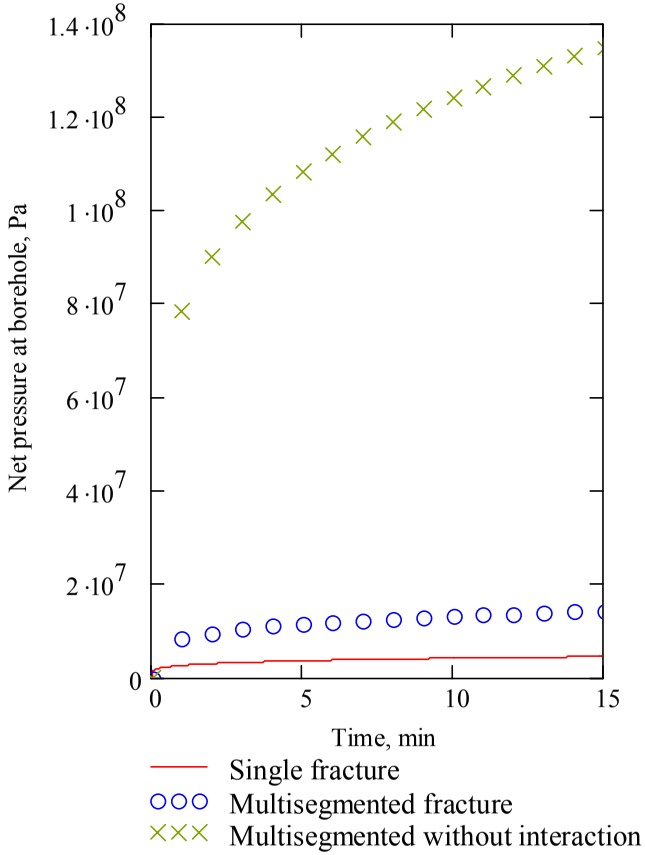

(b)

Figure 1.31 Comparison of hydraulic fracturing parameters with other methods (N = 81) [*Astakhov*, 2000]: (a) hydraulic fracture length, and (b) net pressure at the borehole.

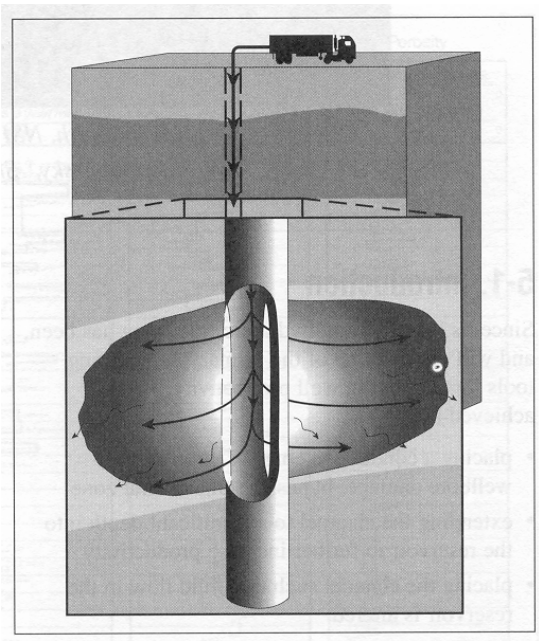

(a)

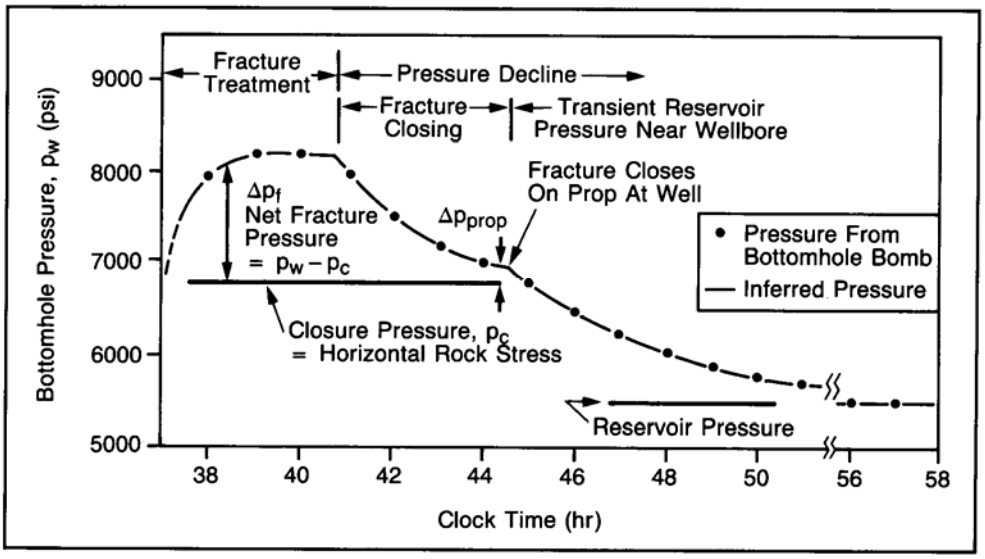

(b)

Figure 1.32 Hydraulic fracturing treatment [*Economides and Nolte*, 2000]: (a) hydraulic fracture created by pumping fluid, and (b) pressure response at the borehole or surface.

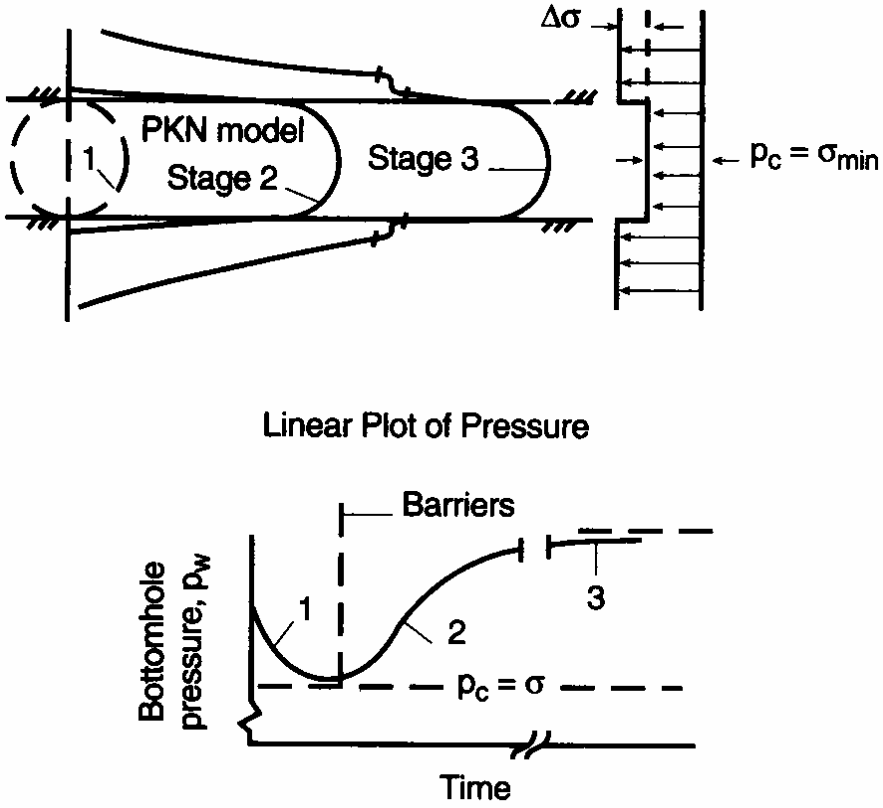

Figure 1.33 Inference of fracture geometry from the time-pressure curve [*Economides and Nolte*, 2000].

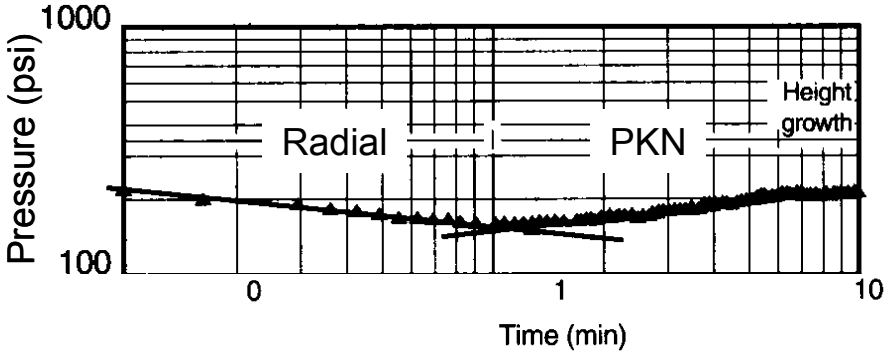

Figure 1.34 Pressure curve and hydraulic fracture geometry from field data [*Economides and Nolte*, 2000].

CHAPTER II

MATHEMATICAL MODELING OF MULTISEGMENTED HYDRAULIC FRACTURES

In this chapter, a mathematical model and numerical code are developed to study the elastic interaction between multiple fractures.

2.1 Elastic interaction between multiple fractures

The problem of multiple defects has been a key issue in many disciplines, because elastic interaction significantly changes the stress and strain fields in materials. In the field of hydraulic fracturing, the displacement and displacement discontinuity across a fracture are of great concern in the evaluation of hydraulic fracturing parameters [e.g., *Narendran and Cleary*, 1983; *Jeffrey et al.*, 1987; *Vandamme et al.*, 1988; *Naceur and Roegiers*, 1990, *Germanovich et al.*, 1998a] that are significantly affected by the mechanical interaction between the segments (refer to section 1.5.2). Because analytical solutions are seldom feasible, many authors have addressed this problem numerically [e.g., *Isida*, 1970; *Erdogan and Gupta*, 1972; *Savruk and Datsyshin*, 1973; *Panasyuk et al.*, 1977; *Horii and Nemat-Nasser*, 1985; *McCartney and Gorley*, 1987].

This section describes a numerical formulation for analyzing the elastostatic fracture-induced stress fields for arbitrarily arranged, multiple, non-intersecting fractures in a homogeneous plane. A boundary collocation method (BCM), which has been used for the solution of problems with multiple cracks [e.g., *McCartney and Gorley*, 1987;

Ukadgaonker and Murali, 1991; *Madensi et al.*, 1998] is employed, because with the development of advanced computing technology it can be developed into a more accurate and efficient method. In this method, the prescribed boundary conditions are satisfied in a finite number of collocation points. In the adopted version of BCM, an approach using Chebyshev polynomials as approximating functions [e.g., *Gladwell and England*, 1977; *McCartney and Gorley*, 1987; *Zhan et al.*, 1998] is employed to accurately evaluate the displacements and displacement discontinuities of multiple defects. An extensive computer program has been developed, for which the formulations are described below. This model not only provides the capability to solve an array of associated elastic problems but also affords simplicity in the determination of stress intensity factors and fracture opening displacements. While many computer codes are currently available to simulate crack interaction, the method considered in this chapter is especially helpful for numerical modeling of closely located sub-parallel fractures. We tested the capability of the method and demonstrated that the number of collocation points can be reduced as much as by an order of magnitude (see below). This allowed us to simulate a real multisegmented fracture (as described in next Chapter III), which would have not been possible otherwise.

First, consider a pair of fractures ($N = 2$) in an infinite plane that are located at $z_1 = x_1 + iy_1$ and $z_2 = x_2 + iy_2$, respectively (Figure 2.1). Known tractions $p_1(z_1) = \sigma_1 + i\tau_1$ and $p_2(z_2) = \sigma_2 + i\tau_2$ are applied to the first and second fracture where σ and τ are the normal and shear traction components, respectively. Based on the superposition principle, this problem can be represented as a sum of two auxiliary problems for a single fracture (Figure 2.1). In the first auxiliary problem, unknown tractions acting on the first fracture

$q_1 = s_1 + it_1$ induce stresses $\Delta q_1 = \Delta s_1 + i\Delta t_1$ at the location of the second fracture. Likewise, in the second auxiliary problem, unknown tractions loading the second fracture $q_2 = s_2 + it_2$ generate stresses $\Delta q_2 = \Delta s_2 + i\Delta t_2$ at the location of the first fracture. Therefore, the tractions in the original problem can be written as:

$$q_1(z_1) + \Delta q_2(z_1) = p_1(z_1), \quad q_2(z_2) + \Delta q_1(z_2) = p_2(z_2) \tag{2.1}$$

Representing the unknown tractions q_1 and q_2 in (2.1) in the form of the Chebyshev polynomial expansions gives

$$q = s + it = -\sum_{m=1}^{M} (\alpha_m + i\beta_m) U_{m-1}(\xi) \qquad (-1 < \xi < 1) \tag{2.2}$$

where α_m and β_m are real unknown coefficients that need to be determined, M is the number of collocation points (which may be different for each fracture), $U_m(\xi) = \sin((m+1)\arccos(\xi))/\sin(\arccos(\xi))$ is the mth order Chebyshev polynomial of the second kind, $\xi = x/c$ is the dimensionless spatial coordinate along the fracture, and c is the half-size of the fracture. For the auxiliary problems, the second terms, Δq_1 and Δq_2, in (2.1) that represent the effect of interaction can be calculated as follows [*Muskhelishvili*, 1953]:

$$\Delta q = \Phi(z) + \overline{\Phi(z)} + e^{2i\theta}[\overline{\Phi(\bar{z})} - \Phi(z) - (z - \bar{z})\Phi'(z)] \tag{2.3}$$

where θ is the inclination angle of the fracture with respect to the global coordinate set (Figure 2.1). The complex potential $\Phi(z)$ is expressed as [*Muskhelishvili*, 1953]:

$$\Phi(z) = \frac{1}{2\pi\sqrt{z^2 - c^2}} \int_{-c}^{c} \frac{\sqrt{c^2 - t^2}}{t - z} \overline{q(t)} dt \tag{2.4}$$

Using the Gauss-Chebyshev integration formula [e.g., *Gladwell and England*, 1977]

$$-\frac{1}{\pi}\int_{-1}^{1}\frac{\sqrt{1-\xi^2}}{\xi-\zeta}U_{m-1}(\xi)d\xi=[\zeta-\sqrt{\zeta^2-1}]^m,\quad |\xi|\le 1,\quad m\neq 0 \tag{2.5}$$

for singular integrals and taking into account (2.2), the *Muskhelishvili* [1953] potential (2.4) can be expressed in the following form

$$\Phi(\zeta)=\frac{1}{2\sqrt{\zeta^2-1}}\sum_{m=1}^{M}(\alpha_m-i\beta_m)[\zeta-\sqrt{\zeta^2-1}]^m \tag{2.6}$$

where $\zeta = z/c = \xi + i\eta$, $\xi = x/c$, and $\eta = y/c$. Therefore, based on (2.3), the auxiliary stress Δq can be also expressed in terms of the coefficients α_m and β_m. Finally, (2.1) forms a linear system of equations with the number of equations depending on the total number of collocation points $M_1 + M_2$. Solving this system produces the unknown coefficients α_m and β_m.

Similar to (2.1), for the N-fracture problem, the general relationship between all tractions can be written as a sum of N auxiliary problems:

$$q_n(z_n)+\sum_{\substack{r=1\\ r\neq n}}^{N}\Delta q_r(z_n)=p_n(z_n)\qquad (n=1, 2, \ldots, N) \tag{2.7}$$

The resulting linear system of equations with the size of $2\sum_{n=1}^{N}M_n$ was derived by *McCartney and Gorley* [1987], and can be written in a slightly modified form as [*Germanovich and Astakhov*, 2004]

$$
\begin{aligned}
&-\sum_{m=1}^{M_n}(\alpha_m^n + i\beta_m^n)U_{m-1}(z_n^j) + \sum_{\substack{r=1\\ r\neq n}}^{N}\sum_{m=1}^{M_r}\{\alpha_m^r I_m^r(z_n^j) + \beta_m^r J_m^r(z_n^j)\} \\
&+\sum_{\substack{r=1\\ r\neq n}}^{N} e^{2i(\theta_r-\theta_n)}\left[\sum_{m=1}^{M_r}\beta_m^r\{iI_m^r(z_n^j) - J_m^r(z_n^j)\} + \sum_{m=1}^{M_r}(\alpha_m^r - i\beta_m^r)\{K_m^r(z_n^j) + iL_m^r(z_n^j)\}\right] \qquad (2.8)\\
&= \sigma_n(z_n^j) - \sigma_\infty + i[\tau_n(z_n^j) - \tau_\infty] \\
&\quad (j = 1, ..., M_n, n = 1, ..., N)
\end{aligned}
$$

where $z_n^j = x_n^j + iy_n^j$ are the discrete collocation points on the fractures at which the boundary conditions are satisfied, θ_r and θ_n are the rth and nth fracture inclination angles to the global x axis, respectively, (Figure 2.1), and the functions I_m^r, J_m^r, K_m^r, and L_m^r are defined as follows:

$$
I_m^r(z) + iJ_m^r(z) = \frac{G_m(\zeta_r)}{\sqrt{\zeta_r^2 - 1}} \qquad (2.9)
$$

$$
K_m^r(z) + iL_m^r(z) = \frac{1}{2}(\zeta_r - \overline{\zeta}_r)\left\{\frac{m}{\sqrt{\zeta_r^2 - 1}} + \frac{\zeta_r}{\zeta_r^2 - 1}\right\}\frac{G_m(\zeta_r)}{\sqrt{\zeta_r^2 - 1}} \qquad (2.10)
$$

$$
G_m(\zeta_r) = \{\zeta_r - \sqrt{\zeta_r^2 - 1}\}^m, \quad m \geq 1 \qquad (2.11)
$$

$$
\zeta_r = \frac{2z - t_1^r - t_2^r}{t_2^r - t_1^r}, \quad z = \frac{1}{2}(t_2^r + t_1^r) + \frac{1}{2}\zeta_r(t_2^r - t_1^r) \qquad (2.12)
$$

where t_1^r and t_2^r are complex numbers indicating the locations of the tips of the rth fracture. The first term on the left side in (2.8) represents the unknown tractions q_n for the nth fracture, while the second and third terms indicate the effect of interaction caused by the other fractures. The term on the right side represents the known tractions that are

determined from the boundary conditions. In other words, $\sigma_n(z) + i\tau_n(z) = p_n(z)$ are the external tractions applied to the nth fracture sides and $\sigma_\infty + i\tau_\infty = p_\infty$ is the remote load.

A FORTRAN program (Appendix A) was developed to solve the linear system of equations (2.8). To determine the unknown real coefficients α_m^n and β_m^n, Crout's algorithm for Lower and Upper (LU) matrice decomposition [e.g., *Press et al*., 1992, §2.3] was used. For the large system of equations, we parallelized the numerical code such that it is compatible with high performance computing.

After the unknown real coefficients α_m^n and β_m^n are determined, the displacements, displacement discontinuities, and stress intensity factors can be calculated easily. The representation of shear and normal displacements in the dimensionless coordinate system ζ associated with a crack is

$$u - iv = \frac{c}{4G} e^{i\theta} \left[\sum_{m=1}^{M} \frac{1}{m} (\alpha_m + i\beta_m) \{ G_m(\varsigma) - \kappa \overline{G_m(\zeta)} \} + (\zeta - \overline{\zeta}) \sum_{m=1}^{M} (\alpha_m - i\beta_m) \frac{G_m(\zeta)}{(\zeta^2 - 1)^{1/2}} \right] \tag{2.13}$$

the displacement discontinuity is given by

$$\Delta v + i\Delta u = \frac{4c}{E_1} \sqrt{1 - \xi^2} \sum_{m=1}^{M} \frac{1}{m} (\alpha_m + i\beta_m) U_{m-1}(\xi) \tag{2.14}$$

and the stress intensity factors are expressed as

$$K_I + iK_{II} = \sqrt{\pi c} \sum_{m=1}^{M} (\pm 1)^{m+1} (\alpha_m + i\beta_m) \tag{2.15}$$

where $G = E/[2(1+\nu)]$ is the shear modulus, ν = Poisson's ratio, $\kappa = 3 - 4\nu$ and $E_1 = E/(1 - \nu^2)$ (since only the plane strain case is considered), and "+" and "–" in (2.15) indicate

the stress intensity factors for the crack tips with $\xi > 0$ and $\xi < 0$, respectively. By integrating the normal displacement discontinuities Δv in (2.14), the fracture aperture area can be given by

$$A = c\int_{-1}^{1} \Delta v(\xi) d\xi = \frac{2\pi c^2}{E_1}\alpha_1 \tag{2.16}$$

Expression (2.13) provides the crack side displacements ($u^{\pm}$ and $v^{\pm}$) only in the corresponding auxiliary problems. To evaluate the displacement in the original problem with multiple cracks, one should add the displacements at the position of this crack in all other auxiliary problems.

Since the computational results of the BCM are sensitive to the disposition of the selected collocation points [e.g., *Tsamasphyros and Eftaxiopoulos*, 1996], Chebyshev's collocation points

$$z_s^j = x_s^j + iy_s^j = \frac{1}{2}(t_2^s + t_1^s) + \frac{1}{2}(t_2^s - t_1^s)\cos\frac{\pi(2j-1)}{2M_s} \tag{2.17}$$

are typically used to obtain the fastest convergency [e.g., *McCartney and Gorley*, 1987; *Germanovich and Astakhov*, 2004]. If the collocation points are assigned according to (2.17), their density becomes denser from the center of the fracture to its tips (Figure 2.2). Furthermore, to obtain satisfactory results for the problems with multiple fracture, it is commonly accepted [e.g., *Astakhov*, 2000] that the distance from one collocation point to adjacent collocation points within one segment (*a* in Figure 2.2) must be smaller than the distance from this point to any collocation point on any other segment (*b* in Figure 2.2). While this condition is sufficient, it may be very restricting and hence make some calculations not feasible. We further show that this condition is not always necessary and

the required number of collocation points (and, therefore, the number of equations) can in some cases be decreased by an order of magnitude.

2.2 Comparison with available solutions

For better confidence, the displacement discontinuities computed with BCM are compared with those obtained from a finite element method (FEM). In the majority of publications on elastic crack theory, the principal goal is to calculate the stress intensity factors rather than evaluating the displacement discontinuities. For hydraulic fracturing simulations, it is usually critically important to compute the fracture apertures. However, even in the simplest case of two arbitrary located segments ($N = 2$), analytical solutions to calculate displacement discontinuities are not available. Hence, to compare FEM to the BCM, the two-dimensional FEM code, FRANC2D [*Wawrzynek and Ingraffea*, 1987] is used.

An example of three segments of different size c and orientation θ (Table 2.1) is shown in Figure 2.3a. The same pressure $p_1 = p_2 = p_3 = 1$ is applied in all segments. A Poisson's ratio of $\nu = 0.21$ and a Young's modulus of $E = 1$ are used for the elastic properties of the material. The portion of the deformed mesh with open fractures is shown in Figure 2.3b. For the BCM, the number of collocation points on the segments (Table 2.1) are $M_1 = 30$, $M_2 = 35$, and $M_3 = 40$, respectively (Figure 2.4).

Table 2.1 Configuration of the three segments.

Segment	Center of segment (x, y)	Inclination angle θ	Half size c	Number of collocation points
1	(1.7, 0.6)	0	0.7	30
2	(0.6, 1.5)	90	0.9	35
3	(1.7, 1.75)	-42.89	0.955	40

The normal and shear displacement discontinuities computed with (2.14) are compared with the FEM analysis and show good agreement (Figures 2.5). All three segments have different sizes, but are plotted in the normalized x-coordinate system associated with each segment. The absolute values of the shear displacement discontinuity are one order of magnitude smaller than the normal one. Since the absolute error of the FEM calculations mainly depends upon the chosen mesh, the relative error should be larger for the former than for the latter. For the density of collocation points shown in Figure 2.4, the results obtained with BCM are practically exact (refer to the next section).

2.3 Asymptotic solution for en echelon of closely spaced fractures

In this section, the asymptotic solution for en echelon of closely spaced fractures is obtained for comparison with the BCM method. This solution is also interesting by itself since the overlapping closely spaced sub-parallel fractures are commonly observed at all scales (e.g., refer to Figure 1.1a).

2.3.1 Geometry and simple bending

Figure 2.6a shows a schematic diagram of en echelon with a total number N of closely spaced overlapping segments. The length of each segment is $2c$ and the overlap is $2a$. It is convenient to consider en entire echelon to be one "effective" single fracture of the same total length x_N (Figures 2.6b and 2.6c). If the spacing S between the individual segments is much smaller than the overlap ($S << 2a$) and the number of segments N is not too large (see below), the resistance of thin ligaments "connecting" the sides of effective fracture (Figure 2.6b) can be ignored to the first order. Then, the opening shape of N will be that of the effective one provided that following condition is satisfied

$$(N-1)S << 2c \tag{2.18}$$

The location of the right tip of each segment in the global coordinate set can be expressed as

$$x_n = 2nc - 2(n-1)a \quad (1 \le n \le N) \tag{2.19}$$

This results in N segments and $N - 1$ ligaments (Figure 2.6a). The deformation of each ligament can be evaluated by modeling it by a ligament beam (plate) and computing the beam deflection. First, displacements by moving the ligament ends in the local coordinate set (Figure 2.7a) can be symmetrized (Figure 2.7b):

$$d_n = \frac{v(x_n) + v(x_n - 2a)}{2} \tag{2.20}$$

$$\Delta a_n = -\frac{u(x_n) - u(x_n - 2a)}{2} \tag{2.21}$$

where $u(x)$ and $v(x)$ are displacements of the sides of the effective fracture in the global coordinate system (Figure 2.6b).

Let the size of the whole fracture (Figure 2.6) be

$$2c_N = x_N \tag{2.22}$$

so that [see (2.19)]

$$c_N = \frac{x_N}{2} = Nc - (N-1)a \tag{2.23}$$

In the global coordinate system associated with the effective crack center, the crack side displacements are

$$v^{\pm}(x) = \pm 2c_N \frac{1-\nu^2}{E} p \sqrt{1 - \frac{x^2}{{c_N}^2}} \tag{2.24}$$

$$u^{\pm}(x) = \frac{\Delta c_N}{c_N} x \tag{2.25}$$

where "+" and "–" denote the displacements of the upper and lower sides, respectively, and

$$\Delta c_N = \frac{c_N (1-2\nu)(1+\nu)}{E} p \tag{2.26}$$

In the global coordinate system associated with the left crack tip (Figure 2.6), expressions (2.24) and (2.25) become

$$v^{\pm}(x) = \pm v(x) = \pm 2c_N \frac{1-\nu^2}{E} p \sqrt{1 - \frac{(x-c_N)^2}{{c_N}^2}} \tag{2.27}$$

$$u^{\pm}(x) = u(x) = -\frac{\Delta c_N}{c_N}(x - c_N) = \Delta c_N\left(1 - \frac{x}{c_N}\right) \tag{2.28}$$

Substituting (2.28) into (2.21) (Figure 2.7), we obtain the horizontal displacements of the ligament ends

$$\Delta a_n = \frac{\Delta c_N}{c_N} a \tag{2.29}$$

Therefore, the longitudinal strain of the *n*th ligament is given by

$$\varepsilon_{xx}^{(n)} = \frac{\Delta a_n}{a} = \frac{\Delta c_N}{c_N} \tag{2.30}$$

and it is the same for all ligaments (Figure 2.8). Substituting (2.26) into (2.30), we have

$$\varepsilon_{xx}^{(n)} = \frac{(1-2\nu)(1+\nu)}{E} p \tag{2.31}$$

Stresses in the *n*th ligament can be obtained by using the plane strain relationship (Figure 2.8)

$$\sigma_{zz} = \nu(\sigma_{xx} + \sigma_{yy}) \tag{2.32}$$

and Hooke's law

$$\varepsilon_{xx} = \frac{1}{E}[\sigma_{xx} - \nu(\sigma_{yy} + \sigma_{zz})] \tag{2.33}$$

Substituting (2.32) into (2.33), we further use the well known expression

$$\varepsilon_{xx} = \frac{1+\nu}{E}[(1-\nu)\sigma_{xx} - \nu\sigma_{yy}] \tag{2.34}$$

so that inserting (2.31) and $\sigma_{yy} = p$ (see Figure 2.8) into (2.34) results in

$$\sigma_{xx}^{(n)} = p \tag{2.35}$$

Therefore, the stress state in each ligament is given by

$$\sigma_{xx}^{(n)} = p, \quad \sigma_{yy}^{(n)} = p, \quad \sigma_{zz}^{(n)} = 2\nu p \tag{2.36}$$

In the linear theory of bending, longitudinal and normal (bending) displacements are uncoupled. The loads (2.36) and displacements (2.28), (2.29) are completely consistent with the Poisson's effect for the entire fracture (Figure 2.6c). Therefore, it is sufficient to compare only normal displacements (deflections) of each ligament to the BCM results.

To consider normal displacements w_n of the beam, we ignore Δa_n (Figure 2.9). Using the differential equation [e.g., *Gere and Timoshenko*, 1991]

$$\frac{d^4 w_n}{dx^4} = 0 \quad (-a \le x \le a) \tag{2.37}$$

The boundary conditions are given by

$$w_n = \mp d_n \quad (x = \pm a) \tag{2.38a}$$

$$\frac{dw_n}{dx} = 0 \quad (x = \pm a) \tag{2.38b}$$

Solution of (2.37) and (2.38) is elementary, and in the local coordinate system (Figure 2.9) it is given by

$$w_n(x) = \frac{d_n}{2}\left(\frac{x^3}{a^3} - \frac{3x}{a}\right), \quad -a \le x \le a \tag{2.39}$$

Then, in the global coordinate system (Figure 2.6a), the deflection (2.39) of the nth ligament becomes

$$w_n(x) = \frac{d_n}{2}\left\{\frac{[x-(x_n-a)]^3}{a^3} - \frac{3[x-(x_n-a)]}{a}\right\} \tag{2.40}$$

where parameter d_n can be used to match the displacements of the ligament ends to the displacements of the effective crack sides (Figure 2.6c). Taking into account (2.20), we have

$$w_n(x) = \frac{v(x_n)+v(x_n-2a)}{4}\left[\frac{(x-x_n+a)^3}{a^3} - \frac{3(x-x_n+a)}{a}\right] - \frac{v(x_n)-v(x_n-2a)}{2} \tag{2.41}$$
$$(n = 1,2,...,N)$$

Once $w_n(x)$ is known, the normal displacements of the sides of individual segments (Figure 2.6a) can be expressed as follows

First segment (n = 1):

$$\begin{cases} v_1^+(x) = v^+(x) = v(x) & (0 < x < x_1 - 2a) \\ v_1^+(x) = w_1(x) & (x_1 - 2a < x < x_1) \\ v_1^-(x) = v^-(x) = -v(x) & (0 < x < x_1) \end{cases} \tag{2.42}$$

Second segment (n = 2):

$$\begin{cases} v_2^+(x) = v^+(x) = v(x) & (x_1 - 2a < x < x_2 - 2a) \\ v_2^+(x) = w_2(x) & (x_2 - 2a < x < x_2) \\ v_2^-(x) = w_1(x) & (x_1 - 2a < x < x_1) \\ v_2^-(x) = v^-(x) = -v(x) & (x_1 < x < x_2) \end{cases} \tag{2.43}$$

nth segment ($n \neq 1$, $n \neq N$):

$$\begin{cases} v_n^+(x) = v^+(x) = v(x) & (x_{n-1} - 2a < x < x_n - 2a) \\ v_n^+(x) = w_n(x) & (x_n - 2a < x < x_n) \\ v_n^-(x) = w_{n-1}(x) & (x_{n-1} - 2a < x < x_{n-1}) \\ v_n^-(x) = v^-(x) = -v(x) & (x_{n-1} < x < x_n) \end{cases} \tag{2.44}$$

Last segment ($n = N$):

$$\begin{cases} v_N^+(x) = v^+(x) = v(x) & (x_{N-1} - 2a < x < x_N) \\ v_N^-(x) = w_{N-1}(x) & (x_{N-1} - 2a < x < x_{N-1}) \\ v_N^-(x) = v^-(x) = -v(x) & (x_{N-1} < x < x_N) \end{cases} \tag{2.45}$$

Expressions (2.27) and (2.43) to (2.45) are asymptotically accurate (for s/a $\rightarrow$ 0) and can be used for comparison with the numerical results obtained by BCM. For the following discussion, it is convenient to introduce the normalized half-aperture of the effective fracture, which, according to (2.27) is given by

$$v_0 = v^+(c_N) = v(c_N) = 2c_N \frac{1-\nu^2}{E} p \tag{2.46}$$

2.3.2 Analysis of the spring effect

The modulus of the shear force in the beam in the nth ligament (per unit length in z-direction) is given by (Figure 2.10) [e.g., *Gere and Timoshenko*, 1991]:

$$F_n = \frac{12ES^3}{1-\nu^2} \frac{d^3w}{dx^3} \tag{2.47}$$

From (2.41),

$$\frac{d^3w}{dx^3} = \frac{3d_n}{a^3} \tag{2.48}$$

so that after substituting (2.20) into (2.48) and the results into (2.47) we have

$$F_n = \frac{18[v(x_n) + v(x_n - 2a)]ES^3}{(1-\nu^2)a^3} \tag{2.49}$$

Since $v(x_n) \le v_0$ and $v(x_n\text{-}2a) \le v_0$, we see from (2.49) that

$$F_n < \frac{36v_0 ES^3}{(1-\nu^2)a^3} \tag{2.50}$$

which, after substituting (2.46) into (2.50) becomes

$$F_n < 72c_N \frac{S^3}{a^3} p \tag{2.51}$$

Based as (2.51) let

$$F_{upper} = 72c_N \frac{S^3}{a^3} p \tag{2.52}$$

be the upper estimate of the shear force F_n. With respect to the sides of the effective fracture these forces can be interpreted as normal (Figure 2.11). To the first order, we represent them by the normal distributed tractions. Then, the tractions corresponding tractions corresponding F_{upper} are (Figure 2.11)

$$p_{upper} = \frac{F_{upper}(N-1)}{2c_N} \tag{2.53}$$

and substituting (2.52) into (2.53) results in

$$p_{upper} = 36(N-1)\frac{S^3}{a^3} p \tag{2.54}$$

if

$$p_{upper} << p \tag{2.55}$$

The effect of the forces F_n on the crack opening can be ignored. Substituting (2.54) into (2.55), this sufficient condition can be written as

$$36(N-1)\frac{S^3}{a^3} << 1 \tag{2.56}$$

and provides another restriction on N (see also (2.18)):

$$N-1 << \frac{1}{288}\frac{(2a)^3}{S^3} \tag{2.57}$$

Since according to (2.18)

$$N-1 << \frac{2c}{S} \tag{2.58}$$

we can write both restrictions (2.57) and (2.58) in a combined form

$$N-1 << \min\left\{\frac{1}{288}\frac{(2a)^3}{S^3}, \frac{2c}{S}\right\} \tag{2.59}$$

For example, let

$$a=1, \quad S=0.01, \quad c=5 \tag{2.60}$$

Then, (2.59) becomes

$$N << 5{,}000 \tag{2.61}$$

Therefore, in this case, our asymptotic solution is accurate if the number of fractures is much less than 5,000.

2.3.3 Two overlapping fractures

The openings of the two overlapping fractures ($N = 2$) are now compared with the asymptotic solution. We use geometric parameters $S/2a = 0.005$ and $a/c = 0.2$. Viewed with an equal scale (Figure 2.12a), the fractures appear as they can be simulated by one single fracture. Viewed with an exaggerated scale in the y-direction (Figure 2.12b), however, the overlap is clearly visible.

Figure 2.13a shows the opening shape of the two fractures when 2,000 collocation points for the BCM calculation are used. Figure 2.13b shows a magnified scale of the ligament deformation of the boxed area in Figure 2.13a. The ligament that connects two fractures appears to be deformed similarly to a deflected beam with clamped ends.

Figures 2.14 and 2.15 show the comparison of the openings of the first fracture with the asymptotic solution (2.27) for two different numbers of collocation points. The crack side displacements are normalized by the half-aperture, v_0 (2.46). Figure 2.14a shows the results when 2,000 collocation points are assigned. The density of the collocation points (Figure 2.14b) is sufficient to satisfy the conventional criterion (refer to section 2.1). As expected, the opening computed by the BCM practically coincides with the asymptotic solution (2.27) (Figure 2.14a).

Figure 2.15a shows the results when 250 collocation points are used for the BCM calculations. Despite a dramatic reduction in the number of collocation points (e.g, by an order of magnitude; also compare Figure 2.15b), the opening is still in very good agreement with the asymptotic solution. Note that the case of $S/2a = 0.005$ (i.e., the spacing is only 0.5% of the overlap) is very unfavorable for numerical calculations. Yet

the BCM produced excellent results even for a greatly reduced number of collocation points.

2.3.4 Six overlapping fractures

In the second example, the openings of six overlapping fractures (N = 6) are compared with the obtained asymptotic solution (2.27). We use the same geometric parameters as in the case of two overlapping fractures ($S/2a$ = 0.005 and a/c = 0.2). Figure 2.16 shows the map view of the six overlapping fractures both at an equal scale and at an exaggerating scale in the y-direction.

Compared to the case of two overlapping fractures, this case is even more unfavorable for numerical calculations because the six fractures generate a large number of equations (2,000 × 6 × 2 = 24,000) to satisfy the usual criterion for the density of the collocation points (section 2.1). Given the matrix structure that is typical for BCM, the numerical calculation is likely to be almost impractical although this certainly depends upon the available computational results.

Figure 2.17a shows the opening shape of six fractures when 2,000 collocation point per fracture are used for the BCM. Figures 2.17b to 2,17e show a magnified scale of the ligament deformations inside the boxed areas (Figure 2.17a). As in the case of two overlapping fractures, all ligaments that connect fractures are also deformed, similar to a beam.

Figures 2.18 and 2.19 show the comparison of the open shapes of the first (n = 1), second (n = 2), and third (n = 3) fractures with the asymptotic solution for two different numbers of collocation points. As in the previous example, the crack side displacements

are normalized by the half-aperture, v_0 (2.46). Figure 2.18 presents the results when 2,000 collocation points are assigned for each fracture. As expected, the opening computed by the BCM again coincides with the asymptotic solution (2.27).

Figure 2.19 shows the results when 250 collocation points are used for the BCM calculations. Despite a dramatic reduction in the number of collocation points (by an order of magnitude), the opening is still in very good agreement with the asymptotic result.

2.4 Asymptotic solution for two parallel fractures

In this section, the asymptotic solution for two parallel fractures is compared to the BCM computations. Figure 2.20a shows two closely spaced parallel fractures of the length of $2c$. For a small spacing ($S << 2c$), the displacement discontinuity (i.e., aperture) of each fracture can be expressed as the sum of the half-opening of the single fracture v^+ in Figure 2.20b, and the small displacement v^- at the side of the thin beam (plate) that represents the solid ligament between the two fractures in Figure 2.20c. The beam is loaded by the pressure p that causes the same amount of displacement as the pressure in the fractures. In addition, the beam contracts by the amount of Δc due to the Poisson's effect (Figure 2.20c) in the material with fractures (Figure 2.20b).

Similar to the previous section, to the first order, a very thin material ligament (beam) does not affect the deformation of the surrounding material. Therefore, both $v^+(x)$ and Δc can be found by considering a single fracture with a length $2c$ subjected to a

pressure, p, in an infinite plate (Figure 2.20b). This is a classic problem and we have in plane strain [e.g., *Tada et al*., 1985, see also (2.24), (2.25)]

$$v^+(x) = 2c\frac{(1-\nu^2)}{E}p\sqrt{1-\frac{x^2}{c^2}} \tag{2.62}$$

$$\Delta c = \frac{c(1-2\nu)(1+\nu)}{E}p \tag{2.63}$$

We now have an elementary problem for a rectangular body loaded by the pressure p in one direction and contracted by the amount of $2\Delta c$ in the perpendicular direction (Figure 2.20c). Similar to (2.36), the solution is obtained directly from Hooke's law (2.33) and the plane strain condition (2.32):

$$\sigma_{xx} = p \tag{2.64}$$

$$v^- = \frac{p}{2E}(1-\nu-2\nu^2)S \tag{2.65}$$

Figures 2.21 and 2.22 show the comparison of the vertical displacements of the sides of the upper fracture with the asymptotic solution (2.65) by varying the number of collocation points. The geometric parameter that was used is $S/(2c) = 0.0005$. Figure 2.21a shows the results (normalized by $2v^+(0) = 4c(1-\nu^2)p/E$) when 4,000 collocation points are assigned for the BCM computation. The density of collocation points (Figure 2.21b) satisfies the conventional criterion (section 2.1). We observe that both vertical displacements, v^+ and v^-, computed with the BCM practically coincide with the asymptotic solution (Figures 2.21a and 2.21c). The maximum displacement v^+ of the upper side approaches 1/2, which is the half-opening of the single fracture.

We also performed several computations with a smaller number of collocation points. Figures 2.22a shows the results when 250 collocation points are used for the BCM calculation. The density of the collocation points is now considerably smaller (Figure 2.22b) and by the usual standard is not accepted. Yet, again, the displacement is still in a good agreement with the asymptotic solution despite the great reduction of the number of collocation points by more than an order of magnitude.

Note again that the considered example is not favorable for numerical calculations because it involves a very thin body (the thickness of the ligament separating the fractures is only 0.05% of the fracture size). This geometry practically prohibits FEM computations. Yet, BCM provides robust results with a relatively small number of equations.

2.5 Summary and conclusions

The boundary collocation method is implemented to model the effect of elastic interaction between multiple fractures. The displacements, as well as the displacement discontinuities, are accurately calculated and compared with existing closed form solutions.

The results computed with the BCM are also compared to the obtained asymptotic solutions for two and six overlapping, as well as for two parallel, closely spaced fractures. Both cases represent important frequents elements observed in the field and in the laboratory (refer to Chapter I). However, most numerical techniques (e.g., FEM) are hardly suitable (if at all) for such cases, involving geometries that are highly unfavorable

for numerical computations due to the large difference in the relevant dimensions. Yet, the BCM provides results that are in excellent agreement with the asymptotic solutions, even when the number of collocation points is reduced by as much as an order of magnitude (and more), compared to conventional implementations. Without such a significant reduction of the number of collocation points, the numerical simulation of more realistic and, hence, more complex fracture geometries (such as in the following chapter) would be prohibitive.

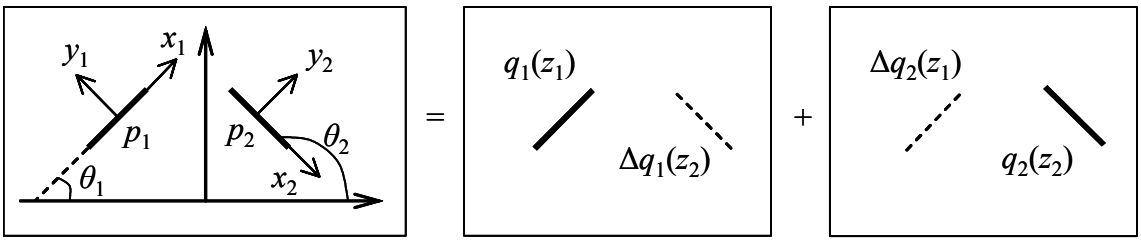

Figure 2.1 Original and auxiliary problems for interacting fractures.

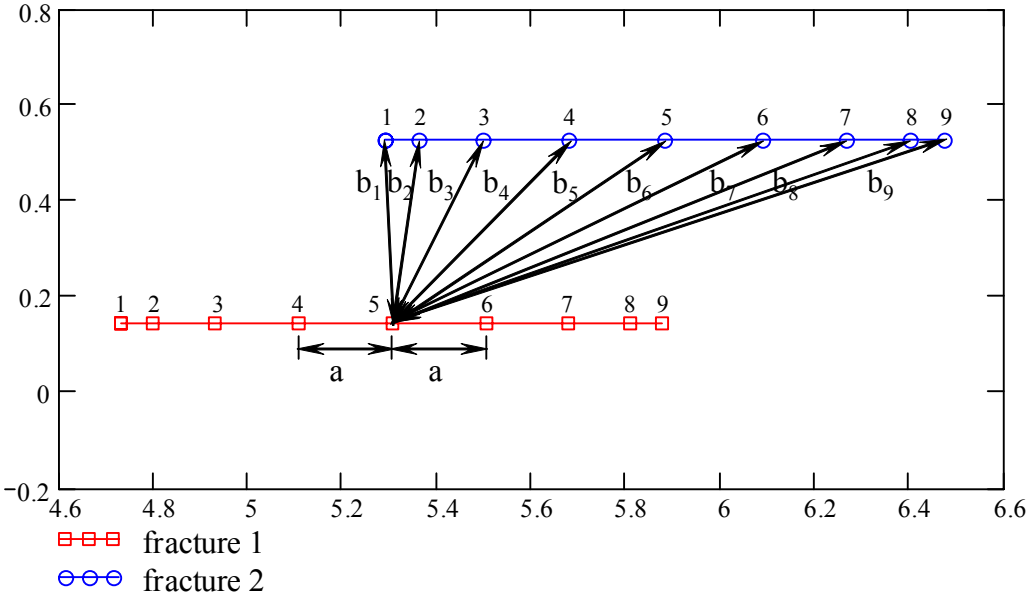

Figure 2.2 Density of collocation points in two parallel fractures.

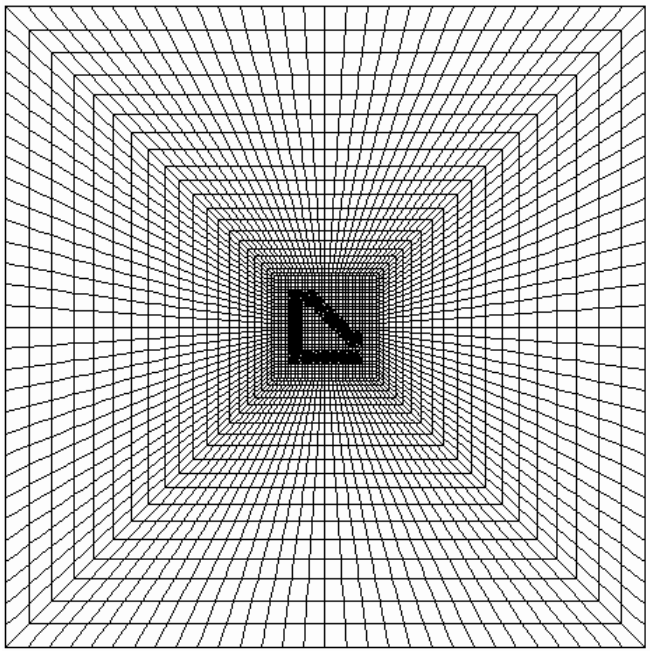

(a)

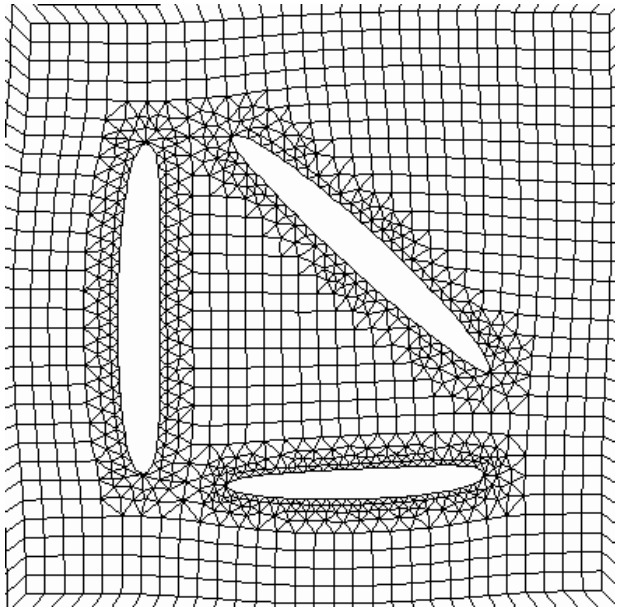

(b)

Figure 2.3 Three fractures in the finite element method (FEM): (a) finite element mesh with three fractures, and (b) the deformed finite element mesh with three fractures.

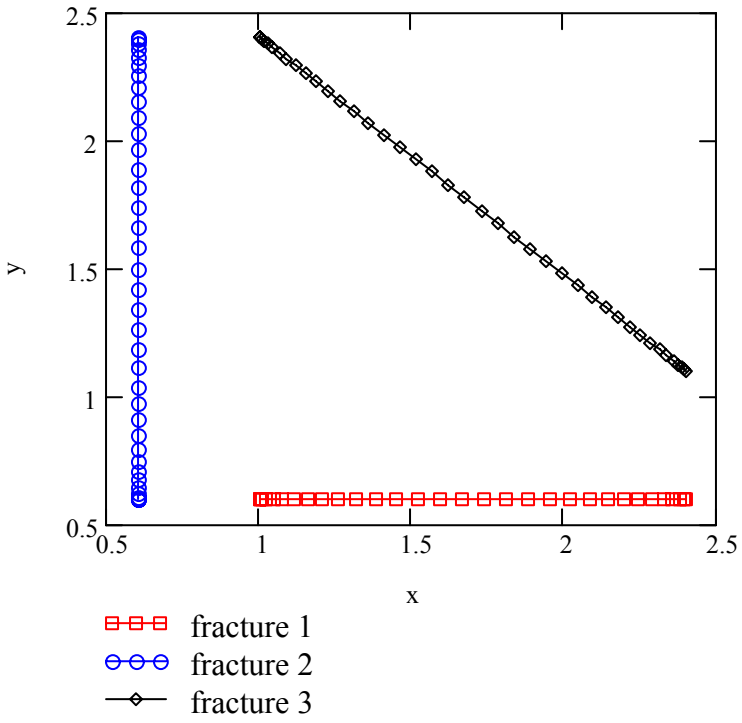

Figure 2.4 Density of collocation points in BCM.

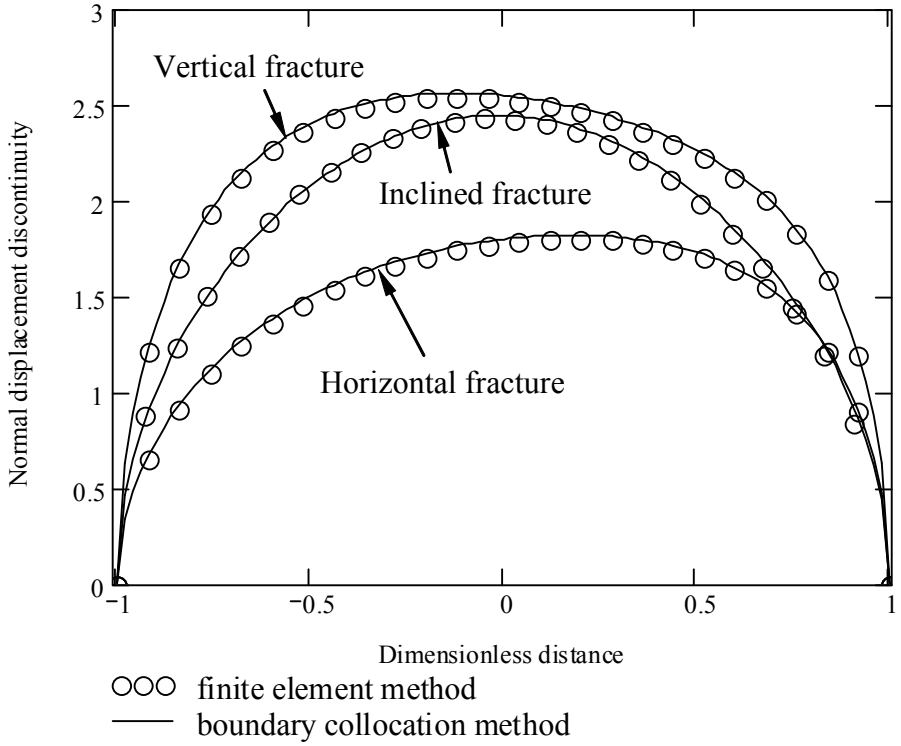

(a)

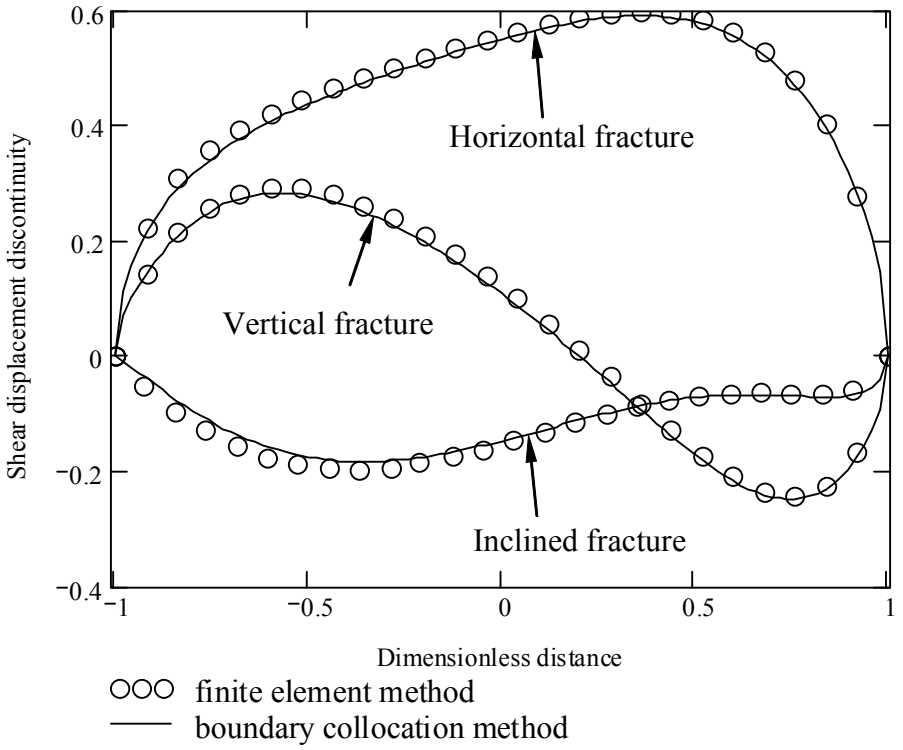

(b)

Figure 2.5 Comparison of displacement discontinuities with FEM: (a) normal displacement discontinuity, and (b) shear displacement discontinuity.

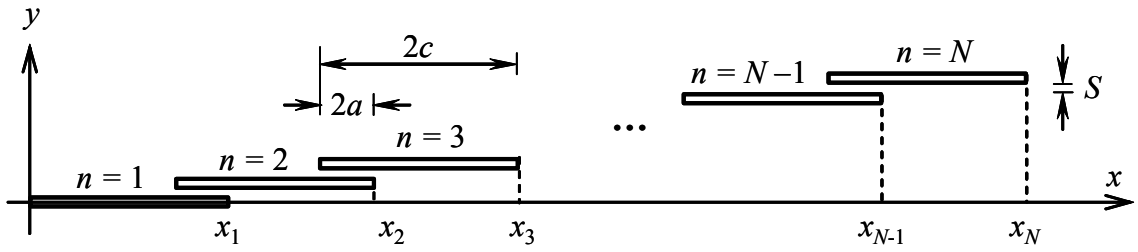

(a)

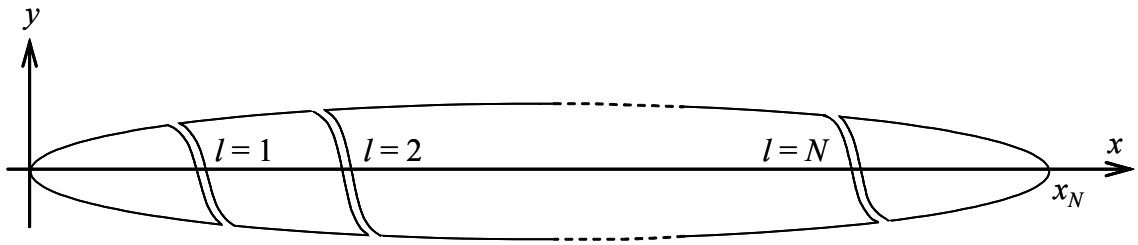

(b)

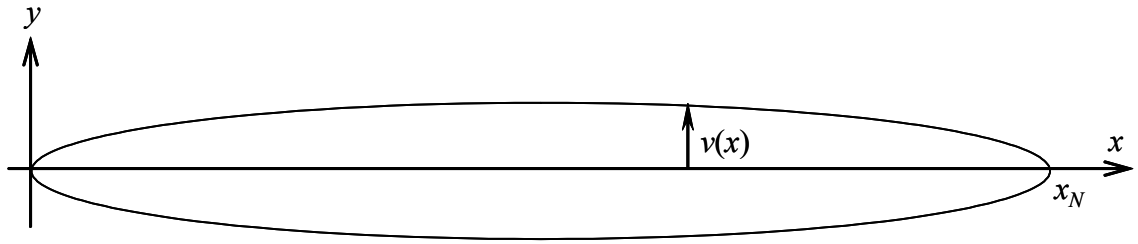

(c)

Figure 2.6 En echelon of closely spaced fractures: (a) geometric configuration of N fractures, (b) opening of the fractures, and (c) opening of the single fracture of the same total length of x_N.

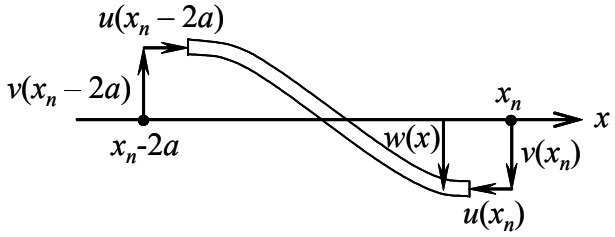

(a)

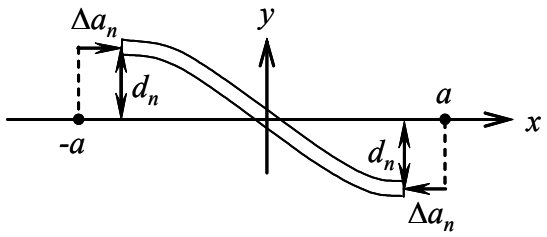

(b)

Figure 2.7 Deformation of ligament: (a) initial deflection of ligament and (b) converted initial deflection.

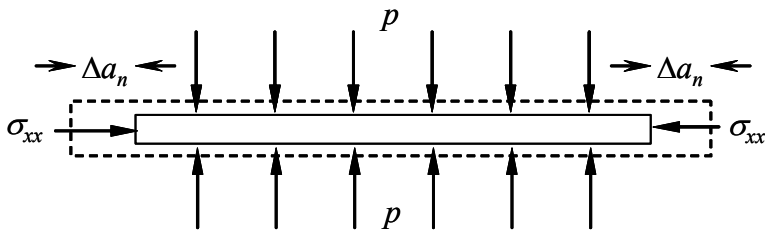

Figure 2.8 Deformation of the ligament by surrounding stresses. The dashed line indicates the state before deformation of ligament.

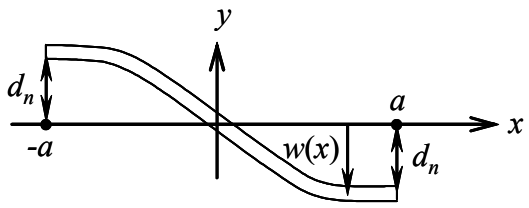

Figure 2.9 Deflection of the ligament without horizontal contraction.

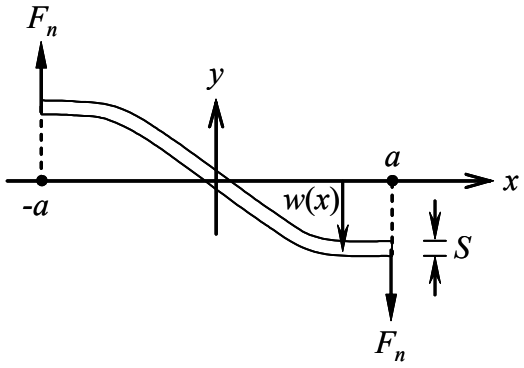

Figure 2.10 Shear force at the ligament end.

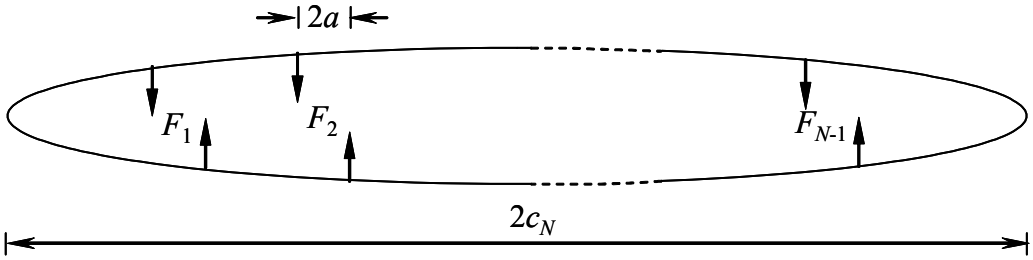

Figure 2.11 Resistance generated by shear forces in the ligament ends.

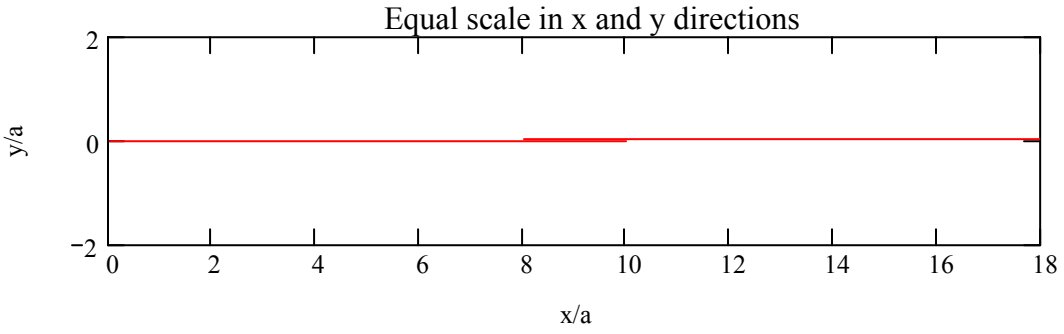

(a)

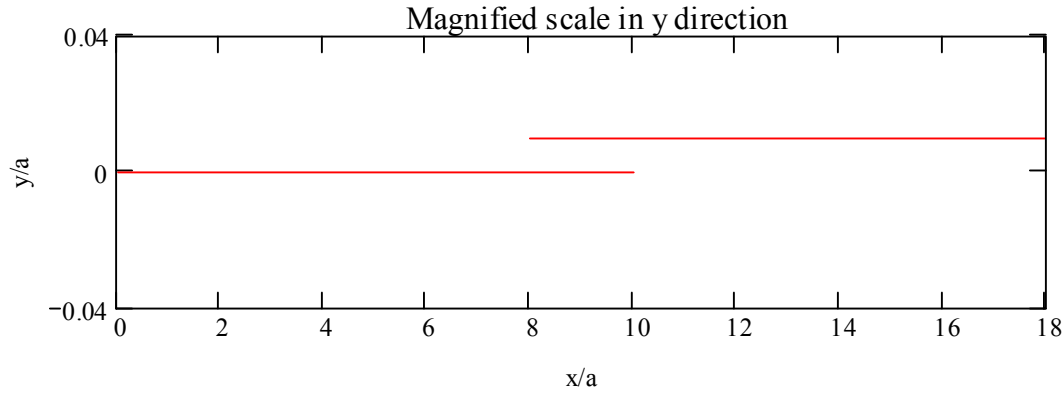

(b)

Figure 2.12 Map views of two overlapping fractures: (a) equal scale, and (b) magnified scale in *y* direction.

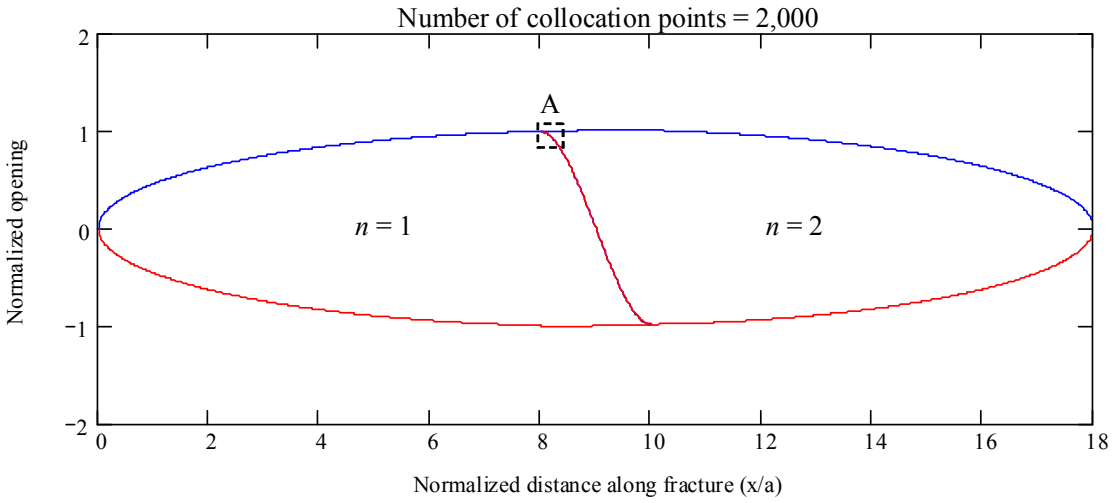

(a)

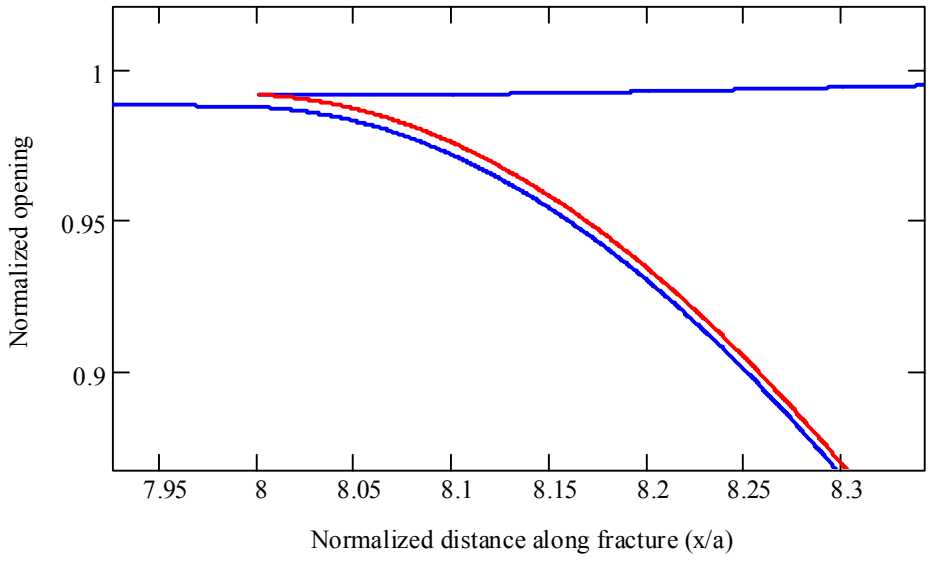

(b)

Figure 2.13 Two closely spaced overlapping fractures: (a) normalized opening when 2,000 collocation points for the BCM calculation are used, and (b) ligament deflection at magnified scale.

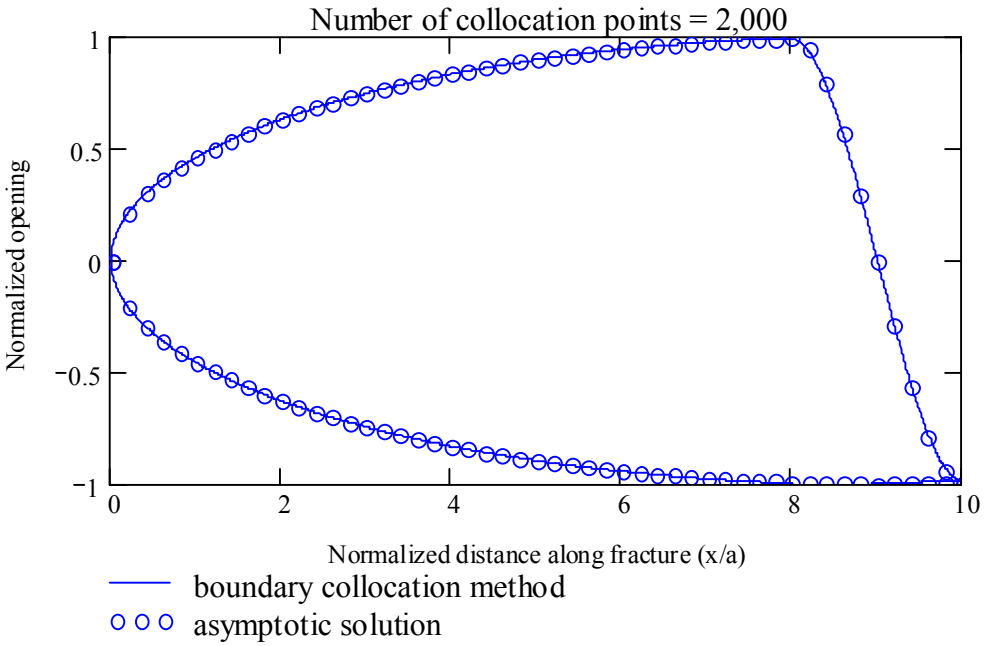

(a)

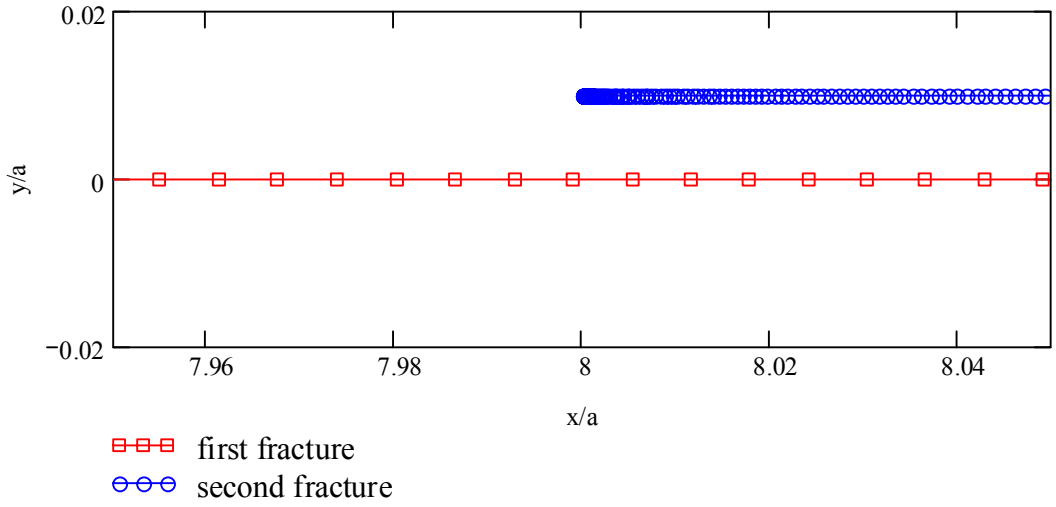

(b)

Figure 2.14 Two closely spaced overlapping fractures: (a) comparison of opening between BCM and asymptotic solution when 2,000 collocation points are used, and (b) density of BCM collocation points at magnified scale.

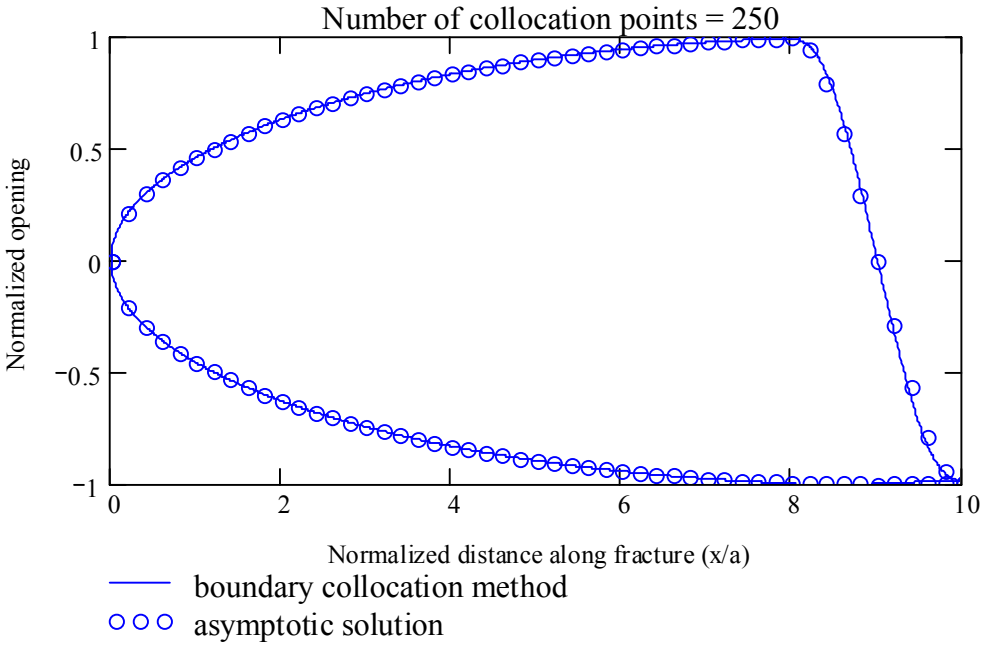

(a)

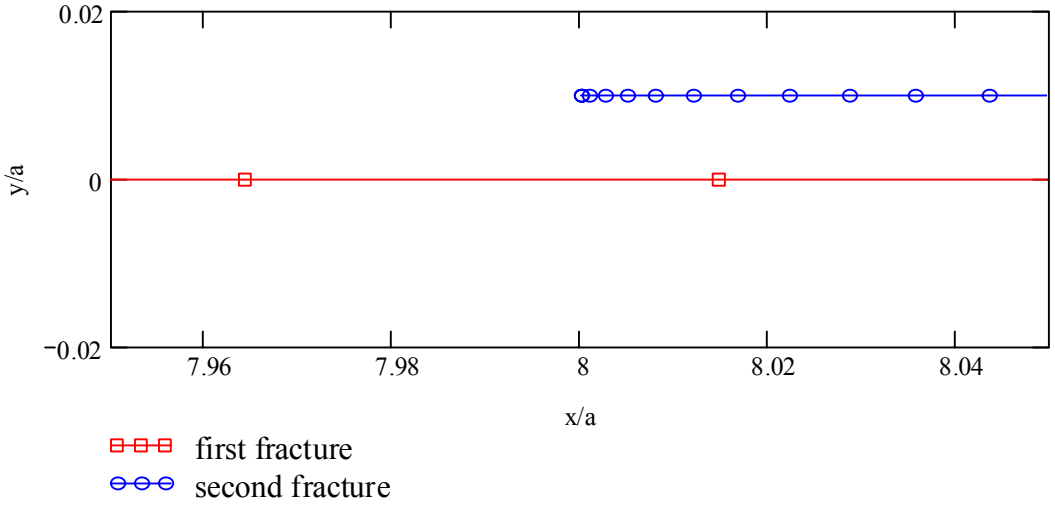

(b)

Figure 2.15 Two closely spaced overlapping fractures: (a) comparison of opening between BCM and asymptotic solution when 250 collocation points are used, and (b) density of BCM collocation points at magnified scale.

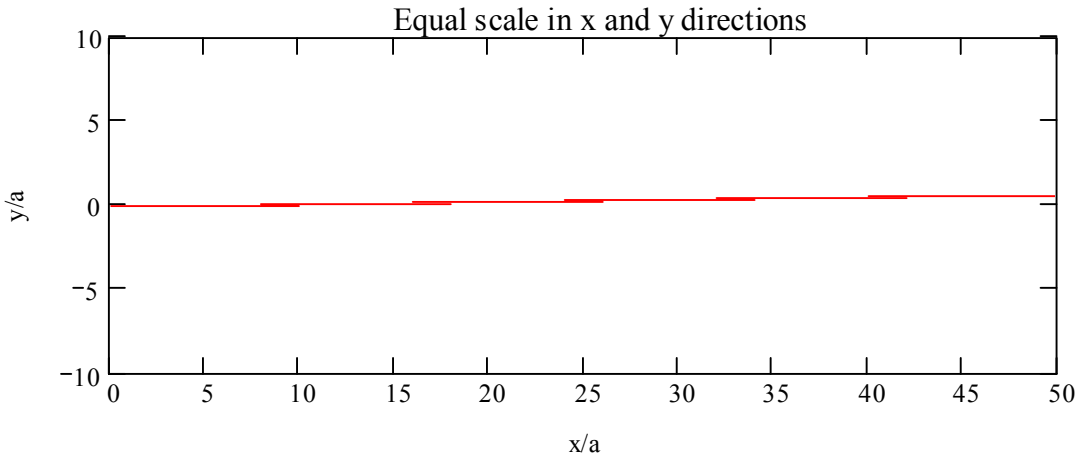

(a)

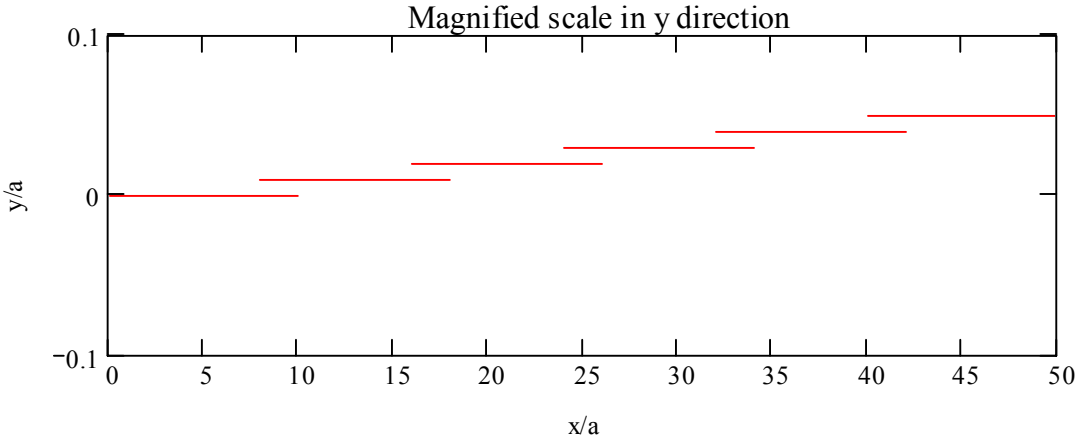

(b)

Figure 2.16 Map view of six overlapping fractures: (a) equal scale, and (b) magnified scale in *y* direction.

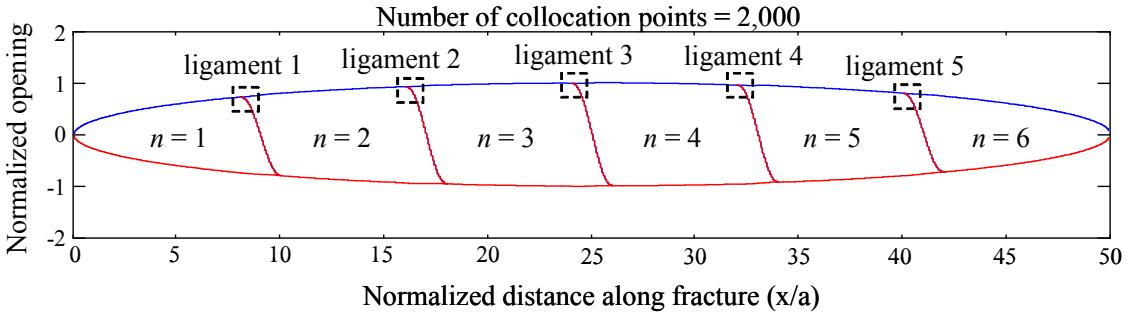

(a)

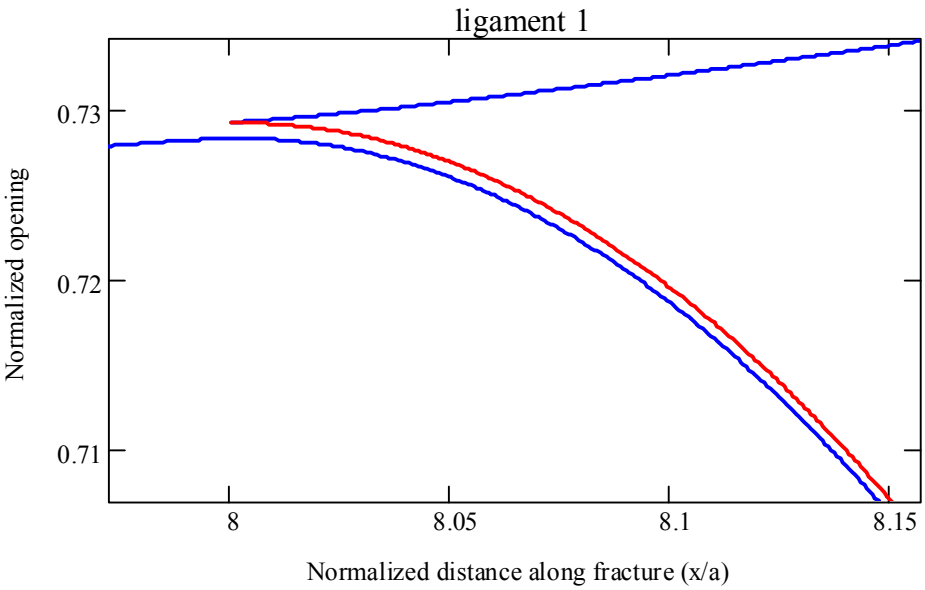

(b)

Figure 2.17 Six closely spaced overlapping fractures: (a) normalized opening when 2,000 collocation points for the BCM calculation are used and ligament deflection at magnified scale for: (b) ligament 1, (c) ligament 2, (d) ligament 3, (e) ligament 4, and (f) ligament 5.

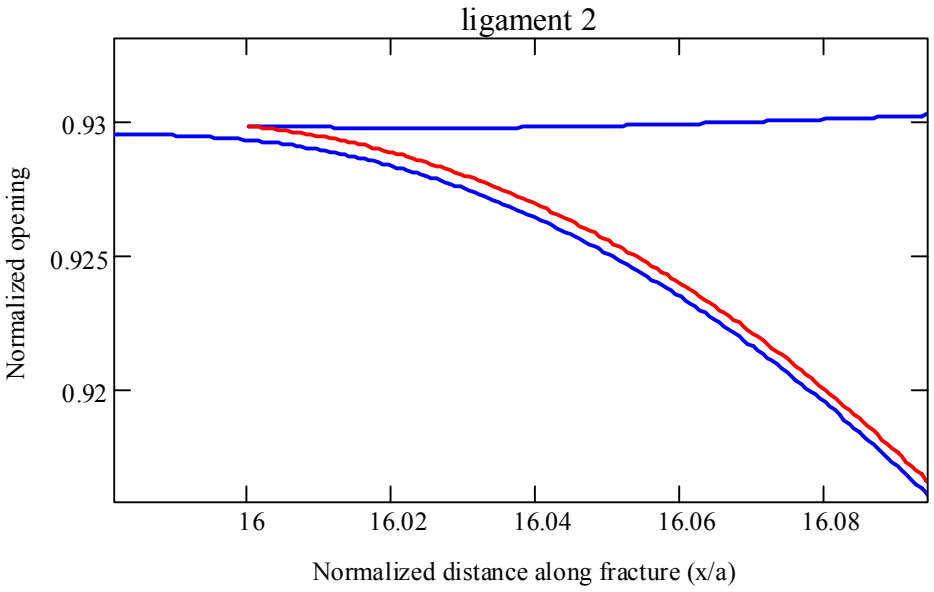

(c)

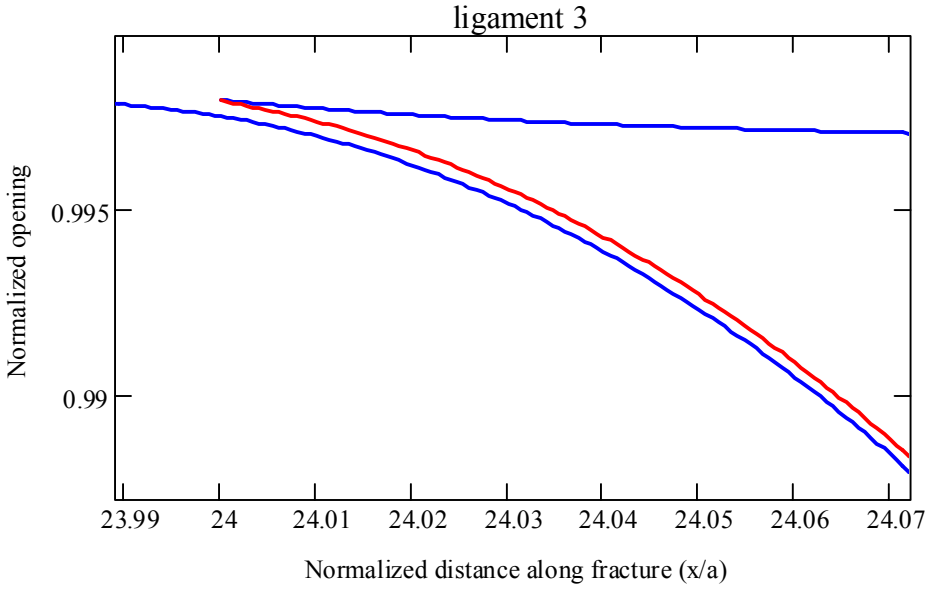

(d)

Figure 2.17 (Continued).

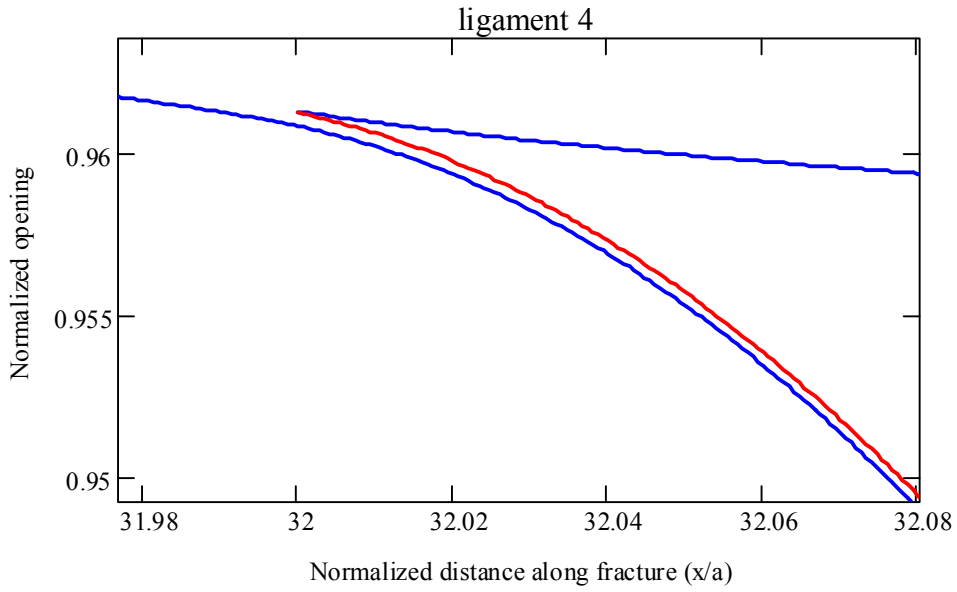

(d)

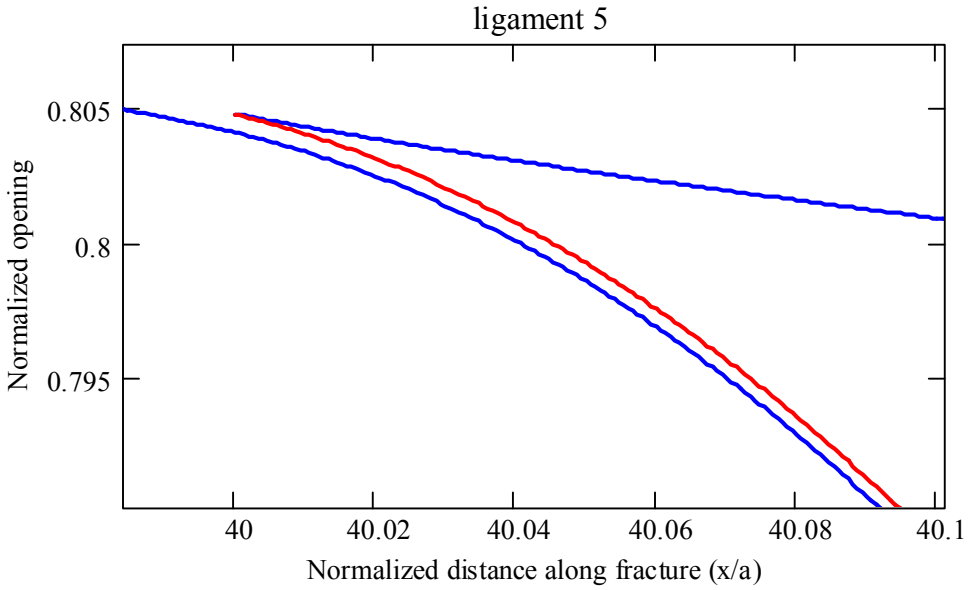

(e)

Figure 2.17 (Continued).

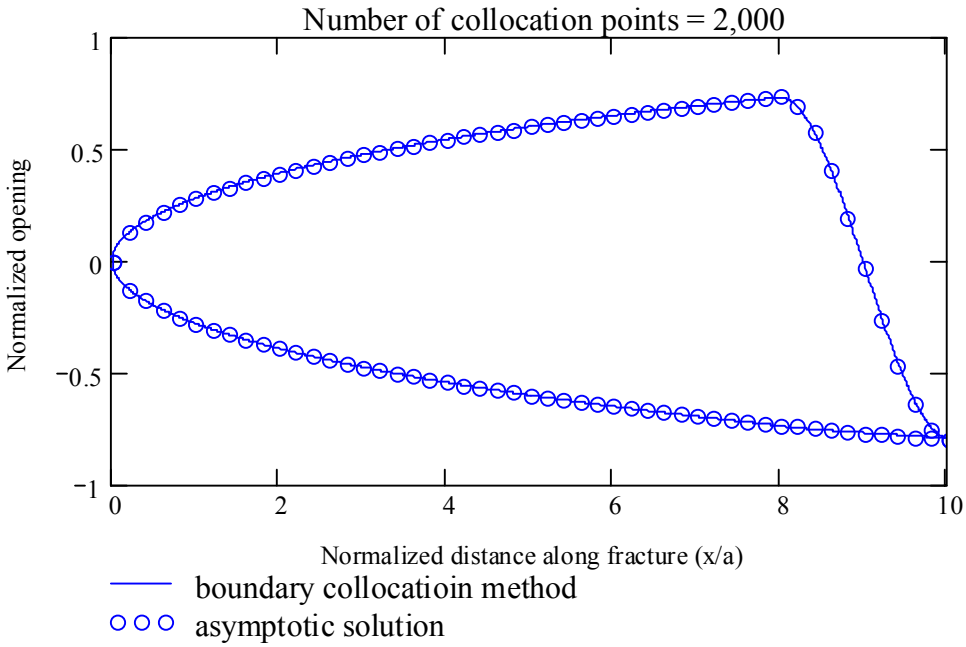

(a)

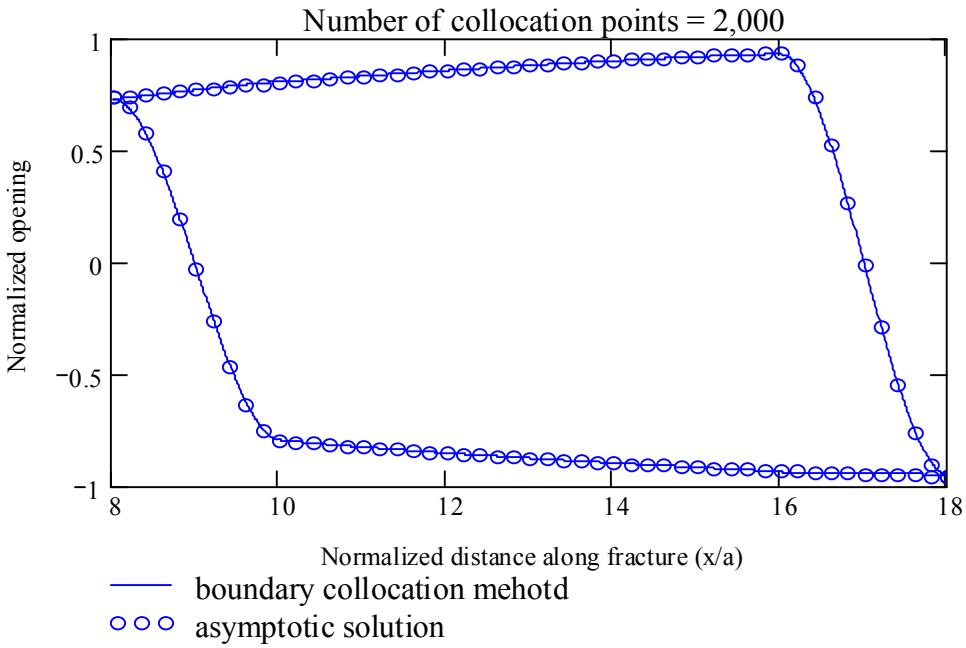

(b)

Figure 2.18 Comparison of opening between BCM and asymptotic solution when 2,000 collocation points are used for closely spaced six overlapping fractures: (a) first segment, (b) second segment, and (c) third segment.

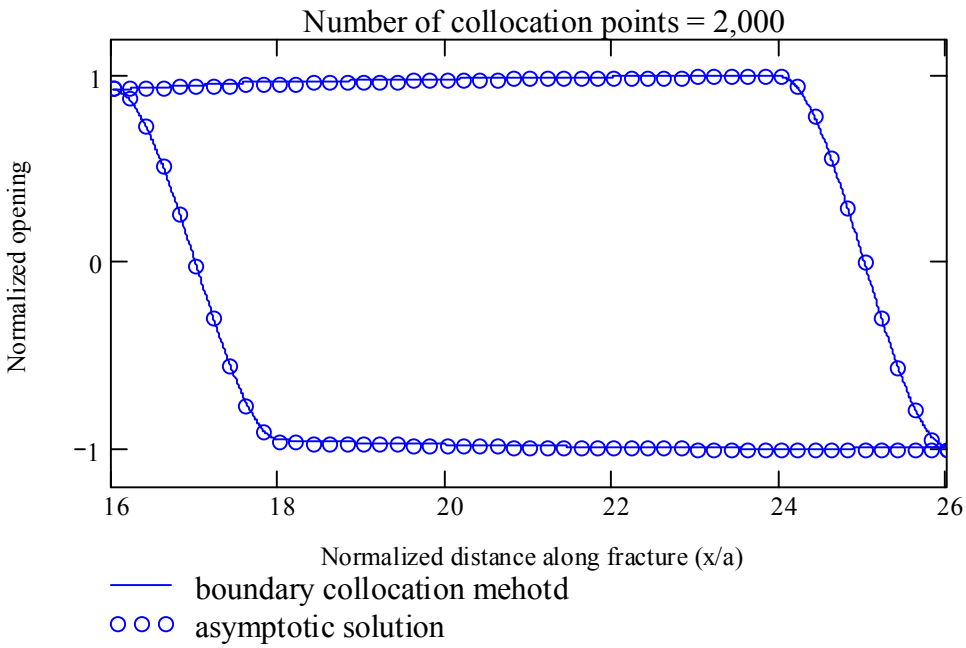

(c)

Figure 2.18 (Continued).

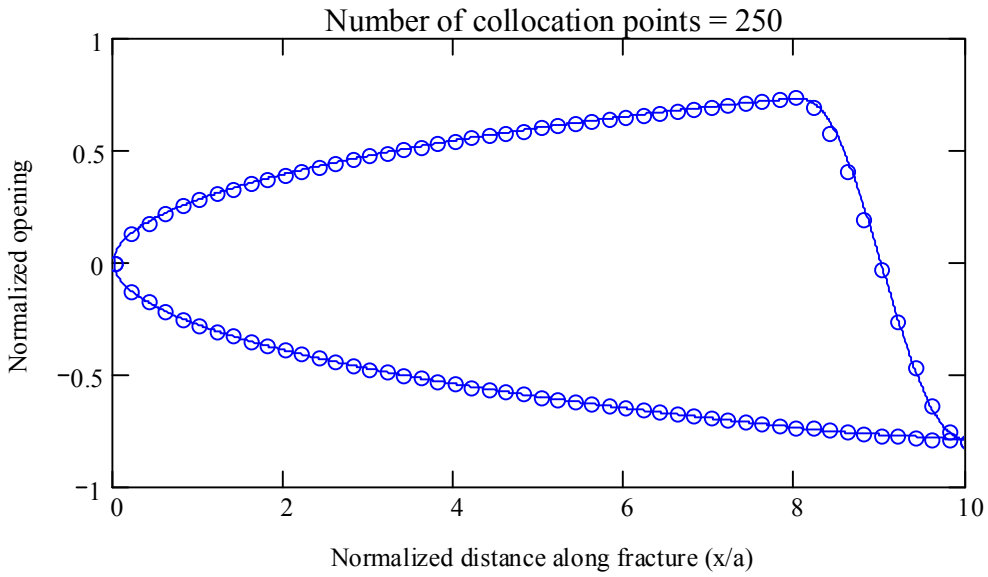

(a)

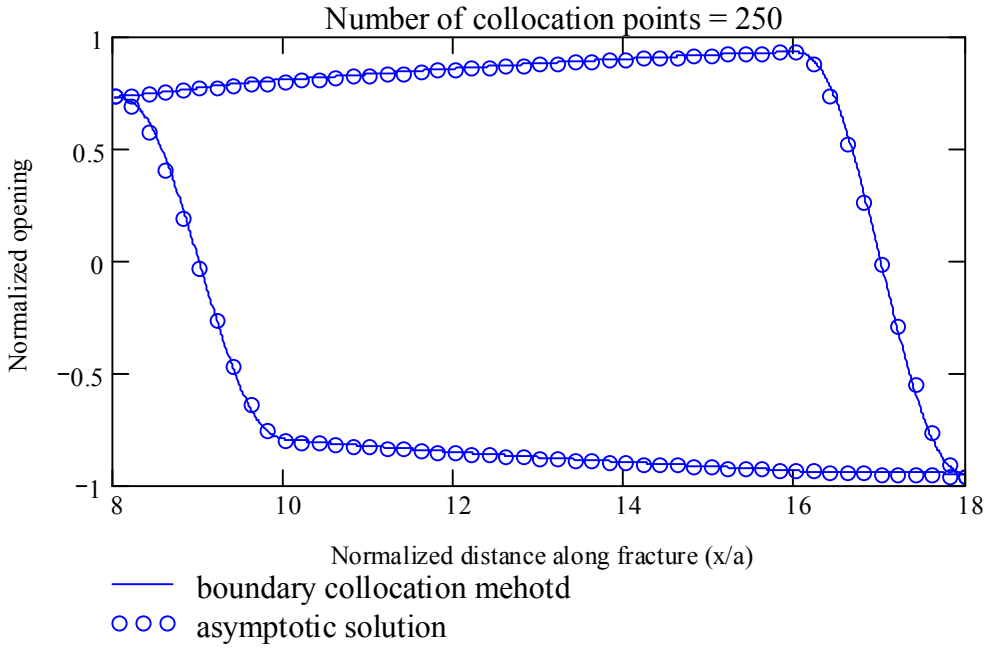

(b)

Figure 2.19 Comparison of opening between BCM and asymptotic solution when 250 collocation points are used for closely spaced six overlapping fractures: (a) first segment, (b) second segment, and (c) third segment.

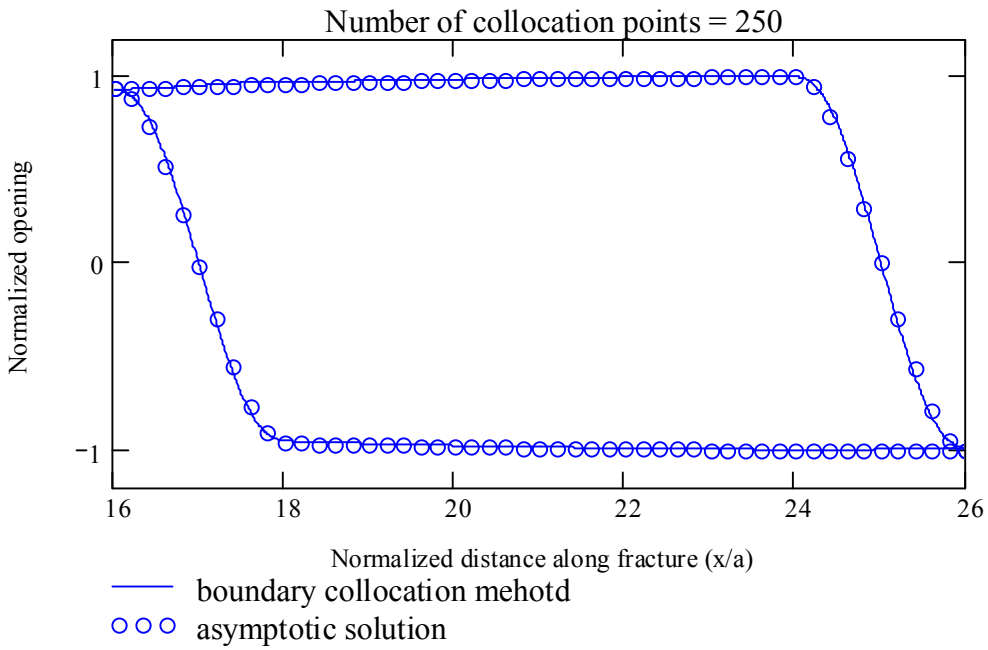

(c)

Figure 2.19 (Continued).

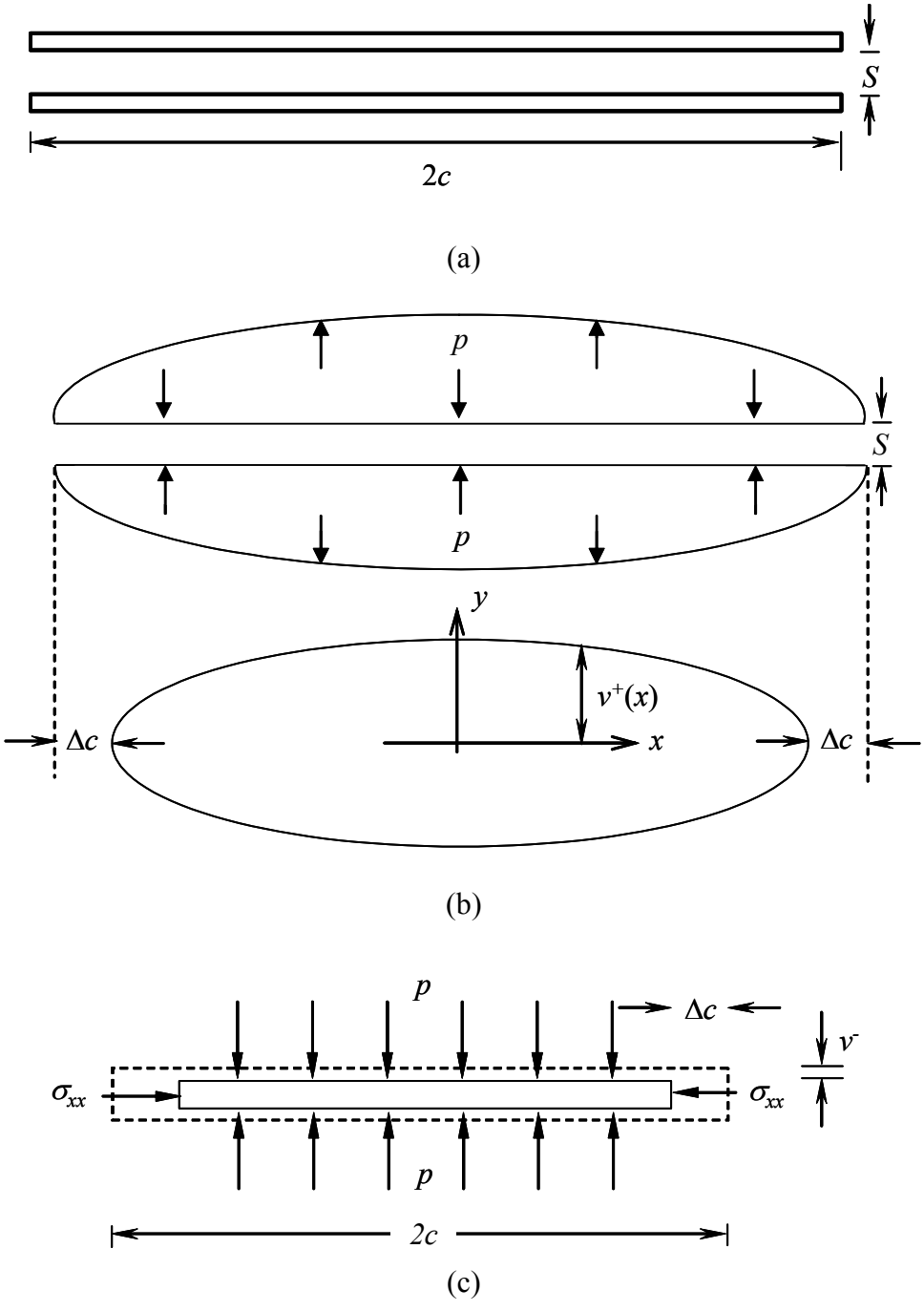

Figure 2.20 Asymptotic solution for two closely spaced parallel fractures: (a) definition of the geometry, (b) opening of the two parallel fractures and opening of a single fracture of the same length, and (c) deformation of the beam by surrounding stresses. The dashed line indicates the boundary of the beam before deformation.

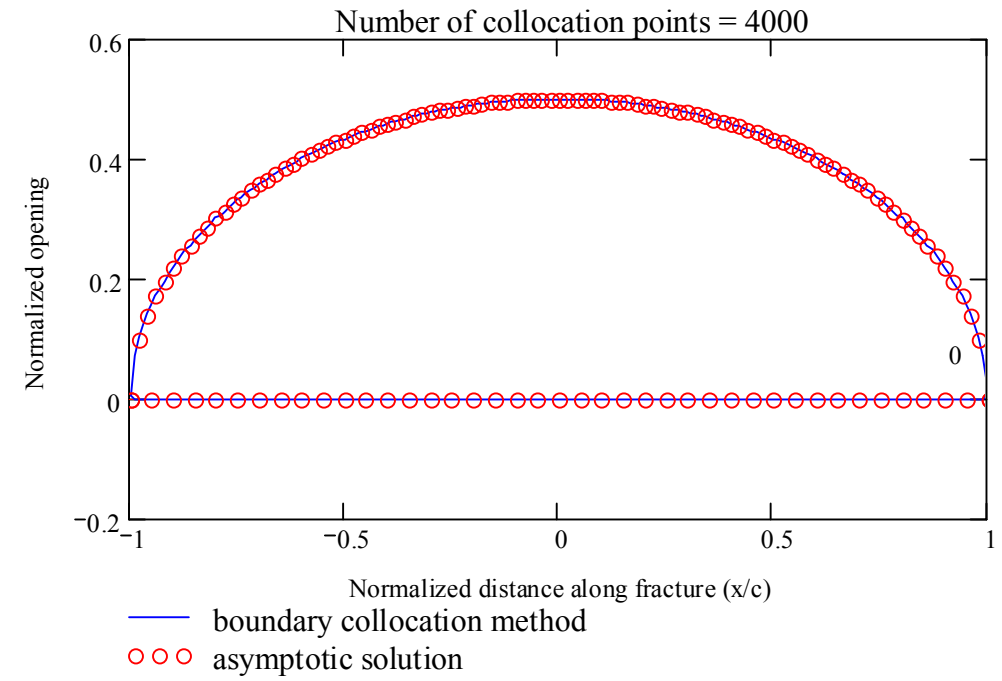

(a)

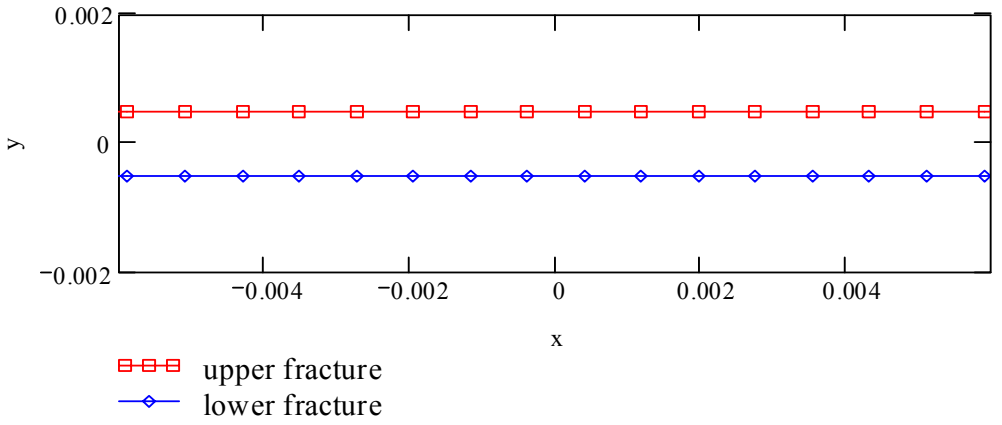

(b)

Figure 2.21 Two closely spaced parallel fractures: (a) comparison of opening between BCM and asymptotic solution when 4,000 collocation points are used, (b) density of BCM collocation points at magnified scale, and (c) normalized vertical displacement at magnified scale.

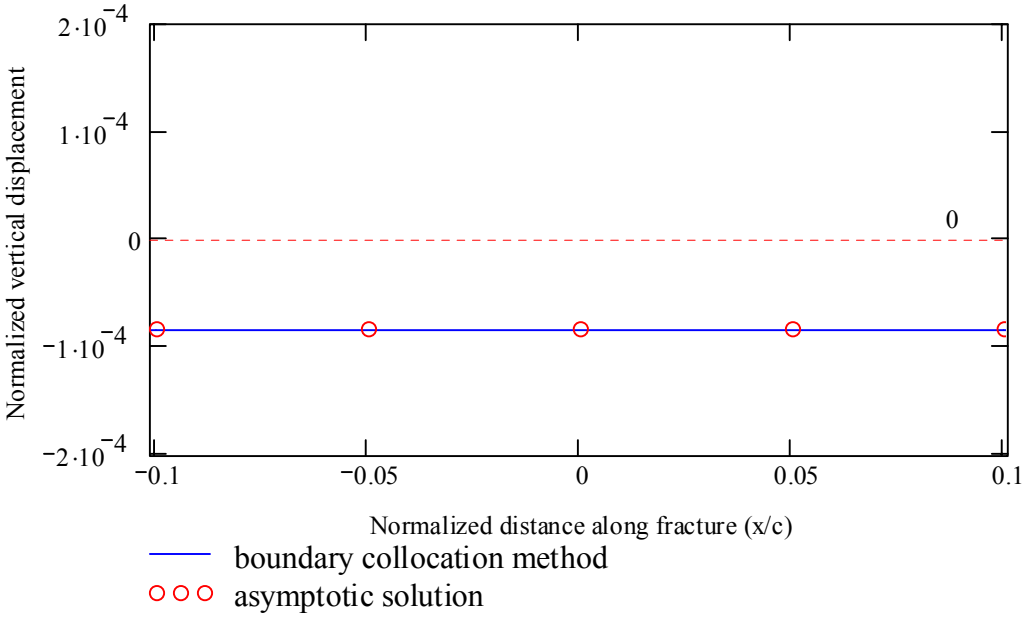

(c)

Figure 2.21 (Continued).

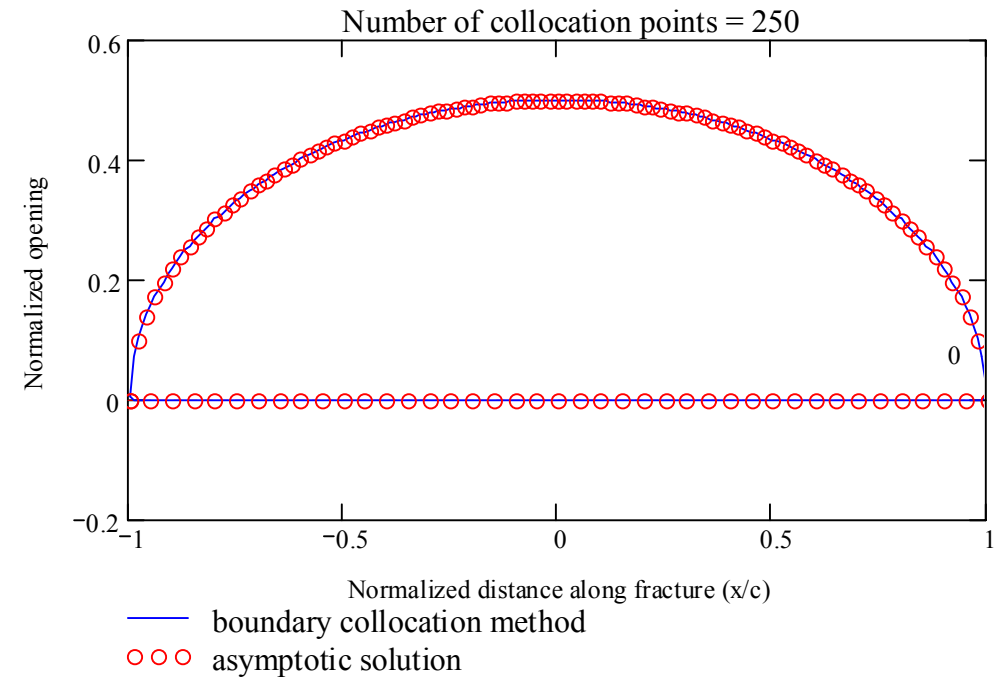

(a)

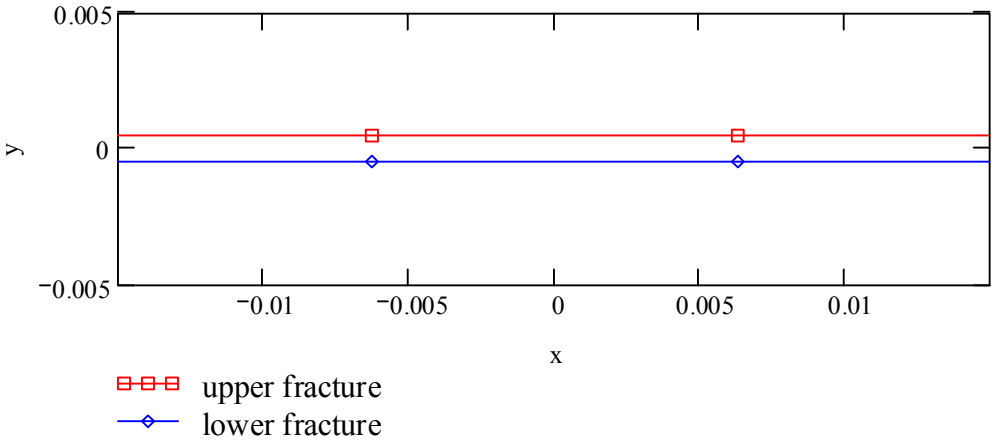

(b)

Figure 2.22 Two closely spaced parallel fractures: (a) comparison of opening between BCM and asymptotic solution when 250 collocation points are used, (b) density of BCM collocation points at magnified scale, and (c) normalized vertical displacement at magnified scale.

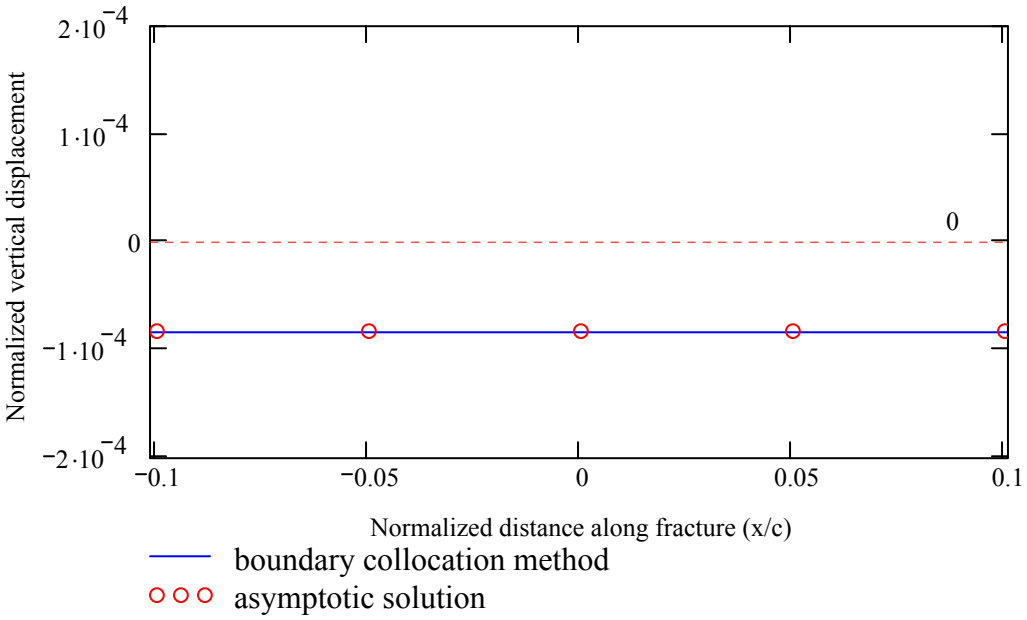

(c)

Figure 2.22 (Continued).

CHAPTER III

MODELING NATURAL MULTISEGMENTED HYDRAULIC FRACTURES

3.1 Introduction

Fluid-driven natural fractures, which we will refer to as natural hydraulic fractures, appear in a variety of forms (i.e., dikes, veins, and joints). These fractures display various structural features due to variation of heterogeneity of the rock, stress regimes, and fracture modes [e.g., see review in *Germanovich et al*., 1997a]. Echelons of multisegmented hydraulic fractures (MHF) with consecutive overlap are one of the most common types of structures in the Earth's crust (Figure 1.1). Due to the interaction between the segments, the mechanical behavior of these fractures may be quite different from that of single fractures. In particular, the mechanical interaction between the fracture segments significantly influences the parameters of industrial hydraulic fracturing (e.g., fracture aperture, length, and net pressure) [e.g., *Jeffrey et al*., 1987; *Nolte*, 1987; *Naceur and Roegiers*, 1990; *Germanovich et al*., 1998a and 1998b; *Olson*, 2003] as well as rock permeability associated with openings of natural multisegmented fractures [*Germanovich and Astakhov*, 2004].

The mechanical behavior of a single natural hydraulic fracture has been studied extensively. In contrast, few efforts have been devoted to the simulation of natural MHF due to the technical difficulties in the evaluation of the interaction between the segments even when using conventional elastic theory.

Delaney and Pollard [1981] investigated 35 distinct north-eastern echelon dike segments near Ship Rock, New Mexico (Figure 1.1). To evaluate the mechanical interaction between dike segments, they used the method of successive approximation and compared computed dike apertures with measured values. The results of their modeling are in good agreement with field data and reproduced in Appendix C.

Olson and Pollard [1991] simulated the growth of echelon veins and vein fillings. They suggested that the mechanical interaction between the segments is responsible for the sigmoid shape of segments after overlap, because the interaction changes local stresses around the tip of the segment. In order to investigate the effects of the interaction on the apertures, they considered two parallel echelon segments and found that the mechanical interaction of the two segments causes a change of the local strain in the fracture tips and therefore leads to the shear offset of the fracture walls.

Bai et al. [2000] investigated the interaction between equally-spaced parallel joints in layered sedimentary rocks. Using FRANC2D [*Wawrzynek and Ingraffea*, 1987], they performed a finite element analysis to compute the aspect ratio (i.e., the ratio of fracture aperture to length) as function of the joint and the layer thickness. The number of fractures used in their simulations ranged from 3 to 23, with varying spacing between the fractures. They concluded that the effect of interaction becomes significant when the spacing-to-thickness ratio is less than 1.3, and that the aspect ratio approaches its upper limit asymptotically when the spacing-to-thickness ratio increases.

Germanovich et al. [1997b and 1998a] computed the effect of interaction between parallel fractures based on the boundary collocation method. Although special attention was paid to the accuracy of the calculations, only specifically selected multisegmented

fracture geometries were chosen for their parametric study. *Germanovich and Astakhov* [2004] evaluated the interaction of up to 50 fractures numerically and ~10^3 segments asymptotically.

To the best of the author's knowledge, no studies simulating a large number of *real* natural MHF with significant interaction currently exist. Therefore, the apertures of a naturally segmented vein, which has a small offset compared to the overlap, are simulated in this study. The boundary collocation method (described in Chapter II) is employed to evaluate the effect of interaction. The computed apertures are compared to the measured apertures at various spatial scales. In addition, the computed net pressures for the case of interacting segments are compared to the case of the non-interacting segments.

3.2 Multiple vein segments

3.2.1 Geometric features of the 71-segment calcite vein

To describe the geometry of the multiple segments, geometric terms are defined as illustrated in Figure 3.1. In a cross-section of the vein segments, the length, 2*c*, is measured along the greater dimension and the aperture is measured along the lesser dimension. The offset is defined as the distance perpendicular to the segment strike and the overlap or separation is measured parallel to the strike.

Vermilye and Scholz [1995] investigated the 71-segment calcite vein in siltstone from the Culpeper Crushed Stone Quarry in Stevensburg, Virginia. The fracture, which is composed of 71 segments, has an outcrop length of 13.23 m and is segmented with

upwards stepping of approximately ~30 cm. These segments have a well-exposed cross-section whose normal lies in the bedding plane. There is no evidence of shear displacement that would indicate extensional opening.

Viewed with an equal scale (Figure 3.2a), the fracture appears quite simple with only slight segmentation. Viewed on an exaggerated scale in the *y*-direction, however, the segmentation of the vein fracture can be identified clearly (Figure 3.2b). These vein segments are filled with white calcite in dark red fine-grained siltstone, resulting in a sharp contrast. Therefore, fine aperture measurements were feasible. The aperture along the segments has been well mapped by *Vermilye* [1996] (Figure 3.2c). For this reason, these vein segments are chosen for the quantitative simulation of the apertures of naturally MHF in this chapter. The vein segments have a length that ranges from 3.4 to 142 cm, with segment apertures ranging from 0.017 to 3.88 mm on average (Table 3.1).

3.2.2 Offset and overlap features of the 71-segment calcite vein

The relative location of multiple segments can be described by their offset and overlap (or separation). Table 3.2 lists the offset and overlap of each segment with respect to the adjacent segment from left to right. Thus, the last segment (number 71) does not have any offset and overlap because it does not have any adjacent segment to its right. Negative overlap indicates separation with the adjacent segment (which is referred to as underlap or positive separation by some authors) as shown in Figure 3.1.

Table 3.1 Geometric data for the 71-segment calcite vein in siltstone from the Culpeper Quarry in Stevensburg, Virginia [after *Vermilye*, 1996].

Segment	Length (cm)	Maximum aperture (mm)	Average aperture (mm)	Segment	Length (cm)	Maximum aperture (mm)	Average aperture (mm)
1	7.5	0.05	0.033	37	48.5	1.6	1.120
2	5.5	0.05	0.033	38	34.5	2.25	1.315
3	8	0.1	0.061	39	38.1	2.5	1.484
4	26.5	0.1	0.065	40	35.5	2.5	1.458
5	9.5	0.1	0.050	41	46.7	2.25	1.358
6	4.2	0.1	0.050	42	13	0.1	0.033
7	4.7	0.1	0.050	43	15.5	0.45	0.214
8	14.3	0.2	0.092	44	38	0.1	0.033
9	19.2	0.4	0.250	45	62	2.7	1.523
10	6.6	0.3	0.146	46	54.5	3.5	2.012
11	26.5	0.55	0.373	47	80.5	3.9	2.787
12	6	0.5	0.292	48	106	4.7	3.179
13	12.5	0.55	0.266	49	25	4.2	2.018
14	20.9	0.65	0.451	50	37.5	4.5	2.771
15	11	0.6	0.360	51	26	4.7	2.798
16	7.7	0.6	0.391	52	52	5	3.740
17	10.9	0.6	0.244	53	14.5	4	1.519
18	17.1	0.7	0.387	54	27.5	3.7	1.141
19	6.2	0.7	0.386	55	31.5	3.8	2.087
20	9.3	0.5	0.245	56	15	3.5	1.831
21	7.6	0.25	0.109	57	8	4.2	2.372
22	12.9	0.5	0.214	58	13	3.9	1.379
23	15	0.7	0.396	59	20.5	4.4	2.778
24	36.4	1	0.646	60	20	4.2	2.089
25	24.8	1.05	0.584	61	24.5	3.7	1.192
26	9.6	0.75	0.330	62	11	4.3	2.802
27	29.5	0.7	0.338	63	73.5	4.85	3.824
28	11.2	0.25	0.113	64	55	4.9	3.881
29	28.2	0.3	0.156	65	142	5	3.327
30	3.4	0.05	0.036	66	76.5	3.9	2.780
31	22.8	0.15	0.081	67	12.5	3.6	1.875
32	14.5	0.05	0.017	68	53	3.6	2.844
33	14.8	0.45	0.241	69	12	3	1.790
34	7.2	0.35	0.165	70	121	3.2	1.527
35	9.4	0.55	0.295	71	28	0.4	0.133
36	38.5	1.1	0.604				

Table 3.2 Offset and overlap (separation) for the 71-segment vein [after *Vermilye*, 1996]. Negative overlap indicates separation between segments (Figure 3.1). The offset and overlap between the *n*th and (*n*+1)th segments are given in the row of the *n*th segment.

Segment	Offset (mm)	Overlap (mm)	Segment	Offset (mm)	Overlap (mm)
1	2.2	-2	37	2.7	60
2	11.3	-9	38	4.5	125
3	7.5	11	39	2.5	46
4	7.5	10	40	3.3	185
5	3.3	5	41	0.3	42
6	4.3	12	42	0.3	45
7	7.5	47	43	38.1	-95
8	2.5	8	44	15.1	85
9	1.3	7	45	10.5	275
10	2.5	36	46	5	190
11	1.1	10	47	8	200
12	1.6	16	48	9.3	170
13	5.2	46	49	3	115
14	5.5	24	50	4.5	175
15	2.1	23	51	0.8	50
16	2.8	21	52	3.9	85
17	7.8	64	53	1.8	70
18	1	22	54	6	260
19	0.6	5	55	10.5	150
20	16.9	54	56	1.6	50
21	0.6	16	57	0.5	30
22	1.1	49	58	4.3	105
23	0.5	65	59	0.7	70
24	0.5	47	60	3.3	200
25	1.5	50	61	1.3	50
26	1.85	51	62	2.5	35
27	0.5	112	63	1.52	70
28	0.3	20	64	2.48	80
29	0.95	32	65	21.4	380
30	0.5	14	66	3.3	40
31	0.5	3	67	2.5	70
32	86.55	-615	68	0.6	25
33	0.5	20	69	2.2	35
34	0.3	21	70	2	180
35	0.3	40	71		
36	2	155			

In this fracture, a maximum offset of 86 mm was observed between segments 32 and 33, and a maximum overlap of 280 mm was observed between segments 70 and 71. Figure 3.3 shows the relationship between the offset and the overlap for the multiple vein segments. The ratio of offset to overlap ranges from 10^{-1} to 10^{-3}. Therefore, it is expected that the effect of interaction should strongly affect the apertures of this fracture. In general, the segments with larger offsets typically have relatively large overlaps. For example, segments pairs 20 and 21, 32 and 33, 43 and 44, 55 and 56, 65 and 66 all have relatively large offsets and large overlaps (or separations) compared to other segment pairs.

3.2.3 Aperture features of the 71-segment calcite vein

To investigate the relationship between the length and the maximum aperture of the veins, *Vermilye and Scholz* [1995] considered different spatial scales (Figure 3.4). Based on the large offset between segments, they divided the entire fracture into several groups, which they referred to as first order subunits. By repeating this procedure, second, third, and fourth order subunits were identified (Figure 3.4). The apertures of the individual segments (i.e., the fourth subunit) revealed that the classic elliptical shape does not apply to all segments because the adjacent segments considerably affect the apertures of each segment. *Vermilye and Scholz* [1995] found that the correlation between the length and the maximum aperture for all subunits decreases as the scale decreases from the first to the fourth subunit. This indicates that subunits do not act independently. They also found that the aspect ratios for the first to third order subunits are less than those of an isolated single fracture with the same length. In contrast, the fourth order subunit has a

higher aspect ratio than that in the same outcrop. The difference between the aspect ratios for single fracture and those for multiple segments has also been found in other research [*Renshaw and Park*, 1997; *Olson*, 2003].

In this chapter, to understand these phenomena, the apertures that are computed by the boundary collocation method (refer to Chapter II) for the 71-segment vein are directly compared with the measured apertures.

3.3 Analysis procedure

The apertures of the naturally segmented veins are simulated at three different spatial scales: microscale, mesoscale, and macroscale. At the microscale, all segments are considered individually, such that the effect of interaction between multiple segments is fully accounted for along the vein segments. At this scale, based on the geometric configuration of the 71 segments, we define six groups as follows (Figure 3.5a):

- Group 1: segments 1 to 20
- Group 2: segments 21 to 32
- Group 3: segments 33 to 43
- Group 4: segments 44 to 55
- Group 5: segments 56 to 65
- Group 6: segments 66 to 71

At the mesoscale, the 71 segments are not "visible" individually. Rather each of the groups defined at the microscale is represented as a single segment, which leads to a total of six segments (Figure 3.5b). Thus, the effect of interaction is partially considered. This considerably reduces the size of the problem compared to the microscale. The location parameters of the six segments (e.g., segment angle) are determined by linear regression. At the macroscale, the multiple segments are represented by a single "effective" fracture (Figure 3.5c). Its location parameters are also determined by linear regression. The three map views at the three different scales in an equal scale coordinate set are shown in Figure 3.6. Summarizing, the 71 segments at the microscale are represented by 6 segments at the mesoscale and one fracture at the macroscale, respectively.

To evaluate the effect of interaction at each scale, the computed apertures for both the non-interacting and the interacting cases are compared with the measured apertures. In the non-interacting case, each segment is treated as a mechanically isolated fracture. Therefore, the aperture, $\Delta v_s = v_s^+ - v_s^-$ of a single isolated fracture with a length of $2c$, under the influence of a net pressure Δp (i.e., the difference between the internal pressure p and the remote stress σ_y^∞; simply referred to as pressure hereafter), in an infinite, homogeneous, and isotropic medium (Figure 3.7), is given by (e.g., *Tada et al*., [1985], see also (2.24))

$$\Delta v_s = 4c\frac{(1-\nu^2)\Delta p}{E}\sqrt{1-\frac{x^2}{c^2}} \qquad |x| \le c \tag{3.1}$$

where E is the Young's modulus, υ is the Poisson's ratio, and x is the local spatial coordinate along the length of the segment.

To take into account the effect of interaction between the segments, the aperture Δv_n of the nth segment that is pressurized by Δp can be calculated as given by (2.14):

$$\Delta v_n = 4c_n \frac{(1-\nu^2)\Delta p}{E}\sqrt{1-\frac{x^2}{c_n^2}}\left(\sum_{m=1}^{M_n}\frac{\alpha_m^n}{m}U_{m-1}\left(\frac{x}{c_n}\right)\right) \qquad |x| \le c \tag{3.2}$$

where M_n is the number of collocation points on the nth segment, α_m^n are the unknown coefficients of the Chebyshev expansion for the nth segment that need to be determined for a given configuration, and $U_m(x/c_n) = \sin((m+1)\arccos(x/c_n))/\sin(\arccos(x/c_n))$ is the mth order Chebyshev polynomial of the second kind. As discussed in section 2.1, after obtaining the coefficients α_m^n by solving the linear system of equations (2.8), the aperture (3.2) as a function of the distance along the fracture for a given pressure Δp can be found. In both cases (i.e., interacting and non-interacting segments), the pressure Δp is evaluated by using the least squares method to minimize the error between computed Δv_n and the measured apertures. If a uniform pressure is not sufficient to fit the data, different pressures are applied to different parts of the multisegmented fracture.

The pressures Δp obtained from both non-interacting and interacting cases at the microscale and mesoscale are also compared. A Young's modulus of $E = 2.5 \times 10^{10}$ Pa and a Poisson's ratio of $\nu = 0.21$ are assumed for the host rock in this analysis. However, as can be seen from (3.1) and (3.2), all results can be easily adjusted for different E and ν since they only appear in a factor in the expression for Δp.

3.4 Microscale consideration

At the microscale, all 71 individual segments are considered. As mentioned previously, these segments do not behave independently since they are located very close to each other. Thus, it is necessary to consider the effect of interaction between the segments. The interaction between all segments can be investigated in detail using the boundary collocation method considered in Chapter II at this level. The case of non-interacting segments is also considered for comparison. The geometric configuration of the multisegmented fracture is shown in Figures 3.2 and 3.3, while the corresponding data is listed in Tables 3.1 and 3.2.

3.4.1 Computational approach

A different number of collocation points is carefully assigned to each segment by considering the relationship between the offset and the overlap for the interacting case. For example, if two adjacent segments are closely spaced, the distribution of the collocation points should be dense. The total number of collocation points assigned to this fracture is $M = 12{,}465$. Accordingly, the size of the set of equations to be solved (refer to section 2.1) is $2M = 24{,}930$.

To solve this large set of linear equations, we used the Silicon Graphics' Scientific Computing Software Library, which includes the multi-processor version of the LAPACK library for parallel computations with double precision. Instead of using the serialized routines *ludcmp* and *lubksb* [*Press et al*., 1992], the parallelized FORTRAN routines *dgetrf* (LU factorization) and *dgetrs* (solution of linear equations) were used to

solve the large sets of equations. The serialized routines are adequate for relatively small-scale computations (Appendix A). For optimal performance, the Georgia Tech high performance computing cluster consisting of SGI Origin 3600 workstations was used.

3.4.2 Evaluation of the pressures, and comparison of computed and measured apertures

As mentioned in section 3.3, the apertures for non-interacting segments can be calculated from (3.1). For interacting segments, after obtaining the coefficients α_m^n by solving the linear set of equations, aperture (3.2) is computed as a function of the distance along the fracture (once the pressure is obtained from the least squares method). The number of pressures required to fit the measured apertures needs to be determined for the case of non-interacting and interacting segments.

Non-interacting case

Figure 3.8 shows the comparison between the computed and the measured apertures for the case of no interaction when a uniform pressure is applied to the entire fracture. In this case, the aperture of each segment is represented by an elliptical shape (refer to (3.1)), and its magnitude (Δp = 45.26 MPa) is proportional to the segment length $2c$. Apparently, there is no aperture trend because each segment is not affected by the behavior of any other segment. Therefore, to obtain a better least square fit, the possibility of applying different pressures is investigated. Figure 3.9 shows the results when two different pressures are applied to the fracture (also with non-interacting segments). The computed apertures still do not match the measured apertures. Even when 71 different pressures are applied to each segment independently, as in Figure 3.10, the

elliptical aperture shapes of individual segments do not fit to the measured apertures, although the entire aperture profile improved considerably.

Interacting case

In the case of interaction, pressurized individual segments affect the apertures of other segments. First, a single uniform pressure is applied to the entire fracture. Although the apertures of individual segments are close to the measured apertures (Figure 3.11), the entire aperture trend is quasi-elliptical and does not fit the measured data sufficiently well. To obtain a better fit, the application of several pressures to the fracture is investigated.

Figure 3.12 shows the results of applying two pressures. The computed apertures are in good agreement with the measured apertures in terms of the aperture shape of individual segments as well as the entire aperture trend. The detailed comparison is shown in Figure 3.13. The regions affected by different pressures are indicated with different colors. The first pressure, that is applied to groups 1, 2 and 3, is negative (Δp_1 = -1.52 MPa). The second pressure, that is applied to groups 4, 5 and 6 is positive (Δp_2 = 5.23 MPa). There is a large pressure difference between groups 3 and 4.

To obtain the final results (Figure 3.12) in this analysis, several computations are repeated to fit the computed apertures to the measured ones. As indicated in the plot for groups 3 and 4 (Figure 3.13), between which the value of pressure is changed abruptly from positive to negative, the parts of several segments that have a negative aperture during the computation (e.g., segments 42 and 43) were removed from the subsequent computation. Negative apertures correspond to segment sides inter-penetrating each

other, which is physically not possible. Since the removed segments have very small apertures (Figure 3.14), these segments are interpreted to be closed (with contacting sides) and, therefore, they do not contribute to the interaction and can be removed from the computation (or more accurately, parts of these segments where the computed aperture is negative).

For example, in the first simulation (Figure 3.14a) in which all segments are included, the computed apertures of segment 42 and 43 in group 3 are negative (i.e. the segments are closed). These segments are removed (Figure 3.14b). The computation is then repeated. This results in a good agreement with the measurements (Figure 3.13).

The narrow segment 44 in group 4 in Figure 3.13 was also removed from the simulation, because it resulted in the negative apertures for the wide segment 41 of group 3 (Figure 3.13). The reason for this effect is the abrupt pressure change between the adjacent groups. In reality, such a large pressure change is unlikely. Instead, a transition zone with a more gradually changing pressure is expected. This zone can be modeled by considering separate pressures in the corresponding segments within this zone. However, this would introduce a number of additional fitting parameters. Although these parameters may have a physical meaning (e.g., segment 44 may have solidified first before the rest of the segments), they are unconstrained by the available measurements. Given the very small aperture of segment 44, it does not contribute significantly to the interaction, and, consequently, it is removed from the computations. After that, two pressure parameters results in reasonable fit (Figure 3.13).

Although the aperture profile simulated with two pressures is much better than that of a single uniform pressure (Figure 3.11), three and six pressures are also applied to

the fracture to further improve the computation (Figures 3.15 and 3.16) and to determine the minimum number of pressure parameters required for an acceptable agreement between the measured and computed results. Compared to the obtained results to those for two pressures (Figure 3.12), the aperture trend is not significantly improved and the pressures have similar values. Table 3.3 lists a summary of results for the full interaction of all segments. For all cases, the negative net pressures are obtained in groups 1, 2 and 3. Consequently, two net pressures are sufficient to simulate the apertures of the 71-segment vein provided that the effect of interaction between the segments is accounted for.

Table 3.3 Results for the net pressures at the microscale.

<table>
<tr><th colspan="2">Number of pressures</th><th>2</th><th>3</th><th>6</th></tr>
<tr><td rowspan="6">pressure, MPa</td><td>Group 1</td><td rowspan="3">-1.52</td><td rowspan="2">-1.38</td><td>-1.17</td></tr>
<tr><td>Group 2</td><td>-1.89</td></tr>
<tr><td>Group 3</td><td>-1.59</td><td>-1.15</td></tr>
<tr><td>Group 4</td><td rowspan="3">5.23</td><td rowspan="3">5.24</td><td>4.90</td></tr>
<tr><td>Group 5</td><td>5.34</td></tr>
<tr><td>Group 6</td><td>5.55</td></tr>
</table>

3.4.3 Convergence study

To verify that the solution has converged in the simulations at the microscale, the results for all cases are compared with those obtained with an increased number (i.e., 75% to 100%) of collocation points (for all segments). The details are given in Appendix B.

3.5 Mesoscale consideration

As mentioned in section 3.3, in order to simplify the analysis, each of the previously defined groups (Figure 3.5a) is represented as a single segment (Figure 3.17a). Consequently, any effect caused by the segmentation within each group is ignored in this consideration. In other words, at the mesoscale, the individual segments are not distinguishable and only the first order segmentation are noticeable (i.e., groups are treated as segments).

Non-interacting case

Similar to the non-interacting segments at the microscale, using a single, uniform pressure or two pressures does not result in a good fit of the measurement (Figures 3.17 and 3.18). Even when six pressures are applied to the fracture (Figure 3.19), the quality of the fit does not improve significantly. Consequently, we further consider the case of the interacting mesoscale segments.

Interacting case

Using the same procedures as for the microscale, first, a uniform pressure is applied to the fracture. As expected, the entire aperture trend shows quasi-elliptical shape (Figure 3.20). This is similar to that of the microscale case (Figure 3.11) and does not really fit the measured apertures.

Figure 3.21 shows the result of applying two pressures. A reasonably good agreement with the measured points in terms of the shape of the overall aperture trend is obtained. However, the computed apertures clearly underestimate the measured apertures. This is the result of including all measured apertures while computing the fit using the least squares method. Indeed, the apertures of the segments at the microscale are small near the segment ends. Yet, the mesoscale segments have small apertures only at their ends, but not in the central points corresponding to the ends of the microscale segments. Including these small aperture values at the intermediate points (with respect to the mesoscale segments) into the least squares fitting decreases the apertures (Figure 3.21). At the microscale, this is not an issue since these small apertures are relevant when all microscale segments are considered explicitly.

Therefore, the data is reduced before using the least square method at mesoscale simulations. Figure 3.22 shows how the data is reduced on the example of group 3. The data points that are below the intersections between the curves representing the segment apertures are removed. This results in a good agreement with the measured apertures (Figures 3.23). The pressures for the mesoscale segments 1, 2 and 3 are negative (Δp_1 = -1.75 MPa), while the pressures for the mesoscale segments 4, 5 and 6 are positive (Δp_2 = 5.14 MPa). Similar to the microscale case, there is a large pressure transition between

groups (or mesoscale segments) 3 and 4. Note that the obtained net pressures at the mesoscale are close to those for the microscale case (-1.52 MPa and 5.23 MPa; refer to Figure 3.12).

Similar to the microscale, to obtain the final results (Figure 3.23), small closed sections of the mesoscale segments were removed. These closed sections correspond to very small measured apertures (Figures 3.23).

The application of two pressures dramatically improves the entire aperture trend compared to the trend for a single uniform pressure (Figure 3.20). Although the implemented data reduction is somewhat arbitrary, it does not affect the data set significantly. Further data reduction would improve the fitting. Again, using two pressure parameters is sufficient (and necessary, since the single pressure model is not reasonably accurate) to fit 2,700 data points (after reduction) at the mesoscale if segment interaction is taken into account.

3.6 Macroscale consideration

The simplest method to simulate the aperture of multiple segments is to represent all vein segments as a single fracture. In this case, segmentation is completely ignored within the fracture. In fact, visually, on a map with an equal scales in the x and y directions, the vein almost appears to be a single fracture (Figure 3.2a). This is due to the fact that the offsets between the adjacent segments are very small. The effective single fracture (determined by the linear regression analysis) has a length of $2c$ = 13.23 m and an inclination with respect to the x direction of $\theta \approx 1°$.

The aperture of the effective fracture can be plotted by using (3.1) or (2.24) if the uniform pressure Δp is applied to its sides. As a result, a pressure of Δp = 2.34 MPa has been obtained by the least square method. Figure 3.24 shows the computed and measured apertures. As expected, the computed aperture shape is simply elliptic and does not represent the aperture shape well. In this respect, this result is similar to those for the mesoscale and microscale (Figures 3.20 and 3.21). Accordingly, two pressure parameters were used to fit the measured apertures.

Effective fracture

At the macroscale, consider a single fracture bounded by two pressures that are determined by fitting the measured apertures. As shown in Figure 3.25, the apertures bounded by two pressures can be simply superimposed in a single fracture. In this case, the aperture of the single macroscale fracture can be calculated as follows:

$$\begin{aligned}\Delta v_s &= 4c\frac{(1-\nu^2)\Delta p_1}{E}\sqrt{1-\frac{x^2}{c^2}} \\ &+ 4\frac{(1-\nu^2)(\Delta p_2-\Delta p_1)}{\pi E}\left[(c-x)\cosh^{-1}\frac{c^2-cx}{c\,|\,x-c\,|}-(b-x)\cosh^{-1}\frac{c^2-bx}{c\,|\,x-b\,|}\right. \qquad |\,x\,|\le c \\ &+ \left.\left(\sin^{-1}\frac{c}{c}-\sin^{-1}\frac{b}{c}\right)\sqrt{c^2-x^2}\right]\end{aligned} \tag{3.4}$$

where b = -2.09 is the boundary between two pressures (the center of the fracture is x = 0; refer to Figure 3.25). The first term in (3.4) represents the case when a single, uniform pressure is applied to the entire fracture while the second term [*Tada et al*., 1985] corresponds to the partial uniform pressure applied to the same fracture (Figure 3.25). As

a result of the least squares fit, the obtained pressures, $\Delta p_1 = -1.90$ MPa and $\Delta p_2 = 5.03$ MPa, are similar to those for the case of segment interaction at the microscale and mesoscale. Therefore, the concept of the effective single fracture is sufficiently accurate for the computation of the vein apertures, but without the difficult and laborious computations of the interaction between the multiple segments. Mechanically, this is the low flexural rigidity of the thin ligaments between the segments that allows the effective fracture to accurately represent the vein, although this condition is not sufficient (see below).

The concept has been already employed in the literature [see *Olson*, 2003, and the references therein] in the case of the uniform pressure applied to the sides of the effective fracture. In our case, homogeneous pressure does not result in a reasonable agreement with the field measurements and minimum two pressure intervals along the effective fracture are necessary. Then the match becomes very good.

Note that while the effective fracture model produced a good result for the studied field case, it may not be valid for all types of segmented fractures, even if the spacing between the segments is small. Consider, for example, en echelon of identical segments that is *well* represented by the effective fracture. Let us do the following thought experiment. Start increasing the number of segments in the echelon (i.e., adding more and more segments to the echelon edges), but maintaining the same pressure in each segment and keeping the geometrical pattern (i.e., offset, overlap, and the segment sizes). As a result, the aperture of the central segment will be approaching that of an infinite array and, therefore, is bounded. In contrast, because the size of the effective fracture grows unlimited (since we continue adding more segments), the aperture of the effective

fracture tends to infinity and, hence, is unbounded. In other words, the difference between the actual aperture and that of the effective fracture will increase without limit. Thus, this example clearly demonstrates that the concept of the effective fracture, which has recently become conventional, needs to be applied with care.

3.7 Discussion

3.7.1 Effect of interaction

For comparison, the changes in the obtained pressures are summarized in Table 3.4 for all cases. The shaded cells in Table 3.4 indicate the pressures that result in the best fits of the measurements. By using two pressures as fitting parameters for the interacting vein, it is possible to obtain an excellent match (Figures 3.12, 3.23, and 3.26) between the computed and measured apertures (based on 3,339 data points) at every scale.

As stated previously, the vein segments that are considered in this study are strongly interacting with each other. Even the application of many pressures in the model of no interaction at both the mesoscale (Figure 3.19) and the microscale (Figure 3.10) does not result in an acceptable match with the measured apertures.

As can be seen from Table 3.4, there are noticeable differences of pressure values between the cases of non-interacting and interacting segments. However, the pressures for the interacting segments for different scales are similar to each other when two pressures are applied to the fracture (shaded area in Table 3.4). In addition, regions with negative pressures (group 1-3) are detected, while all pressures are positive for the non-interacting case.

Table 3.4 Comparison of computed pressures when a single uniform or two pressures are applied to the fracture at different scales.

Scale		Microscale				Mesoscale				Macroscale	
Interaction		No		Yes		No		Yes		No	Yes
Number of pressures		1	2	1	2	1	2	1	2	1	2
Pressure (MPa)	Groups 1 – 3	45.26	42.12	3.45	-1.52	11.32	5.42	2.62	-1.75	2.34	-1.90
	Groups 4 – 6		45.49		5.23		12.62		5.14		5.03

Furthermore, when applying two pressures at the microscale (Table 3.4), the positive pressure obtained for non-interacting segments (Δp_2 = 45.49 MPa) is an order of magnitude greater than that for interacting segments (Δp_2 = 5.23 MPa). At the mesoscale, the deviation becomes less significant. However, the positive pressure obtained for non-interacting segments (Δp_2 = 12.62 MPa) is still greater than that for the interacting segments (Δp_2 = 5.14 MPa). This is due to the fact that the strong interaction between the segments results in larger segment apertures, such that the pressure is much lower than that for the non-interacting segments.

Therefore, ignoring the segment interaction in the hydraulic fracturing analysis may overestimate the pressure by an order of magnitude (or more). Furthermore, this overestimation could be even more significant since the sign of the pressure values may be misinterpreted (refer to Table 3.4).

3.7.2 Effect of scale

The effect of spatial scale can be considered by comparing both the pressures and the apertures at different scales. In this analysis, the microscale and mesoscale both show an excellent fits of the measurements if the effect of interaction is taken into account while using two pressures. At the microscale, the individual aperture shape of the segments, as well as the aperture shape of the entire fracture, can be simulated. Obviously, at the mesoscale, the individual apertures of the segments cannot be simulated, but it is much easier to simulate the entire aperture shape because of the reduced size of the problem.

The pressures obtained from the three different spatial scales show slight deviations when the effect of the interaction is considered. For example, for a single uniform pressure (Table 3.4), the pressure for the interacting case at the microscale (Δp = 3.45MPa) is slightly greater than that at the mesoscale (Δp = 2.62MPa) and the macroscale (Δp = 2.34MPa). For two pressures (Table 3.4), the pressures at the microscale (Δp_1 = -1.52 MPa, Δp_2 = 5.23 MPa) are also slightly greater than those at the mesoscale (Δp_1 = -1.75 MPa, Δp_2 = 5.14 MPa) and the macroscale (Δp_1 = -1.90 MPa, Δp_2 = 5.03 MPa). This difference, even if it is small, could stem from the method of data reduction (Figure 3.22). In fact, the data has not been sufficiently reduced for the mesoscale (Figure 3.23) and microscale (Figure 3.26). Removing more data points could increase the pressures and lead to the decrease of the pressure difference at all spatial scales.

On the other hand, when the effect of interaction is ignored, the pressures are very different. For example, for two pressures (Table 3.4), the pressures at the microscale (Δp_1 = 42.12 MPa, Δp_2 = 45.49 MPa) are much greater than that at the mesoscale (Δp_1 = 5.42 MPa, Δp_2 = 12.62 MPa). Consequently, neglecting the interaction can result in the pressure misinterpretation.

In general, as the amount of segmentation increases, the pressure required to achieve the same aperture increases (if the overall fracture dimension does not change). In other words, it is expected that the pressure at a smaller scale (microscale) should be higher than those at a larger scale (mesoscale and macroscale). This behavior has not been clearly identified for the interacting segments of this fracture, since it has extremely small spacing and large overlaps. Nevertheless, it is possible to properly simulate fracture

shapes and pressures at every scale as long as the effect of interaction is taken into account.

3.7.3 Non-elliptical aperture shape

An elliptical aperture shape is generally associated with a uniform pressure distribution. However, a fracture typically has a variety of cross-sectional shapes that are not simply elliptical due to the non-uniform pressure distribution and the inherent nature of the rock heterogeneity [e.g., *Pollard and Muller*, 1976]. For example, the entire aperture profile of the 71-segment vein, which was studies in this chapter (Figure 3.2c), is not elliptical. The profile is low and concave at the left and high and convex at the right (refer to Figure 3.2c), which is referred to as a teardrop shape [e.g., *Secor and Pollard*, 1975; *Pollard and Muller*, 1976]. Moreover, the apertures of individual segments are neither elliptical nor teardrop because of the interaction between adjacent segments.

If two pressures caused the asymmetry of the 71-segment vein, it is expected that the internal pressure p has changed while the remote stress σ_y^∞ remained constant because the total length of this fracture, $2c$ = 13.23 m, is not sufficiently large for the remote stress to be affected. In other words, the left side of the aperture profile (groups 1-3) indicates that the remote stress σ_y^∞ is greater than the internal pressure (i.e., the net pressure is negative), whereas the right side of the aperture profile (groups 4-6) indicates that the internal pressure overcame the remote stress (i.e., the net pressure is positive).

3.7.4 Geological interpretation

The Culpeper basin of northern Virginia, where Culpeper Quarry is located, is a fault-bounded trough containing a thick sequence of Upper Triassic to Lower Jurassic nonmarine sedimentary rocks (e.g., siltstone) [*Lee and Froelich*, 1987]. A relatively high fluid pressure (5 MPa) could result from tectonic extension. *Vermilye and Scholz* [1995] stated that the orientation of this vein set is compatible with the northwest extension direction postulated for the formation of Culpeper basin.

Later, the lower Jurassic strata of the Culpeper basin were interbedded with a series of basalt flows that erupted on the surface and subsurface intrusions of basaltic magma known as diabase [*Lee and Froelich*, 1987]. Accordingly, it cannot be excluded that the potential hydrothermal activity generated by the intrusion of diabase and the higher percentage of hydrothermal minerals [*Junium* et al., 2000] could be another reason for the high fluid pressure.

Our computations recreate the final stage of the vein evolution. The simulated apertures represent segments that have been opened by the two calculated net pressures. These two distinct pressures indicate that the pressure communication between the two corresponding vein parts is weak or non-existent. Further geological interpretation, perhaps, based on our results, is required to reconstruct the complete history of the vein (e.g., initiation, propagation, fluid flow, and precipitation) [refer to *Ramsay*, 1980; *Fisher and Brantley*, 1992; *Laubach*, 2003], which is beyond the scope of this work. Yet, we concluded that as long as the vein was pressurized, mechanical interaction was always a major mechanism regardless of whether other processes were active or not.

3.8 Summary and conclusions

In this chapter, a typical field example, a highly segmented vein, is studied and used to determine the effects of segment interaction at different spatial scales. For this well-mapped vein that represents a well constrained case, the simplest constitutive model, based on an ideal elastic material, has been tested for its capability to capture the complex behavior of multisegmented fractures.

The mathematical model is tested by comparing computed segment apertures to the measured apertures at three different spatial scales. By using this simple constitutive model and by including the effect of interaction between the segments, an excellent match was obtained at all considered scales. Only two net pressures were needed to fit 3,339 highly irregular measured apertures. This simulation also suggests that the interaction between the segments strongly affects the apertures of the fractures and their net pressures. In contrast, by neglecting the interaction between the segments, the net pressures can be grossly overestimated, by as much as an order of magnitude or more.

In addition, the concept of the effective fracture, as currently accepted in the literature, has been employed for a simple simulation of fractures with closely spaced and interacting segments. In the studied field case, the effective fracture model provided rather robust and accurate results. In general, however, due to the complex interplay between the parameters of segmentation, this concept may not always be applicable and may lead to unbounded inaccuracy.

Our computations recreate the final stage of the vein evolution. The simulated apertures represent those that have been opened by the two calculated net pressures.

These two distinct pressures indicate that the pressure communication between the two corresponding vein parts is weak or non-existent. Further geological interpretation, based, perhaps, on our results, is required to reconstruct the complete history of the vein (e.g., initiation, propagation, fluid flow, and precipitation). Yet, our computations indicate that as long as the vein was pressurized, mechanical interaction was always a major mechanism regardless of whether other processes were active or not.

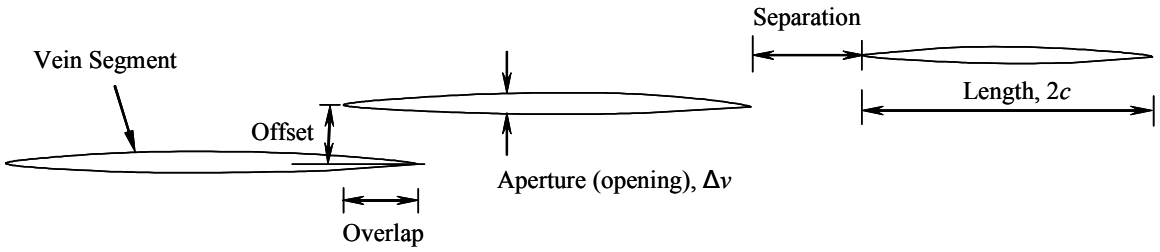

Figure 3.1 Geometric terms for a multisegmented fracture. Negative overlap indicates separation and vice versa (e.g., overlap of -2 cm means 2 cm of separation and the separation of -5 cm indicates the 5 cm overlap).

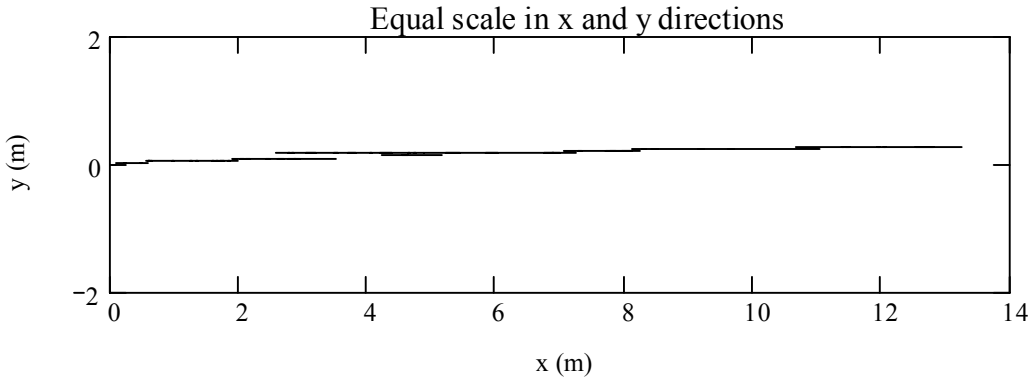

(a)

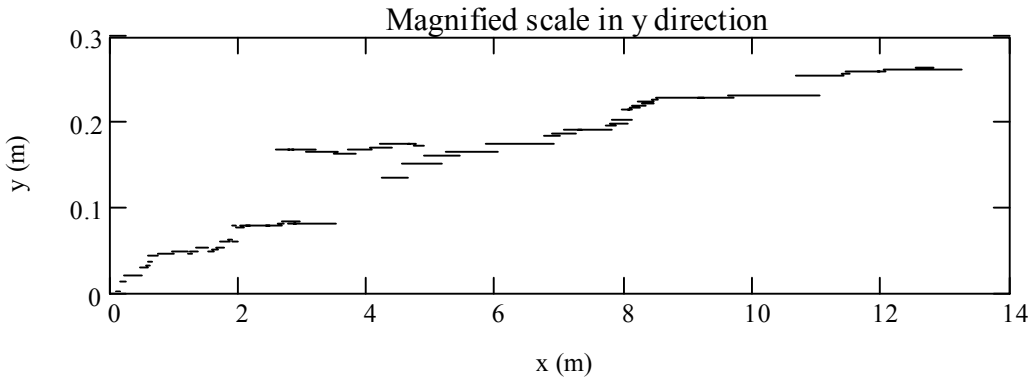

(b)

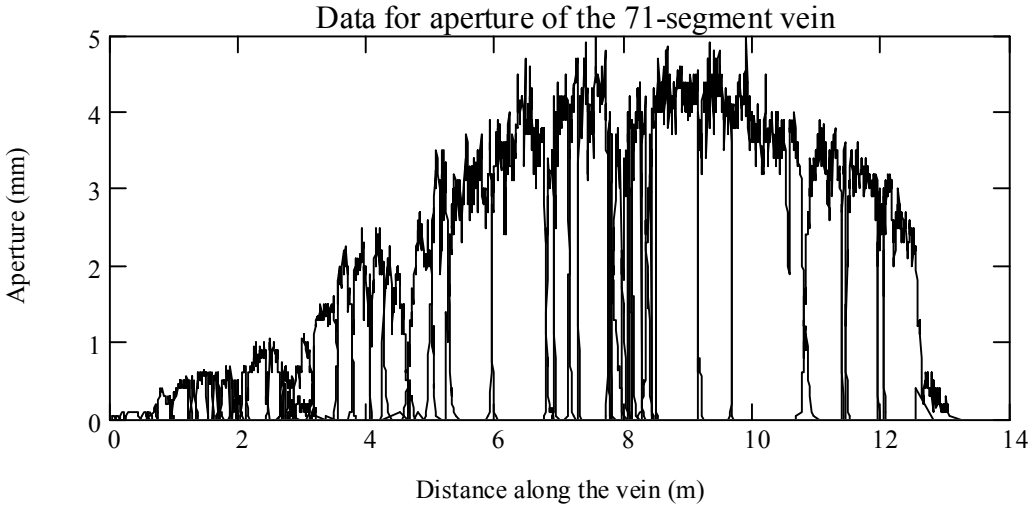

(c)

Figure 3.2 Map view and aperture distribution of the 71-segment calcite vein in siltstone in Culpeper Quarry (Stevensburg, Virginia) [after *Vermilye and Scholz*, 1995]: (a) map view for equal scales, (b) map view at magnified scale in *y* direction, and (c) aperture versus distance along the vein segments.

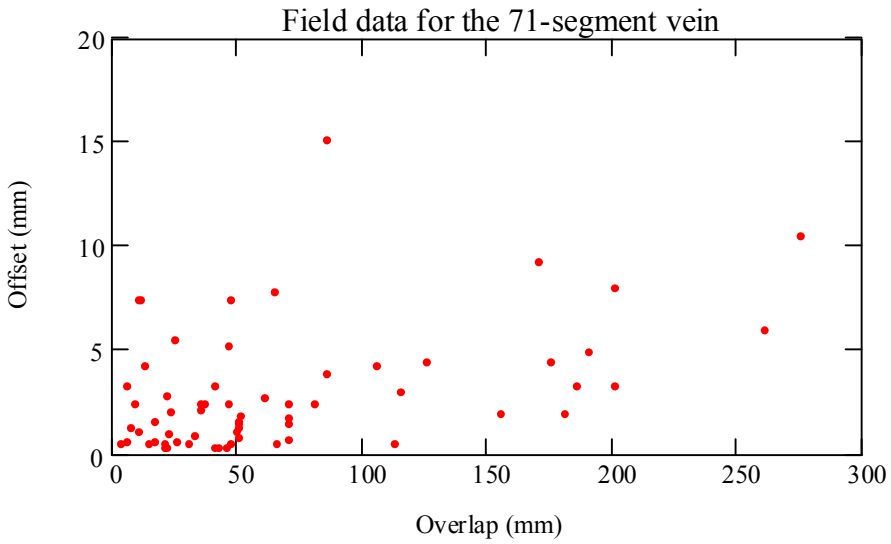

Figure 3.3 Offset versus overlap in the 71-segment vein markers based on the data in Table 3.2. Data points for separation (negative overlaps) in Table 3.2 are not shown.

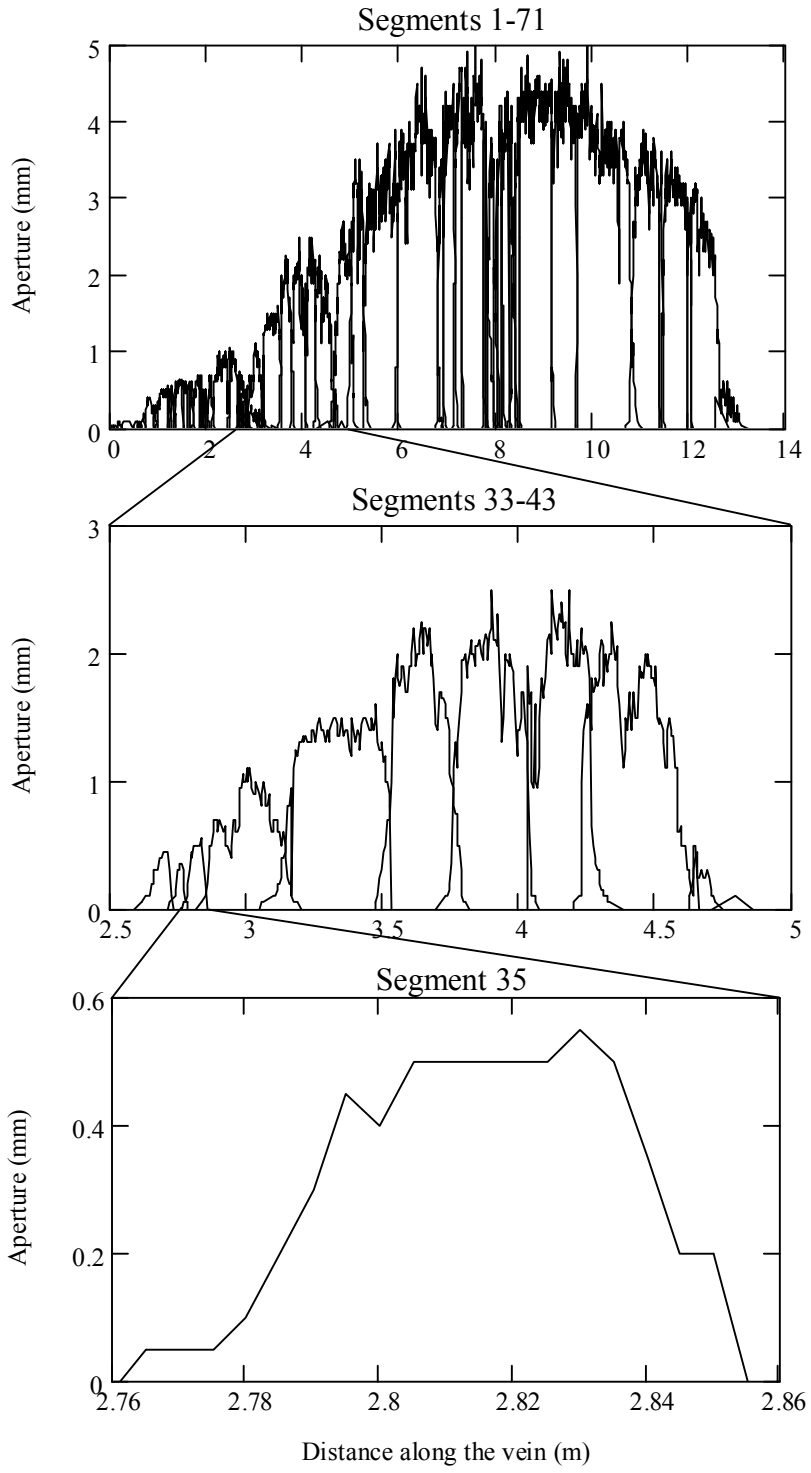

Figure 3.4 Aperture versus distance along vein at different spatial scales [*Vermilye and Scholz*, 1995].

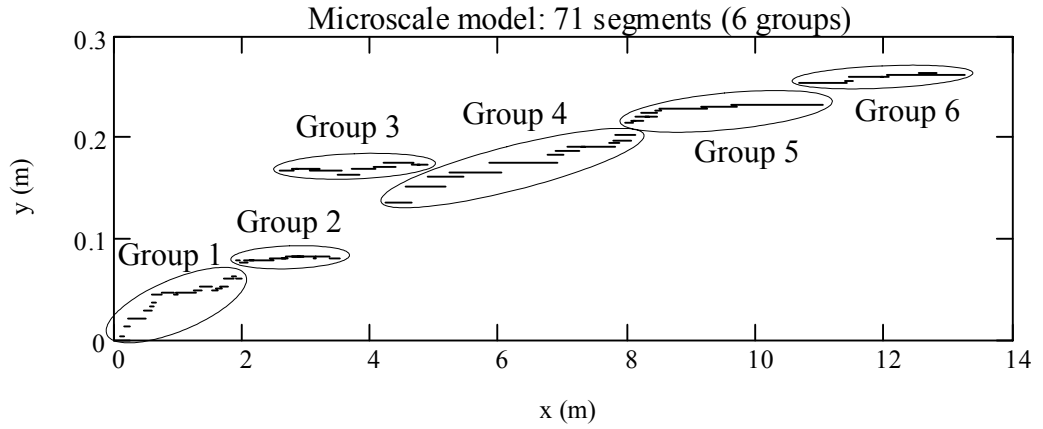

(a)

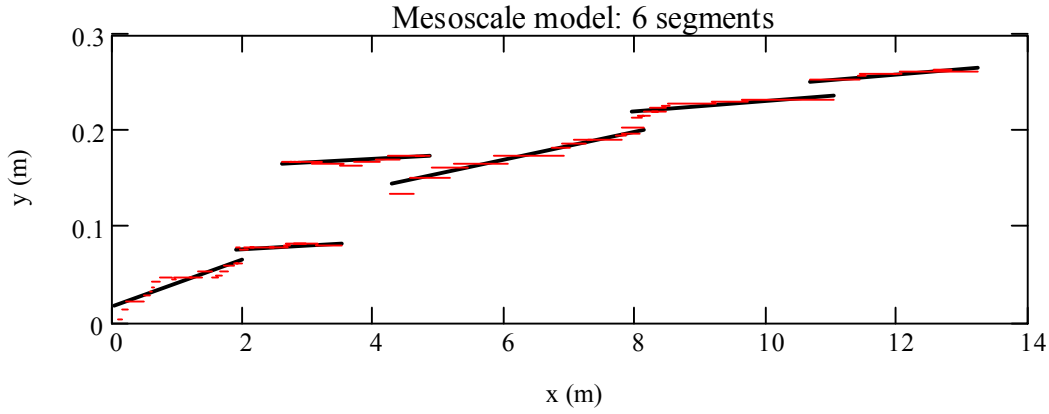

(b)

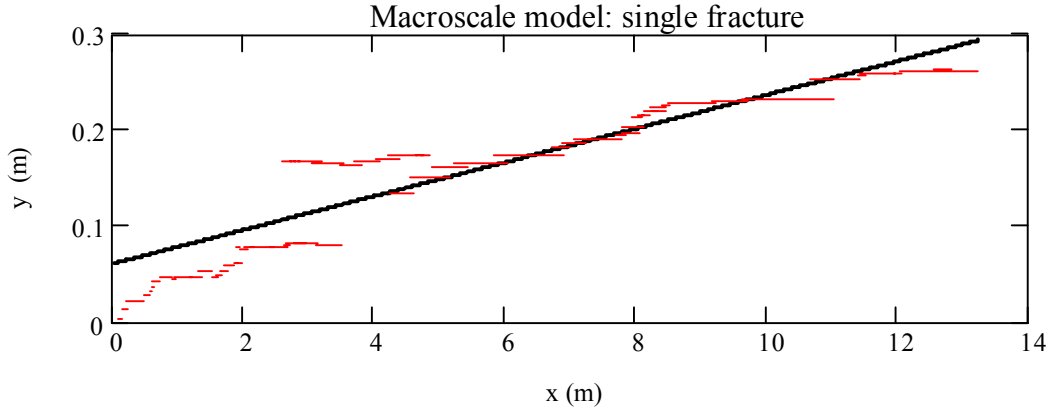

(c)

Figure 3.5 Map views at three different spatial scales (exaggerated vertical scale): (a) microscale (71-segment model), (b) mesoscale (6-segment model), and (c) macroscale (single fracture model).

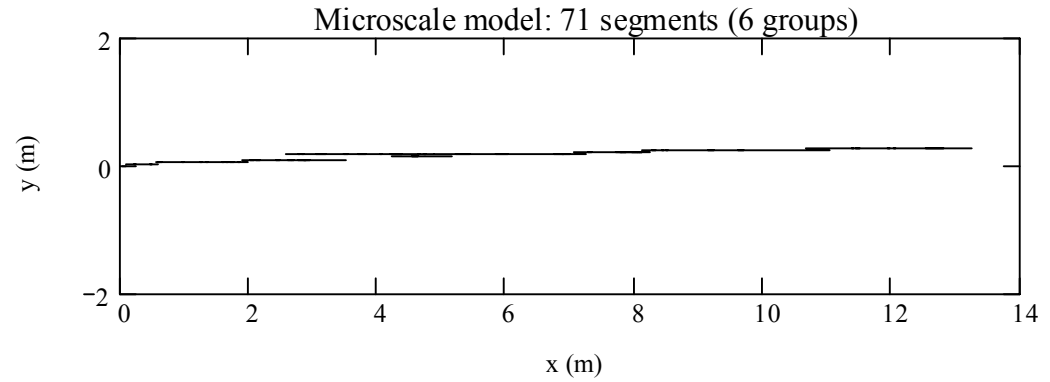

(a)

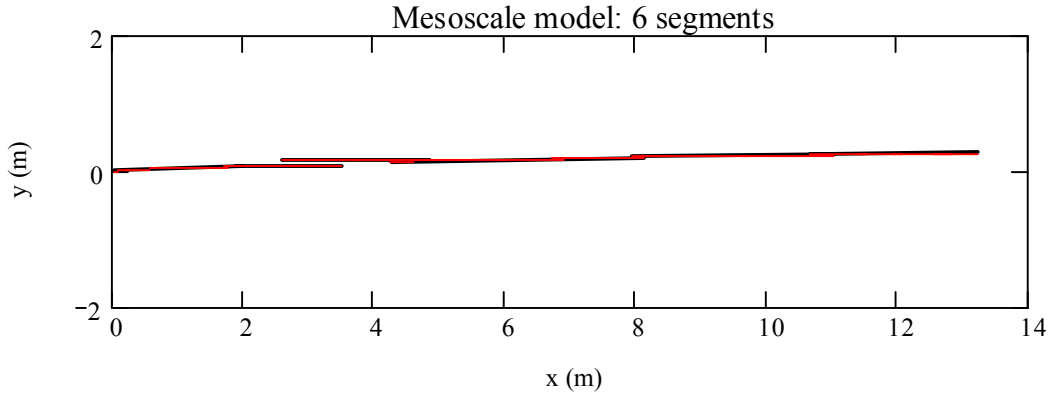

(b)

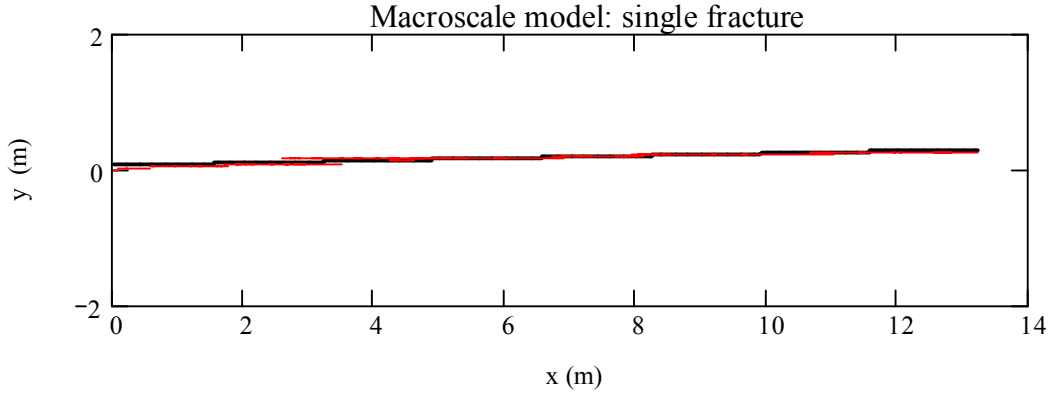

(c)

Figure 3.6 Map views at three different spatial scales (equal scales): (a) microscale (71-segment model), (b) mesoscale (6-segment model), and (c) macroscale (single fracture model).

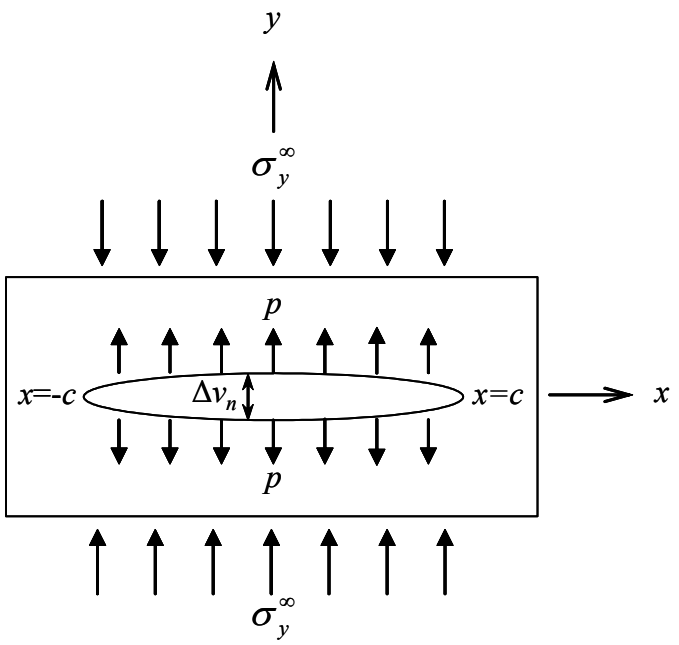

Figure 3.7 Aperture of a single isolated fracture under the influence of the pressure $\Delta p = p - \sigma_y^\infty$, where σ_y^∞ is remote stress and p is internal pressure, in an infinite elastic medium.

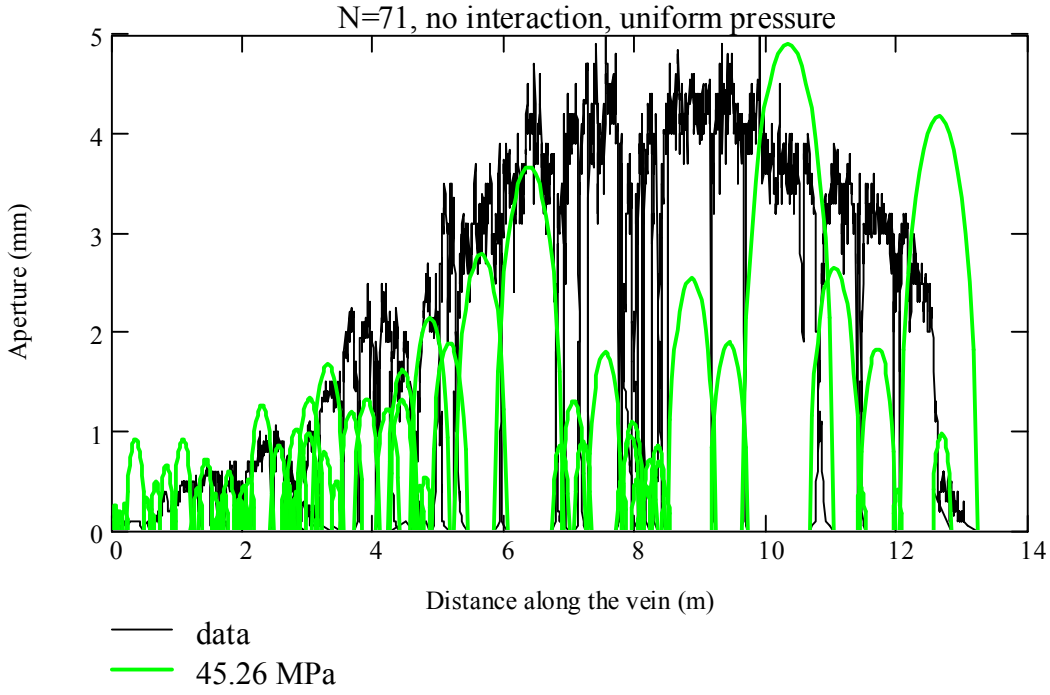

Figure 3.8 Comparison of computed and measured apertures for a single uniform pressure for non-interacting segments at the microscale (value in the legend indicates the magnitude of the computed uniform pressure).

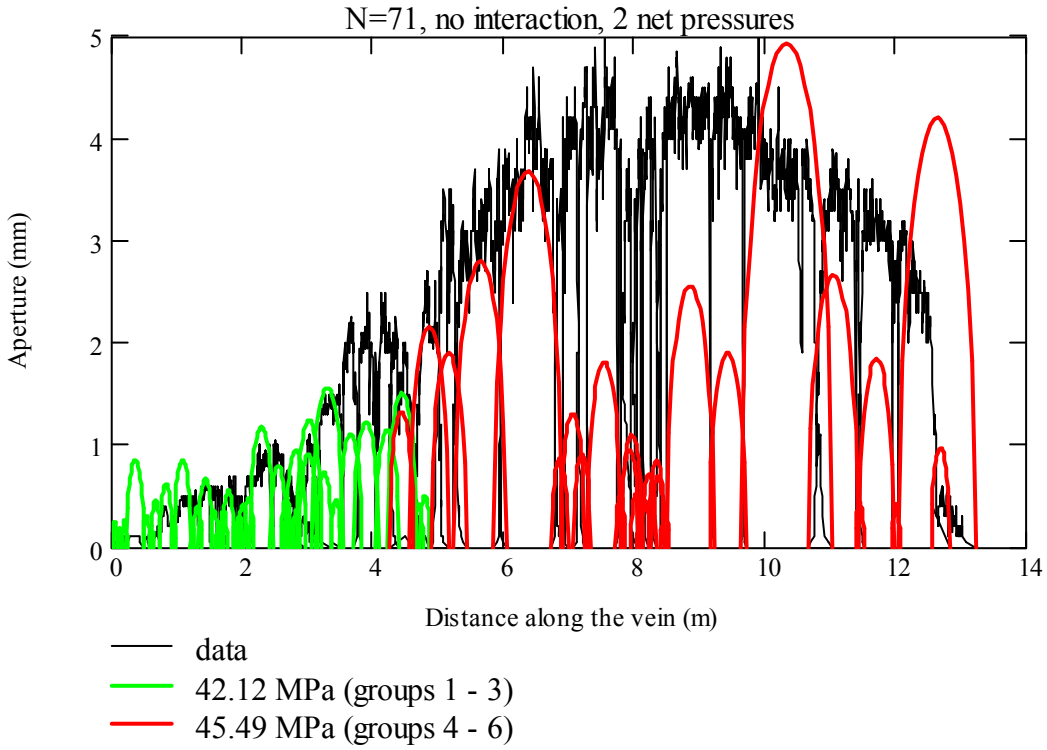

Figure 3.9 Comparison of computed and measured apertures for two pressures for non-interacting segments at the microscale (values in the legend indicate the computed pressure magnitudes).

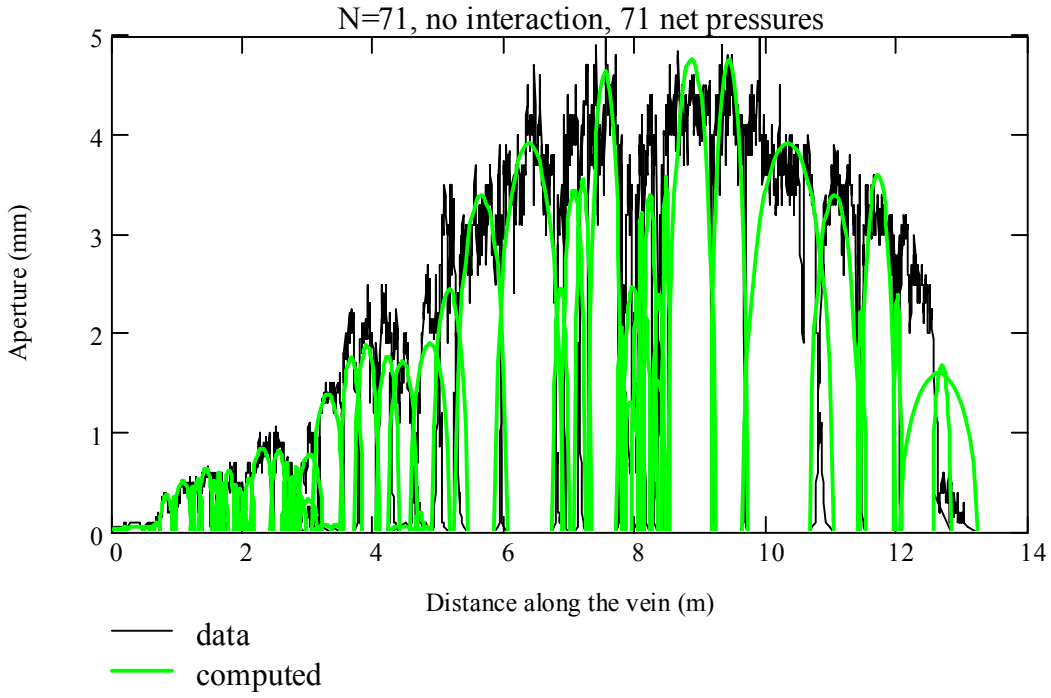

(a)

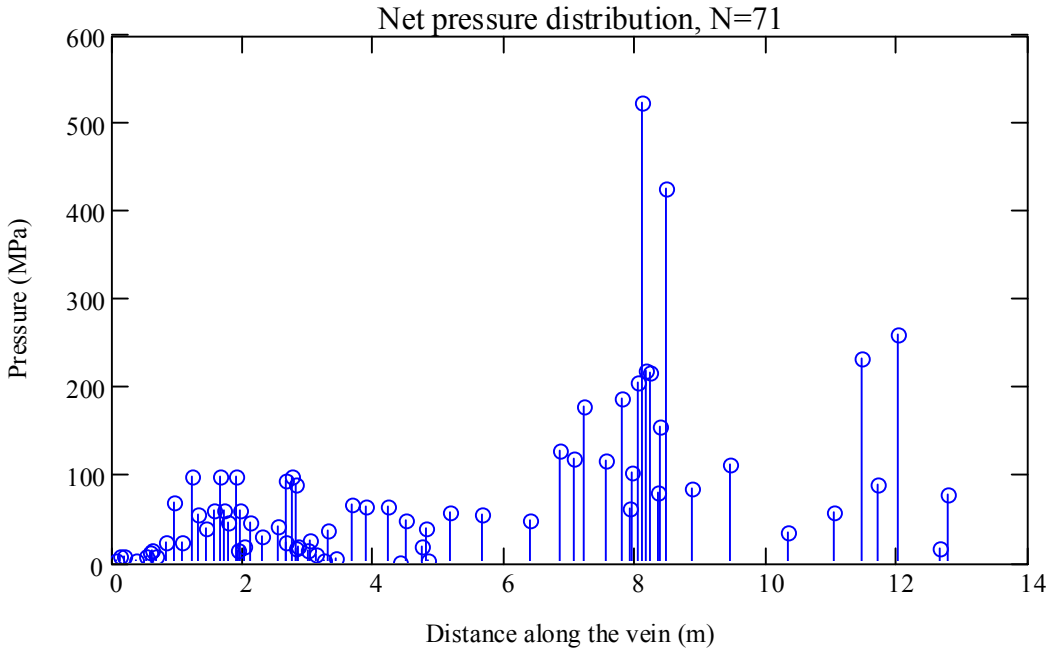

(b)

Figure 3.10 Application of 71 pressures for non-interacting segments at the microscale: (a) comparison of computed and measured apertures, and (b) variation of 71 pressures along the segments.

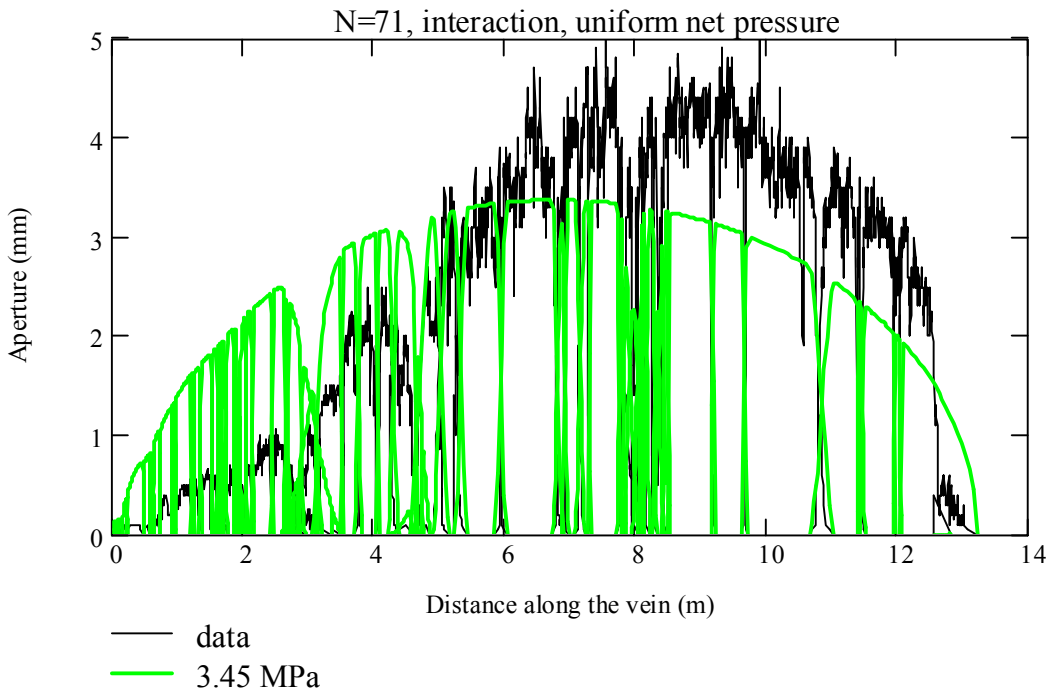

Figure 3.11 Comparison of computed and measured apertures for a single uniform pressure for interacting segments at the microscale (value in the legend indicates the magnitude of the computed uniform pressure).

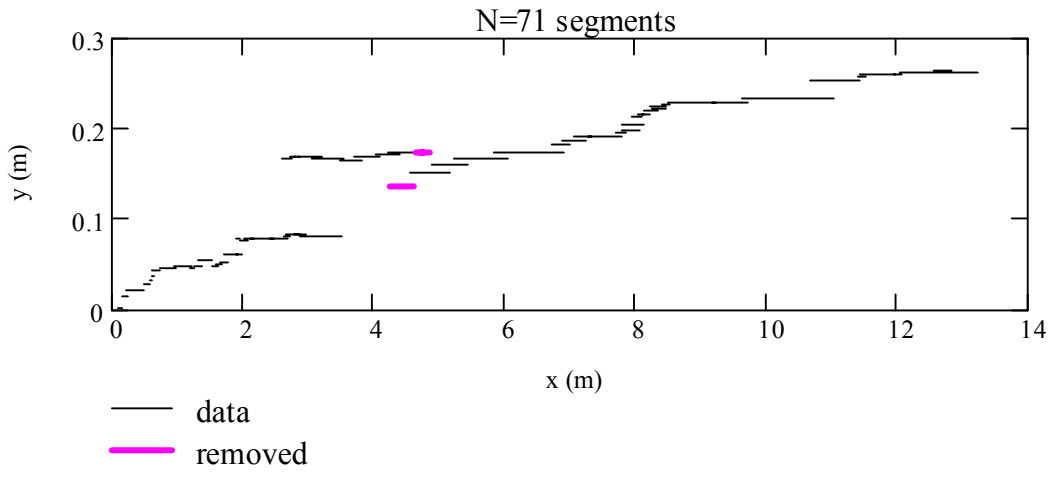

(a)

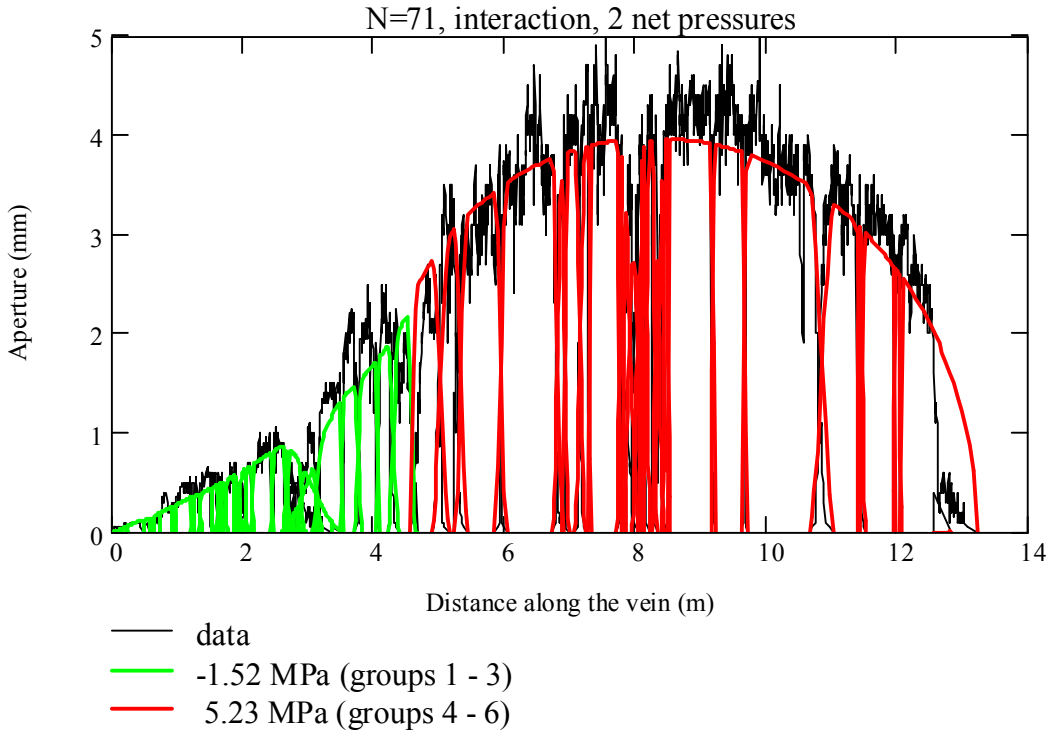

(b)

Figure 3.12 Application of two pressures for interacting segments at the microscale: (a) 71 segments, and (b) comparison of computed and measured apertures (values in the legend indicate the computed pressure magnitudes).

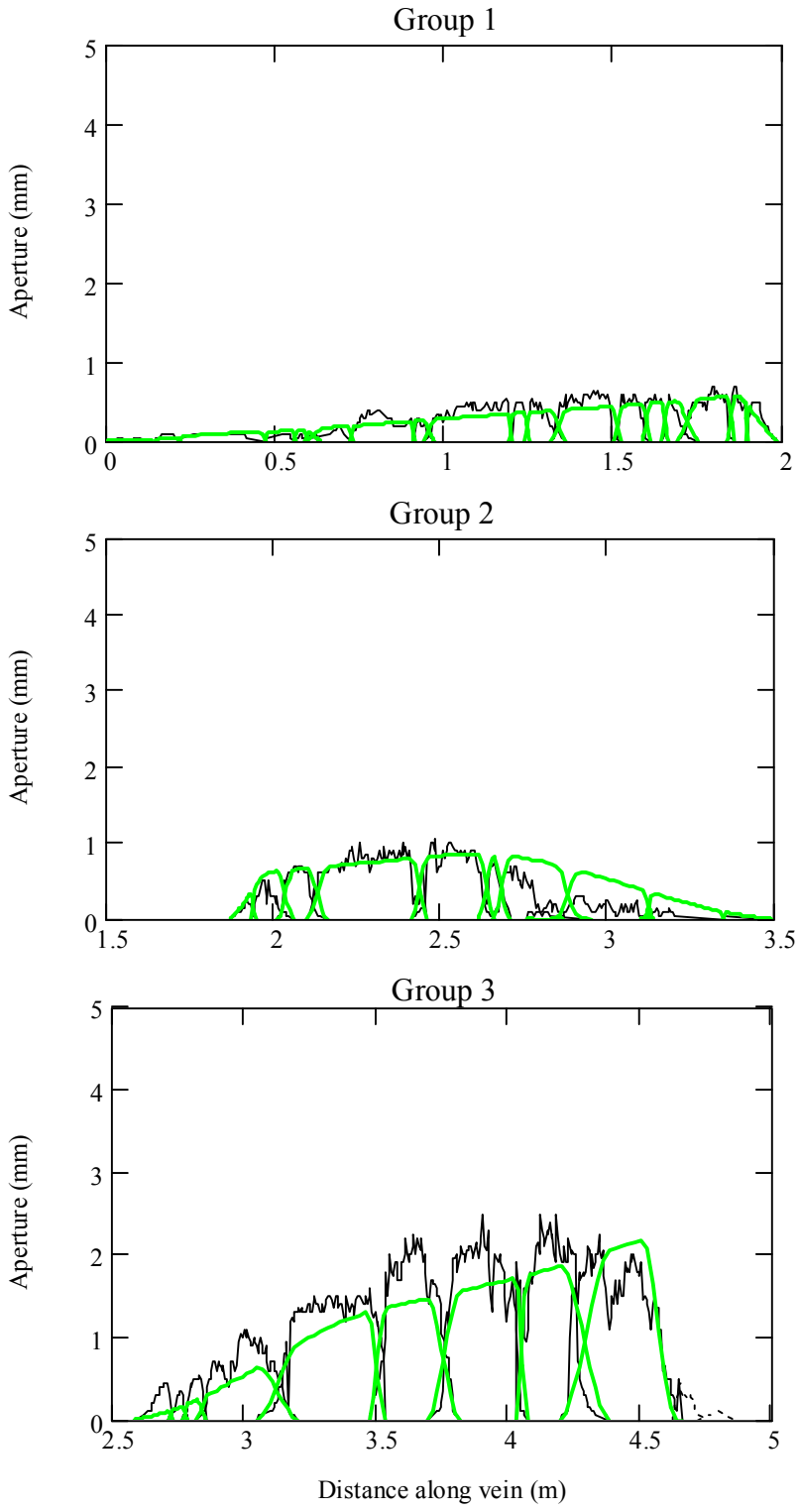

Figure 3.13 Detailed comparison of computed (bold line) and measured (thin line) apertures for two pressures for interacting segments at the microscale.

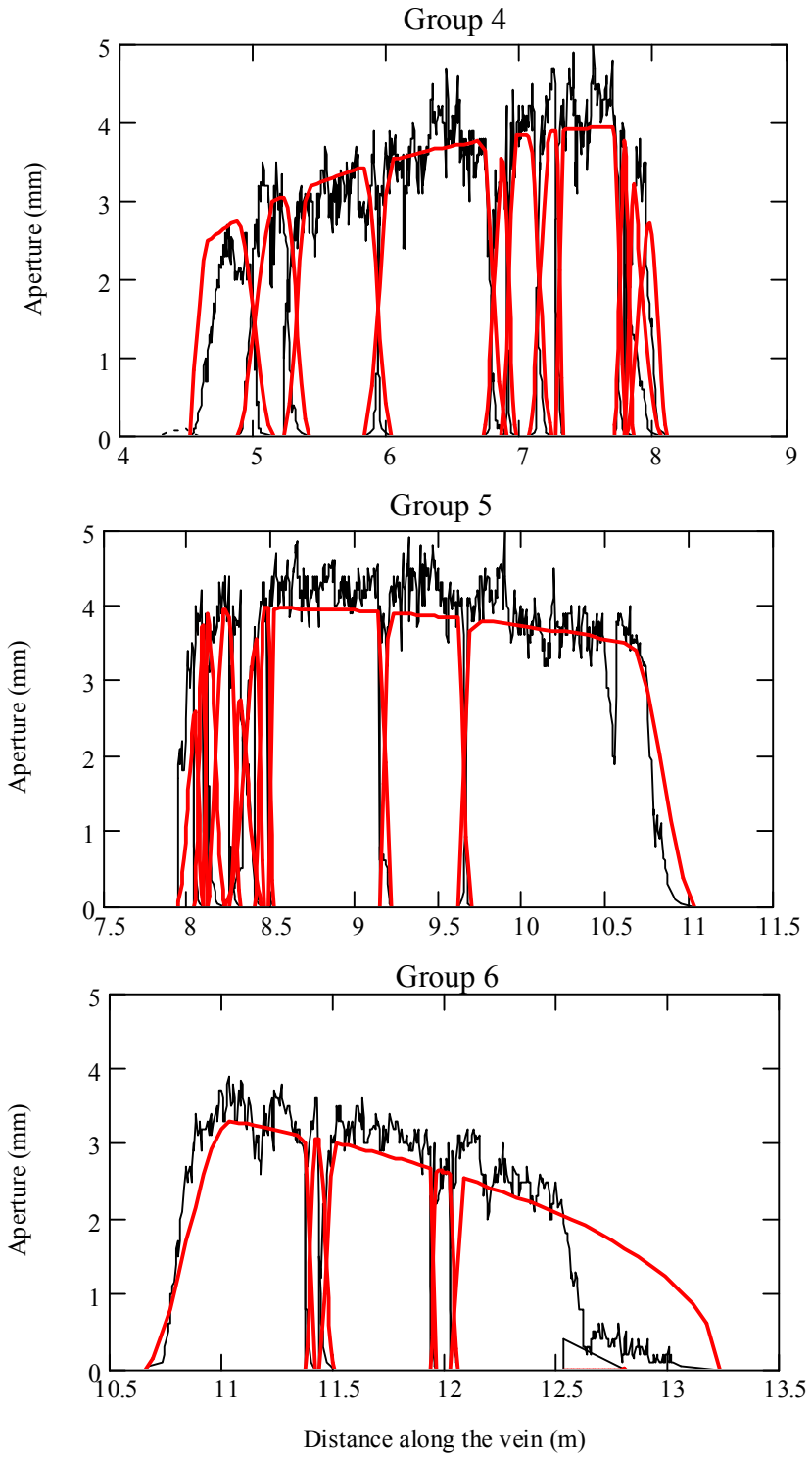

Figure 3.13 (Continued).

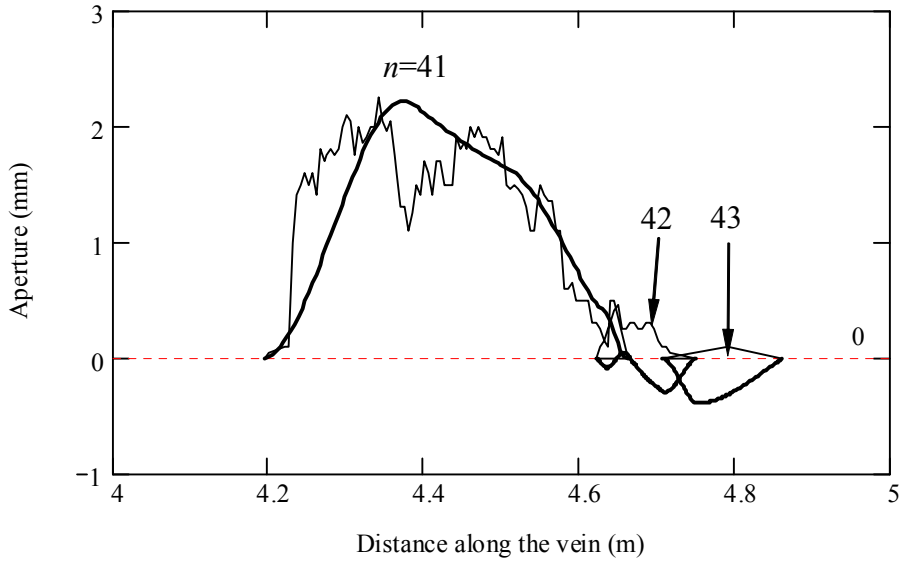

(a)

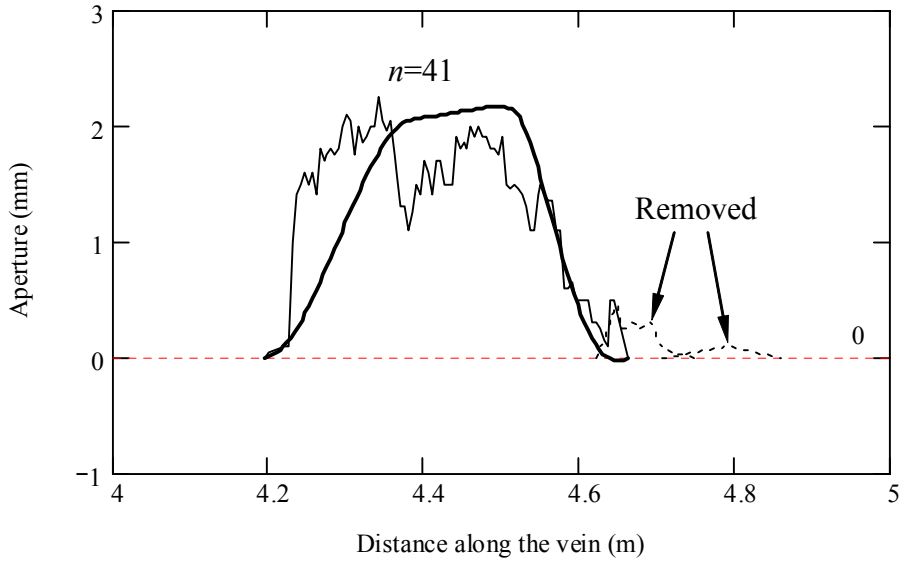

(b)

Figure 3.14 Change of apertures after removing the closed segments at the pressure boundary: (a) apertures before removing segments, and (b) apertures after removal of segments (segment 42 and 43) that have a negative computed aperture in (a). Thin line represents measured apertures and bold line represents computed apertures. Dotted line indicates segments removed for calculation.

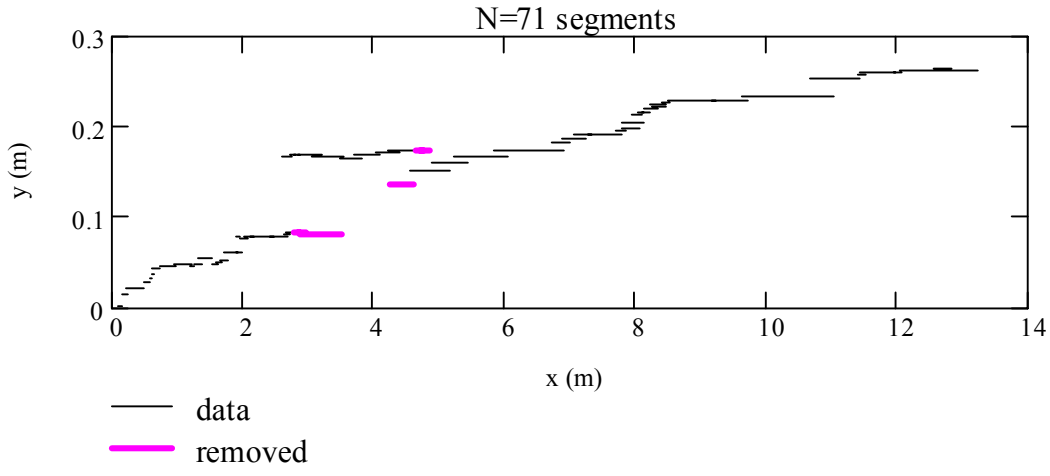

(a)

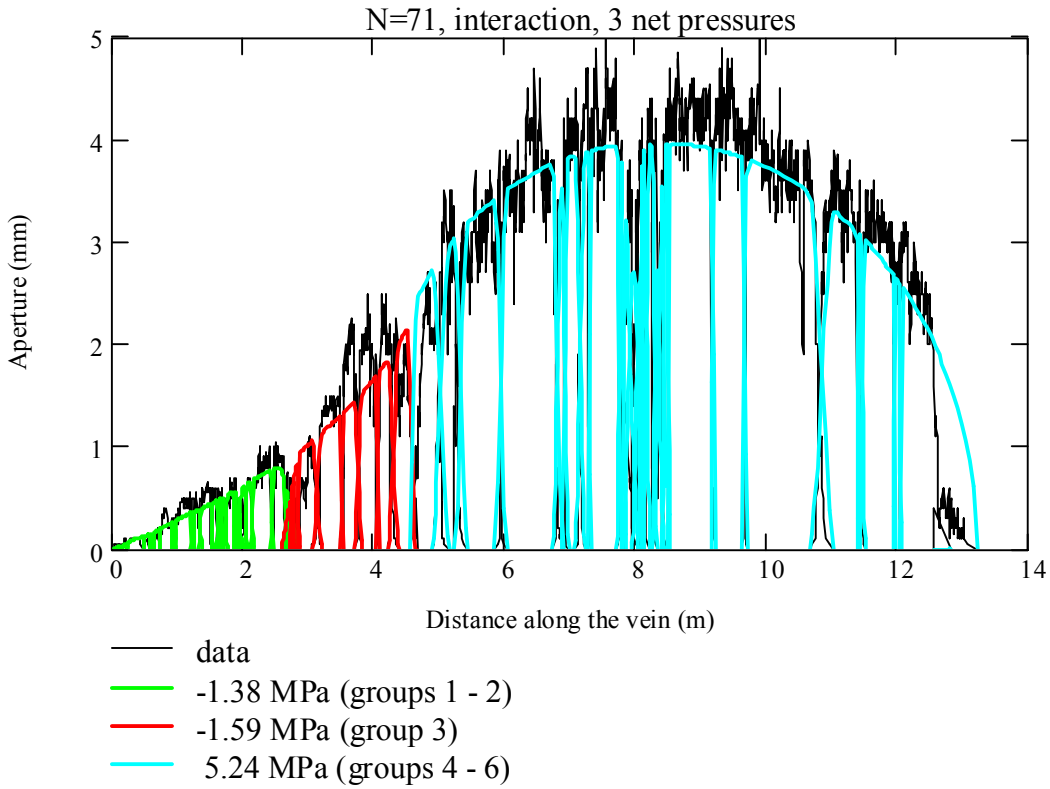

(b)

Figure 3.15 Application of three pressures for interacting segments at the microscale: (a) 71 segments, and (b) comparison of computed and measured apertures (values in the legend indicate the computed pressure magnitudes).

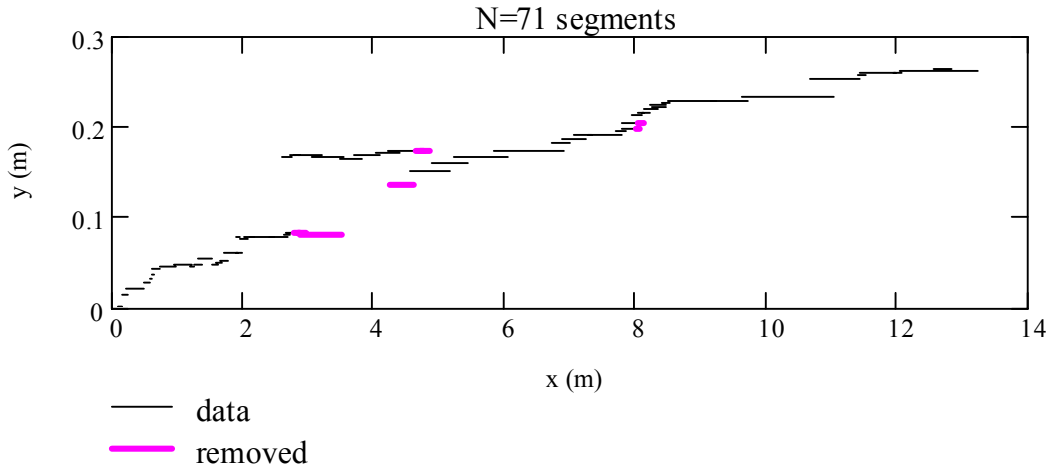

(a)

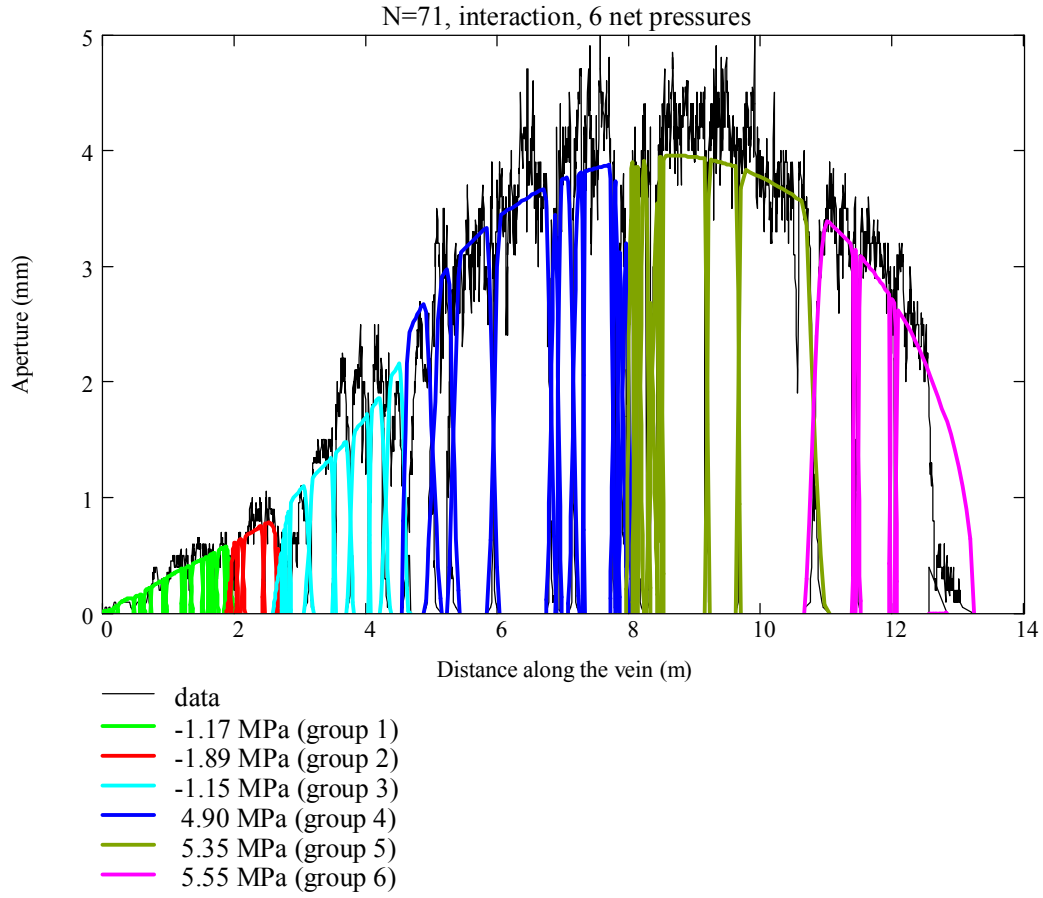

(b)

Figure 3.16 Application of six pressures for interacting segments at the microscale: (a) 71 segments, and (b) comparison of computed and measured apertures (values in the legend indicate the computed pressure magnitudes).

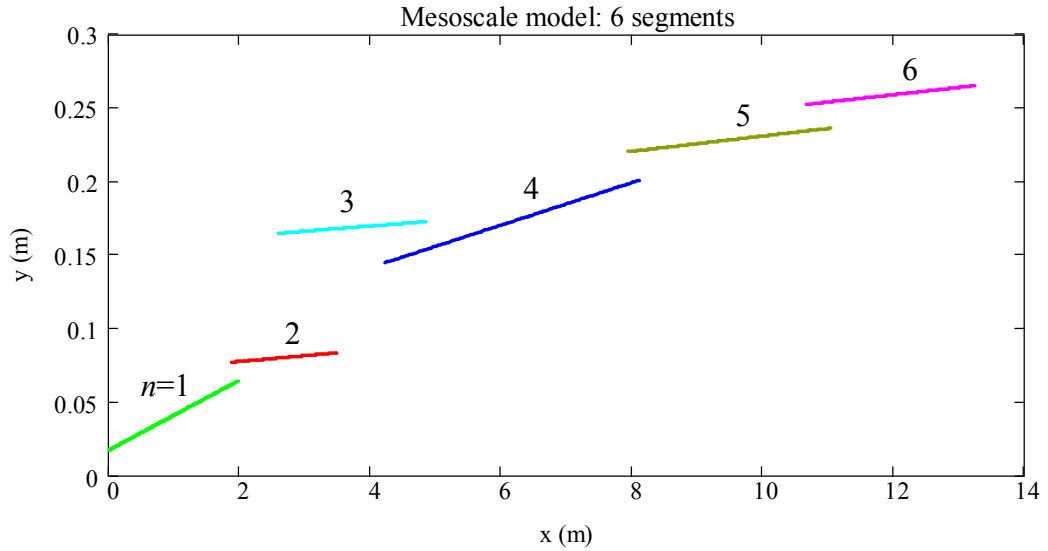

(a)

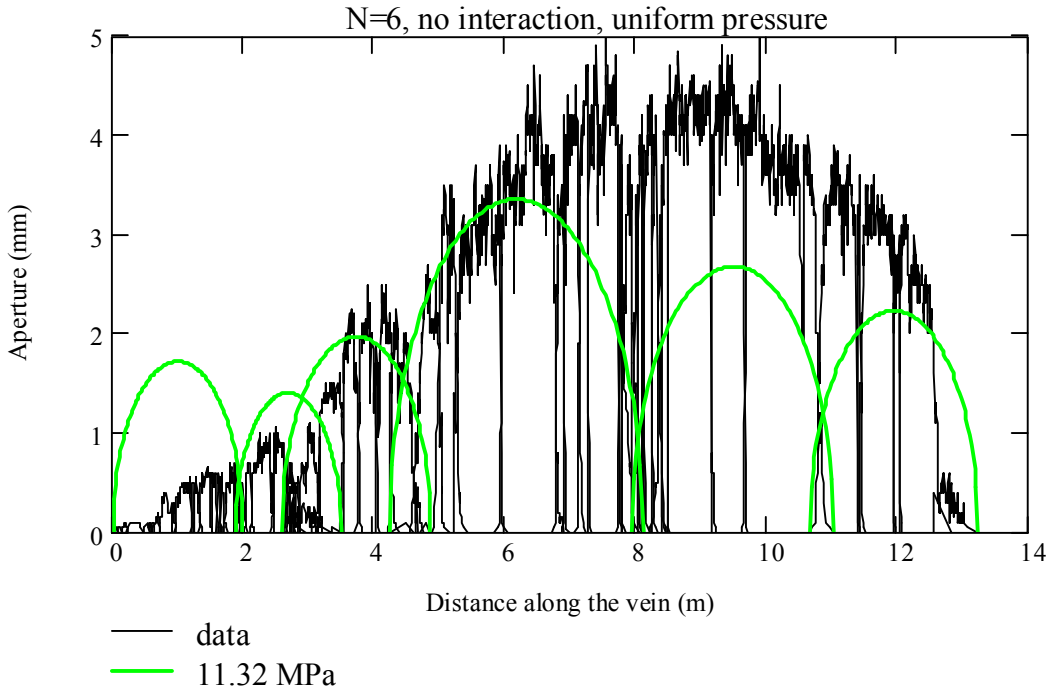

(b)

Figure 3.17 Application of a single uniform pressure for non-interacting segments at the mesoscale: (a) six segments, and (b) comparison of computed and measured apertures (value in the legend indicates the computed pressure magnitude).

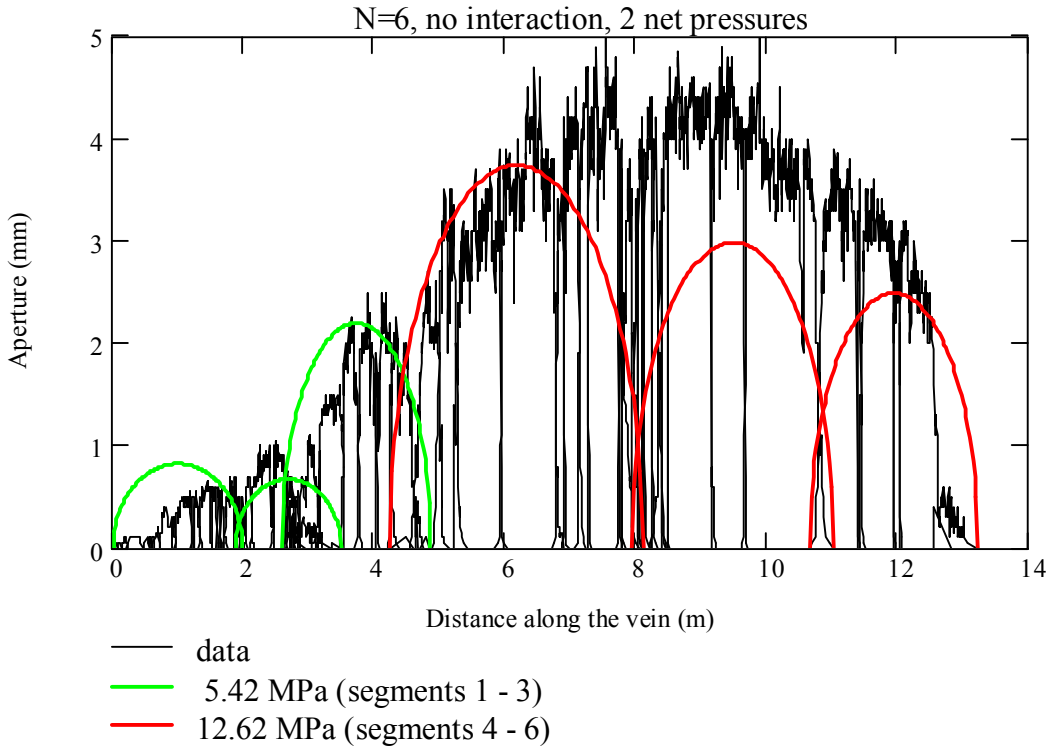

Figure 3.18 Comparison of computed and measured apertures for two pressures for non-interacting segments at the mesoscale (values in the legend indicate the computed pressure magnitudes).

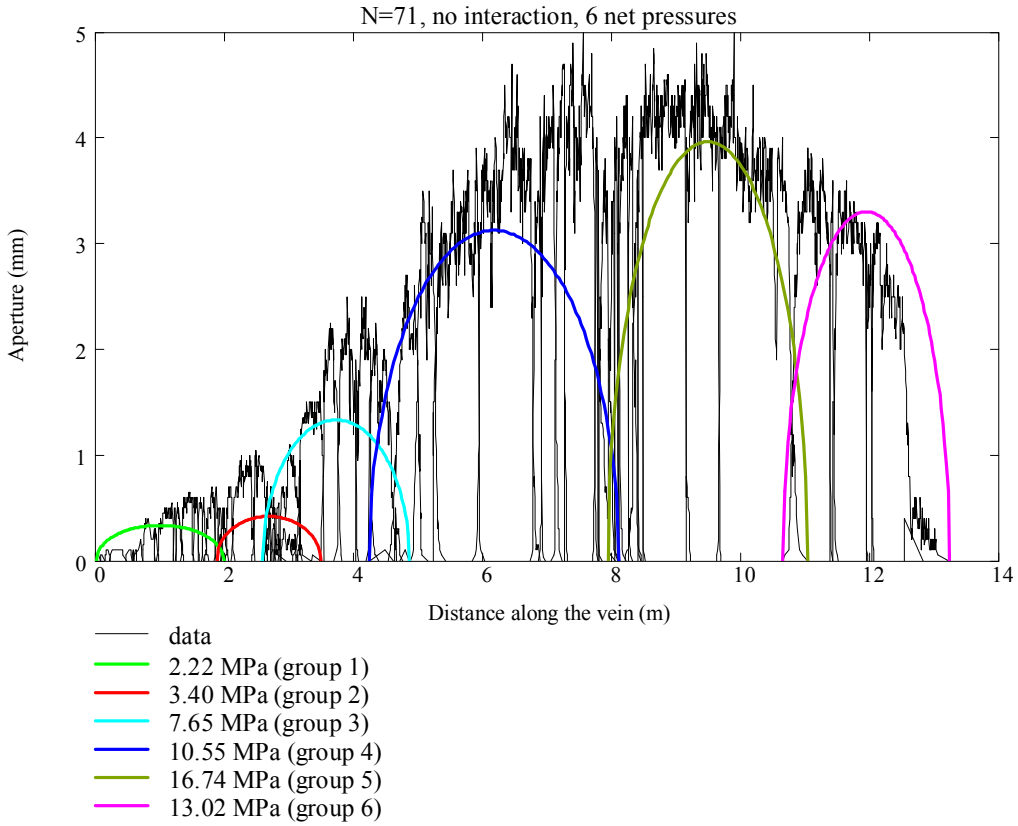

Figure 3.19 Comparison of computed and measured apertures for six pressures for the non-interacting segments at the mesoscale (values in the legend indicate the computed pressure magnitudes).

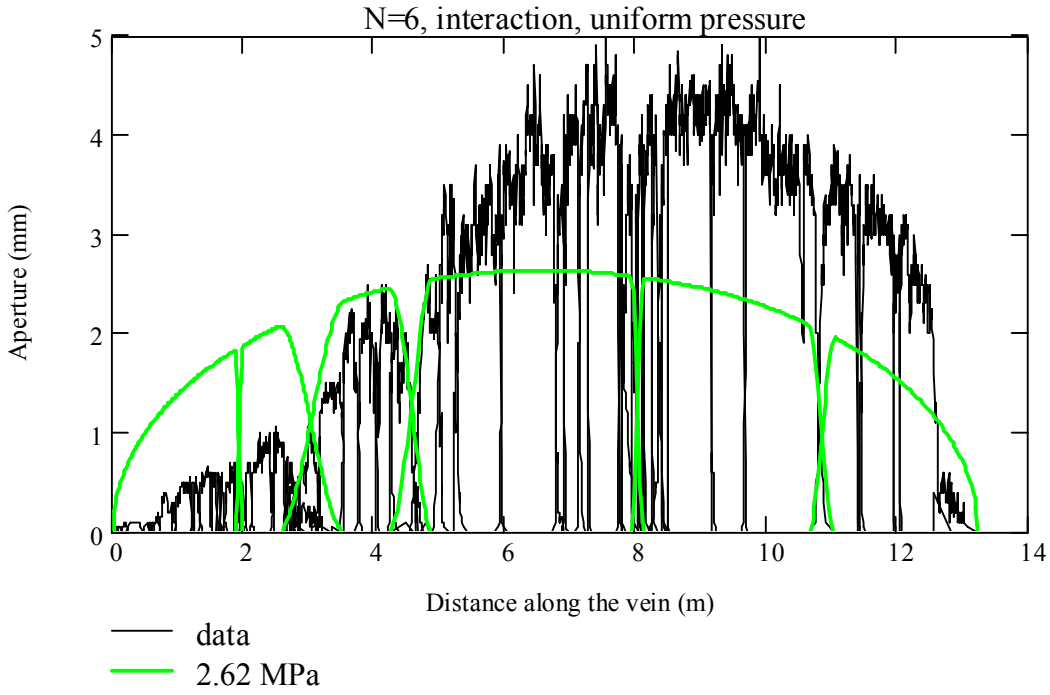

Figure 3.20 Comparison of computed and measured apertures for a single uniform pressure for interacting case at the mesoscale (values in the legend indicates the computed pressure magnitude).

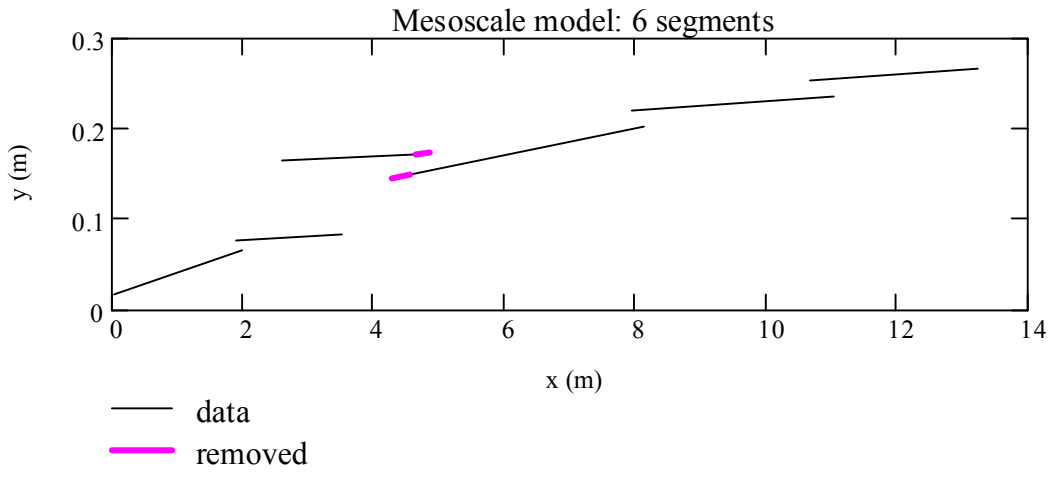

(a)

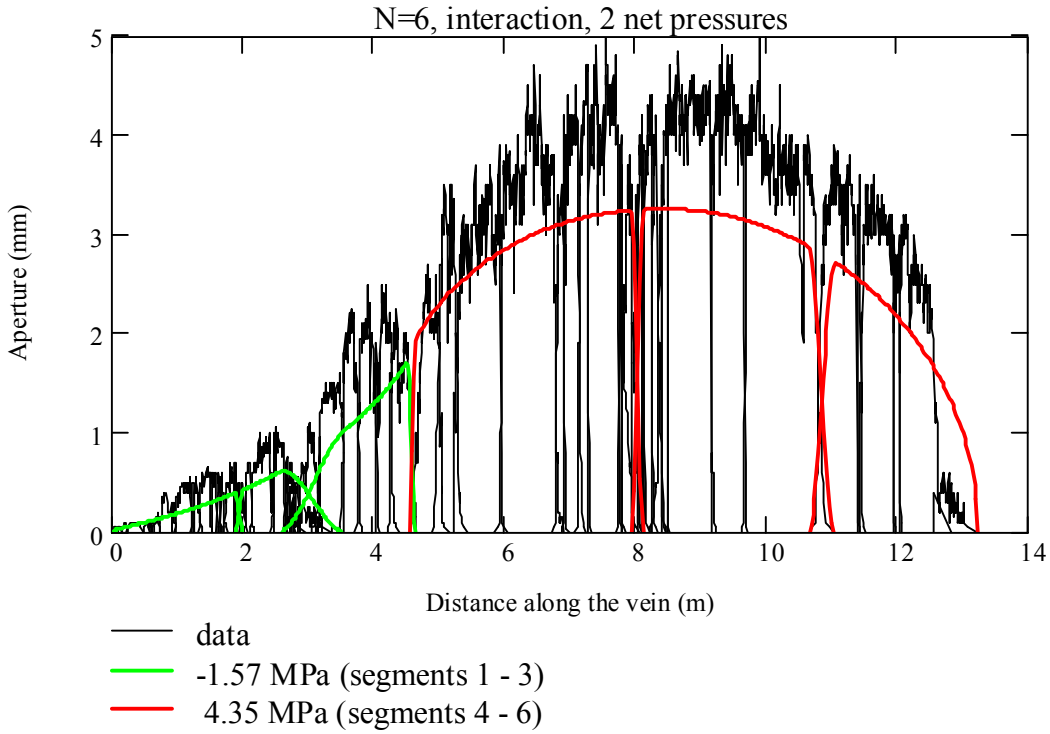

(b)

Figure 3.21 Application of two pressures for interacting segments at the mesoscale (before reduction): (a) six segments, and (b) comparison of computed and measured apertures (values in the legend indicate the computed pressure magnitudes).

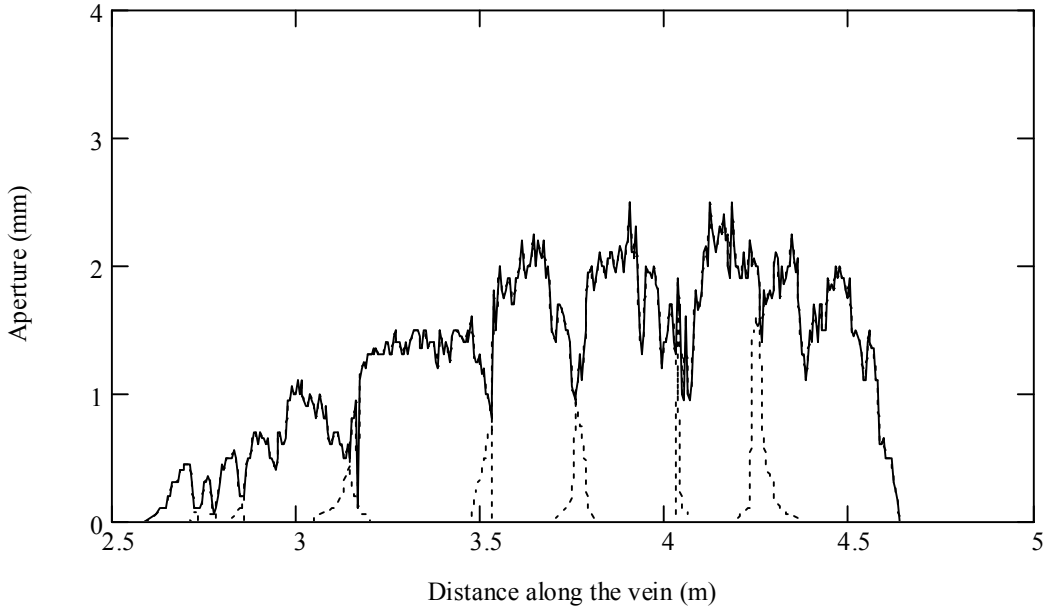

(a)

Figure 3.22 Data reduction in group 3 for the least squares method. Dotted line indicates data removed for the least squares method.

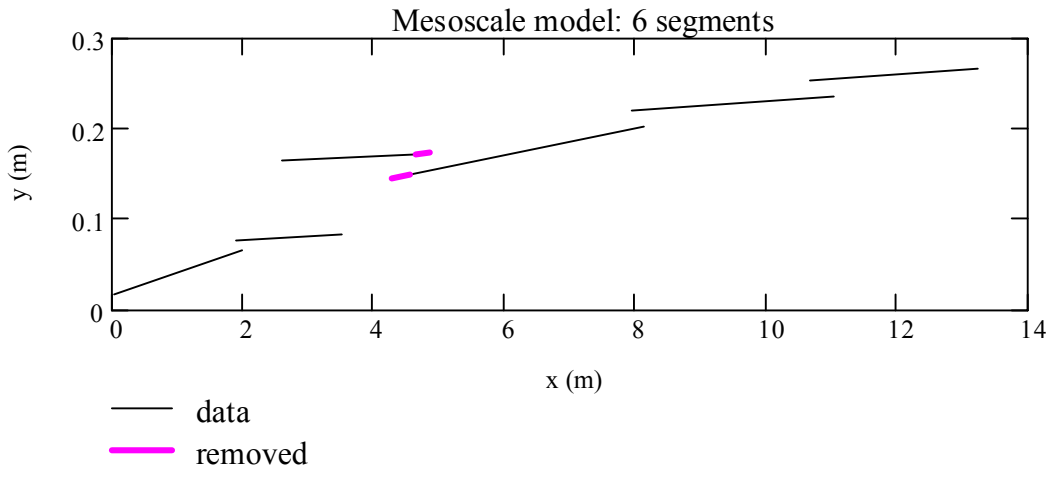

(a)

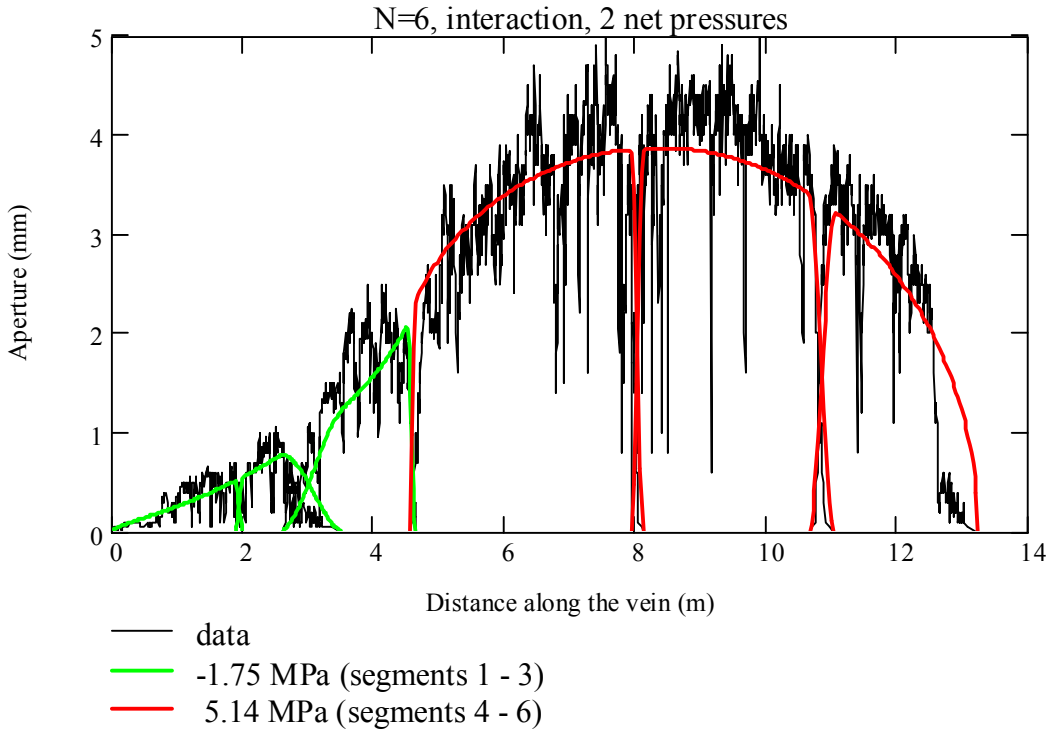

(b)

Figure 3.23 Application of two pressures for interacting segments at the mesoscale (after reduction): (a) six segments, and (b) comparison of computed and measured apertures (values in the legend indicate the computed pressure magnitudes).

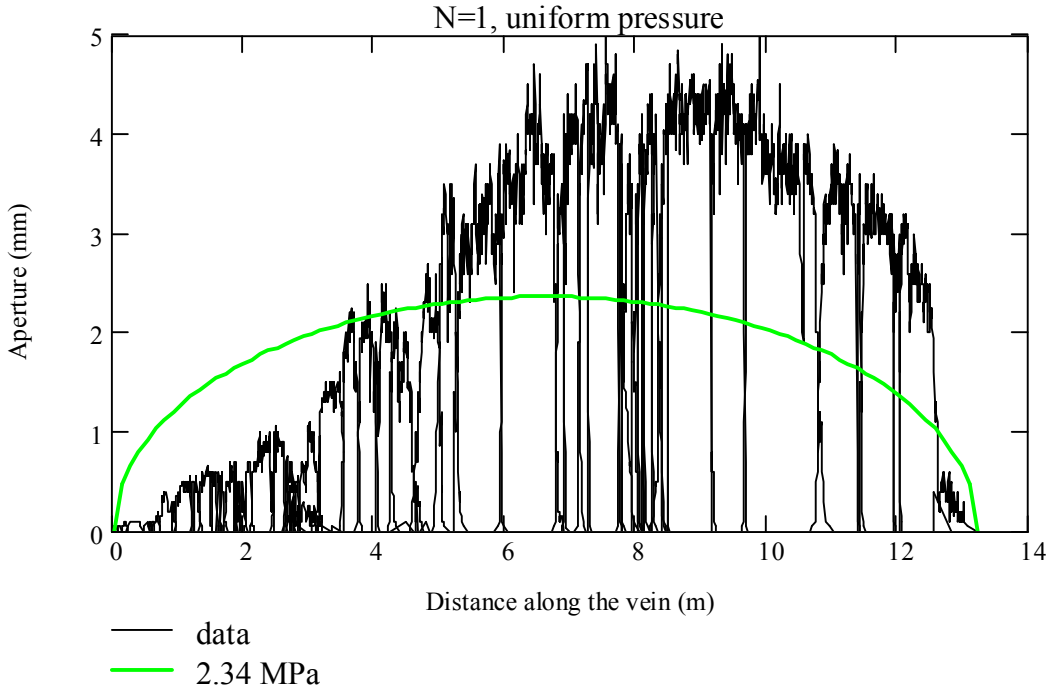

Figure 3.24 Comparison of computed and measured apertures for a single uniform pressure at the macroscale (value in the legend indicates the magnitude of the computed uniform pressure).

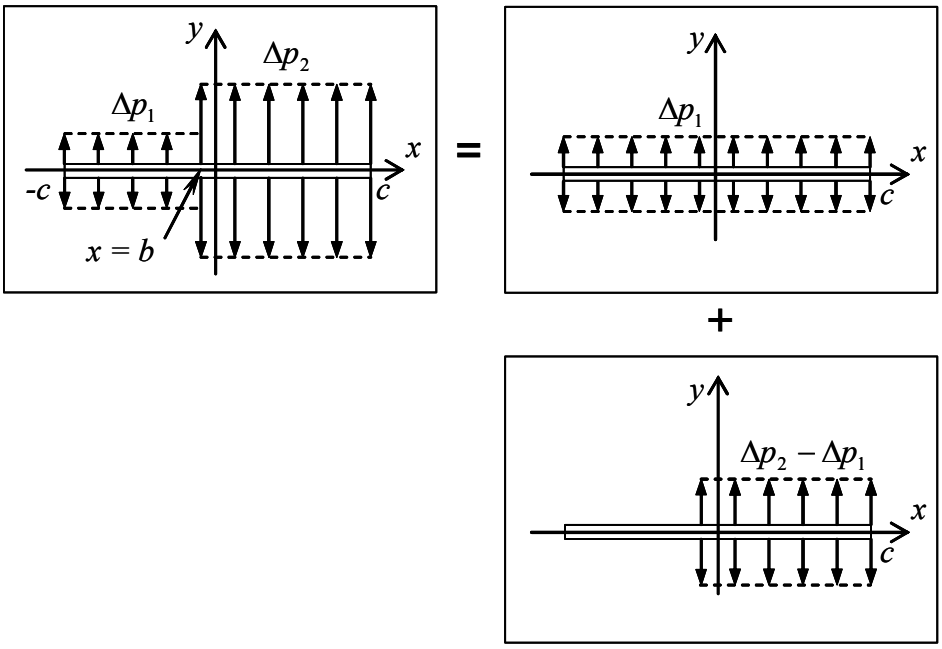

Figure 3.25 Superposition of two pressures in a single fracture.

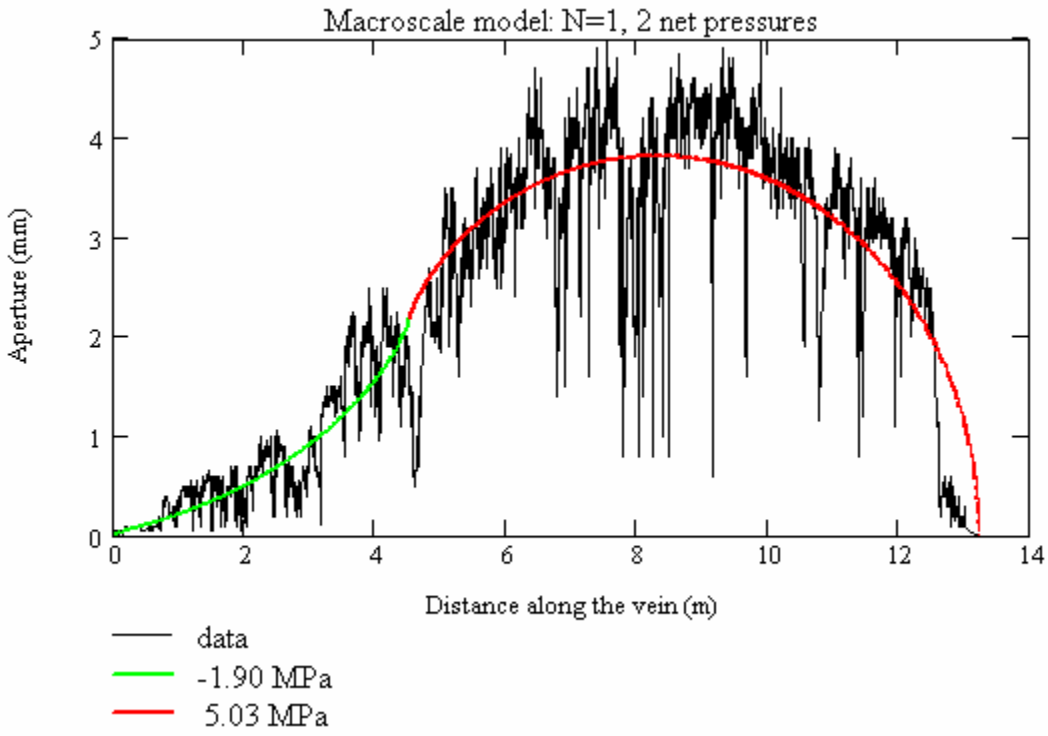

Figure 3.26 Comparison of computed and measured apertures for two pressures at the macroscale (value in the legend indicates the magnitudes of the computed pressures with reduced data).

CHAPTER IV

DIKING PROCESSES AT MID-OCEANIC RIDGES

4.1 Magma chambers and dike emplacement at mid-oceanic ridges

Mid-oceanic ridges (MOR) (Figure 4.1), the sites of seafloor spreading, are characterized by dynamic volcanic activity at the ocean floor. MOR are found in all of the major oceans occupying the Earth's surface, where the new lithosphere is created (dashed area in Figure 4.2). Magma chambers beneath MOR play a major role in crustal formation and hydrothermal activity [e.g., see review by *Lowell et al*., 1995]. Several studies have been conducted over the past decades to elucidate the locations, dimensions and properties of the magma chambers. Although the magma chambers are the subject of debate due to their inaccessibility, the understanding has been much improved due to accumulated geophysical evidence and observations. From direct observations of ophiolites, which are thought to be ancient sections of the oceanic crust exposed on land initially, the magma chambers were initially believed to be huge molten reservoirs [*Cann*, 1974; *Pallister and Hopson*, 1981]. However, seismic studies on MOR (Table 4.1) have indicated that the cross section of the magma chambers appear to be thin (< 200 m) and narrow (1 to 4 km) at a depth of approximately 1 to 3 km below the seafloor [*Detrick et al*., 1987, 1993; *Harding et al*., 1989; *Toomey et al*., 1990; *Burnett et al*., 1989; *Vera et al*., 1990; *Kent et al*., 1990, 1993a, 1993b; *Caress et al.*, 1992; *Wilcock et al*., 1992; *Babcock et al*., 1998]. The liquid magma overlies the top of the seismic low

Table 4.1 Magma lens geometry at mid-oceanic ridges.

References	Magma lens geometry			Comments on magma lens and low velocity zone (LVZ)	Location
	Thickness (m)	Width (km)	Depth (km)		
Fast spreading mid-oceanic ridge					
Detrick et al. [1987]	-	< 3 – 4	1.2 – 2.4	Continuous for tens of kilometers along the axis.	EPR: 8°50'N – 13°30'N
Harding et al. [1989]	-	< 4 – 5	2.2	A broad and deep LVZ with velocities reduced by 0.5-1.0 km/s underlies the partial melt layer.	EPR: 13°N
Vera et al. [1990]	180	< 4	1.6	LVZ Extends farther, but no more than 10 km. Most of axial LVZ behaves as a solid.	EPR: 9°N
Kent et al. [1990]	~10 – 50	0.8 – 1.2	1.6	A narrow and thin magma lens would inhibit along-axis mixing and might account for variations in magma composition along the EPR.	EPR: 9°30'N
Caress et al. [1992]	-	< 1.5	1.5	Consistent with a 7-km-wide LVZ in which velocities are reduced by 0.4 – 0.7 km/s.	EPR: 12°50'N
Detrick et al. [1993]	-	< 1 – 2	~1	Small sill-like mid-crustal bodies that overlies a broader, largely solidified lower crustal section.	EPR: 14°15'S, 17°20'S
Singh et al. [1998]	50	-	1	Melt to mush variations in magma properties.	EPR: 14°00'S
Babcock et al. [1998]	-	0.5	1.3	The magma lens is predominantly continuous feature and its width is fairly constant.	EPR: 12°20'N – 13°30'N
Crawford et al. [1999]	30	0.5	1.4	V_s = 1.7 km/s indicating 2.5-18% melt in LVZ.	EPR: 9°48'N
	40 – 2000	0.1 – 1.7	4 – 6	Deep axial melt lens	
Dunn et al. [2000]	-	-	1.5	LVZ is narrow in the crust (5 – 7 km) and broad in the mantle (~18 km).	EPR: 9°30'N
Intermediate spreading mid-oceanic ridge					
Collier and Sinha [1990]	~50 – 100	1 – 2.5	3	Magma lens having sharply defined edges.	VFR: 22°10'S – 22°30'S
Detrick et al. [2002]	-	< 1	2.3 – 2.6	Asymmetric magma lens on some cross-axis profile	JdFR: Endeavor segment
Carbotte et al. [2002a]	-	-	2.5	Bright axial magma lens reflection beneath portions of all of the JdFR segments.	JdFR
Van Ark et al. [2003]		1 – 2	1.9 – 4.0	Salty Dawg vent fields above the lens tip	JdFR: Endeavor segment
Slow spreading mid-oceanic ridge					
Sinha et al. [1998]; *Navin et al.* [1998]	100	4	2.5	LVZ is larger region of partial melt in a largely crystalline mush zone and approximately 8 km in width.	MAR: 57°45'N

velocity zone (LVZ), which is partially melted and extends to the Mohorovicic discontinuity. Figure 4.3 represents the crustal structure including the magma lens of the axial magma chamber at the East Pacific Rise (EPR) near 9°30'N by *Kent et al*. [1993b]. Such a magma lens also lies beneath the intermediate spreading MOR, the Endeavor segment on the Juan de Fuca Ridge (JFR) [*Rohr et al*., 1988; *Sinton and Detrick*, 1992; *Detrick et al*., 2002; *Carbotte et al*., 2002a], and the Valu Fa Ridge (VFR) [*Collier and Sinha*, 1990], and beneath parts of the slow spreading Mid-Atlantic Ridge (MAR) [*Sinha et al*., 1998; *Navin et al*., 1998]. In addition, more recent studies suggest the existence of deep melt lenses near the crust-mantle interface [*Crawford et al*., 1999; *Dunn et al*., 2000] (Figure 4.4) and multiple lenses in the lower crust [*Kelemen et al*., 1997; *Garrido et al*., 2001].

It has also been suggested that the magma chambers are generally continuous along the EPR [*Detrick et al*., 1987 and 1993; *Burnett et al*., 1989; *Babcock et al*., 1998] with significant variation in width across the major and minor ridge axis discontinuities [*Kent et al*., 1993a, 1993b, and 1994]. *Sinton and Detrick* [1992] interpreted that the LVZ of a tomographic image of the near 9°30'N EPR [*Toomey et al*., 1990] is also continuous across small ridge axis discontinuities, with variation of its width and internal velocity structure.

The properties of the rock beneath the EPR can be inferred from seismic data. However, this is difficult because seismic waves vary with pressure, mineral composition, and magma melt distribution. Figure 4.5 shows a schematic cross section of the magma chamber with a *p*-wave velocity, V_p, profile [*Vera et al*. 1990]. Figure 4.6 shows *p*-wave (V_p) and *s*-wave velocity (V_s) profiles at 9°N on the EPR by *Vera et al*.

[1990]. According to these profiles, the top of the magma chamber lies 1.6 km beneath the seafloor where both wave velocities decrease abruptly (V_p = 3 km/s and $V_s \approx 0$ km/s). This indicates that the magma chamber is composed of fully molten material. However, in other places, the magma chamber could consist of partially molten material indicated by $V_s \neq 0$ km/s [*Hussenoeder et al*., 1996; *Singh et al*., 1998]. Also, in the *Vp*-profile represented in Figure 4.5, most of the upper crust above the magma chamber shows V_p = 5.3 to 6.7 km/s. In the lower crustal region, V_p and V_s gradually increase, to V_p = 5.5 km /s and V_s = 2.97 km/s on average. Moreover, the compliance measurements method suggested by *Crawford et al*. [1999] shows a 25% lower V_s in the upper crust and a 40% lower V_s in the lower crust compared to those found by *Vera et al*. [1990] (Figure 4.6).

It is not clearly understood how magmatic dikes can initially be generated from the pressurized magma chambers and propagate to the seafloor. It is commonly believed that dikes propagate from the center of pressurized magma lenses (Figures 4.7a and 4.7b). However, this is not consistent with conventional fracture mechanics, because for the thin crack-like magma lens, the stress concentration occurs at the tip if it is pressurized. Recent seafloor studies also suggest that volcanic and hydrothermal activities are not restricted to the ridge axis but may also occur at some distance away from the axis as well, ranging from a kilometer to several kilometers [*Perfit et al*., 1994; *Alexander and Macdonald*, 1996; *Van Ark et al*., 2003]. Therefore, this lens-shaped magma chamber indicates that the pressurization of the magma chamber is likely to result in a stress concentration near the tips of the lens while the rest of the host rock is in a state of compression. As such, if an episode of magma replenishment in the magma lens results in

diking, the dikes will likely initiate near the tip of the lens. The continued propagation of these dikes can then be described by the principles of fracture mechanics.

Alternatively, diking may result from solidification of the magma lens as a result of rapid hydrothermal cooling. Because the density of magma is lower than that of fresh rock, crystallization leads to a pressure decrease in the lens. Consequently, the stress distribution in the host rock changes and becomes tensile in the middle part of the magma lens, and compressive in the regions near the tips. In this scenario, indeed, the dikes are likely to initiate from the center of the magma lens, and the hydrothermal sites would be expected to occur along the ridge axis.

Based on the thin melt lens model of an axial magma chamber, two scenarios (i.e., dike propagation from the tip and the center of the magma lens) of dike evolution from the magma lens are simulated to investigate the mechanisms of dike propagation and its effect on hydrothermal activity.

4.2 Major mechanisms and mathematical model

4.2.1 Model of magma lens and its properties

Model of magma lens

In this section, dike propagation from a lens-shaped magma chamber is simulated numerically the in plane strain condition. Figure 4.8 depicts the mathematical model that is used to model the mechanical interaction between the magma lens, the dike and the seafloor. The magma lens is trapped beneath the impermeable sheeted dikes and is located above the LVZ.

The magma lens is assumed to be $2b$ = 100 m thick and $2c$ = 1 to 2 km wide at a depth of H = 1 to 2 km beneath the seafloor. Although a constant width is suggested for the LVZ [*Dunn et al*., 2000], a width that broadens as it extends into the lower crust with an angle of approximately 45° with respect to the tip of the magma lens is also used as a limiting case. The typical value for the seawater pressure is p_w = 25 MPa that indicates an ocean floor depth of h_w = 2.5 km. The seafloor is assumed to be horizontal.

Mesh and boundary conditions

To simulate dike propagation from the magma lens, the finite element code FRANC2D [*Wawrzynek and Ingraffea*, 1987] is used. Figure 4.9 shows the typical FRANC2D mesh with the magma chamber and the boundary conditions. The applied mesh has a width of 20 km and a depth of 10 km to minimize the boundary effect. The magma chamber is located in the rectangular region within the finer mesh (i.e., 100 m per grid). Figure 4.10 shows the FRANC2D mesh of the magnified magma lens area for a width of $2c$ = 1 km and 2 km. Each tip of the magma lens is modeled by a semi-circle with a radius of r = 50 m. The lens has a thickness of 100 m.

The left and right side boundaries have no horizontal displacement (u_x = 0), assuming that these boundaries are sufficiently far away from the magma chamber. The boundary condition at the lower surface is assumed to have no vertical displacement (u_y = 0). A seawater pressure of p_w = 25 MPa is applied to the upper surface, and a constant body forces are applied to simulate the gravitational acceleration (g = 10 m/sec^2).

Properties

The elastic properties for the numerical simulation are determined from elastic wave velocities. The magma lens is assumed to consist of fully molten liquid (V_s = 0 m/s), although this may not be always vaild [*Hussenoeder et al*., 1996; *Singh et al*., 1998], as previously stated in section 4.1.

For the case of a homogeneous crust, V_p = 5.3 km/s and V_s = 3.0 km/s are used for the crustal rocks, resulting in the Young's modulus of $E_r = 6.144 \cdot 10^{10}$ Pa and Poisson's ratio of ν_r = 0.264. For the heterogeneous case, the LVZ is assumed to have different material properties. Using V_p = 5.3 km/s, which is the same as homogeneous crust, and V_s = 2.0 km/s, which is the average value suggested by *Vera et al*. [1990] and *Crawford et al*. [1999], we have $E_l = 3.061 \cdot 10^{10}$ Pa and $\nu_l = 0.417$. The density of the rock and magma are assumed to be ρ_r = 2,700 kg/m^3 and ρ_m = 2,600 kg/m^3, respectively, resulting in a 100 kg/m^3 difference [e.g., *Murase and McBirney*, 1973; *Hussenoeder et al*., 1996]. The material properties used for the numerical simulations are summarized in Table 4.2.

Table 4.2 Material properties for numerical model.

Material	Property		Value	
Upper and lower crust	*p*-wave velocity	V_p	5.3	km/s
	s-wave velocity	V_s	3.0	km/s
	Density	ρ_r	2,700	kg/m^3
	Fracture toughness	K_{Ic}	10^7	Pa·m$^{1/2}$
Low velocity zone	*p*-wave velocity	V_p	5.3	km/s
	s-wave velocity	V_s	2.0	km /s
	Density	ρ_r	2,700	kg/m^3
Magma	Density	ρ_m	2,600	kg/m^3

4.2.2 Dike initiation and pressure

Dike initiation at the tip of the magma lens

If the pressure inside the magma lens due to the replenishment from the melt source exceeds the overburden stress σ_1 at the location in the magma lens (i.e., the sum of seawater pressure and the lithostatic pressure), the stress will initially be concentrated near the tip of the magma lens. Figure 4.11 shows a contour plot of the major principal stress σ_1 in the vicinity of a 1 km wide magma chamber at a depth of 1 km in homogeneous crust. The applied initial pressure is only 1% greater than the overburden pressure, i.e., $p_i = 1.01\sigma_1$. Tensile stresses occur at the tip while compressive stresses are generated at the center of the magma chamber. Figure 4.12 shows the details of dike initiation during numerical simulation. The right tip of the magma lens area is shown in a magnified scale with a tensile stress bar (Figure 4.12a). According to the tensile stress distribution along the surface of the chamber tip (Figure 4.12b), the maximum tensile stress at the tip is approximately 24 MPa, located at an angle of $\theta = 70°$ with respect to the plane of the magma lens. Therefore, it is expected that the dike will initiate at the tip if the maximum tensile stress, $\sigma_{\theta\theta}^{max}$, exceeds the tensile strength of the crustal rock, σ_t. Figure 4.12c shows dike initiation along the line $\overline{aa'}$ in the vicinity of the tip of magma lens.

Dike initiation at the center of the magma lens

Dike initiation may also result from the solidification of the magma lens. Since the magma density is lower than that of the fresh rock, crystallization leads to a pressure decrease inside the lens. Consequently, the stress distribution in the host rock changes

and becomes tensile in the central part of the magma lens, and compressive in the tip regions. In this scenario, the dikes are likely to initiate from the central areas. Consequently, some hydrothermal sites may occur along the ridge axis.

Figure 4.13 shows the contour plot of the major principal stress σ_1 in the vicinity of a 1 km wide magma chamber at a depth of 1 km in a homogeneous crust. The applied initial pressure is 40% less than the overburden pressure, i.e., $p_i = 0.60\sigma_1(0)$. A compressive stress is generated on the surface of the entire magma lens, except the lens center. Figure 4.14 shows the details of dike initiation at the center of the magma lens for this case. The initial pressure, p_i, can be obtained by decreasing the pressure in the magma lens until the tensile stress exceeds the tensile strength of the rock at the center of the lens. Figures 4.14a and 4.14b show the deformation of the magma chamber and the horizontal stress distribution, σ_{xx}, along the upper part of the lens, indicating the maximum horizontal stress, $\sigma_{xx}^{\max} = 10$ MPa, at the lens center. Figure 4.14c shows the dike initiation at the center of the magma lens.

Dike pressure

Due to the high viscosity of the magma, the actual dike pressure will be distributed nonlinearly. Here, we employ the hydrostatic pressure distribution applied to the fracture to induce continued dike propagation, as shown in Figure 4.15. In other words, the pressure in the dike decreases hydrostatically with depth:

$$p(y) = p_i - \rho_m g y \tag{4.1}$$

where y is the difference in depth between the dike tip and the base (at the depth of the magma chamber) Pressure (4.1) can be seen as an upper bound for the actual pressure

distribution in the dike (Figure 4.15). This bound cannot be further improved since it becomes accurate when the dike stops and can be viewed as an asymptotic limit for slowly propagating dikes.

4.2.3 Trajectories of dike propagation

Dike propagation from the magma lens tip

Consider dike trajectories for different lens depths, H, and widths, $2c$, in both a homogeneous and a heterogeneous crust. Calculations suggest that dikes propagate almost vertically towards the seafloor from the lens tips for all upper bound cases (Figures 4.16 – 4.18), regardless of the crustal condition (Figure 4.19).

Fialko [2001] has suggested different dike trajectories using the boundary element method. He suggested that the dike originating from pressurized chamber does not propagate vertically towards the seafloor and that the distance between the ridge and the emerging dike is much greater than the width of the magma lens. This is due to the fact that the body force, that affects the direction of dike propagation, was omitted in his calculations for simplicity. Based on the results presented in our study, the dike can indeed propagate farther than the distance of magma lens tip, provided that the initial pressure p_i is much greater than the overburden.

Dike propagation from the magma lens center

For dike propagation from the lens center, the dike always propagates vertically towards the seafloor as expected based on the symmetry of the model adopted here (Figure 4.20).

4.3 Dike propagation from the magma lens center

The numerical analyses described in section 4.2 intend only to simulate the possible dike trajectories. The pressure inside the magma lens remains constant and the chamber volume increases as the dike propagates. In reality, the total magma volume (chamber plus dike) is expected to remain constant because the dike propagates much more rapidly than that rate of magma to replenishment. Accordingly, the pressure in the magma lens should decrease as the dike propagates. This constrain represents the main difference of our problem compared to those typical studied in mechanics of hydraulic fracturing and diking (where the constant flow rate or constant pressure conditions are usually assumed). In this section, the magma conservation is taken into account. After the initial pressure for the central dike propagation is estimated, it is determined whether a dike indeed propagates to the surface (in the model of the homogeneous crust). The pressure in the magma lens, the volume of the dike, and the opening of the dike are also evaluated.

4.3.1 Initial pressure

In section 4.2, the initial pressure, p_i, of dike initiation was defined based on the condition that it exceeds the tensile strength of the rock. Numerically this condition leads to a rather laborious procedure because the values for the pressure are computed iteratively, for a particular instance of the tensile strength of the rock, the depth and the geometry of the magma lens. Therefore, in this section, the stress state in the vicinity of

the magma lens is addressed analytically to quantify the initial pressure for the dike propagation from the lens tip and center.

Since the magma lens is relatively close to the seafloor surface, it may interact with the surface mechanically before and during dike propagation. Figure 4.21 shows the physical problem. The chamber is loaded by an internal pressure p while the in-situ stresses, $\sigma_1(y)$ and $\sigma_3(y)$, can be expressed as

$$\sigma_1(y) = p_w + \rho_r g(H - y) = \rho_w g h_w + \rho_r g(H - y) \tag{4.2}$$

$$\sigma_3(y) = \lambda \sigma_1(y) \qquad (\lambda < 1) \tag{4.3}$$

where ρ_w is the seawater density, h_w is the seawater depth, and λ is the stress ratio of horizontal to vertical in-situ stress.

The physical problem for a thin cavity that is filled with magma can be represented by an idealized mathematical problem for a fracture with the same pressure (Figure 4.22), because

$$b << c \tag{4.4}$$

Further, this problem can be represented as a sum of two auxiliary problems: the half-space without the magma lens but with gravity and given boundary conditions (Figure 4.23a), and a half-space with a pressurized magma lens but zero gravity and other boundary conditions (Figure 4.23b).

In the later auxiliary problem, the tractions on the fracture sides (σ in Figure 4.23b) can be expressed as

$$\sigma = p - \sigma_1(0) \tag{4.5}$$

where $\sigma_1(0)$ is the overburden stress at the fracture location ($y = 0$) and can be obtained from (4.2):

$$\sigma_1(0) = p_w + \rho_r gH = \rho_w gh_w + \rho_r gH \tag{4.6}$$

Here h_w is the ocean depth.

Consider first the fracture open by the internal pressure p in an infinite plane loaded by the remote stresses σ_1 and σ_3 (Figure 4.24a). The maximum stress σ_{max} at the center of the magma lens (Figure 4.24b) is

$$\sigma_{\max} = \sigma_1 - \sigma_3 - p \tag{4.7}$$

Substituting (4.3) into (4.7) yields

$$\sigma_{\max} = \sigma_1(1-\lambda) - p \tag{4.8}$$

For dike initiation, the maximum stress should be equal to or greater than the tensile strength of the rock:

$$\sigma_{\max} \geq \sigma_t \tag{4.9}$$

Therefore, substituting (4.8) into (4.9) results in the initiation condition

$$p \leq \sigma_1(1-\lambda) - \sigma_t \tag{4.10}$$

In our case, because of the free surface (Figure 4.23b), the stress

$$\sigma_r = \frac{3\sigma c^2}{4H^2} \tag{4.11}$$

needs to be added to stress σ in (4.5). This stress is the first-order correction corresponding to the fracture-surface interaction [*Dyskin et al*., 2000]. Rearranging then (4.7) as

$$\sigma_{\max} = -(p - \sigma_1) - \sigma_3 \tag{4.12}$$

and adding (4.11) to the first term in (4.12) yields

$$\sigma_{\max} = -(p - \sigma_1)\left(1 + \frac{3c^2}{4H^2}\right) - \sigma_3 \tag{4.13}$$

Therefore, to initiate a dike at the center of the magma lens, (4.13) needs to satisfy condition (4.9). As a result, the pressure of dike initiation

$$p_i = \frac{\sigma_1\left(1 + \frac{3c^2}{4H^2} - \lambda\right) - \sigma_t}{1 + \frac{3c^2}{4H^2}} \tag{4.14}$$

4.3.2 Dimensional analysis

Figure 4.25 shows the superposition of problem for the dike propagation from the lens center at a MOR. Again, the magma lens is represented by a fracture (i.e., mathematical discontinuity). The dike is assumed to propagate vertically from the center of the magma lens (section 4.2.3). The original problem is simply represented as the sum of two sub-problems: the in-situ stress problem and the dike problem (Figure 4.25). The in-situ stress problem describes the body of the crust with gravity and other boundary conditions, but without a magma lens and without a dike. The dike problem describes the

body with a pressurized magma lens and with a pressurized dike but with zero gravity and other boundary conditions.

In the original problem (Figure 4.25), the pressure (4.1) on the dike can be expressed as

$$p(y) = \frac{p(l) - p(0)}{l} y + p(0) \tag{4.15}$$

where $p(l)$ is the pressure at the dike tip, $p(0)$ is the pressure in the magma lens equal to the pressure at the dike base, and l is the dike length.

In the in-situ stress problem (Figure 4.25), the solution must satisfy (e.g., *Muskhelishivili* [1953, §28]) equilibrium

$$\frac{\partial \sigma_{xx}}{\partial x} + \frac{\partial \tau_{xy}}{\partial y} = 0 \tag{4.16}$$

$$\frac{\partial \tau_{xy}}{\partial x} + \frac{\partial \sigma_{yy}}{\partial y} = \rho_r g \tag{4.17}$$

and compatibility

$$\nabla^2 (\sigma_{xx} + \sigma_{yy}) = 0 \tag{4.18}$$

conditions, where

$$\sigma_{yy} \to -\sigma_1(y) \quad (x \to \pm\infty) \tag{4.19}$$

$$\sigma_{xx} \to -\sigma_3(y) \quad (x \to \pm\infty) \tag{4.20}$$

$$\sigma_{yy} = -p_w \quad (y = H) \tag{4.21}$$

and compressive stresses are negative. The solution of this boundary value problem (4.16 – 4.21) is obviously

$$\tau_{xy} = 0 \tag{4.22}$$

$$\sigma_{xx}(x, y) = -\sigma_3(y) \tag{4.23}$$

$$\sigma_{yy}(x, y) = -\sigma_1(y) \tag{4.24}$$

where $\sigma_1(y)$ and $\sigma_3(y)$ are given by (4.2) and (4.3). Substituting (4.2) and (4.3) into (4.23) and (4.24) yields

$$\sigma_{xx}^{in-situ}(x, y) = -\lambda[p_w + \rho_r g(H - y)] \tag{4.25}$$

$$\sigma_{yy}^{in-situ}(x, y) = -[p_w + \rho_r g(H - y)] \tag{4.26}$$

$$\tau_{xy}^{in-situ}(x, y) = 0 \tag{4.27}$$

In the dike problem (Figure 4.25), the pressure on the dike and magma lens can be defined as

$$s(y) = p(y) - \sigma_3(y) \tag{4.28}$$

$$\sigma = p(0) - \sigma_1(0) \tag{4.29}$$

respectively.

The dike problem (Figure 4.25), in turn, can be also represented as the sum of three auxiliary problems (Figure 4.26). Let

$$p_A = \sigma \tag{4.30}$$

$$p_B = s(l) \tag{4.31}$$

$$p_C(y) = s(y) - s(l) \tag{4.32}$$

be the loads in these problems (see Figure 4.26). Since $p_C(y)$ is a linear function of y (because both $p(y)$ and $\sigma_3(y)$ in (4.28) are linear function of y). Each of problems A, B, and C depends only on one loading parameter, i.e., p_A, p_B, and $p_C(0)$, respectively.

In each of these problems, the parameter set is

$$\Omega = \{p_Z, E_r, \nu_r, l, H, c, x, y\} \tag{4.33}$$

where subscript Z represents A, B, or C. In two dimensions, the stresses σ_{ij} are independent of elastic moduli for our boundary conditions [e.g., *Muskhelishivili*, 1953]. Therefore,

$$\sigma_{ij} = \sigma_{ij}(p_Z, l, H, c, x, y) \tag{4.34}$$

or

$$\sigma_{ij} = p_Z f_{ij}\left(\frac{l}{c}, \frac{H}{c}, \frac{x}{c}, \frac{y}{c}\right) \tag{4.35}$$

Similarly, the displacements in two dimensions are given by

$$u_i = u_i(p_Z, E_r, \nu_r, l, H, c, x, y) \tag{4.36}$$

or

$$u_i = \frac{p_Z c}{E_r} F_i\left(\nu, \frac{l}{c}, \frac{H}{c}, \frac{x}{c}, \frac{y}{c}\right) \tag{4.37}$$

Finally, the stress intensity factors (SIFs) for the dike and magma lens are

$$K_I^{dike} = p_Z \sqrt{\pi c}\, k_I^{dike}\left(\frac{l}{c}, \frac{H}{c}\right) \tag{4.38}$$

$$K_I^{chamber} = p_Z \sqrt{\pi c} k_I^{chamber}\left(\frac{l}{c}, \frac{H}{c}\right) \tag{4.39}$$

Here f_{ij}, F_i, K_I^{dike}, and $K_I^{chamber}$ are some dimensionless function yet to be determined. For our purposes, only the SIFs and volumes (i.e., areas) of the dike and magma chamber are needed:

$$K_{IZ}^{dike} = p_Z \sqrt{\pi c} k_{IZ}^{dike}\left(\frac{l}{c}, \frac{H}{c}\right) \tag{4.40}$$

$$V_Z^{dike} = \frac{p_Z c^2}{E_r} f_Z^{dike}\left(\nu, \frac{l}{c}, \frac{H}{c}\right) \tag{4.41}$$

$$V_Z^{chamber} = \frac{p_Z c^2}{E_r} f_Z^{chamber}\left(\nu, \frac{l}{c}, \frac{H}{c}\right) \tag{4.42}$$

where again Z is A, B, or C and $V_Z^{chamber}$ volume of crack modeling the magma chamber in Problem Z.

In (4.40) to (4.42), functions k_I^{dike}, f_Z^{dike}, and $f_Z^{chamber}$ are dimensionless. Suppose that all three functions with respect to the dike propagation length, l, are known from the numerical calculations. Then, the superposition of problems A, B, and C results in

$$K_I^{dike} = \left[p_A k_{IA}^{dike}\left(\frac{l}{c}, \frac{H}{c}\right) + p_B k_{IB}^{dike}\left(\frac{l}{c}, \frac{H}{c}\right) + p_C(0) k_{IC}^{dike}\left(\frac{l}{c}, \frac{H}{c}\right)\right]\sqrt{\pi c} \tag{4.43}$$

$$V_{dike} = \frac{p_A c^2}{E_r} f_A^{dike}\left(\nu, \frac{l}{c}, \frac{H}{c}\right) + \frac{p_B c^2}{E_r} f_B^{dike}\left(\nu, \frac{l}{c}, \frac{H}{c}\right) + \frac{p_C(0) c^2}{E_r} f_C^{dike}\left(\nu, \frac{l}{c}, \frac{H}{c}\right) \tag{4.44}$$

$$V_{chamber} = \frac{p_A c^2}{E_r} f_A^{chamber}\left(\nu, \frac{l}{c}, \frac{H}{c}\right) + \frac{p_B c^2}{E_r} f_B^{chamber}\left(\nu, \frac{l}{c}, \frac{H}{c}\right) + \frac{p_C(0) c^2}{E_r} f_C^{chamber}\left(\nu, \frac{l}{c}, \frac{H}{c}\right) \tag{4.45}$$

Our notations can be further simplified by introducing the function

$$f_Z\left(\nu, \frac{l}{c}, \frac{H}{c}\right) = f_Z^{dike}\left(\nu, \frac{l}{c}, \frac{H}{c}\right) + f_Z^{chamber}\left(\nu, \frac{l}{c}, \frac{H}{c}\right) \tag{4.46}$$

and the "total" volume

$$\begin{aligned} V &= V_{dike} + V_{chamber} = \\ &= \frac{p_A c^2}{E_r} f_A\left(\nu, \frac{l}{c}, \frac{H}{c}\right) + \frac{p_B c^2}{E_r} f_B\left(\nu, \frac{l}{c}, \frac{H}{c}\right) + \frac{p_C(0) c^2}{E_r} f_C\left(\nu, \frac{l}{c}, \frac{H}{c}\right) \end{aligned} \tag{4.47}$$

Since at this stage, the magma chamber is represented by a fracture (Figure 4.25), V in (4.47) gives the total volume of the dike-chamber system minus the initial volume of the magma chamber. The word "initial" here may refer to different moments in the evolution of the dike-chamber system. To calculate the *change* of the magma chamber volume due to the dike propagation, the volume of the fracture (modeling the chamber) that was pressurized by the pressure p_i at dike initiation, should first be subtracted (Figure 4.27a).

Similar to Figure 4.23, this volume is equal to that of a fracture in a half-space loaded by pressure (Figure 4.27b)

$$\sigma_i = p_i - \sigma_1(0) \tag{4.48}$$

Since the pressurized fracture shown in Figure 4.27b is the same as Problem A (Figure 4.26), in the case of $l = 0$, the volume of this fracture (Figure 4.27b) at dike initiation can be expressed as:

$$\Delta V_i = \frac{\sigma_i c^2}{E_r} f_A\left(\nu, 0, \frac{H}{c}\right) \tag{4.49}$$

where we took into account that

$$f_B\left(\nu,\frac{l}{c},\frac{H}{c}\right)\to 0 \qquad (l\to 0) \tag{4.50}$$

$$f_C\left(\nu,\frac{l}{c},\frac{H}{c}\right)\to 0 \qquad (l\to 0) \tag{4.51}$$

because

$$V_Z^{dike}\to 0 \qquad (l\to 0,\ Z = A,\ B,\ or\ C) \tag{4.52}$$

Then the total volume change due to the dike propagation (with respect to that at the dike initiation moment) is obtained by substituting (4.49) from (4.47):

$$\begin{aligned}\Delta V = &\frac{p_A c^2}{E_r} f_A\left(\nu,\frac{l}{c},\frac{H}{c}\right)-\frac{\sigma_i c^2}{E_r} f_A\left(\nu,0,\frac{H}{c}\right)\\ &+\frac{p_B c^2}{E_r} f_B\left(\nu,\frac{l}{c},\frac{H}{c}\right)+\frac{p_C(0) c^2}{E_r} f_C\left(\nu,\frac{l}{c},\frac{H}{c}\right)\end{aligned} \tag{4.53}$$

Assuming now that the magma is incompressible, the two conditions determining the dike growth can be written in the form of

$$K_I^{dike}\ge K_{Ic} \tag{4.54}$$

$$\Delta V = 0 \tag{4.55}$$

where K_I^{dike} and ΔV are given by (4.43) and (4.53), respectively.

Substituting (4.53) into (4.55), magma conservation condition becomes

$$p_A f_A(l)-\sigma_i f_A(0)+p_B f_B(l)+p_C(0) f_C(l)=0 \tag{4.56}$$

where for brevity, the function $f_Z(\nu, l/c, H/c)$ is replaced with $f_Z(l)$. Rewriting (4.30) to (4.32) yields

$$p_A = p(0) - \sigma_1(0) \tag{4.57}$$

$$p_B = p(l) - \lambda\sigma_1(l) \tag{4.58}$$

$$p_C(y) = p(y) - p(l) - [\sigma_3(y) - \sigma_3(l)] \tag{4.59}$$

$$p_C(0) = p(0) - p(l) - \lambda[\sigma_1(0) - \sigma_1(l)] \tag{4.60}$$

so that the condition (4.56) can be expressed as

$$\begin{aligned}&[p(0) - \sigma_1(0)]f_A(l) - \sigma_i f_A(0) + [p(l) - \lambda\sigma_1(l)]f_B(l) \\ &+ [p(0) - p(l) - \lambda\sigma_1(0) + \lambda\sigma_1(l)]f_C(l) = 0\end{aligned} \tag{4.61}$$

If $p(l)$ is known, $p(0)$ is given by

$$\begin{aligned}p(0) = \frac{\sigma_1(0)f_A(l) + [p_i - \sigma_1(0)]f_A(0) - [p(l) - \lambda\sigma_1(l)]f_B(l)}{f_A(l) + f_C(l)} + \\ + \frac{[p(l) + \lambda\sigma_1(0) - \lambda\sigma_1(l)]f_C(l)}{f_A(l) + f_C(l)}\end{aligned} \tag{4.62}$$

From (4.50) and (4.51), we see that $p(0)$ satisfies

$$p(0) \to p_i \qquad (l \to 0) \tag{4.63}$$

which makes our model consistent with respect to choosing the initial moment of dike initiation as a lens for volume comparison.

Inserting (4.57), (4.58), and (4.60) into (4.43) yields

$$\begin{aligned}K_I^{dike} = &[p(0) - \sigma_1(0)]k_{IA}^{dike}\sqrt{\pi c} + [p(l) - \lambda\sigma_1(l)]k_{IB}^{dike}\sqrt{\pi c} \\ &+ [p(0) - p(l) - \lambda\sigma_1(0) - \lambda\sigma_1(l)]k_{IC}^{dike}\sqrt{\pi c}\end{aligned} \tag{4.64}$$

Given (4.62), the two conditions (4.54) and (4.55) can be effectively reduced to a single condition (4.54) or

$$[p(0)-\sigma_1(0)]k_{IA}^{dike}\sqrt{\pi c}+[p(l)-\lambda\sigma_1(l)]k_{IB}^{dike}\sqrt{\pi c} \\ +[p(0)-p(l)-\lambda\sigma_1(0)-\lambda\sigma_1(l)]k_{IC}^{dike}\sqrt{\pi c}\geq K_{Ic} \tag{4.65}$$

Once l is found from (4.65), $p(0)$ can be calculated from (4.62).

Since the pressure $p(y)$ inside the dike follows a hydrostatic (i.e., "magmastatic") pressure gradient,

$$\frac{p(l)-p(0)}{l}=-\rho_m g \tag{4.66}$$

in (4.15), which can be rewritten as

$$p(y)=-\rho_m g y+p(0) \tag{4.67}$$

so that

$$p(l)=p(0)-\rho_m g l \tag{4.68}$$

Substituting (4.68) into (4.58) and (4.60) yields

$$p_B=p(0)-\rho_m g l-\lambda\sigma_1(l) \tag{4.69}$$

$$p_C(0)=\rho_m g l-\lambda[\sigma_1(0)-\sigma_1(l)] \tag{4.70}$$

Consequently, substituting (4.57), (4.69), and (4.70) into (4.56) or directly in (4.61) produces

$$[p(0)-\sigma_1(0)]f_A(l)-\sigma_i f_A(0)+[p(0)-\rho_m g l-\lambda\sigma_1(l)]f_B(l) \\ +[\rho_m g l-\lambda\sigma_1(0)+\lambda\sigma_1(l)]f_C(l)=0 \tag{4.71}$$

which, in turn, yields

$$p(0) = \frac{\sigma_1(0) f_A(l) + [p_i - \sigma_1(0)] f_A(0) + [\rho_m g l + \lambda \sigma_1(l)] f_B(l)}{f_A(l) + f_B(l)} + \\ + \frac{-[\rho_m g l - \lambda \sigma_1(0) + \lambda \sigma_1(l)] f_C(l)}{f_A(l) + f_B(l)} \tag{4.72}$$

which, obviously, can be also obtained from (4.62). Then (4.72) with (4.54) or, which is the same, (4.65) with (4.57), (4.67) – (4.70), result in the condition

$$[p(0) - \sigma_1(0)] k_{IA}^{dike} \sqrt{\pi c} + [p(0) - \rho_m g l - \lambda \sigma_1(l)] k_{IB}^{dike} \sqrt{\pi c} \\ + [\rho_m g l - \lambda \sigma_1(0) - \lambda \sigma_1(l)] k_{IC}^{dike} \sqrt{\pi c} \geq K_{Ic} \tag{4.73}$$

which determines l.

Finally we need $f_A(0)$ to determine the dike size from (4.73) or (4.65). It can be found, based on the discussion in section 4.3.1. Accordingly, we consider a fracture (i.e., magma lens) in an infinite space loaded by the effective pressure equal to the sum of stresses (4.5) and (4.11):

$$p_{ef} = \sigma + \sigma_r \tag{4.74}$$

Substituting (4.11) into (4.74) results in

$$p_{ef} = \sigma \left[1 + \frac{3c^2}{4H^2} \right] \tag{4.75}$$

where, again, the term $3c^2/(4H^2)$ accounts for the interaction with the surface (seafloor).

The area of the fracture open by p_{ef} is given by

$$A = \frac{2\pi(1-\nu^2)}{E_r} c^2 p_{ef} \tag{4.76}$$

and substituting (4.48) and (4.75) into (4.76) yields the change of the volume of the lens at the moment of dike initiation with respect to the moment when the pressure in the dike is still equals overburden:

$$\Delta V_i = \frac{2\pi(1-\nu^2)c^2}{E_r}\sigma_i\left[1+\frac{3c^2}{4H^2}\right] \tag{4.77}$$

From comparing (4.49) and (4.77)

$$f_A(0) = 2\pi(1-\nu^2)\left[1+\frac{3c^2}{4H^2}\right] \tag{4.78}$$

This dimensionless value is consistent with $f_A(l)$ for small dike propagation (e.g., l = 50 m); (see Appendix D).

4.3.3 Results

Figure 4.28 shows an example of a FEM mesh used in calculation of the dimensionless functions $f_Z^{dike}(l)$, $f_Z^{chamber}(l)$, and $k_{IZ}^{dike}(l)$ for H = 1 km, $2c$ = 1 km, and l = 0.5 km (Table 4.3). In particular, to calculate $f_Z^{dike}(l)$ and $f_Z^{chamber}(l)$, which are associated with the fracture volume, the displacements from all node points in the magma lens and the dike are recorded and used for the computing both volumes. In Appendix D, these functions are compared with the available analytical solutions (refer to Appendix D).

Figures 4.29 to 4.30 show the normalized SIF (K_I/K_{Ic}), the normalized pressure in the magma lens ($p(0)/p_i$), the normalized dike volume (V_{dike}/V_i), and the dike opening at the base along the dike propagation in the homogeneous crust. As expected, the pressure in the magma lens decreases as the dike propagates since the total magma volume is constant. Three different stress ratios λ are used for the comparison. For extensional ridge

environments, the stress ratio λ is less than one. The lower limit for the stress ratio is probably given by the normal faulting condition or the condition of zero horizontal strain (whatever is larger). For all cases, the central dike cannot propagate to the seafloor surface, because the dike-seafloor interaction is not sufficient. In the previous numerical analysis for H = 1 km and $2c$ = 1 km (Figure 4.20a), in which the magma volume is not constant, the dike can propagate to the surface. Therefore, the magma conservation condition is critical for obtaining physically reasonable results.

Table 4.3 Dimensionless functions (f_Z^{dike}, $f_Z^{chamber}$, and k_{IZ}^{dike}) for dike propagation from the lens center.

H = 1 km and $2c$ = 1 km									
l (m)	Problem A			Problem B			Problem C		
	f_A^{dike}	$f_A^{chamber}$	k_{IA}^{dike}	f_B^{dike}	$f_B^{chamber}$	k_{IB}^{dike}	f_C^{dike}	$f_C^{chamber}$	k_{IC}^{dike}
50	-0.042	6.929	-0.386	0.036	-0.040	0.350	0.022	-0.024	0.132
100	-0.151	7.04	-0.465	0.143	-0.149	0.491	0.086	-0.090	0.188
200	-0.474	7.283	-0.439	0.553	-0.471	0.669	0.329	-0.292	0.245
300	-0.806	7.467	-0.331	1.165	-0.806	0.772	0.693	-0.512	0.275
400	-1.071	7.562	-0.218	1.932	-1.072	0.847	1.146	-0.705	0.291
500	-1.246	7.597	-0.118	2.835	-1.252	0.914	1.672	-0.853	0.305
600	-1.331	7.606	-0.029	3.888	-1.340	0.99	2.276	-0.956	0.323
700	-1.317	7.607	0.061	5.135	-1.330	1.085	2.975	-1.008	0.350
800	-1.169	7.621	0.173	6.682	-1.185	1.231	3.811	-0.997	0.395
900	-0.768	7.697	0.361	8.828	-0.791	1.525	4.900	-0.877	0.488
950	-0.336	7.809	0.550	10.480	-0.362	1.891	5.668	-0.728	0.605
H = 1.5 km and $2c$ = 1 km									
50	-0.037	6.465	-0.35	0.036	-0.037	0.35	0.022	-0.022	0.132
100	-0.138	6.560	-0.43	0.144	-0.138	0.492	0.086	-0.084	0.188
200	-0.430	6.760	-0.405	0.547	-0.428	0.665	0.326	-0.265	0.242
300	-0.738	6.921	-0.317	1.150	-0.738	0.766	0.683	-0.468	0.271
400	-0.980	6.992	-0.219	1.891	-0.983	0.835	1.120	-0.641	0.284
500	-1.164	7.034	-0.144	2.764	-1.170	0.897	1.628	-0.786	0.296
600	-1.279	7.044	-0.083	3.748	-1.287	0.954	2.193	-0.895	0.305
700	-1.350	7.049	-0.039	4.877	-1.361	1.018	2.832	-0.979	0.320
800	-1.372	7.049	-0.003	6.144	-1.387	1.084	3.538	-1.035	0.336
900	-1.357	7.049	0.028	7.609	-1.375	1.162	4.341	-1.071	0.360
1000	-1.298	7.051	0.059	9.273	-1.320	1.249	5.240	-1.083	0.387
1100	-1.188	7.057	0.092	11.236	-1.214	1.356	6.282	-1.068	0.423
1200	-1.008	7.069	0.135	13.598	-1.04	1.506	7.505	-1.021	0.476
1300	-0.703	7.099	0.198	16.625	-0.742	1.737	9.021	-0.919	0.558
1400	-0.152	7.167	0.311	20.973	-0.202	2.194	11.079	-0.720	0.717
1450	0.406	7.086	0.431	23.658	0.353	2.718	12.173	-0.482	0.890

4.4 Dike propagation from the lens tip

4.4.1 Initial pressure

Consider first dike initiation from the tip of the magma chamber (Figure 4.31). The criterion for dike initiation is the same as (4.9):

$$\sigma_{\max} \geq \sigma_t \tag{4.79}$$

where σ_{max} is now the maximum tensile stress near the lens tips. The effect of mode II fracturing is ignored at the moment of initiation. To estimate σ_{max}, the solution of the problem shown in Figure 4.22 is used. According to (4.11), this solution is equivalent (to the first order) to the solution of the problem in an infinite plane if σ is replaced with $\sigma + \sigma_r$, where the second term is given by (4.11). Therefore

$$K_I = [\sigma + \sigma_r]\sqrt{\pi c} \tag{4.80}$$

Substituting (4.11) into (4.80) yields

$$K_I = \sigma\left[1 + \frac{3c^2}{4H^2}\right]\sqrt{\pi c} \tag{4.81}$$

Then, σ_{max} at the lens tips can be estimated as

$$\sigma_{\max} = \frac{K_I}{\sqrt{2\pi\kappa}} \tag{4.82}$$

where κ is the typical characteristic dimension at the lens tips. For example, it can be equal to the curvature radius

$$\kappa = \frac{b^2}{c} \tag{4.83}$$

for an elliptical lens. Alternatively, it can be equal to the characteristic thickness

$$\kappa = 2b \tag{4.84}$$

if the lens is of a rectangular shape.

Substituting (4.81) into (4.82) yields

$$\sigma_{\max} = \sigma\left(1 + \frac{3c^2}{4H^2}\right)\sqrt{\frac{c}{2\kappa}} \tag{4.85}$$

At the moment of dike initiation

$$\sigma = \sigma_i \tag{4.86}$$

where σ_i is defined by (4.48). Using then (4.48) and (4.86), (4.85) is rewritten as

$$\sigma_{\max} = [p_i - \sigma_1(0)]\left(1 + \frac{3c^2}{4H^2}\right)\sqrt{\frac{c}{2\kappa}} \tag{4.87}$$

and from condition (4.79) and (4.87), the dike initiation pressure p_i can be expressed as

$$p_i = \sigma_1(0) + \frac{\sigma_t}{1 + \frac{3c^2}{4H^2}}\sqrt{\frac{2\kappa}{c}} \tag{4.88}$$

In the case of an elliptic magma lens, (4.83) and (4.88) suggest that

$$p_i^{elliptic} = \sigma_1(0) + \frac{\sqrt{2}\sigma_t}{1 + \frac{3c^2}{4H^2}}\frac{b}{c} \tag{4.89}$$

while in the case of a rectangular magma lens,

$$p_i^{rect} = \sigma_1(0) + \frac{2\sigma_t}{1 + \frac{3c^2}{4H^2}}\sqrt{\frac{b}{c}} \tag{4.90}$$

due to (4.84).

4.4.2 Dimensional analysis and results

Using the same procedure as that for the central dike problem (Figure 4.25), this problem can be represented as the sum of two sub-problems as shown in Figure 4.31. The dike is assumed to propagate vertically from the tip of the magma lens as in the case of the dike propagation from the lens center, although the dike trajectories in the previous numerical analyses (Figures 4.16 and 4.17) were not exactly vertical. To verify this assumption, the normalized dike volumes (V_{dike}/V_0) and SIFs (K_I and K_{II}) normalized by (4.81) at $p(0) = \sigma_1(0)$ are compared with those obtained from the previous numerical analysis (Figure 4.16). Here, V_0 is the original volume of the magma lens. This results in a good agreement (Figure 4.32) for vertical and sub-vertical dikes. Accordingly, the dike problem can indeed be represented as the sum of three sub-problems (Figure 4.33) where dike propagation is vertical.

Figure 4.34 shows one example of a typical FRANC2D mesh to calculate the dimensionless functions $f_Z^{dike}(l)$, $f_Z^{chamber}(l)$, and $k_{IZ}^{dike}(l)$ for H = 1 km, $2c$ = 1 km, and l = 0.5 km (Table 4.4) in the case of dike originating at the magma chamber tips. Dimensionless parameter $f_A(0)$ is again defined by (4.78). Another dimensionless parameter for the dike propagation from the lens tip, $k_{IA}^{dike}(0)$, is available from the work of *Melin* [1994], and is equal to 0.3718838. This is obtained by considering a straight

crack terminated by an infinitesimally small kink which forms an angle 90° to the main crack.

Because the normalized SIF remains greater than one until the dike reaches the seafloor, in contrast to the central dike, the tip dike propagates to the surface in all considered cases (Figure 4.35 and 4.36). The pressure drop in the magma lens is unfavorable for dike propagation. However, the pressure decrease is compensated by the dike-seafloor interaction. The deeper magma lens has a greater pressure drop, and results in a larger dike volume, as well as larger dike apertures.

Table 4.4 Dimensionless functions (f_Z^{dike}, $f_Z^{chamber}$, and k_{IZ}^{dike}) for dike propagation from the lens tip.

H = 1 km and $2c$ = 1 km									
l (m)	Problem A			Problem B			Problem C		
	f_A^{dike}	$f_A^{chamber}$	k_{IA}^{dike}	f_B^{dike}	$f_B^{chamber}$	k_{IB}^{dike}	f_C^{dike}	$f_C^{chamber}$	k_{IC}^{dike}
0	0.000	6.941	0.372	0.000	0.000	0.000	0.000	0.000	0.000
50	0.025	7.126	0.171	0.029	0.023	0.314	0.017	0.014	0.111
100	0.037	7.266	0.068	0.115	0.033	0.436	0.067	0.021	0.155
200	-0.006	7.596	-0.054	0.456	-0.016	0.620	0.263	-0.005	0.212
300	-0.126	8.017	-0.099	1.009	-0.142	0.747	0.580	-0.081	0.256
400	-0.300	8.509	-0.110	1.764	-0.324	0.854	1.013	-0.194	0.291
500	-0.500	9.098	-0.094	2.727	-0.530	0.953	1.562	-0.331	0.324
600	-0.699	9.776	-0.060	3.903	-0.736	1.049	2.227	-0.478	0.356
700	-0.865	10.576	-0.003	5.339	-0.908	1.161	3.031	-0.621	0.394
800	-0.96	11.562	0.087	7.108	-1.007	1.309	4.001	-0.749	0.443
900	-0.865	13.002	0.265	9.518	-0.911	1.592	5.260	-0.820	0.535
950	-0.621	14.238	0.465	11.299	0.659	1.947	6.120	-0.802	0.649
H = 1.5 km and $2c$ = 1 km									
0	0.000	6.332	0.372	0.000	0.000	0.000	0.000	0.000	0.000
50	0.019	6.516	0.130	0.029	0.017	0.312	0.017	0.011	0.110
100	0.024	6.629	0.027	0.115	0.020	0.440	0.066	0.013	0.154
200	-0.032	6.890	-0.079	0.449	-0.042	0.612	0.258	-0.022	0.207
300	-0.162	7.212	-0.123	0.983	-0.178	0.731	0.564	-0.103	0.277
400	-0.342	7.566	-0.138	1.702	-0.364	0.829	0.975	-0.217	0.302
500	-0.551	7.962	-0.136	2.598	-0.580	0.913	1.485	-0.355	0.325
600	-0.773	8.380	-0.124	3.667	-0.808	0.991	2.090	-0.504	0.344
700	-0.983	8.799	-0.104	4.889	-1.025	1.061	2.777	-0.654	0.365
800	-1.181	9.231	-0.080	6.299	-1.228	1.132	3.565	-0.802	0.390
900	-1.351	9.665	-0.052	7.901	-1.403	1.211	4.451	-0.940	0.420
1000	-1.484	10.126	-0.018	9.746	-1.541	1.300	5.463	-1.066	0.455
1100	-1.566	10.623	0.023	11.873	-1.624	1.406	6.612	-1.171	0.506
1200	-1.565	11.184	0.078	14.415	-1.624	1.550	7.958	-1.245	0.506
1300	-1.442	11.856	0.155	17.544	-1.498	1.760	9.564	-1.273	0.578
1400	-1.023	12.823	0.301	21.970	-1.068	2.192	11.705	-1.195	0.724
1450	-0.52	13.617	0.465	25.428	-0.550	2.743	13.245	-1.059	0.906

4.5 Geophysical implications

4.5.1 Hydrothermal vents at Juan de Fuca Ridge

Our model suggests the location of the propagating dike with respect to the location of the pressurized magma lens. In addition to heat, the dike increases the permeability near its margin [*Lowell and Germanovich*, 1995; *Curewits and Karson*, 1998]. Consequently, hydrothermal activity may become localized [*Lowell*, 1990]. As a result, our model can be constrained by comparing the locations of observed hydrothermal vents to the location of the magma lens at MOR.

Figure 4.37a shows a location of the Juan de Fuca Ridge (JdFR). The Endeavor segment is located inside the dashed circle. Four main hydrothermal sites appear on this segment (Figure 4.37b). One of them, the Salty Dawg hydrothermal site on the Endeavor segment, appears to be located above the tip of the seismically imaged magma lens [*Van Ark et al*., 2003].

Figure 4.37c shows a scenario of how a dike propagating from the tip of the pressurized magma lens could result in a hydrothermal vent located above the tip of the lens. Summarizing, dike propagation from the tip of a magma lens is consistent with hydrothermal vents located off the ridge axis, and with an episode of recent pressurization of the magma lens.

4.5.2 Hydrothermal vents at East Pacific Rise

Our model can be further constrained by comparing the locations of the observed hydrothermal vents to the location of the magma lens at MOR. Figure 4.38a shows a

geographic location of the EPR. Most of the hydrothermal sites of the EPR appear above the center of the magma lens (Figure 4.38b).

Figure 4.38c shows a scenario of how a dike propagating from the center of the depressurized magma lens can result in a hydrothermal vent located above the center of the lens. Although the dike does not propagate to the seafloor, hydrothermal activity becomes localized because the dike increases the permeability near its margin and further fracturing may occur due to the magmatic gases resulting from the depressurization of the magma chambers.

Summarizing, dike propagation from the center of the magma lens is consistent with hydrothermal cooling that controls the permeability distribution and, perhaps, with a shallow magma source [*Von Damm*, 2004].

4.6 Dike propagation from tip of the deep magma lens

4.6.1 Single deep melt lens

As introduced in section 4.1, recent seismic studies suggest that the magma lens may also exist at the base of the crust [*Crawford et al*., 1999; *Dunn et al*., 2000]. In this section, dike propagation from a tip of a deep melt lens is analyzed.

A dike originating from the deep melt lens is likely to initiate from the tip of the magma lens, because it is expected that hydrothermal cooling is rather weak (or absent) and magma is being replenished from the mantle. As in the case of dike propagation from a shallow magma lens, the dike propagates sub-vertically. Figure 4.39 shows an example of a typical FEM mesh with a cavity modeling the lens. The dike propagates to the

surface and its trajectory deviates slightly from the vertical (solid line in Figure 4.40a). The normalized dike volumes (V/V_0) and SIFs (K_I and K_{II}) are also compared in Figure 4.40 for vertical and sub-vertical dikes. They appear to be in good agreement.

Figure 4.41 shows an example of a FEM mesh used to calculate the dimensionless functions $f_Z^{dike}(l)$, $f_Z^{chamber}(l)$, and $k_{IZ}^{dike}(l)$ for H = 5.5 km, $2c$ = 1 km, and l = 2.5 km (Table 4.5). It appears that the dike does not propagate to the surface (Figure 4.42). For all stress ratios, λ, the dike terminates at a similar depth, but with greater pressure drop inside the magma lens, a larger dike volume, and a larger dike opening at the base for smaller λ.

To test the effect of the size of the magma lens, the dimensionless functions for H = 6 km and $2c$ = 2 km are also calculated (Table 4.6). In this case, the dike does not reach the surface either, but it propagates nearly twice as far as for the case of the small magma lens ($2c$ = 1 km) (Figure 4.43). Compared to the small magma lens, a greater pressure drop in the magma lens, a larger dike volume, and a larger dike openings are obtained.

From these two previous simulations, it can be concluded that dike-seafloor interaction for deep magma lenses is too weak to overcome the pressure decrease in the magma chamber and for the dikes to reach the seafloor.

Table 4.5 Dimensionless functions (f_Z^{dike}, $f_Z^{chamber}$, and k_{IZ}^{dike}) for dike propagation from the deep lens tip (H = 5.5 km and $2c$ = 1 km).

H = 5.5 km and $2c$ = 1 km									
l (m)	Problem A			Problem B			Problem C		
	f_A^{dike}	$f_A^{chamber}$	k_{IA}^{dike}	f_B^{dike}	$f_B^{chamber}$	k_{IB}^{dike}	f_C^{dike}	$f_C^{chamber}$	k_{IC}^{dike}
0	0	5.882	0.372	0.000	0.000	0.000	0.000	0.000	0.000
50	0.017	5.971	0.111	0.029	0.014	0.314	0.017	0.009	0.109
100	0.021	6.057	0.015	0.114	0.013	0.438	0.066	0.009	0.150
200	-0.032	6.261	-0.081	0.443	-0.051	0.606	0.254	-0.028	0.204
300	-0.155	6.511	-0.123	0.966	-0.186	0.723	0.554	-0.108	0.241
500	-0.513	7.074	-0.137	2.509	-0.568	0.888	1.431	-0.345	0.285
750	-1.008	7.776	-0.109	5.235	-1.089	1.035	2.963	-0.691	0.317
1000	-1.432	8.381	-0.076	8.736	-1.534	1.155	4.904	-1.013	0.342
1250	-1.751	8.875	-0.048	12.978	-1.867	1.263	7.221	-1.281	0.364
1500	-1.970	9.273	-0.028	17.984	-2.095	1.367	9.918	-1.493	0.387
1750	-2.108	9.596	-0.013	23.782	-2.237	1.467	13.002	-1.654	0.411
2000	-2.179	9.863	-0.003	30.429	-2.311	1.568	16.516	-1.773	0.437
2250	-2.200	10.087	0.005	37.972	-2.330	1.668	20.464	-1.856	0.463
2500	-2.178	10.279	0.010	46.491	-2.306	1.771	24.891	-1.909	0.493
2750	-2.120	10.448	0.015	56.058	-2.244	1.875	29.835	-1.937	0.524
3000	-2.029	10.598	0.019	66.800	-2.147	1.988	35.352	-1.940	0.560
3250	-1.906	10.735	0.023	78.842	-2.016	2.106	41.506	-1.922	0.599
3500	-1.748	10.863	0.026	92.396	-1.849	2.238	48.391	-1.881	0.644
3750	-1.549	10.986	0.031	107.732	-1.639	2.384	56.125	-1.816	0.696
4000	-1.299	11.106	0.036	125.257	-1.377	2.557	64.892	-1.724	0.76
4250	-0.983	11.226	0.043	145.563	-1.043	2.764	74.941	-1.599	0.839
4500	-0.571	11.352	0.052	169.609	-0.609	3.032	86.696	-1.427	0.941
4750	-0.012	11.489	0.064	199.146	-0.022	3.398	100.833	-1.188	1.081
5000	0.800	11.650	0.083	237.817	0.833	3.974	118.871	-0.838	1.298
5250	2.166	11.865	0.120	295.907	2.270	5.144	144.657	-0.257	1.725
5400	3.794	12.072	0.181	358.814	3.985	7.187	170.674	0.413	2.444

Table 4.6 Dimensionless functions (f_Z^{dike}, $f_Z^{chamber}$, and k_{IZ}^{dike}) for dike propagation from the deep lens tip (H = 6 km and $2c$ = 2 km).

H = 6.0 km and $2c$ = 2 km									
l (m)	Problem A			Problem B			Problem C		
	f_A^{dike}	$f_A^{chamber}$	k_{IA}^{dike}	f_B^{dike}	$f_B^{chamber}$	k_{IB}^{dike}	f_C^{dike}	$f_C^{chamber}$	k_{IC}^{dike}
0	0.000	5.967	0.372	0.000	0.000	0.000	0.000	0.000	0000
100	0.018	6.065	0.112	0.029	0.015	0.315	0.017	0.0092	0.108
200	0.022	6.154	0.000	0.114	0.014	0.438	0.066	0.0094	0.151
400	-0.032	6.362	-0.081	0.444	-0.051	0.607	0.255	-0.028	0.204
600	-0.156	6.621	-0.123	0.968	-0.187	0.723	0.555	-0.109	0.242
1000	-0.521	7.215	-0.139	2.529	-0.577	0.894	1.443	-0.351	0.288
1500	-1.031	7.963	-0.112	5.310	-1.114	1.049	3.007	-0.707	0.325
2000	-1.468	8.625	-0.076	8.921	-1.572	1.179	5.009	-1.039	0.355
2500	-1.799	9.189	-0.047	13.408	-1.918	1.308	7.457	-1.318	0.388
3000	-2.018	9.670	-0.022	18.851	-2.146	1.441	10.384	-1.537	0.426
3500	-2.135	10.095	-0.002	25.492	-2.267	1.594	13.902	-1.697	0.475
4000	-2.141	10.488	0.018	33.619	-2.272	1.775	18.143	-1.797	0.538
4250	-2.095	10.682	0.030	38.467	-2.223	1.887	20.638	-1.821	0.580
4500	-2.008	10.878	0.043	43.935	-2.131	2.021	23.424	-1.825	0.631
4750	-1.864	11.084	0.059	50.306	-1.979	2.181	26.623	-1.802	0.692
5000	-1.650	11.303	0.078	57.688	-1.753	2.384	30.286	-1.746	0.770
5250	-1.313	11.550	0.106	66.909	-1.398	2.676	34.750	-1.636	0.882
5500	-0.779	11.850	0.147	78.941	-0.835	3.134	40.396	-1.442	1.055
5700	-0.047	12.166	0.204	92.751	-0.064	3.804	46.599	-1.160	1.303
5900	1.449	12.685	0.350	116.878	1.512	5.666	56.728	-0.579	1.966

4.6.2 Magma replenishment mechanism

Although a dike from a deep melt lens does not propagate to the surface, based on the above calculations it may reach a shallow magma lens because of the mechanical interaction between the dike and shallower lenses. Figure 4.44a shows the concept of a possible magmatic injection from a deep melt lens to a shallow magma lens [*Crawford et al*., 1999]. Figure 4.44b shows the hypothesized dike propagation from the center of magma lens [*Korenaga and Kelemen*, 1997]. This could be related to the magma replenishment of the shallower magma lenses.

To simulate and test this phenomenon, two magma lenses are created in the mesh (Figure 4.45). First, the dike propagation from the tip of the deep magma lens (H = 6 km and $2c$ = 2 km) to the shallow magma lens (H_1 = 2 km and $2c$ = 2 km) is simulated by using FRANC2D. The pressure condition in the shallow magma lens is assumed to be the in-situ stress σ_1 at its depth. The pressure in the dike follows the hydrostatic distribution, which represents the upper bound estimate. Figure 4.46 shows the calculated and the simplified dike trajectories. The latter is used to calculate the volume of the lens and the dike. The SIFs for the vertical and sub-vertical dikes appear to be in good agreement, although the calculated trajectory deviates slightly from the vertical (Figure 4.47).

After the deep dike reaches the shallow lens, this can lead to the subsequent dike propagation from the tip of this lens caused by the fast lens pressurization. Figure 4.48 shows the dike propagation simulation with FRANC2D. The dike from the deep to the shallow magma lens is connected using the mesh generator CASCA because a crack simply cannot be connected to the shallow lens in FRANC2D. The SIFs (K_I) normalized

by (4.81) are also compared between the vertical and sub-vertical dike propagations from the shallow lens (Figure 4.49), and they are found to be in good agreement.

Using the same procedure that was introduced previously for the dike propagation from a single lens, the original problem can be decomposed as the sum of two sub-problems as shown in Figure 4.50. Accordingly, the dike problem can also be represented as the sum of four sub-problems (Figure 4.51), where the pressure in the shallow magma lens is included in additional Problem D.

Until the dike reaches the shallow lens, the magma conservation condition should be expressed for the shallow and deep magma lenses separately. Similar to (4.55), we have

$$\Delta V = 0 \tag{4.91}$$

$$\Delta V_1 = 0 \tag{4.92}$$

where $V(l)$ is the values of the deep magma lens plus dike volume while $V_1(l)$ is the volume of the shallow lens (it depends upon l due to the lens-dike interaction).

From conditions (4.49) and (4.92), similar to (4.56), we obtain:

$$p_A f_A(l) - \sigma_i f_A(0) + p_B f_B(l) + p_C(0) f_C(l) + p_D f_D(l) - p_{Di} f_D(0) = 0 \tag{4.93}$$

$$p_A g_A(l) - \sigma_i g_A(0) + p_B g_B(l) + p_C(0) g_C(l) + p_D g_D(l) - p_{Di} g_D(0) = 0 \tag{4.94}$$

where $f_A(l)$, $f_B(l)$, and $f_C(l)$ are the same as before, and $g_Z(l)$

$$g_Z(l) = V_Z^{\substack{upper \\ chamber}} \cdot \frac{E_r}{p_Z c^2} \tag{4.95}$$

is the dimensionless volumes of the shallow lens in problem Z, and

$$p_D = s_1 = p_1 - \sigma_1(H - H_1) \tag{4.96}$$

is the initial pressure in the shallow lens in problem D (Figure 4.51) Now, Z is A, B, C, and D.

Assuming that the interaction between two melt lenses is weak (if the distance between them considerably exceeds their sizes), we have that

$$g_A(0) \approx 0 \tag{4.97}$$

and the initial pressure in the shallow lens (again, at the moment when the dike initiates from the deep lens) is given by

$$p_{1i} \approx \sigma_1(H - H_1) \tag{4.98}$$

Therefore,

$$p_{Di} = p_{1i} - \sigma_1(H - H_1) \approx 0 \tag{4.99}$$

Using conditions (4.96) – (4.99), we obtain $p(0)$ and p_1 as follows:

$$\begin{aligned} p(0) = {} & \frac{\sigma_1(0)D_A(l) + [p_i - \sigma_1(0)][f_A(0)g_D(l)]}{D_A(l) + D_C(l)} + \\ & + \frac{[\rho_m g l + \lambda\sigma_1(l)]D_B(l) - [\rho_m g l - \lambda\sigma_1(0) + \lambda\sigma_1(l)]D_C(l)}{D_A(l) + D_B(l)} \end{aligned} \tag{4.100}$$

$$\begin{aligned} p_1 = {} & \frac{[\sigma_1(0) - p(0)]g_A(l) + \sigma_i g_A(0) + [\rho_m g l - p(0) + \lambda\sigma_1(l)]g_B(l)}{g_D(l)} + \\ & + \frac{-[\rho_m g l - \lambda\sigma_1(0) + \lambda\sigma_1(l)]g_C(l) + \sigma_1(H - H_1)g_D(l)}{g_D(l)} \end{aligned} \tag{4.101}$$

where $D_A(l) = f_A(l)g_D(l) - g_A(l)f_D(l)$, $D_B(l) = f_B(l)g_D(l) - g_B(l)f_D(l)$, and

$$D_C(l) = f_C(l)g_D(l) - g_C(l)f_D(l).$$

Similar to (4.64), the SIF can be defined as:

$$\begin{aligned} K_I^{dike} &= [p(0) - \sigma_1(0)]k_{IA}^{dike}\sqrt{\pi c} + [p(l) - \lambda\sigma_1(l)]k_{IB}^{dike}\sqrt{\pi c} \\ &+ [p(0) - p(l) - \lambda\sigma_1(0) - \lambda\sigma_1(l)]k_{IC}^{dike}\sqrt{\pi c} + [p_1 - \sigma_1(H - H_1)]k_{ID}^{dike}\sqrt{\pi c} \end{aligned} \quad (4.102)$$

Figure 4.52 shows one example of a FEM mesh to calculate the dimensionless functions ($f_Z^{dike}(l)$, $f_Z^{chamber}(l)$, $k_{iZ}^{dike}(l)$, $g_Z(l)$) for the deep (H = 6 km and $2c$ = 2 km) and shallow magma (H_1 = 2 km and $2c$ = 2 km) lenses (Table 4.7). Figure 4.53 shows the normalized SIF (K_I/K_{Ic}), the normalized pressure in the magma lens ($p(0)/p_i$), the normalized dike volume (V_{dike}/V_i), the dike opening at the base, and the normalized pressure in the shallow magma lens ($p_1/\sigma_1(H\text{-}H_1)$) along the dike propagation.

As a result, a dike from a deep melt lens (H = 6 km) may indeed propagate to a shallow lens (H_1 = 2 km) because the SIF remains greater than K_{Ic} during the entire dike propagation. In turn, this may lead to the subsequent dike propagation from the shallow magma lens tip. Whether the dike from a shallow lens can reach the seafloor surface, requires further investigation. The answer is not obvious since this dike will further decrease the pressure in the dike-lenses system.

Note that pressure in the deep magma lens, the dike volume and the dike opening at the base show similar behavior as for the case of dike propagation from a deep magma lens, i.e., without a shallow magma lens present (Figure 4.43). The pressure in the shallow magma lens p_1, computed with (4.101), monotonically decreases as the dike propagates (Figure 4.53).

Table 4.7 Dimensionless functions (f_Z^{dike}, $f_Z^{chamber}$, k_{IZ}^{dike}, and g_Z) for dike propagation from the deep lens tip (H = 6 km and $2c$ = 2 km) to shallow magma lens (H_1 = 2 km and $2c$ = 2 km).

H = 6.0 km and $2c$ = 2 km for deep magma lens and H_1 = 2.0 km and $2c$ = 2 km for shallow magma lens																
l (m)	Problem A				Problem B				Problem C				Problem D			
	f_A^{dike}	$f_A^{chamber}$	k_{IA}^{dike}	g_A	f_B^{dike}	$f_B^{chamber}$	k_{IB}^{dike}	g_B	f_C^{dike}	$f_C^{chamber}$	k_{IC}^{dike}	g_C	f_D^{dike}	$f_D^{chamber}$	k_{ID}^{dike}	g_D
0	0	5.967	0.372	0	0	0	0	0	0	0	0	0	0	0	6.941	0
500	-0.088	6.505	-0.108	-0.325	0.683	-0.112	0.671	0.001	0.392	-0.064	0.226	0	0..001	-0.332	6.978	0.006
1000	-0.525	7.243	-0.14	-0.403	2.530	-0.579	0.894	0.043	1.444	-0.353	0.290	0.025	0.043	-0.417	6.987	0.014
1500	-1.040	8.01	-0.113	-0.521	5.317	-1.123	1.049	0.111	3.012	-0.713	0.328	0.068	0.110	-0.542	7.006	0.013
2000	-1.486	8.703	-0.077	-0.681	8.939	-1.59	1.179	0.181	5.020	-1.051	0.358	0.119	0.180	-0.71	7.045	0.005
2500	-1.823	9.323	-0.044	-0.898	13.441	-1.943	1.308	0.214	7.478	-1.339	0.391	0.162	0.214	-0.938	7.128	-0.017
3000	-2.029	9.909	-0.007	-1.219	18.897	-2.157	1.439	0.119	10.412	-1.564	0.425	0.165	0.122	-1.275	7.322	-0.069
3500	-2.043	10.564	0.050	-1.771	25.609	-2.169	1.610	-0.331	13.941	-1.712	0.425	0.055	-0.320	-1.855	7.846	-0.183
3800	-1.850	11.135	0.122	-2.434	30.711	-1.962	1.848	-1.018	16.490	-1.740	0.530	-0.128	-0.996	-2.551	8.695	-0.326

4.7 Discussion

4.7.1 Effect of the compressibility of the magma

Ignoring the compressibility of the magma underestimates the size of the dike and may affect the dike propagation. The effect of magma compressibility can be included by considering the magma mass conservation rather than the volume. In other words, the total mass of magma during the dike propagation remains constant. Therefore,

$$M_{chamber} + M_{dike} = M_i \tag{4.103}$$

where $M_{chamber}$ and M_{dike} are the total mass of magma in the magma lens and the dike, respectively, and M_i is the mass of magma in the lens at the moment of dike initiation.

In the simplest model, the density of the magma, ρ_m, linearly depends upon the pressure:

$$\rho_m = \rho_{mi}\left(1 + \frac{p - p_i}{K_m}\right) \tag{4.104}$$

where ρ_{mi} is the density of the magma at the moment of dike initiation, and K_m is the magma bulk modulus. Further,

$$M_i = V_i \rho_{mi} \tag{4.105}$$

$$M_{chamber} = V_{chamber} \rho_m \tag{4.106}$$

$$M_{dike} = \rho_m V_{dike} = \int_0^l \rho_m (p(y)) W(y) dy \tag{4.107}$$

where V_i and $V_{chamber}$ are the volume of the magma lens at the moment of dike initiation and during the dike propagation, respectively, and $W(y)$ is the width of the dike.

Inserting (4.104) into (4.107) yields

$$M_{dike} = \rho_{mi} \int_0^l W(y)dy + \rho_{mi} \int_0^l \frac{p(y) - p_i}{K_m} W(y)dy \tag{4.108}$$

The volume of the dike (per unit thickness in plane strain) is

$$V_{dike} = \int_0^y W(y)dy \tag{4.109}$$

so that (4.108) reads

$$M_{dike} = \rho_{mi} V_{dike} + \rho_{mi} \int_0^l \frac{p(y) - p_i}{K_m} W(y)dy \tag{4.110}$$

Substituting (4.105), (4.106) and (4.110) into (4.103) yields

$$V_{chamber}\rho_m + \rho_{mi} V_{dike} + \rho_{mi} \int_0^l \frac{p(y) - p_i}{K_m} W(y)dy = V_i \rho_{mi} \tag{4.111}$$

and (4.104), (4.111) give

$$V_{chamber}\left[1 + \frac{p(0) - p_i}{K_m}\right] + V_{dike} + \int_0^l \frac{p(y) - p_i}{K_m} W(y)dy = V_i \tag{4.112}$$

The change of the lens volume is defined as

$$\Delta V_{chamber} = V_{chamber} - V_i \tag{4.113}$$

Inserting (4.113) into (4.112) yields

$$\Delta V_{chamber} + V_{dike} = -(V_i + \Delta V_{chamber}) \frac{p(0) - p_i}{K_m} - \int_0^l \frac{p(y) - p_i}{K_m} W(y) dy \qquad (4.114)$$

where the last term ΔV_{dike} can be written as

$$\int_0^l \frac{p(y) - p_i}{K_m} W(y) dy = \frac{p(0) - p_i}{K_m} \int_0^l W(y) dy + \int_0^l \frac{p(y) - p(0)}{K_m} W(y) dy \qquad (4.115)$$

Considering (4.109) and (4.115), we obtain from (4.114)

$$(\Delta V_{chamber} + V_{dike}) \left[1 + \frac{p(0) - p_i}{K_m} \right] = V_i \frac{p_i - p(0)}{K_m} + \int_0^l \frac{p(0) - p(y)}{K_m} W(y) dy \qquad (4.116)$$

where

$$p(0) - p(y) = g \int_0^y \rho_m(y) dy \qquad (4.117)$$

or, (4.104), recalling

$$p(0) - p(y) = \rho_{mi} g \int_0^y \left[1 + \frac{p(y) - p_i}{K_m} \right] dy \qquad (4.118)$$

Differentiating (4.118) with respect to y yields the first order differential equation

$$-p'(y) = \rho_{mi} g \left[1 + \frac{p(y) - p_i}{K_m} \right] \qquad (4.119)$$

for $p(y)$, which has the solution

$$1 + \frac{p(y) - p_i}{K_m} = Ce^{-\frac{\rho_{mi} g y}{K_m}} \qquad (4.120)$$

where the constant C

$$C = 1 + \frac{p(0) - p_i}{K_m} \tag{4.121}$$

is obtained by substituting $y = 0$ into (4.120).

With (4.121), (4.120) becomes

$$\frac{p(0) - p(y)}{K_m} = \left[1 - \frac{p_i - p(0)}{K_m}\right]\left[1 - e^{-\frac{\rho_{mi} g y}{K_m}}\right] \tag{4.122}$$

and we further assume that the following condition is satisfied:

$$\frac{\rho_{mi} g l}{K_m} << 1 \tag{4.123}$$

This condition simply means that the magma bulk modulus is much greater than the pressure generated by the weight of the magma in the dike. For the MOR conditions, (4.123) is satisfied with great confidence. Then,

$$e^{-\frac{\rho_{mi} g y}{K_m}} = 1 - \frac{\rho_{mi} g y}{K_m} + \ldots \tag{4.124}$$

with a sufficient accuracy and (4.122) can be written as

$$p(0) - p(y) = \rho_{mi} g y\left[1 - \frac{p_i - p(0)}{K_m}\right] \qquad \left(\frac{\rho_{mi} g l}{K_m} << 1\right) \tag{4.125}$$

Because we used a linear pressure gradient while decomposing the problems in section 4.3.2, we can only employ the dependence (4.125) rather than (4.122), which is not linear. Substituting (4.122) into (4.116), we obtain

$$\left[\Delta V_{chamber} + \int_0^l e^{-\frac{\rho_{mi} g y}{K_m}} W(y) dy\right]\left[1 - \frac{p_i - p(0)}{K_m}\right] = V_i \frac{p_i - p(0)}{K_m} \tag{4.126}$$

and, if taking (4.123) into account, (4.126) can be simplified as

$$\left[\Delta V_{chamber} + V_{dike} - \frac{\rho_{mi} g}{K_m}\int_0^l yW(y)dy\right]\left[1 - \frac{p_i - p(0)}{K_m}\right] = V_i \frac{p_i - p(0)}{K_m}$$

$$\left(\frac{\rho_{mi} gl}{K_m} << 1\right) \qquad (4.127)$$

We further assume that

$$\frac{p_i - p(0)}{K_m} << 1 \qquad (4.128)$$

which means that the pressure change in the magma chamber is much smaller than the magma bulk modulus. Considering condition (4.128), (4.125) and (4.127) can be written as

$$p(0) - p(y) = \rho_{mi} gy \qquad (4.129)$$

and

$$\Delta V_{chamber} + V_{dike} - \frac{\rho_{mi} g}{K_m}\int_0^l yW(y)dy = V_i \frac{p_i - p(0)}{K_m} \qquad (4.130)$$

respectively. Since, $0 \le y \le l$ and $W(y) \ge 0$, the estimate

$$\frac{\rho_{mi} g}{K_m}\int_0^l yW(y)dy \le \frac{\rho_{mi} gl}{K_m}\int_0^l W(y)dy = \frac{\rho_{mi} gl}{K_m} V_{dike} \qquad (4.131)$$

is always valid. Therefore, due to (4.123), the third term in (4.130) can be ignored when compared to the second one. Hence, (4.130) becomes

$$\Delta V_{chamber} + V_{dike} = V_i \frac{p_i - p(0)}{K_m} \qquad \left(\frac{\rho_{mi} g l}{K_m} << 1, \frac{p_i - p(0)}{K_m} << 1 \right) \quad (4.132)$$

Expression (4.132) immediately allows us to rewrite equation (4.56), obtained for the case of incompressible magma as

$$p_A f_A(l) + p_B f_B(l) + p_c(0) f_c(l) = (V_0 + \Delta V_i) \frac{p_i - p(0)}{K_m} \frac{E_r}{c^2} \quad (4.133)$$

where

$$V_0 = V_i - \Delta V_i \quad (4.134)$$

is the original volume of the magma lens (at pressure equal to the overburden stress at the lens depth), and ΔV_i is defined by (4.49).

Compared to (4.56), the right hand side in (4.133) is not zero and accounts for the magma compressibility. Also, since V_0 is estimated by

$$V_0 = kbc \qquad (k \sim 4) \quad (4.135)$$

equation (4.133) now depends upon the lens thickness. Substituting (4.57), (4.69) and (4.70) into (4.132), we obtain

$$p(0) = \frac{\sigma_1(0) f_A(l) + [p_i - \sigma_1(0)] f_A(0) + [\rho_m g l + \lambda \sigma_1(l)] f_B(l)}{f_A(l) + f_B(l) + \frac{V_0 + \Delta V_i}{K_m} \frac{E_r}{c^2}} + \\ + \frac{-[\rho_m g l - \lambda \sigma_1(0) + \lambda \sigma_1(l)] f_C(l) + p_i \frac{V_0 + \Delta V_i}{K_m} \frac{E_r}{c^2}}{f_A(l) + f_B(l) + \frac{V_0 + \Delta V_i}{K_m} \frac{E_r}{c^2}} \quad (4.136)$$

Figures 4.54 and 4.55 show the normalized SIF (K_I/K_{Ic}), the normalized pressure in the magma lens ($p(0)/p_i$), the normalized dike volume (V_{dike}/V_i), and the dike opening

at the base for the dike propagating from the lens center (H = 1 km, $2c$ = 1 km) and from the lens tip (H = 6 km, $2c$ = 1 km), respectively. They are compared to the case where the compressibility of the magma is ignored. The bulk modulus of the magma is assumed to be $K_m = 10^{10}$ Pa [e.g., *Murase and Mcbirney*, 1973; *Genge et al*., 1995]. For both cases, the effect of the compressibility of the magma does not change the results compared to the case of the incompressible magma.

4.7.2 Effect of topography

It was initially assumed that the seafloor is horizontal. Here, we check whether the observed topography of MOR may affect the dike propagation. The axial caldera at EPR is rather small (~ 200 m wide and ~ 15 m deep) [*Fornari et al*., 1998] and, in general, the depth of the ocean floor gradually decreases from the ridge axis to the 10 km off-axis by 200 to 400 m [*Cochran and Buck*, 2001; *Shah and Buck*, 2001], which is the scale of the typical mesh in our numerical simulation (Figure 4.9). Therefore, it is highly unlikely that the topographic effects influence the dike propagation at our scale.

The axial region at the JdFR is much larger and characterized by the 1 – 3 km wide smooth terrain bounded to the east and to the west by the linear ridges that are 100 – 200 m higher [*Carbotte et al*., 2002b; *Canales et al*., 2003]. This is the case we simulated to asses if the dike propagation may change compared to the model of the flat ocean floor.

Figure 4.56 shows the FEM mesh featuring a typical topography at the intermediate spreading ridges. The magma lens is located at the depth of 2.5 km (refer to Table 4.1). Its size is assumed to be 2 km. The same boundary conditions are applied as

in section 4.2.1 and the dikes still propagate nearly vertically (Figure 4.57). Compared to the horizontal seafloor, dike trajectories and SIFs (K_I and K_{II}) normalized by (4.81) are practically indistinguishable (Figure 4.58). Consequently, it appears that the topography of MOR does not affect the dike propagation from the magma lens, not at the global scales.

4.7.3 Time scale of magma crystallization

The crystallization of the magma caused by the hydrothermal cooling leads to the dike propagation from the center of the magma lens. The time scales of the crystallization of the magma lens will be now discussed. First, we estimate the fraction of the crystallized magma corresponding to the dike initiation.

Let us consider

$$p = p_0 - \Delta p \tag{4.137}$$

where p_0 is the original pressure in the magma lens and Δp is the pressure drop as a result of magma crystallization. Also let

$$\varepsilon = \frac{\Delta M}{M_0} \tag{4.138}$$

be the fraction of crystallized magma. Here

$$M_0 = V_0 \rho_{m0} \tag{4.139}$$

is the original mass of the magma, ρ_{m0} is the magma density at $p = p_0$, V_0 is the cross sectional area of the magma chamber (i.e., the original magma volume).

We assume

$$\rho_{r0} > \rho_{m0} \tag{4.140}$$

and employ

$$\Delta p = p_0 - p \tag{4.141}$$

from (4.137). We also assume linear density-pressure dependence for both rock and magma densities:

$$\rho_r = \rho_{r0}\left(1 - \frac{\Delta p}{K_r}\right) \tag{4.142}$$

$$\rho_m = \rho_{m0}\left(1 - \frac{\Delta p}{K_m}\right) \tag{4.143}$$

where K_r is the rock bulk modulus.

Once the mass ΔM of the magma chamber solidifies, the new volume of the magma chamber becomes

$$V_{chamber} = V_{\substack{liquid \\ magma}} + V_{\substack{frozen \\ magma}} = \frac{M_0 - \Delta M}{\rho_m} + \frac{\Delta M}{\rho_r} \tag{4.144}$$

Substituting (4.138) into (4.144) gives

$$V_{chamber} = \frac{M_0 - \varepsilon M_0}{\rho_m} + \frac{\varepsilon M_0}{\rho_r} = M_0\left[\frac{1-\varepsilon}{\rho_m} + \frac{\varepsilon}{\rho_r}\right] \tag{4.145}$$

and inserting (4.138) and (4.139) into (4.145) yields

$$V_{chamber} = M_0\left[\frac{1-\varepsilon}{\rho_{m0}\left(1 - \Delta p / K_m\right)} + \frac{\varepsilon}{\rho_{r0}\left(1 - \Delta p / K_r\right)}\right] \tag{4.146}$$

Similar to the previous section, it is safe to conclude that

$$\left|\frac{\Delta p}{K_m}\right| << 1 \tag{4.147}$$

$$\left|\frac{\Delta p}{K_r}\right| << 1 \tag{4.148}$$

and (4.146) can be written as

$$V_{chamber} = \frac{M_0}{\rho_{m0}}\left[(1-\varepsilon)\left(1+\frac{\Delta p}{K_m}\right)+\varepsilon\frac{\rho_{m0}}{\rho_{r0}}\left(1+\frac{\Delta p}{K_r}\right)\right] \tag{4.149}$$

which, after the substitution of (4.139) reads

$$V_{chamber} = V_0\left[1+\frac{\Delta p}{K_m}-\varepsilon\left(1+\frac{\Delta p}{K_m}\right)+\varepsilon\frac{\rho_{m0}}{\rho_{r0}}\left(1+\frac{\Delta p}{K_r}\right)\right] \tag{4.150}$$

Therefore, the volume change can be written as

$$\Delta V = V_{chamber} - V_0 = V_0\left[\frac{\Delta p}{K_m}(1-\varepsilon)-\varepsilon\left(1-\frac{\rho_{m0}}{\rho_{r0}}\right)+\varepsilon\frac{\rho_{m0}}{\rho_{r0}}\frac{\Delta p}{K_r}\right] \tag{4.151}$$

or, in the normalized form, as

$$\frac{\Delta V}{V_0} = -\varepsilon\left(1-\frac{\rho_{m0}}{\rho_{r0}}\right)+\frac{\Delta p}{K_m}\left(1-\varepsilon+\varepsilon\frac{\rho_{m0}K_m}{\rho_{r0}K_r}\right) \tag{4.152}$$

This volume is accommodated by the displacements of the chamber sides as shown in Figure 4.59. The maximum side displacement Δb in the chamber center scales as

$$\Delta b \cong \frac{\Delta p}{E_{r1}}(2c) = \frac{2\Delta p}{E_{r1}}c \tag{4.153}$$

The original volume can be approximated by

$$V_0 \cong (2c)(2b) \equiv 4cb \tag{4.154}$$

Therefore, the change of the magma volume as a result of crystallization is

$$\Delta V \cong -4c\Delta b \tag{4.155}$$

and from (4.153) to (4.155), the volume change ratio can be derived as

$$\frac{\Delta V}{V_0} \cong -\frac{1}{4cb}\frac{2\Delta pc}{E_{r1}}4c = -2\frac{c}{b}\frac{\Delta p}{E_{r1}} \tag{4.156}$$

where

$$E_{r1} = \frac{E_r}{1-\nu_r^2} \tag{4.157}$$

Note that in the case of a thin elliptical magma lens, (4.156) is also "accurate" because (4.154) and (4.155) become

$$V_0 = \pi cb \tag{4.158}$$

$$\Delta V = -\pi c\Delta b \tag{4.159}$$

resulting in

$$\frac{\Delta V}{V_0} = -\frac{1}{\pi cb}\pi c\frac{2\Delta p}{E_{r1}}c = -2\frac{c}{b}\frac{\Delta p}{E_{r1}} \tag{4.160}$$

which coincides with (4.156).

Introducing the lens aspect ratio

$$\beta = \frac{b}{c} \tag{4.161}$$

we rewrite (4.160) as

$$\frac{\Delta V}{V_0} = -\frac{2}{\beta}\frac{\Delta p}{E_{r1}} \tag{4.162}$$

Equating (4.152) and (4.162) gives

$$\frac{\Delta p}{K_m} = \frac{\varepsilon\left(1-\frac{\rho_{m0}}{\rho_{r0}}\right)}{\frac{2}{\beta}\frac{K_m}{E_{r1}} + 1 - \varepsilon + \varepsilon\frac{\rho_{m0}K_m}{\rho_{r0}K_r}} \tag{4.163}$$

According to (4.138),

$$0 \le \varepsilon \le 1 \tag{4.164}$$

and typically

$$\frac{\rho_{m0}}{\rho_{r0}} < 1 \tag{4.165}$$

$$\frac{K_m}{K_r} \le 1 \tag{4.166}$$

Because for a thin magma lens,

$$\beta << 1 \tag{4.167}$$

the main term in the denominator of (4.163) is $2K_m/(\beta E_{r1})$. Since

$$E_{r1} \sim K_r \tag{4.168}$$

substituting (4.164)-(4.167) into (4.163) gives

$$\frac{\Delta p}{K_m} = \frac{\beta\varepsilon}{2}\left(1-\frac{\rho_{m0}}{\rho_{r0}}\right)\frac{E_{r1}}{K_m} \tag{4.169}$$

and taking (4.147) into consideration yields

$$\frac{\beta\varepsilon}{2}\left(1-\frac{\rho_{m0}}{\rho_{r0}}\right)\frac{E_{r1}}{K_m} << 1 \tag{4.170}$$

which is satisfied given (4.164) to (4.168).

Now, the condition for dike initiation from the center of the magma lens can be obtained by substituting (4.137) into (4.14):

$$p_0 - \Delta p \le p_i = \sigma_1\left(1-\lambda^*\right) - \sigma_t^* \tag{4.171}$$

where

$$\lambda^* = \frac{\lambda}{1+\dfrac{3c^2}{4H^2}},\ \sigma_t^* = \frac{\sigma_t}{1+\dfrac{3c^2}{4H^2}} \tag{4.172}$$

Since the pressure decreases as a result of crystallization,

$$\Delta p \ge p_0 - p_i \tag{4.173}$$

and (4.169) with (4.173) give the condition of dike initiation:

$$\varepsilon \ge \frac{2}{\beta E_{r1}}\frac{p_0 - p_i}{1-\dfrac{\rho_{m0}}{\rho_{r0}}} \tag{4.174}$$

This means that in order to initiate the dike from the center of the magma lens, the fraction of the crystallized magma in the lens should be sufficiently large. The critical fraction is given by

$$\varepsilon_i = \frac{2}{\beta E_{r1}}\frac{p_0 - p_i}{1-\dfrac{\rho_{m0}}{\rho_{r0}}} \tag{4.175}$$

and shown in Figure 4.60 as a function of the depth H of the magma lens assuming $p_0 = \sigma_1$. For example, when $\lambda = 0.36$ and $\beta = 0.1$, $\varepsilon_i = 30\%$ at $H = 2000$ m. This indicates that the about 30% of magma in the lens should crystallize to initiate a dike from the center of the lens at this depth. In general, as the depth of the magma H and the stress ratio λ increase, more magma needs to be crystallized for the dike initiation.

The time scale of the magma crystallization can be estimated from the heat diffusion time scale [e.g., *Carslaw and Jaeger*, 1959]:

$$t \sim \frac{d^2}{a_r} \tag{4.176}$$

where a_r is the thermal diffusivity of the rock. Figure 4.61 shows the time scale (4.176) of magma crystallization for a typical value $a_r = 10^{-6}$ m^2/sec. We can see that it may take several decades to crystallize 50% of the magma in the lens.

In addition, the normalized side displacement of the lens ($\delta = \Delta b/b$) (Figure 4.59) can be calculated at the moment of dike initiation by substituting (4.158) and (4.159) in (4.156):

$$\delta = \frac{\Delta b}{b} = 2\frac{c}{b}\frac{\Delta p}{E_{r1}} \tag{4.177}$$

Figure 4.62 shows the lens side displacement δ as a result of crystallization.

4.8 Summary and conclusions

In many field cases, very little (if any) directly measured data on fracture and material properties is available. An important example of such a weakly constrained case,

involving hydraulic fracturing, is diking beneath the seafloor at mid-oceanic ridges. In this study, it is shown that the conventional scenario of a dike propagating from the center of a magma chamber to the ocean floor is not consistent with conventional fracture mechanics, because the chamber has the shape of a thin lens. Even at such a large scale (i.e., one kilometer or more), the mechanical principles of elastic interaction appear to be applicable. The dikes that initiate from the subsurface magma lens, and the magma lens itself, can be considered as mechanically interacting segments in an elastic half-space bounded by the seafloor.

Model calculations show that dike propagation from a thin axial magma lens beneath the seafloor depends primarily on the pressure magnitude within the magma lens. Excess magma pressure due to magma replenishment results in nearly vertical dike propagation originating from the vicinity of the tips of the lens. In contrast, a deficit of magma pressure stemming from hydrothermal cooling and magma crystallization results in vertical dike propagation from the center of the magma lens.

The propagating dike withdraws magma from the magma lens, which decreases the lens pressure. Despite this pressure decrease, the tip dike does propagate to the seafloor, because the dike-seafloor interaction is sufficiently strong to compensate for the pressure decrease. In contrast, the central dike does not propagate to the seafloor, because of insufficient dike-seafloor interaction.

Since diking is likely to generate a region of high permeability near its margin, in addition to heat, the ongoing hydrothermal activity becomes localized. Our calculations suggest the possible positions of the propagating dikes. Consequently, comparing the

observed locations of the hydrothermal sites with respect to that of the magma chamber could be useful for constraining the magma lens modeling.

The occurrence of hydrothermal vents near the tips of the magma lens at the Salty Dawg hydrothermal sites of the Juan de Fuca Ridge is consistent with an episode of recent pressurization of the subsurface magma lens and dike propagation from one of its tips. The fact that hydrothermal venting at the East Pacific Rise occurs above the center of the magma lens suggests that rapid hydrothermal cooling and magma crystallization in the lens may be important in controlling the permeability distribution at that site.

As has recently been speculated in the literature, the pressurization of the magma lens may be result from the dikes originating from the underlying, deep magma chambers (also of a lens shape). Our quantitative results support this hypothesis. Furthermore, not only may these dikes pressurize overlying shallow magma lenses, but this may then also lead to the subsequent dike propagation from the tips of these shallow lenses to the seafloor although further detailed modeling is required.

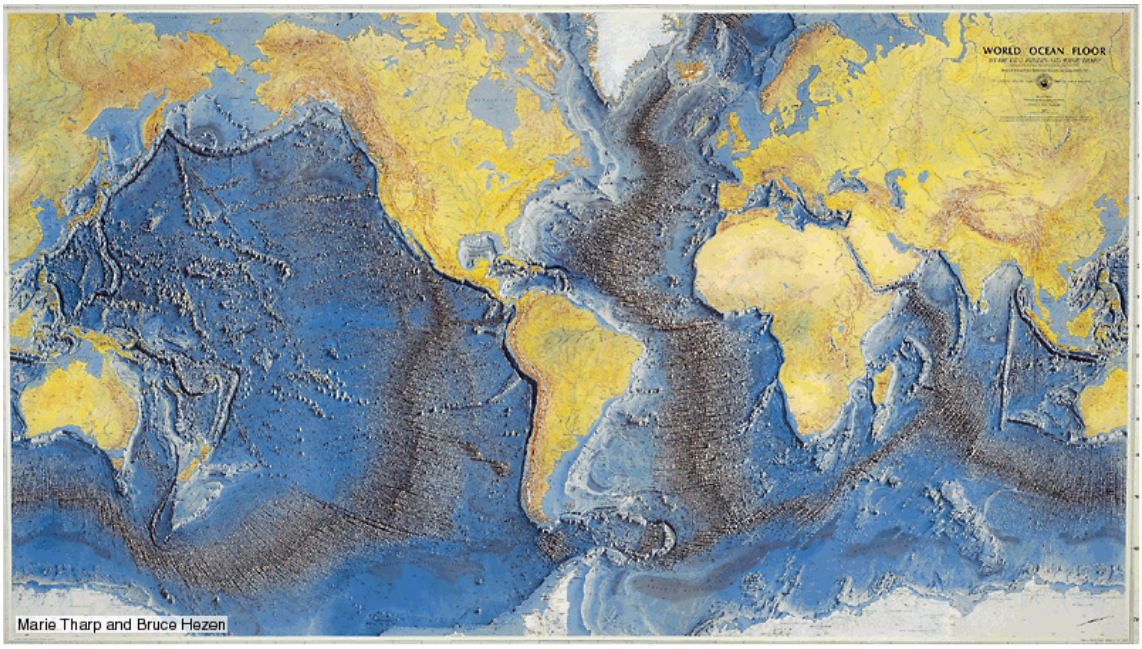

Figure 4.1 The topography of Earth's solid surface [*Heezen and Tharp*, 1977].

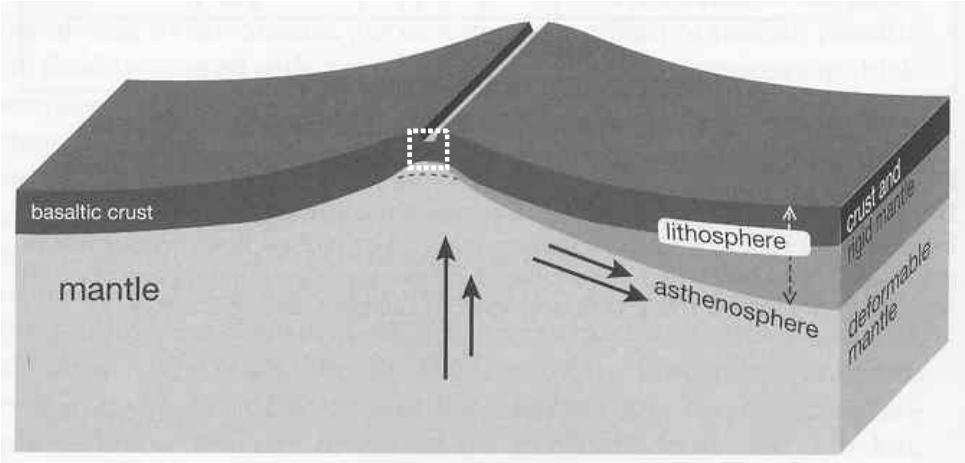

Figure 4.2 Crustal formation at mid-oceanic ridges [*Nicolas*, 1995].

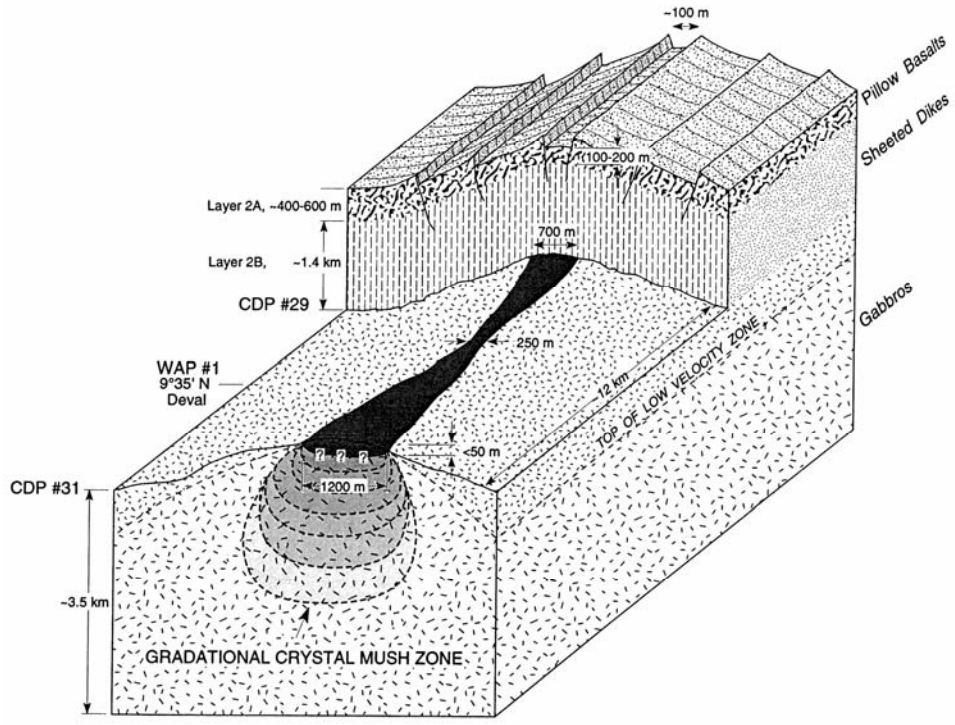

Figure 4.3 Cross-section of a model of the melt lens (black color) model of the axial magma chamber at 9°30'N [*Kent et al*., 1993b].

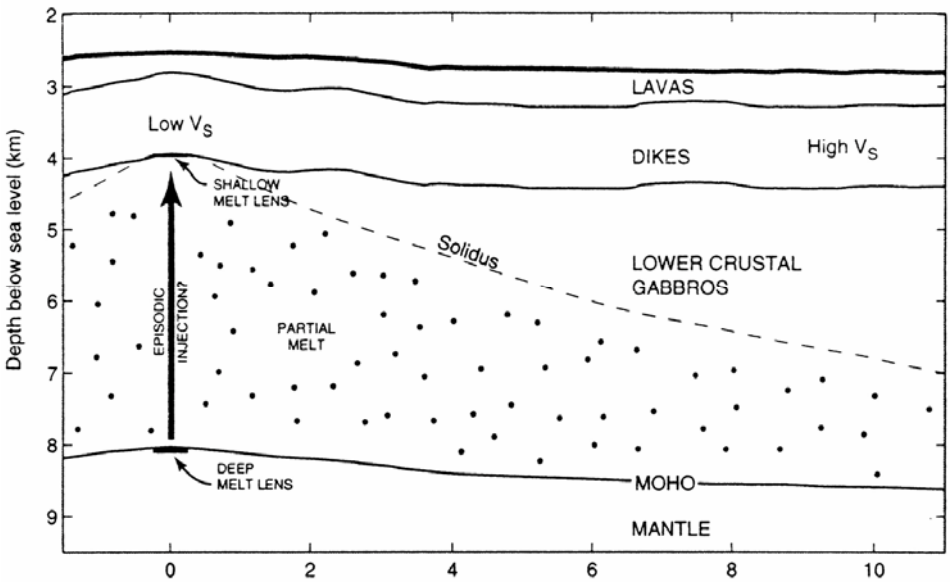

Figure 4.4 Cross-section of a model of two melt lenses of an axial magma chamber at 9°48'N [*Crawford et al*. 1999].

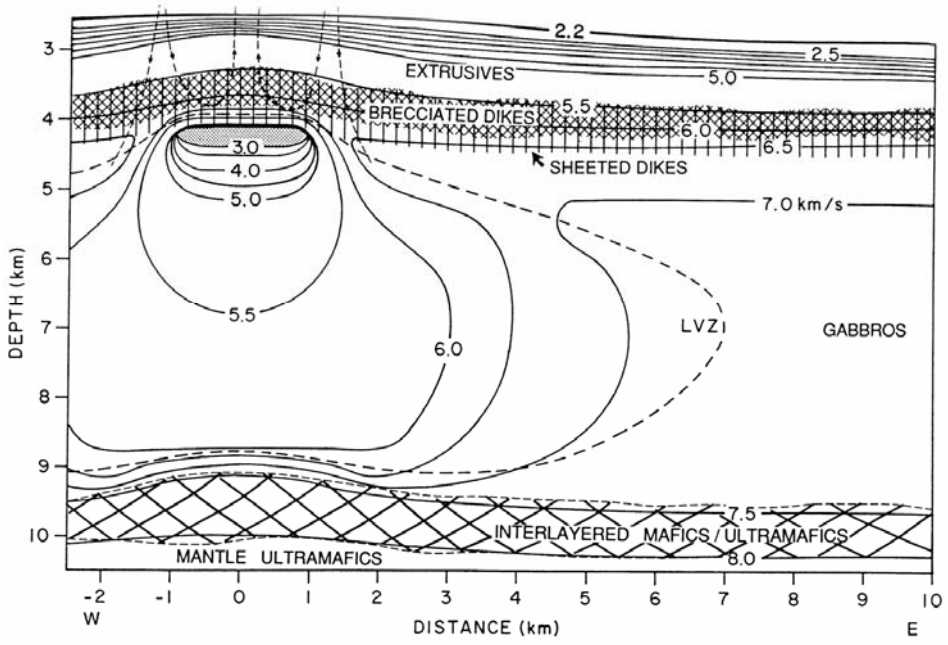

Figure 4.5 Cross-section of a seismic profile of a mid-oceanic ridge [*Vera et al*., 1990].

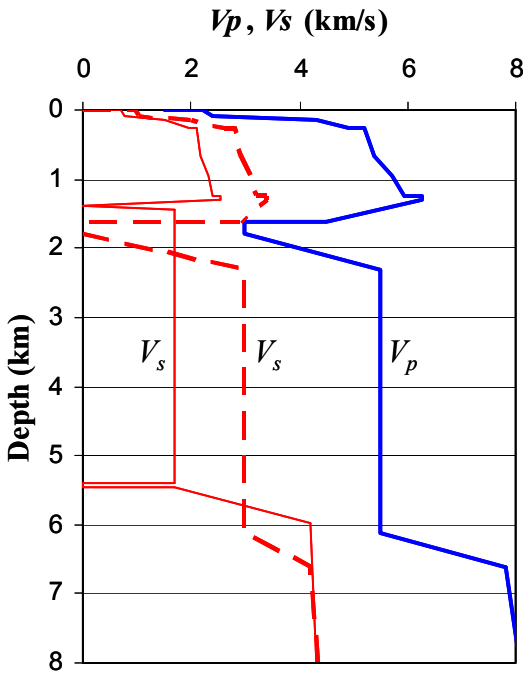

Figure 4.6 *p*-wave (V_p) and *s*-wave velocity (V_s) profiles. Thick solid line and dashed line indicate V_p and V_s, respectively, at 9°35'N by *Vera et al*. [1990]. Thin solid line indicates V_s at 9°48'N as inferred by compliance measurements [*Crawford et al*., 1999].

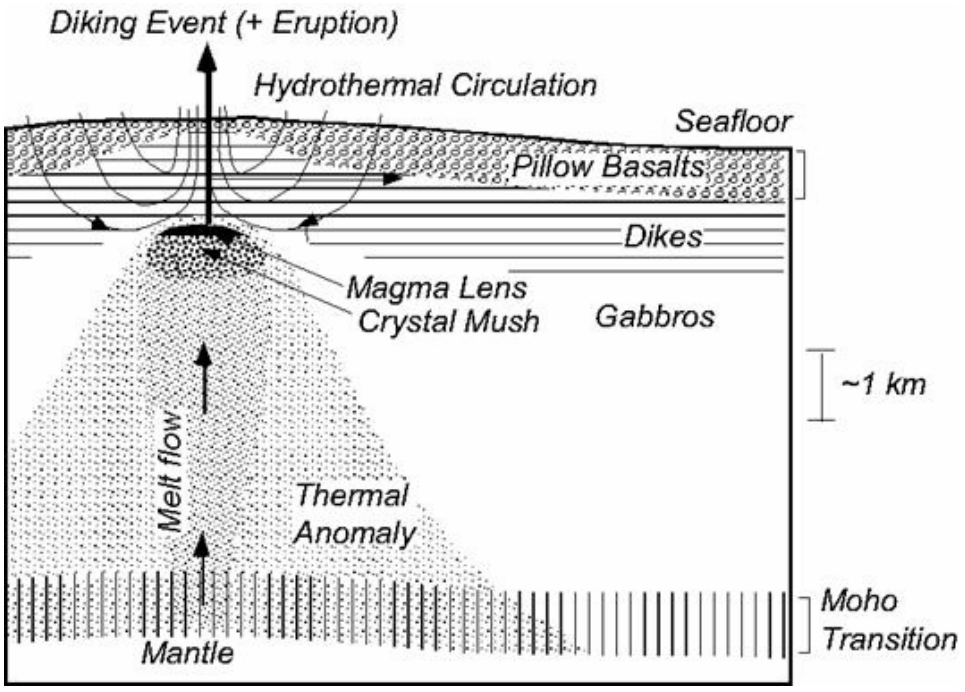

(a)

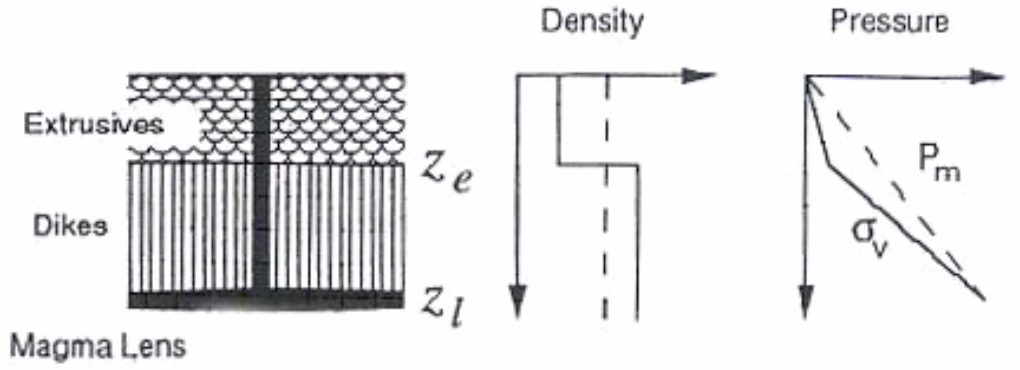

(b)

Figure 4.7 Conventional scenario of diking event [*Wilcock*, 2001] and (b) the dike accommodating the spreading of the ocean plates [*Buck et al*., 1997].

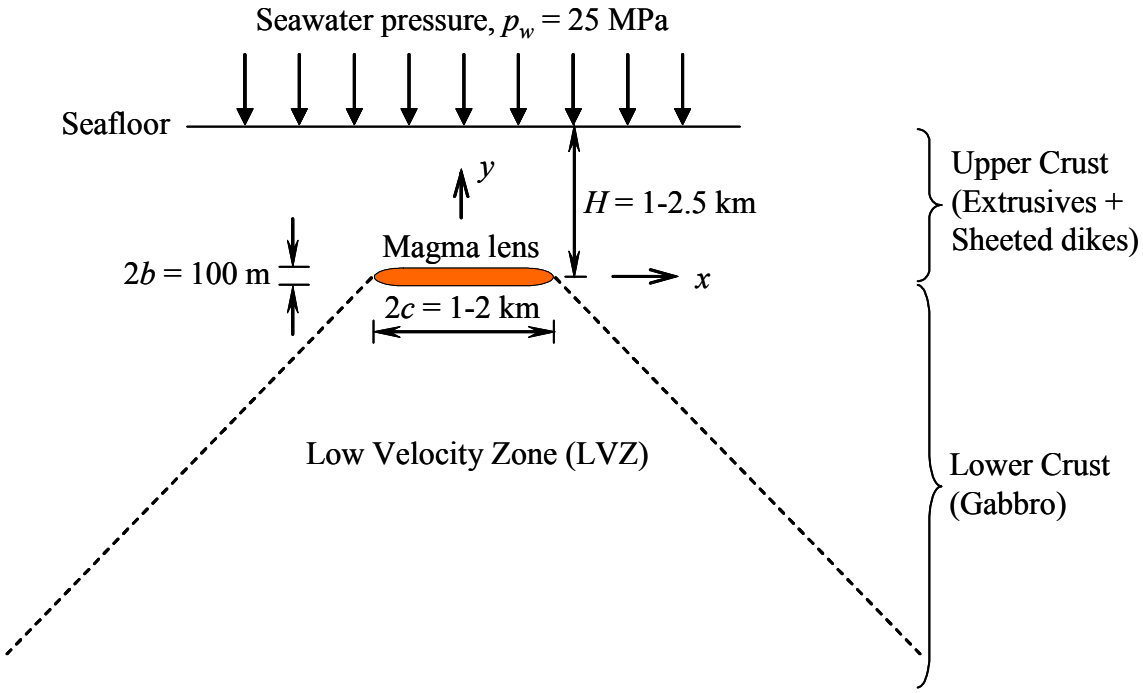

Figure 4.8 Cross-section of a magma chamber at a mid-oceanic ridge.

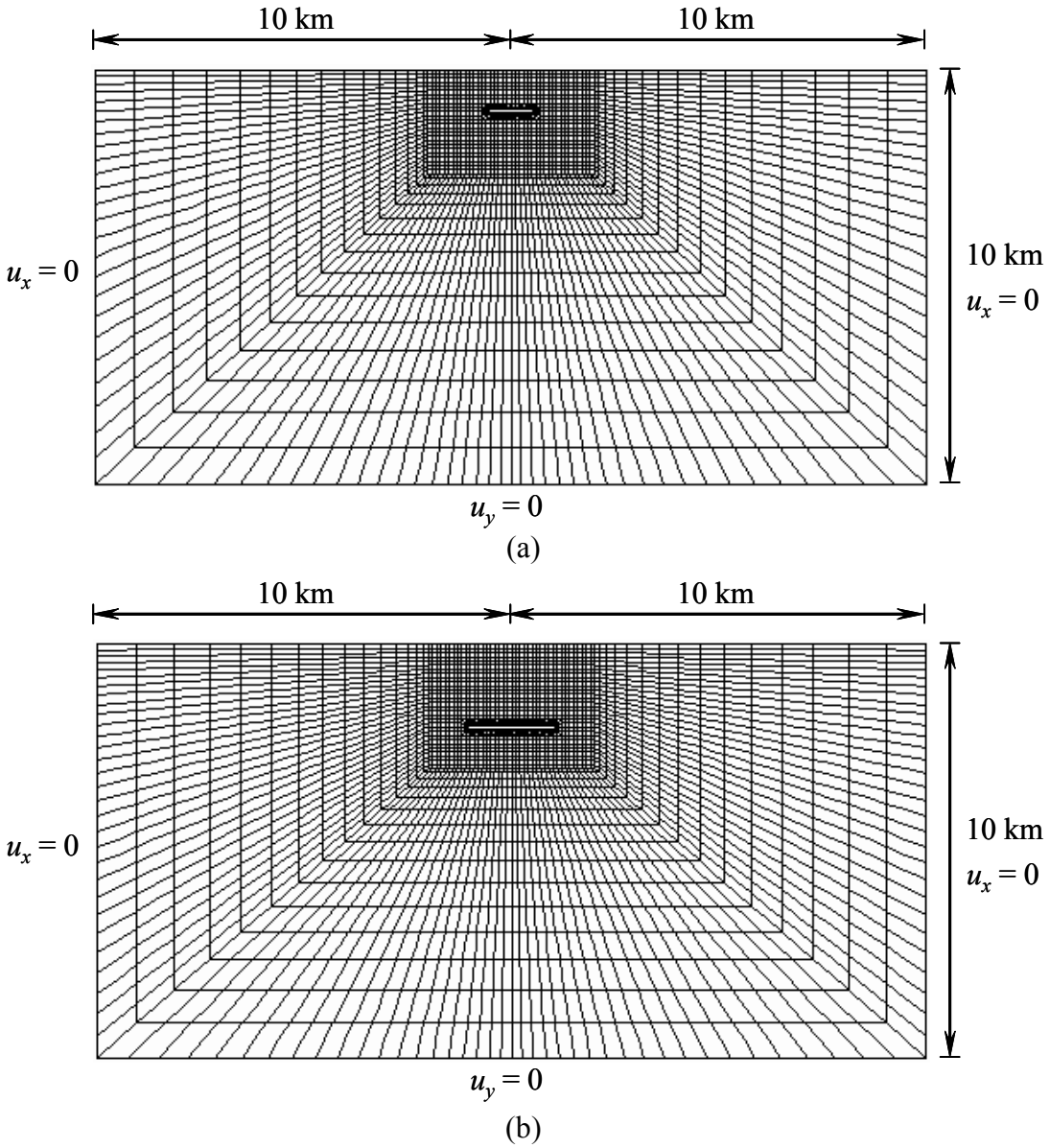

Figure 4.9 Example of FRANC2D mesh for the numerical model of a magma lens: (a) melt lens with a width of $2c$ = 1 km at the depth of H = 1 km, and (b) melt lens with a width of a $2c$ = 2 km at the depth of H = 2 km.

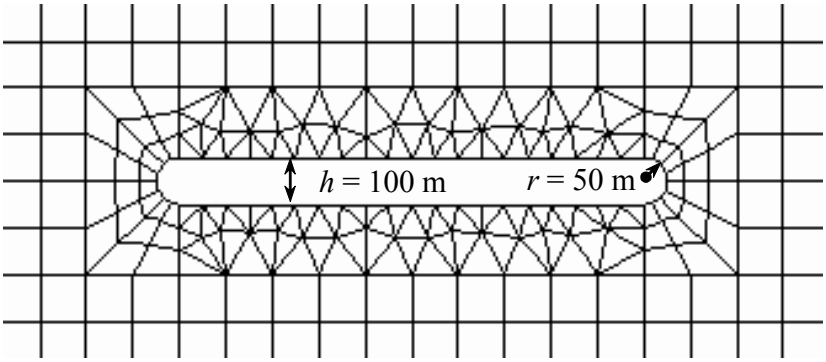

(a)

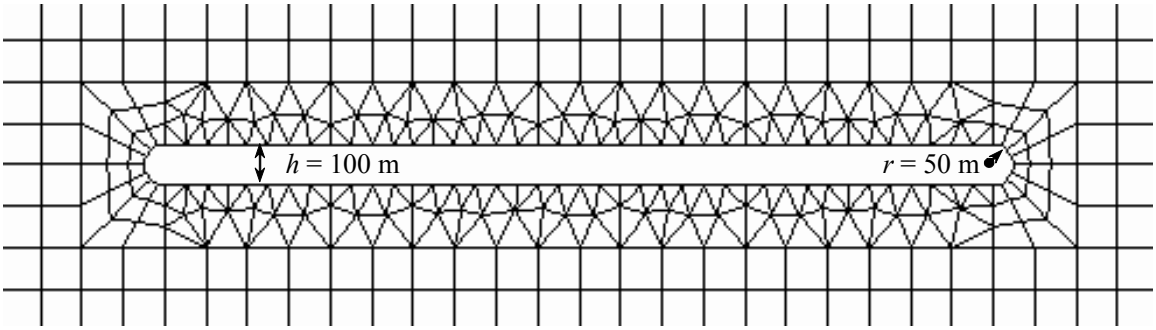

(b)

Figure 4.10 Magnified mesh of the magma lens area in FRANC2D: (a) melt lens with a width of $2c$ = 1 km, and (b) melt lens with a width of $2c$ = 2 km.

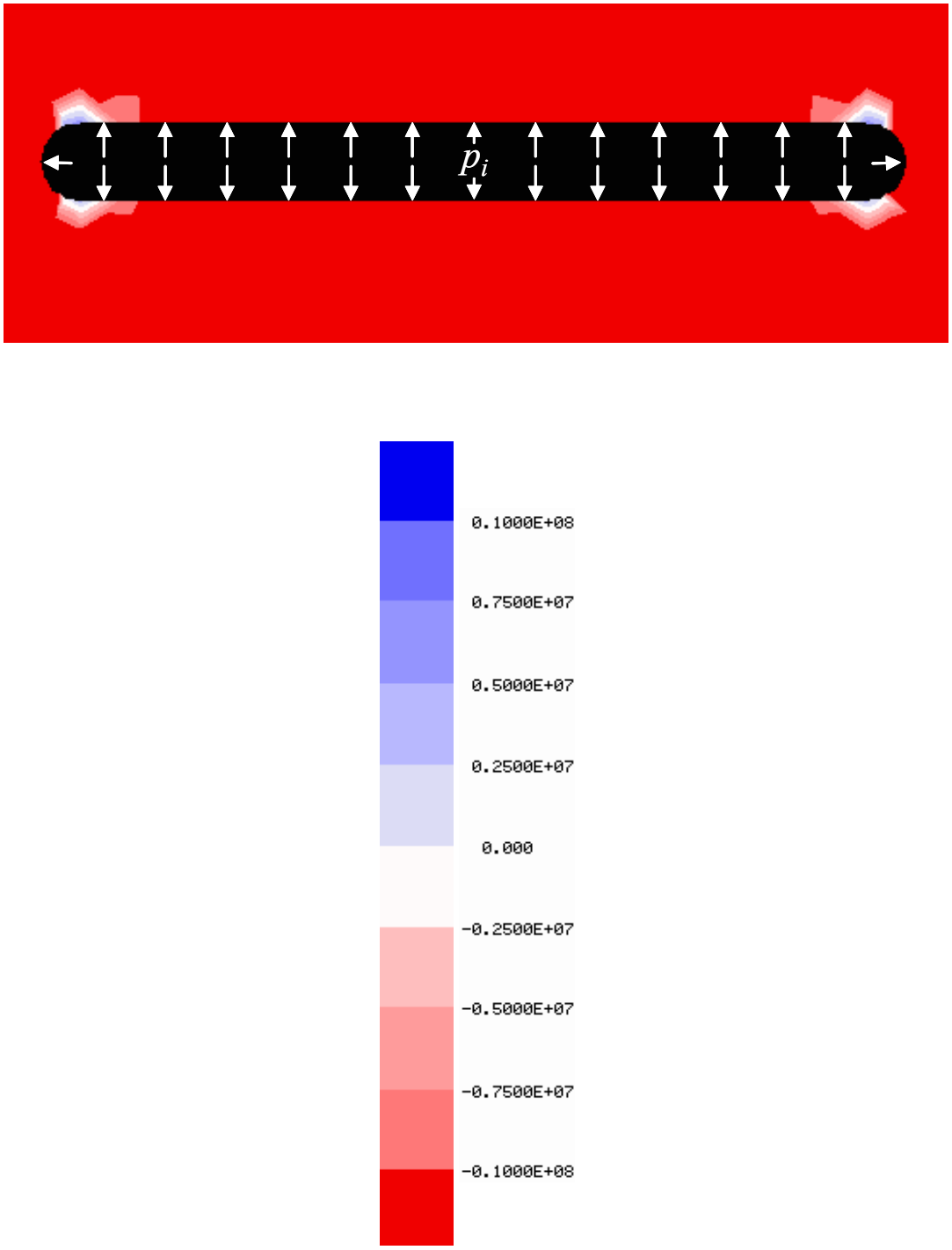

Figure 4.11 Contour of major principal stress (Pa) in the vicinity of magma lens in homogeneous crust in FRANC2D (H = 1 km, $2c$ = 1 km, and p_i/σ_z = 1.01).

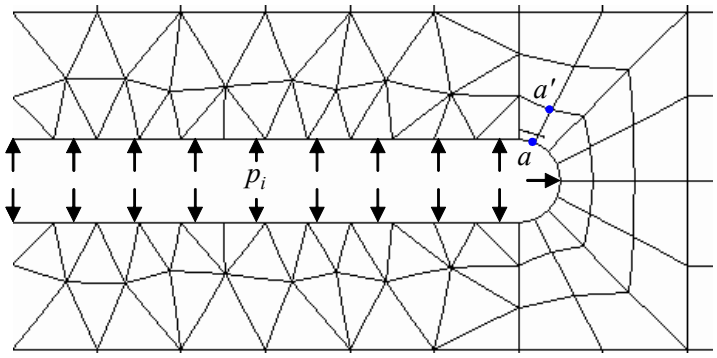

(a)

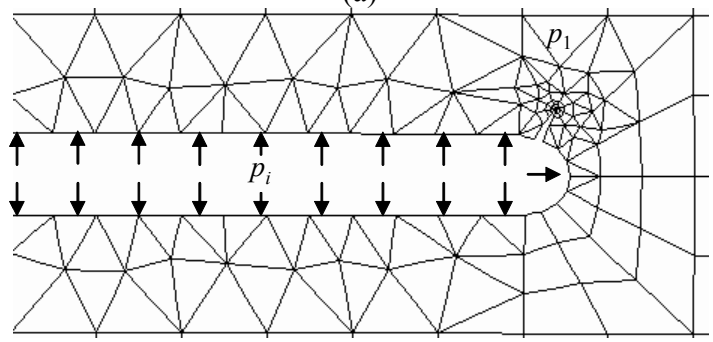

(b)

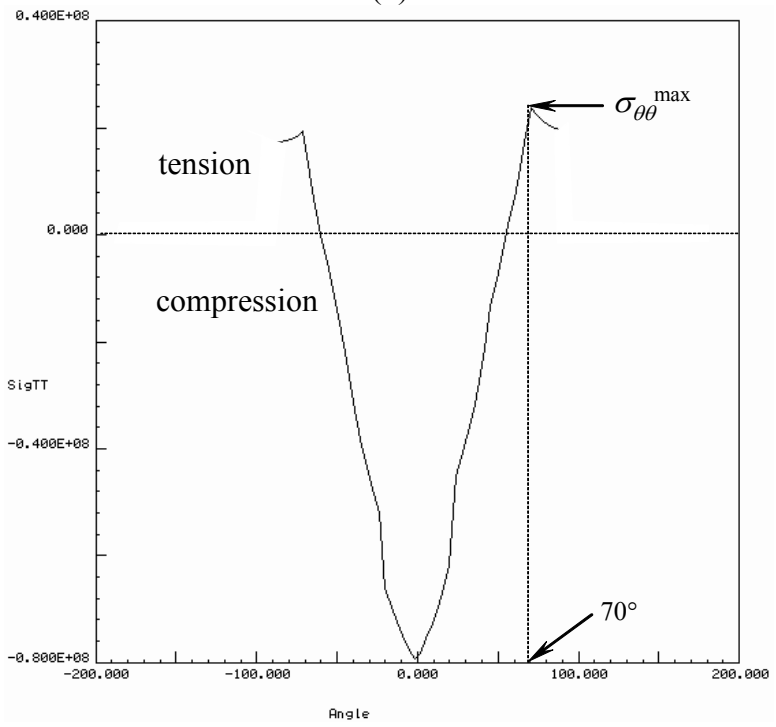

(c)

Figure 4.12 Dike initiation at the tip of a magma lens in a homogeneous crust in FRANC2D (H = 1 km, $2c$ = 1 km, and $p_i/\sigma_1(0)$ = 1.01): (a) tensile stress bar near the tip of the magma lens by internal pressure p_i, (b) tangential stress ($\sigma_{\theta\theta}$) distribution along the surface of the tip and maximum tangential stress $\sigma_{\theta\theta}^{max}$ = 24 Mpa at 70°, and (c) dike nucleation along $\overline{aa'}$ in (a).

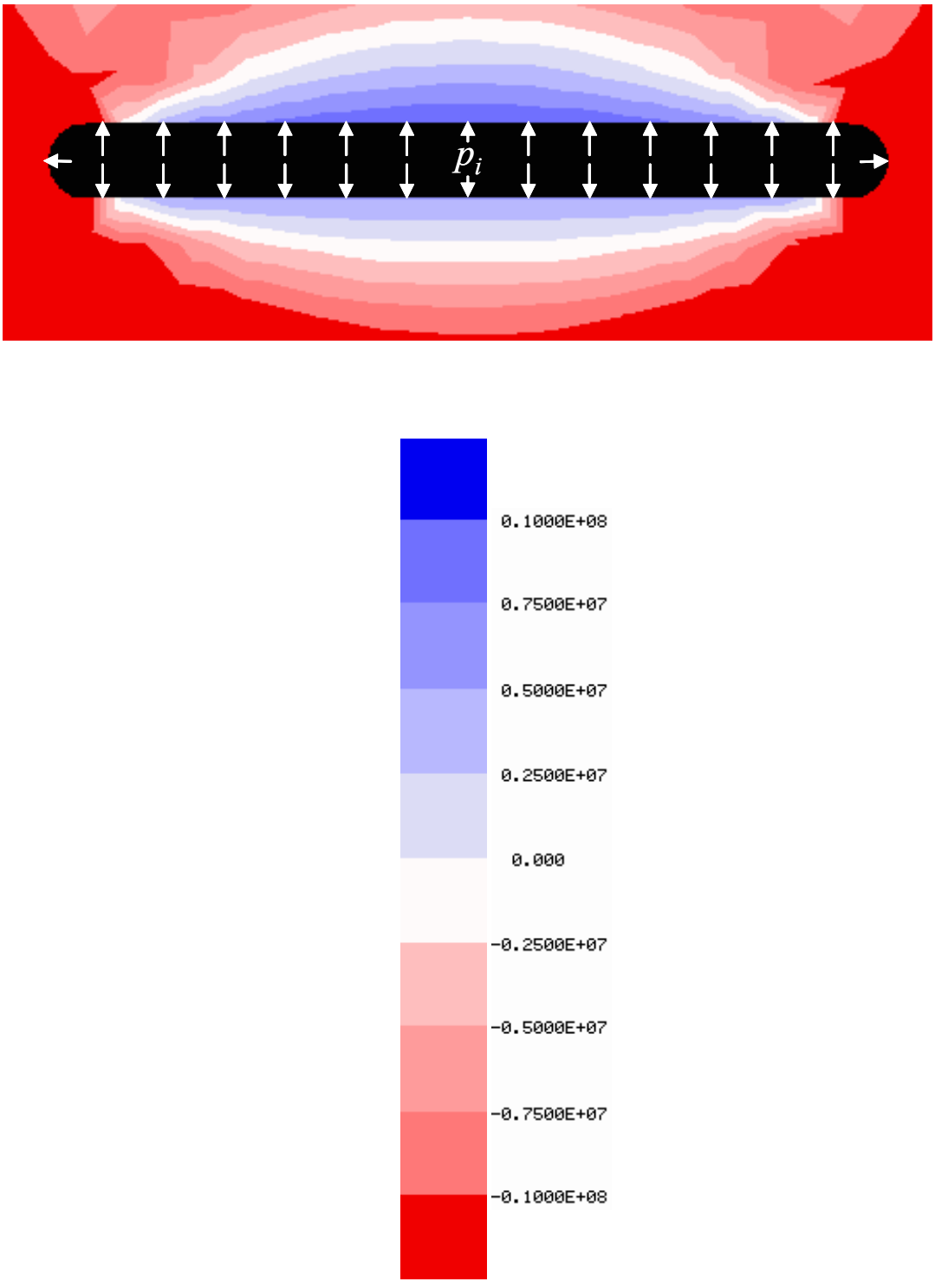

Figure 4.13 Contour of major principal stress (Pa) in the vicinity of a magma lens in a homogeneous crust in FRANC2D (H = 1 km, $2c$ = 1 km, and p_i/σ_z = 0.60).

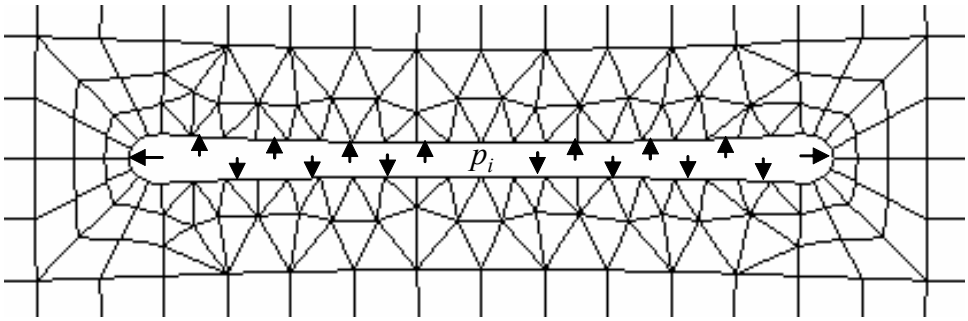

(a)

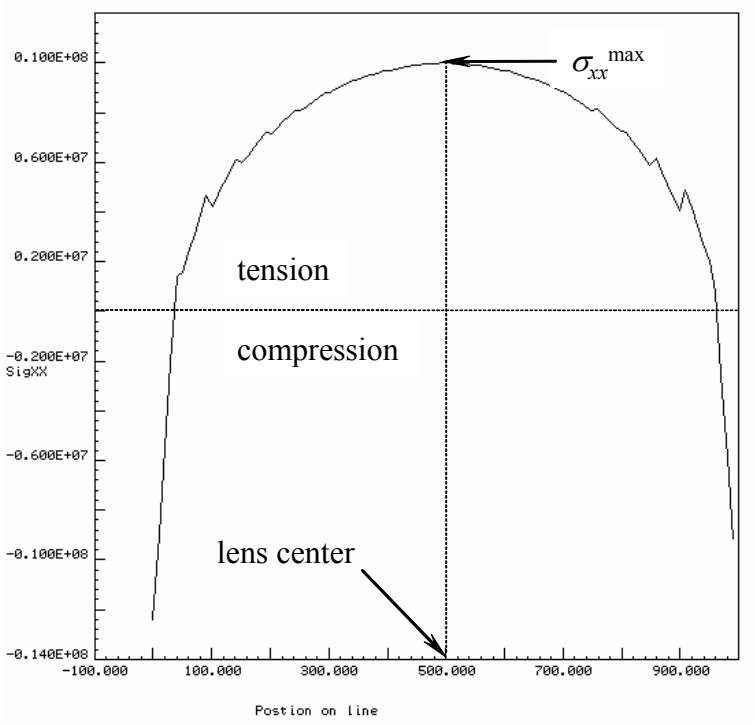

(b)

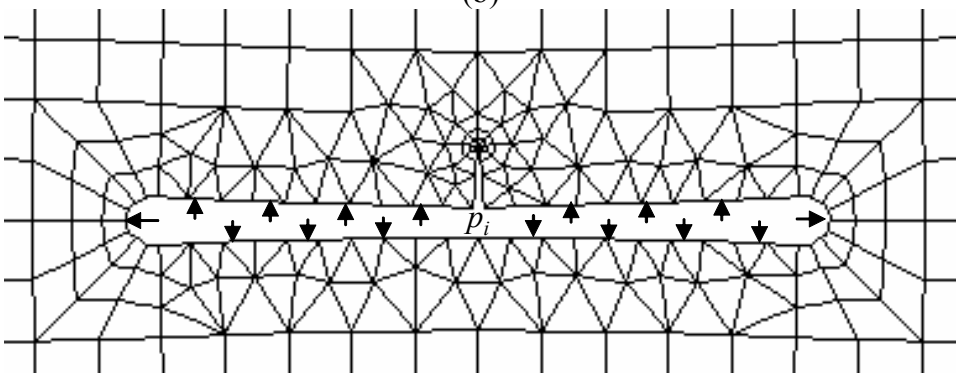

(c)

Figure 4.14 Dike initiation at the center of a magma lens in a homogeneous crust in FRANC2D (H = 1 km, $2c$ = 1 km and $p_i/\sigma_1(0)$ = 0.60): (a) deformation of magma lens caused by pressure decrease inside magma lens, (b) maximum tensile stress σ_{xx}^{max} = 10 MPa at the center of the lens, and (c) dike initiation at the center.

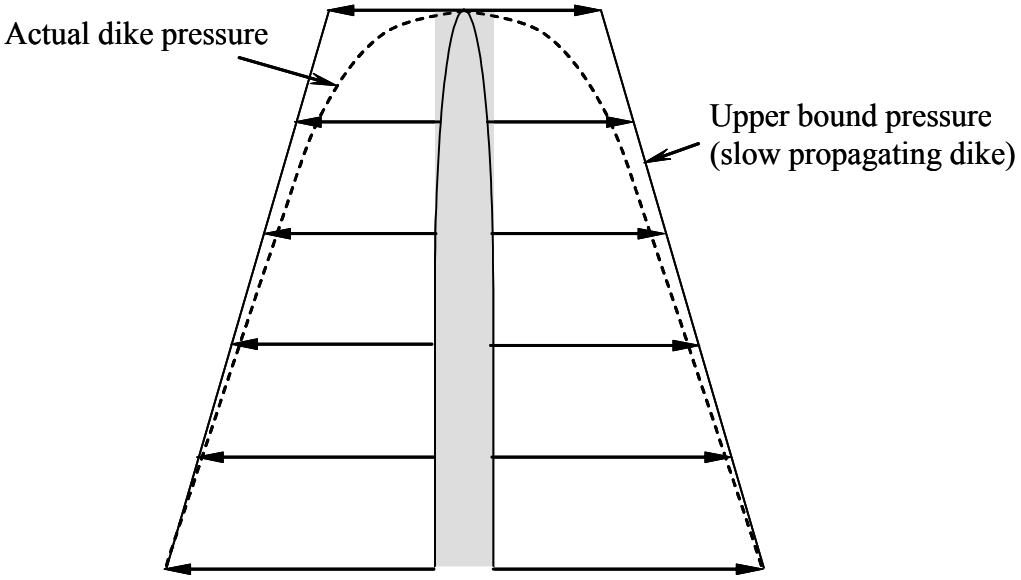

Figure 4.15 Pressure distribution inside a dike.

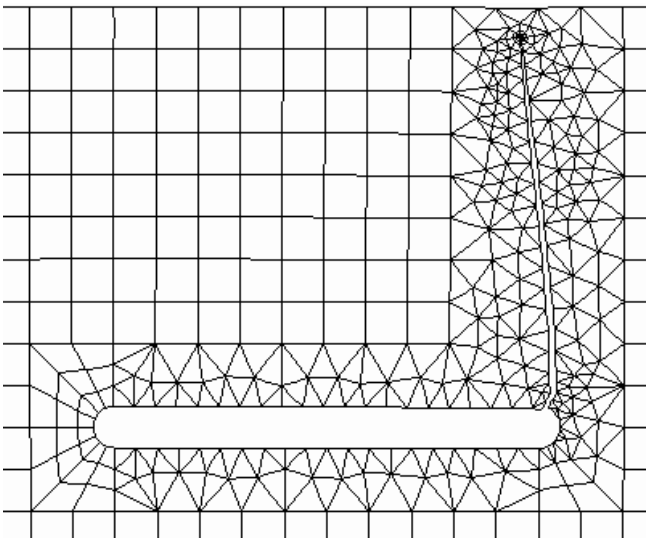

(a)

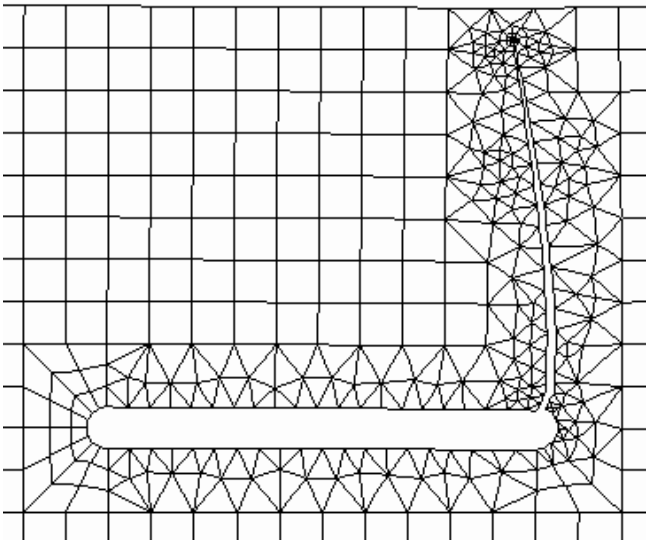

(b)

Figure 4.16 Dike trajectories from the magma lens for the upper bound estimate in FRANC2D ($2c$ = 1 km and H = 1 km, and $p_i/\sigma_1(0)$ = 1.01): (a) homogeneous, and (b) heterogeneous crust.

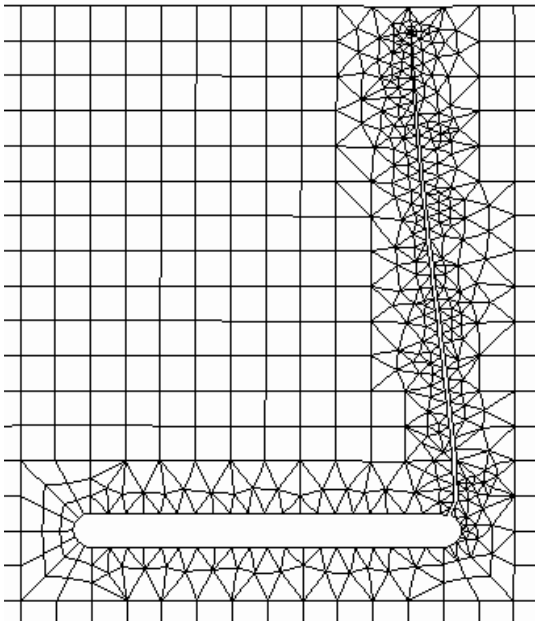

(a)

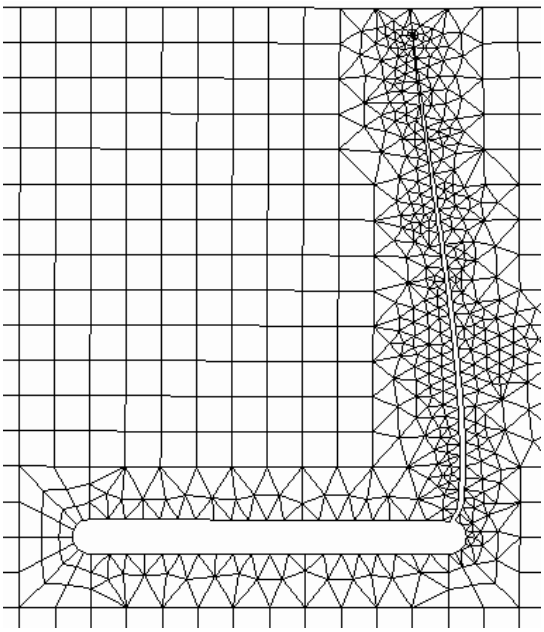

(b)

Figure 4.17 Dike trajectories from the magma chamber for the upper bound estimate in FRANC2D ($2c$ = 1 km, H = 1.5 km, and $p_i/\sigma_1(0)$ = 1.01): (a) homogeneous, and (b) heterogeneous crust.

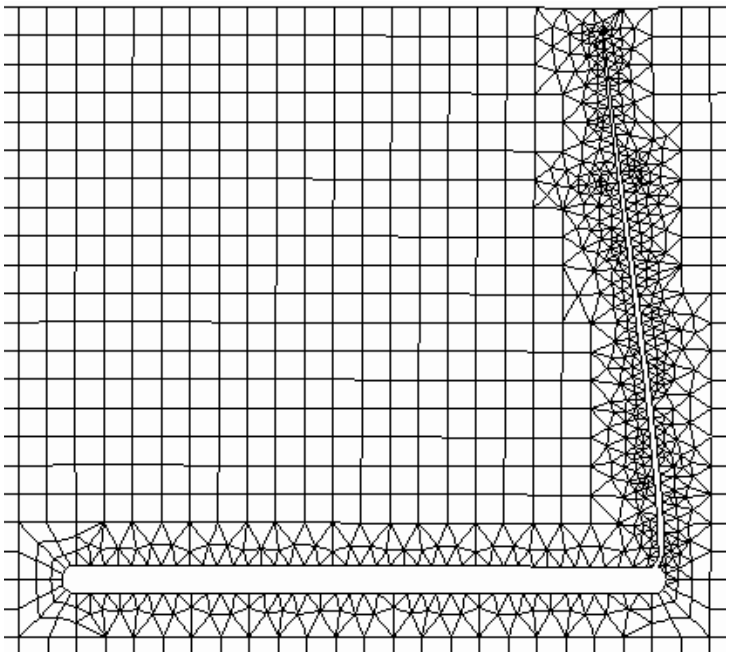

(a)

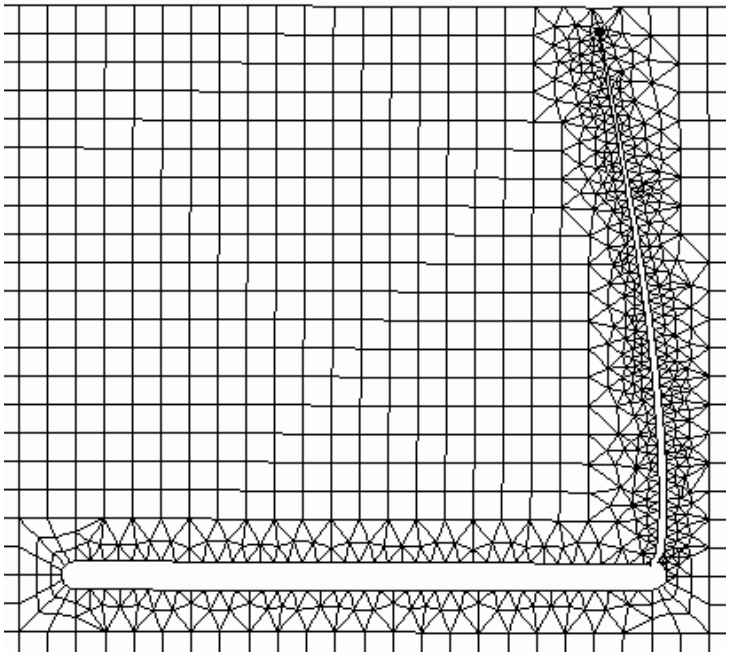

(b)

Figure 4.18 Dike trajectories from the magma chamber for the upper bound estimate in FRANC2D ($2c$ = 2 km, H = 2 km, and $p_i/\sigma_1(0)$ = 1.01): (a) homogeneous, and (b) heterogeneous crust.

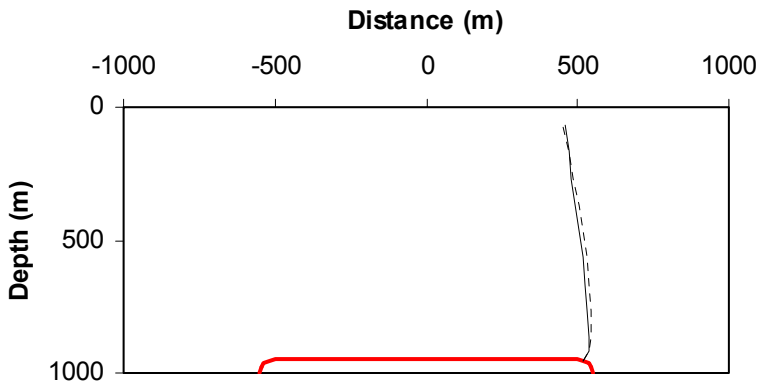

(a)

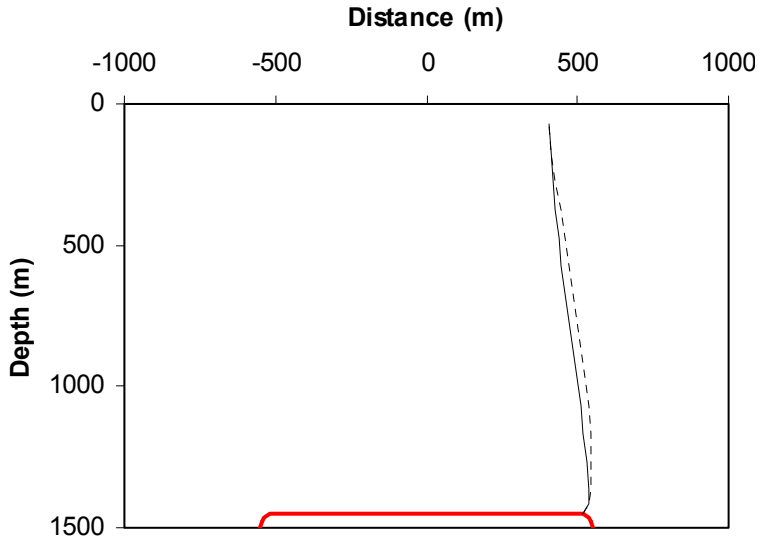

(b)

Figure 4.19 Comparison of dike propagation between homogeneous and heterogeneous crust: (a) $2c$ = 1 km and H = 1 km, (b) $2c$ = 1 km and H = 1.5 km, and (c) $2c$ = 2 km and H = 2 km. Solid line indicates homogeneous crust, and dotted line indicates heterogeneous crust.

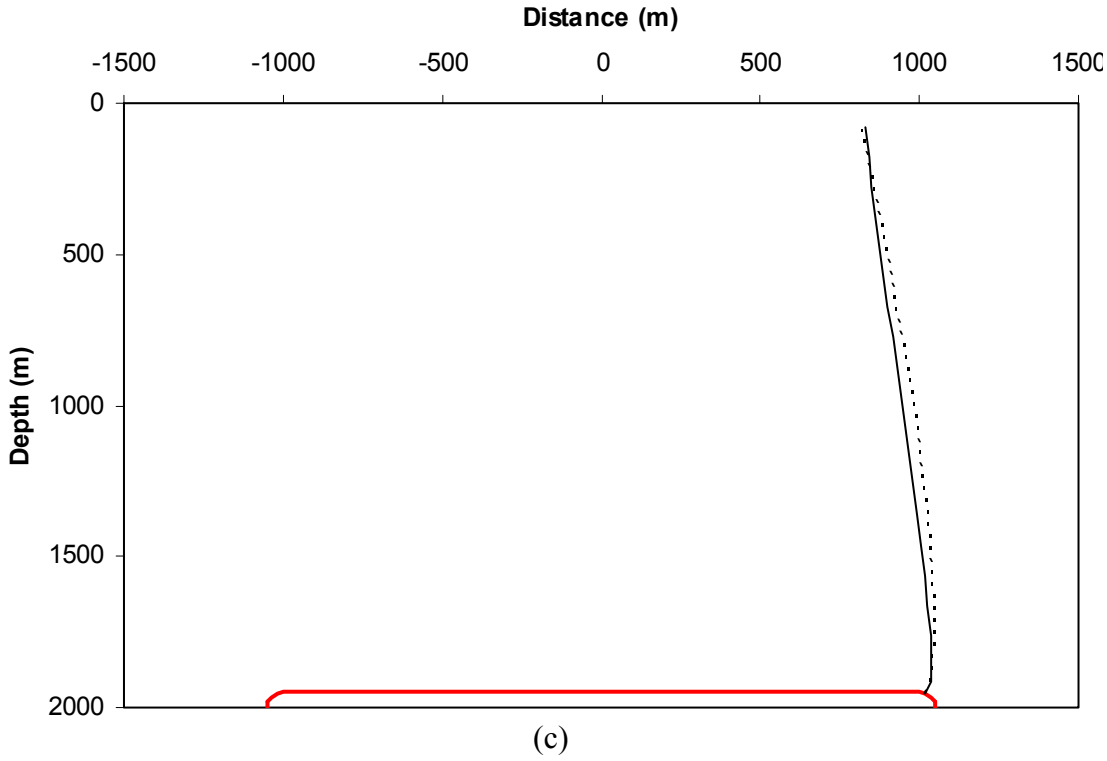

(c)

Figure 4.19 (Continued).

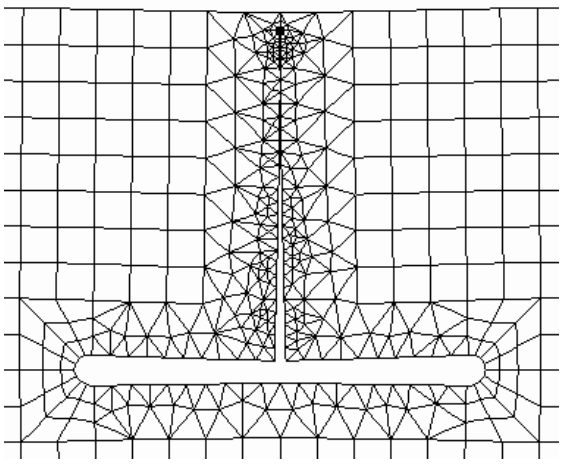

(a)

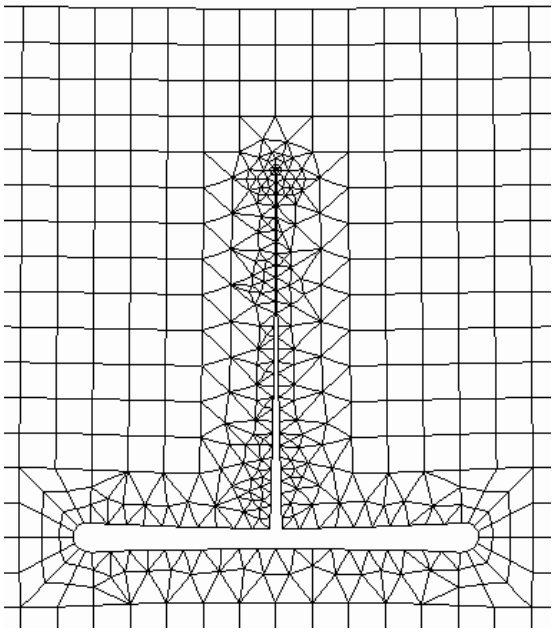

(b)

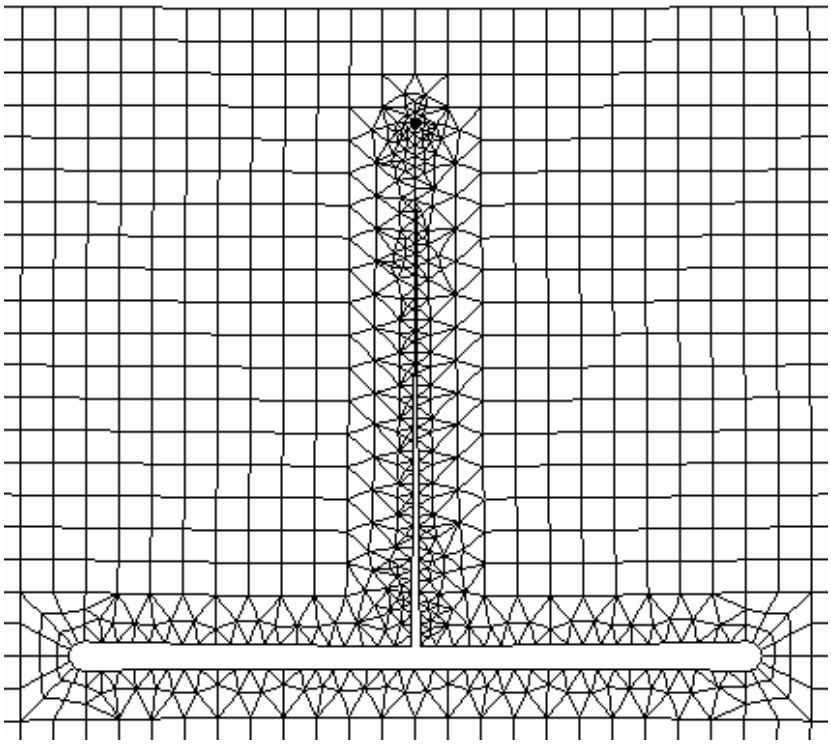

(c)

Figure 4.20 Dike propagation from the center of a magma lens due to magma solidification in a homogeneous crust in FRANC2D: (a) $2c$ = 1 km, H = 1 km and $p_i/\sigma_1(0)$ = 0.60; (b) $2c$ = 1 km, H = 1.5 km and $p_i/\sigma_1(0)$ = 0.55; (c) $2c$ = 2 km, H = 2 km and $p_i/\sigma_1(0)$ = 0.63; and (d) $2c$ = 2 km, H = 1.5 km, and $p_i/\sigma_1(0)$ = 0.68.

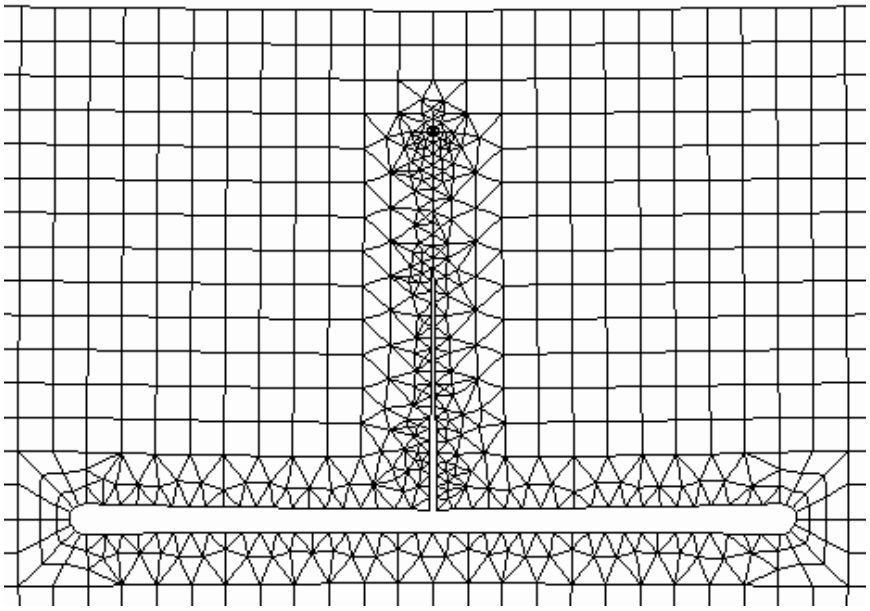

(d)

Figure 4.20 (Continued).

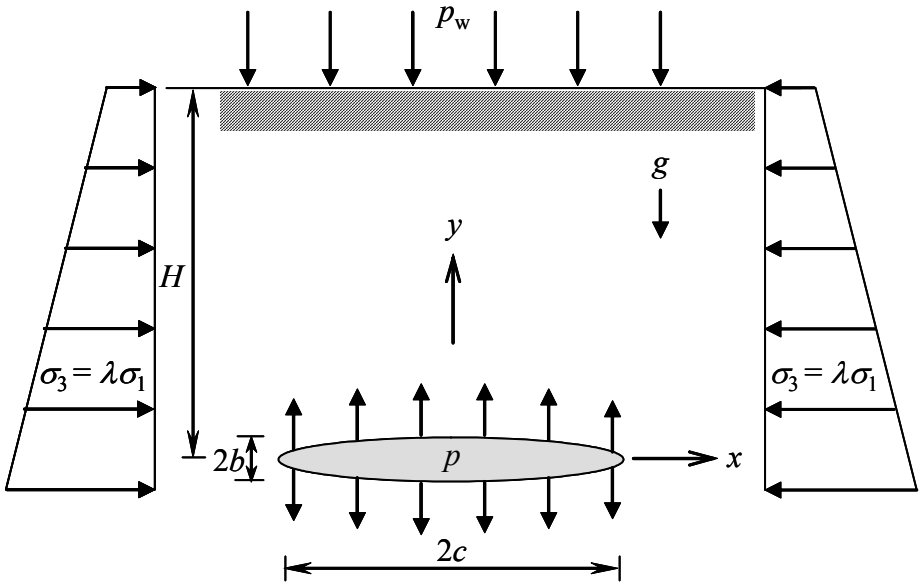

Figure 4.21 A magma lens pressurized by internal pressure p at a mid-oceanic ridge.

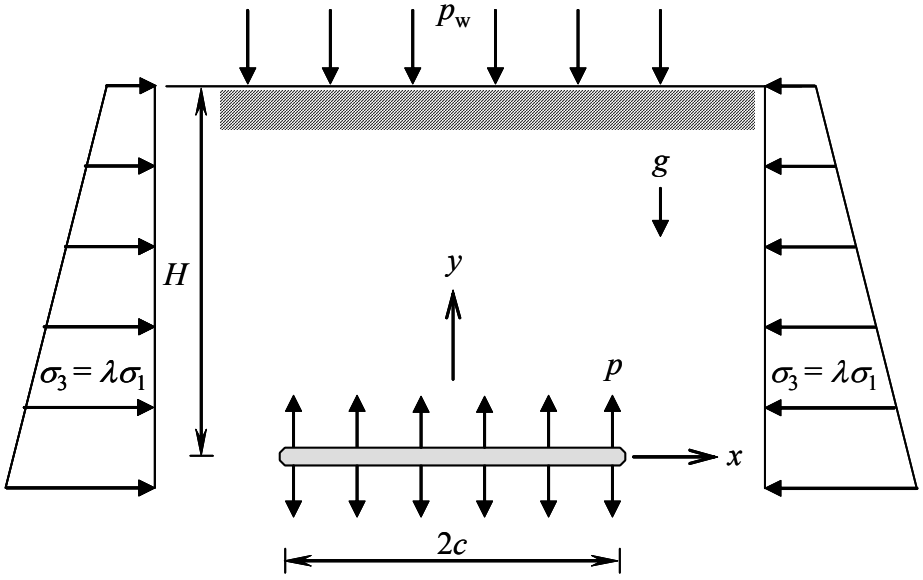

Figure 4.22 Magma lens represented as a fracture.

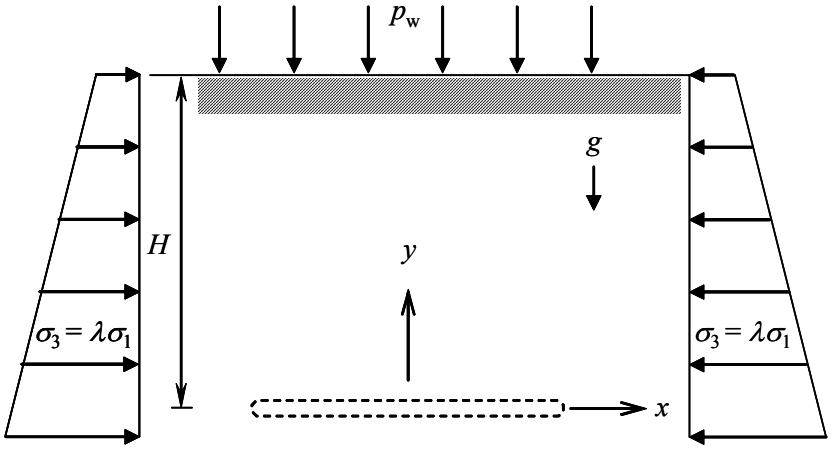

(a)

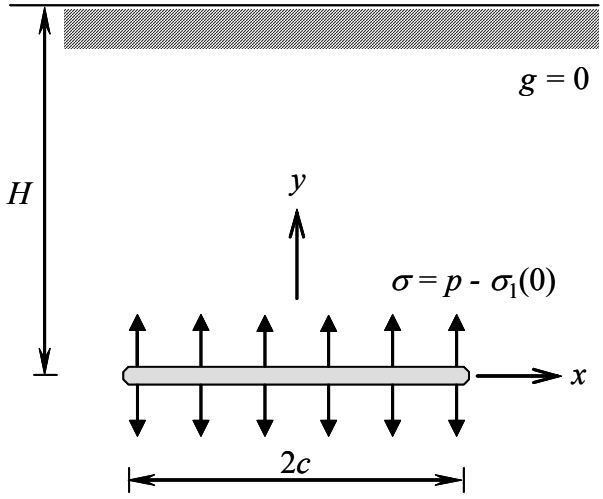

(b)

Figure 4.23 Decomposition of the physical problem: (a) half-space without magma lens, (b) half-space with magma lens but without boundary conditions and without gravity.

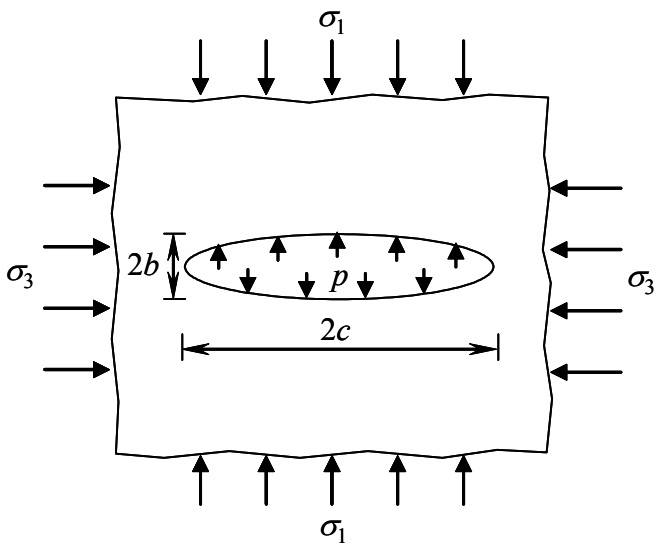

(a)

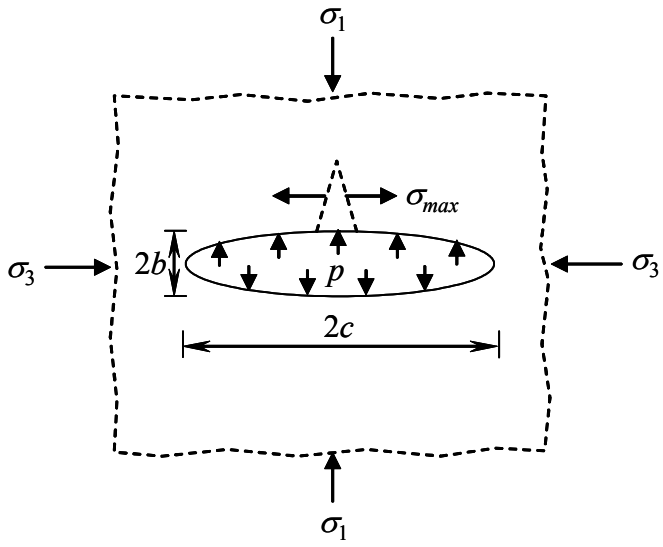

(b)

Figure 4.24 Dike initiation at the center of the magma lens: (a) pressurized magma lens at an infinite plane, and (b) dike initiation by maximum stress, σ_{max} at the center of magma lens.

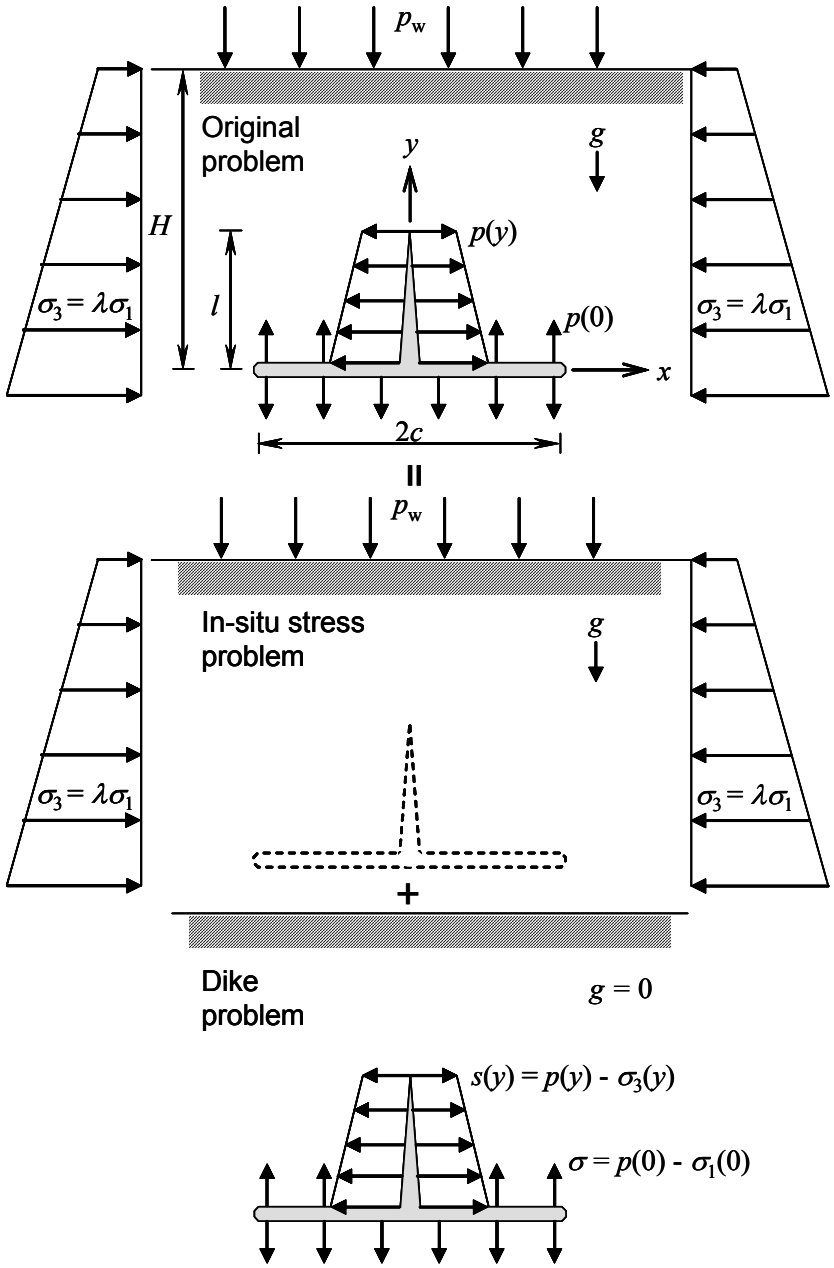

Figure 4.25 Superposition of problem for the dike propagation from the lens center.

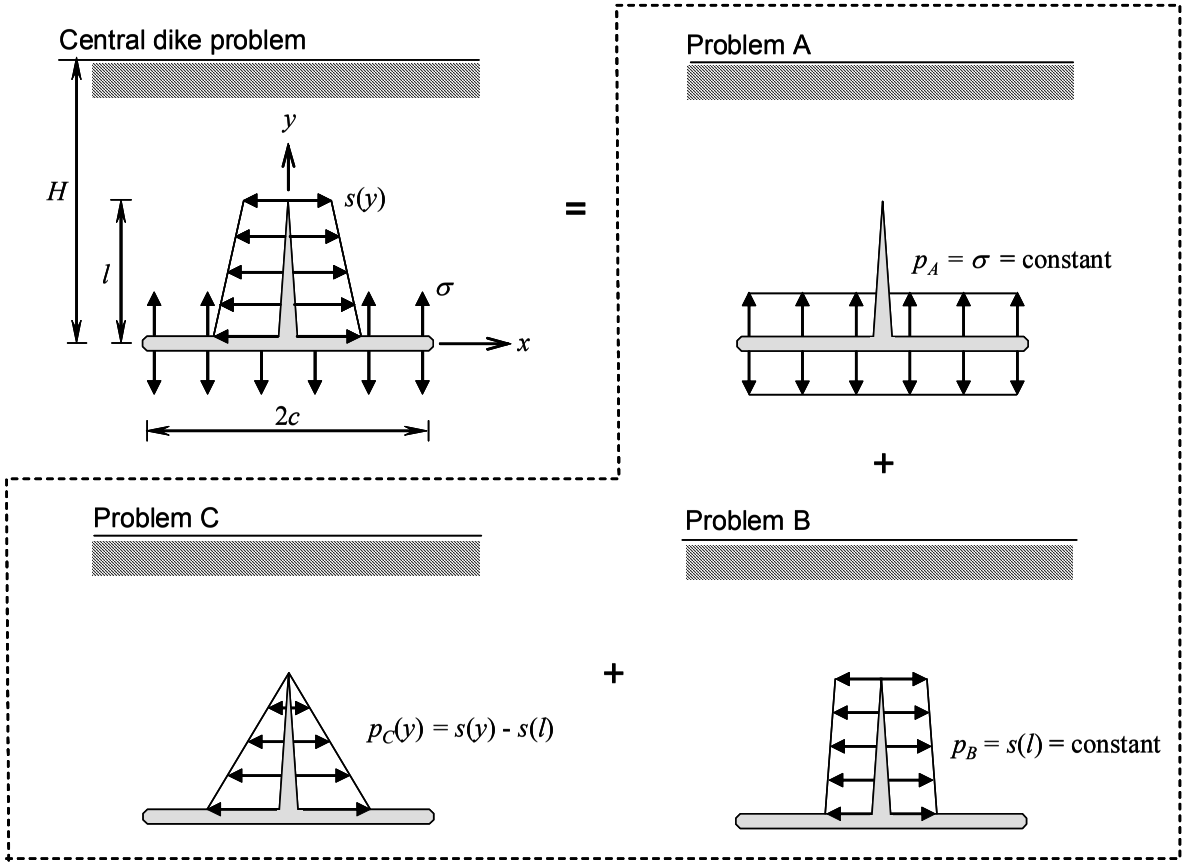

Figure 4.26 Decomposition of the central dike problem into three sub-problems.

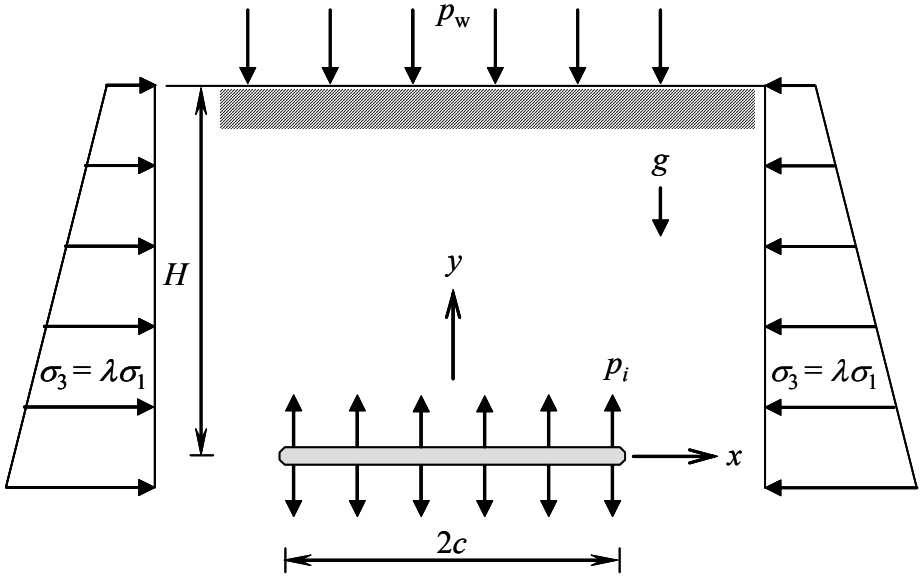

(a)

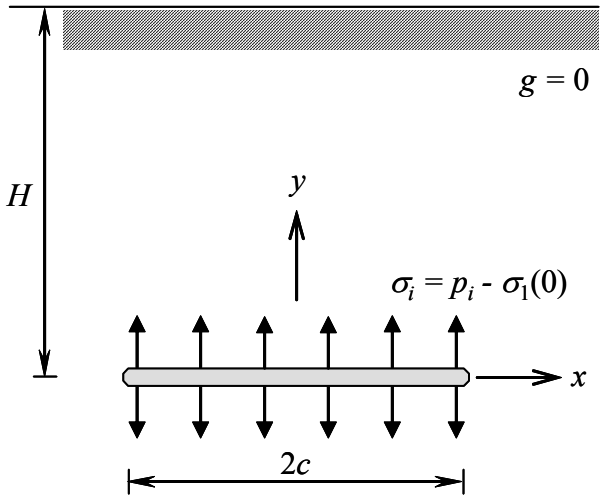

(b)

Figure 4.27 Pressurization by initial pressure p_i: (a) original problem before propagation, and (b) "dike" problem before propagation (refer to Figure 4.25).

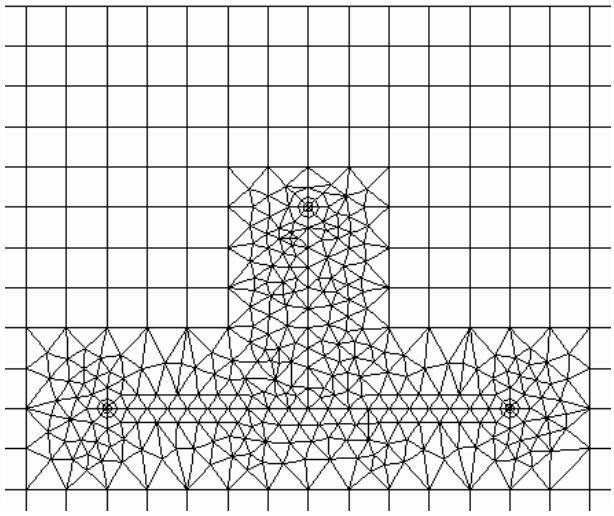

Figure 4.28 Example of typical FRANC2D mesh for the dike propagation from the lens center (H = 1 km, $2c$ = 1 km, and l = 0.5 km).

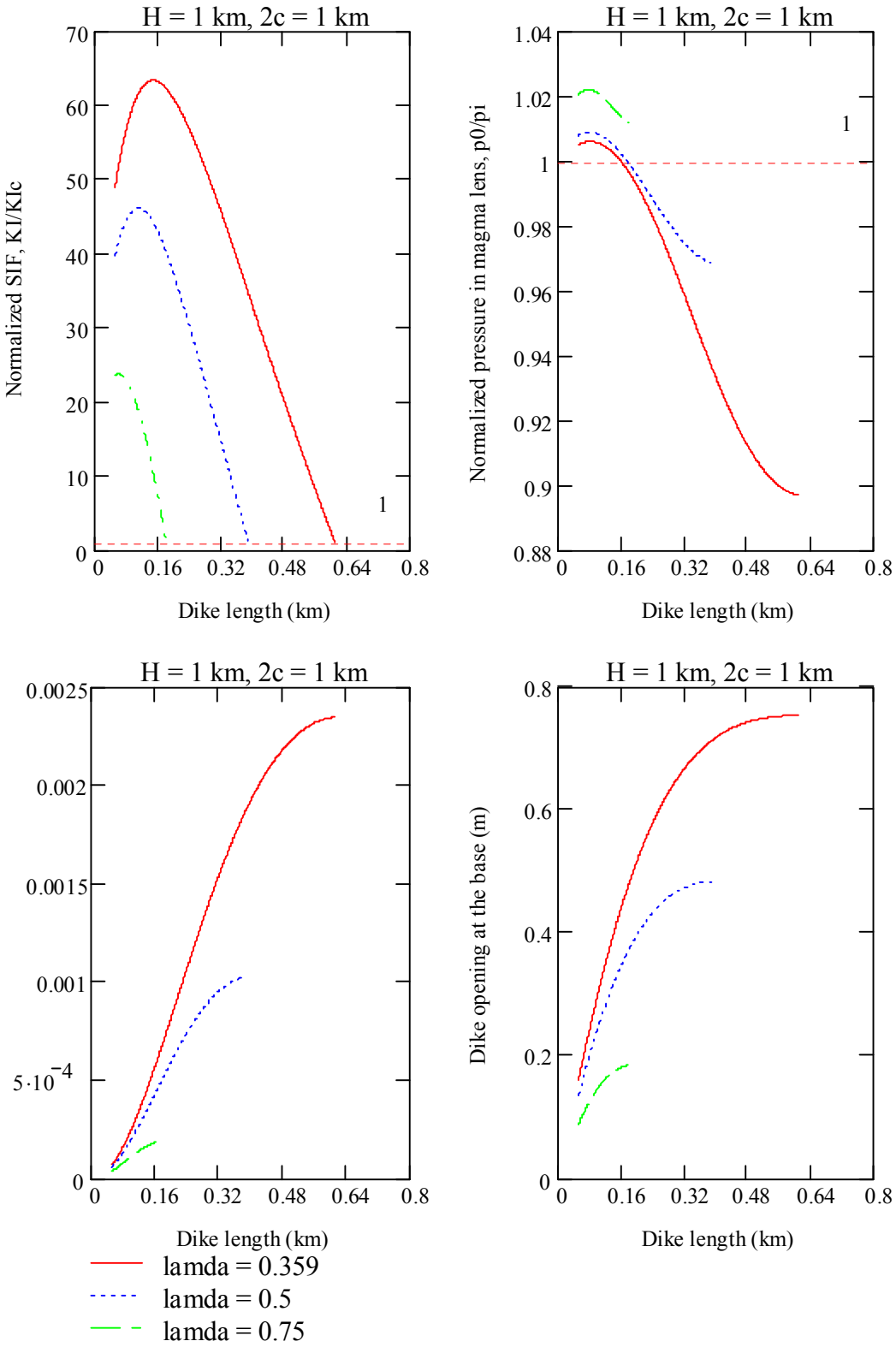

Figure 4.29 Results of the dike propagation from the lens center in the upper bound estimate (H =1 km and $2c$ = 1 km).

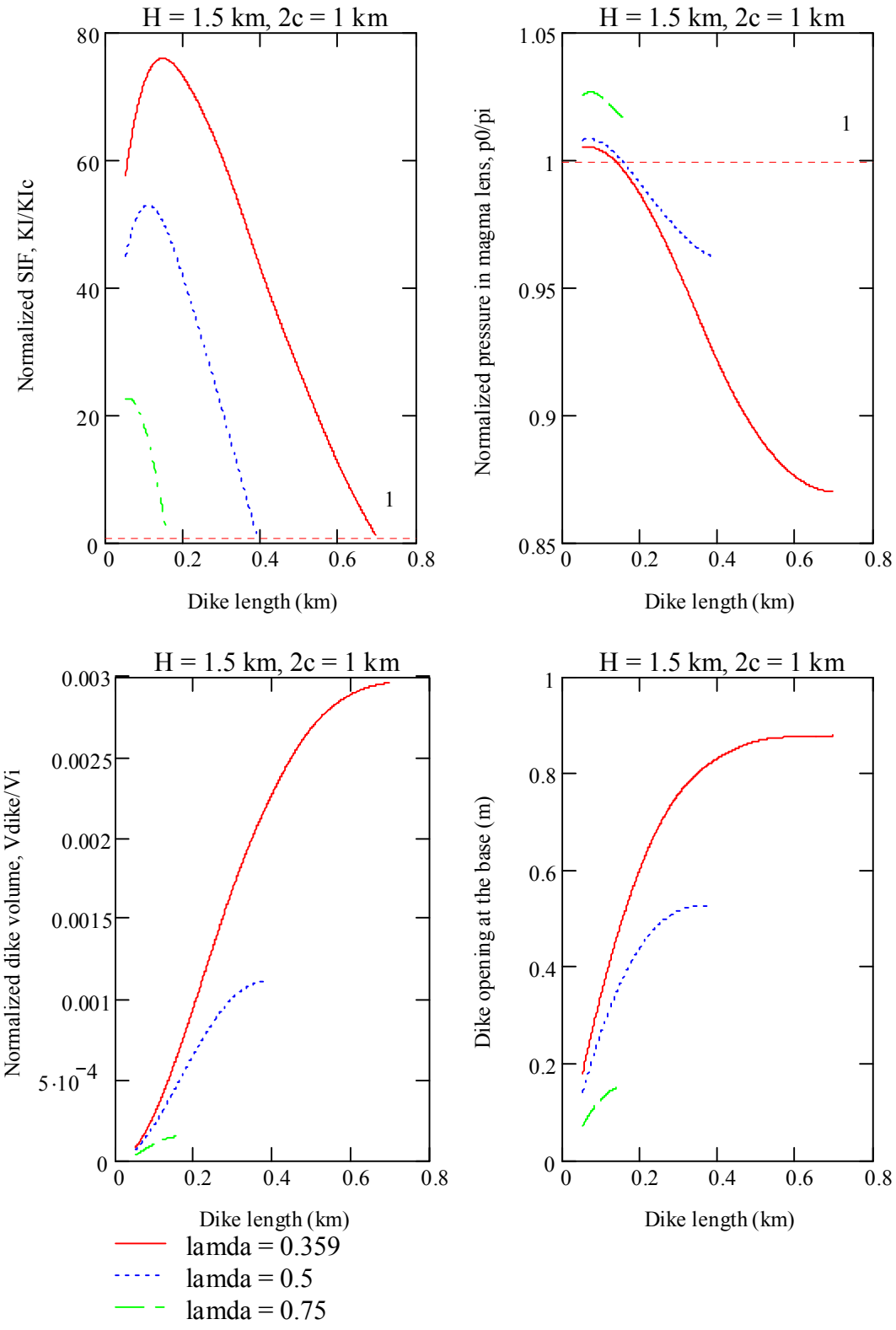

Figure 4.30 Results of the dike propagation from the lens center in the upper bound estimate (H =1.5 km and $2c$ = 1 km).

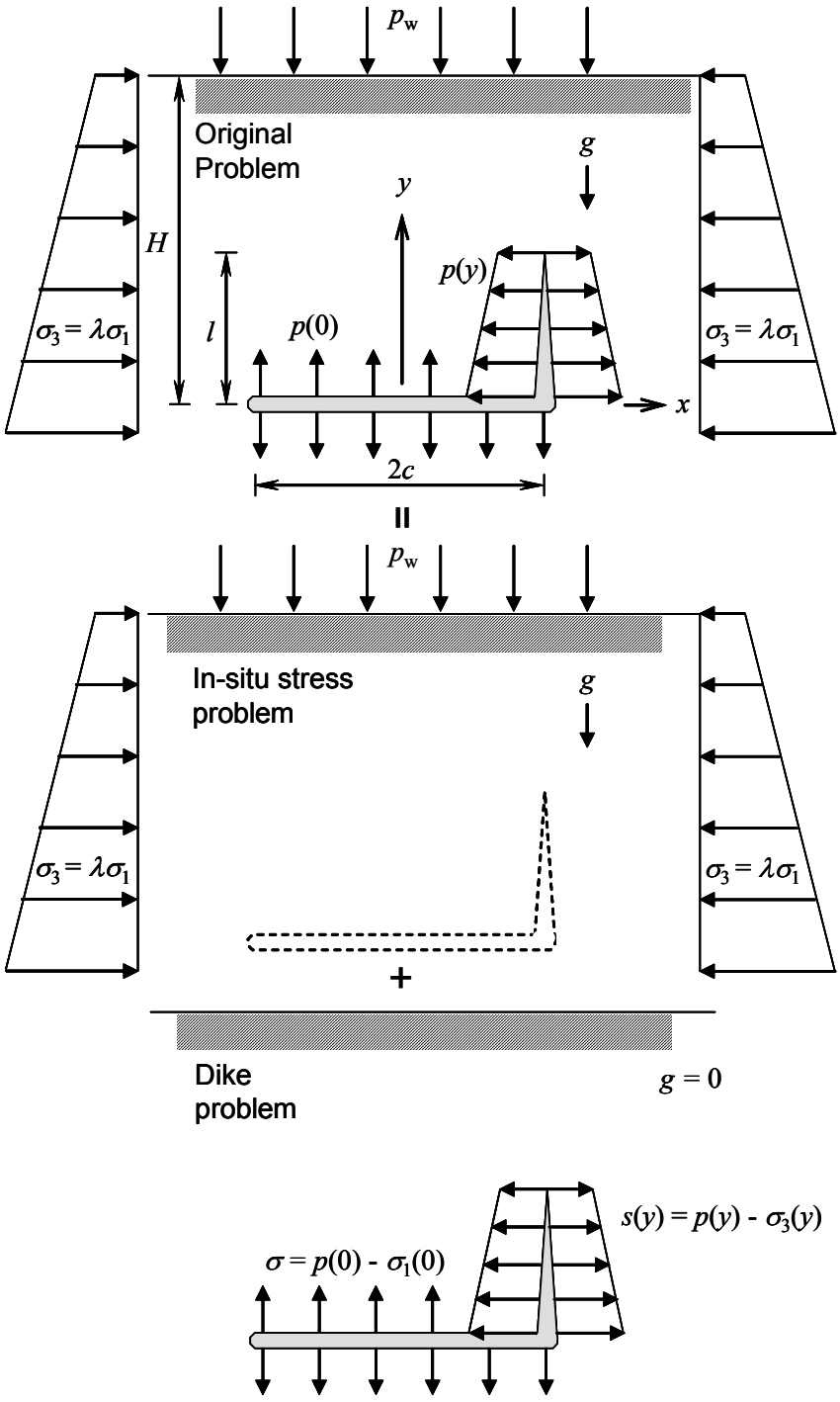

Figure 4.31 Superposition of problem for the dike propagation from the lens tip.

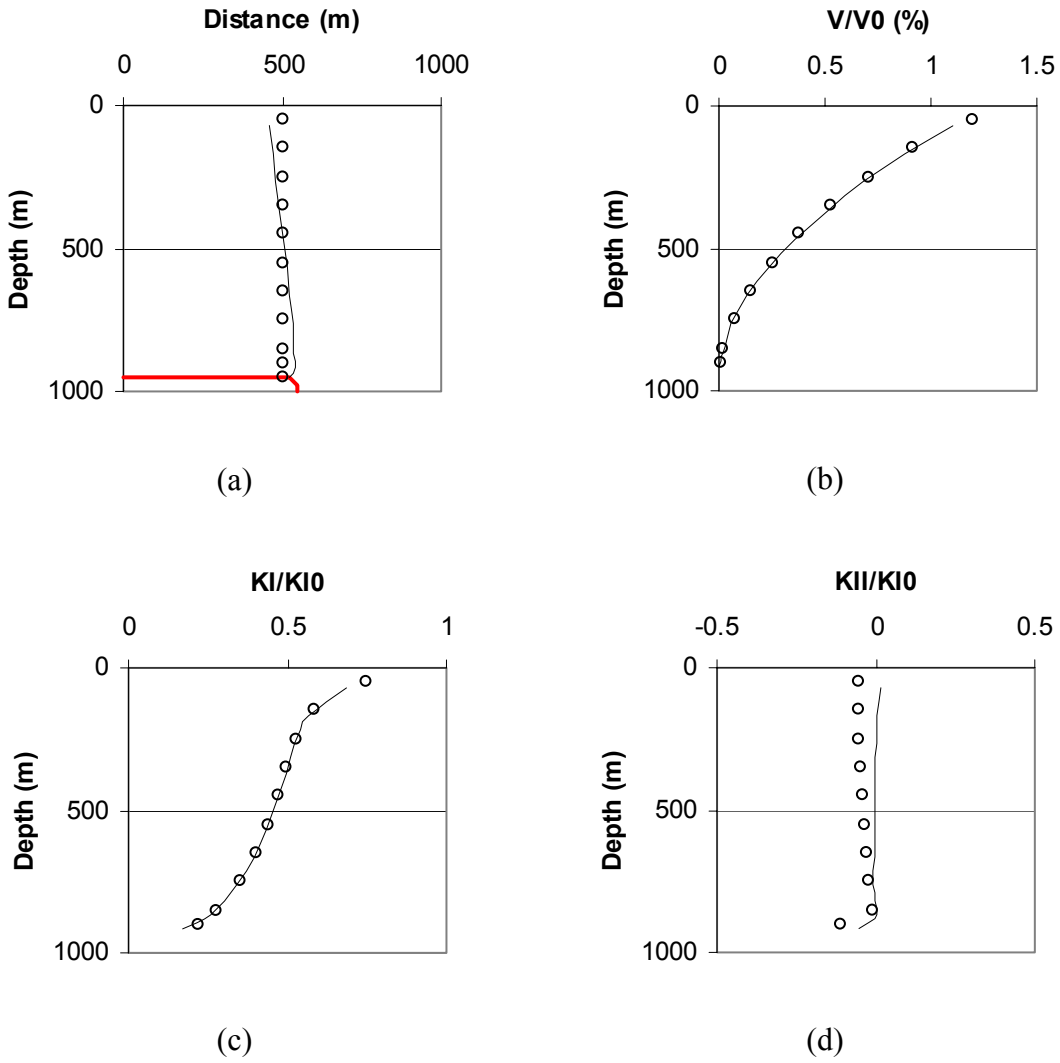

Figure 4.32 Comparison between numerical simulations of the vertical propagation of the dike originating from the tip of the magma lens in a homogeneous crust for a depth of H = 1 km and a lens width of $2c$ = 1 km – simulated propagation path (solid line) versus simplified propagation path that is forced to be straight and completely vertical (markers): (a) dike trajectories, (b) normalized volume, (c) normalized K_I, and (d) normalized K_{II}.

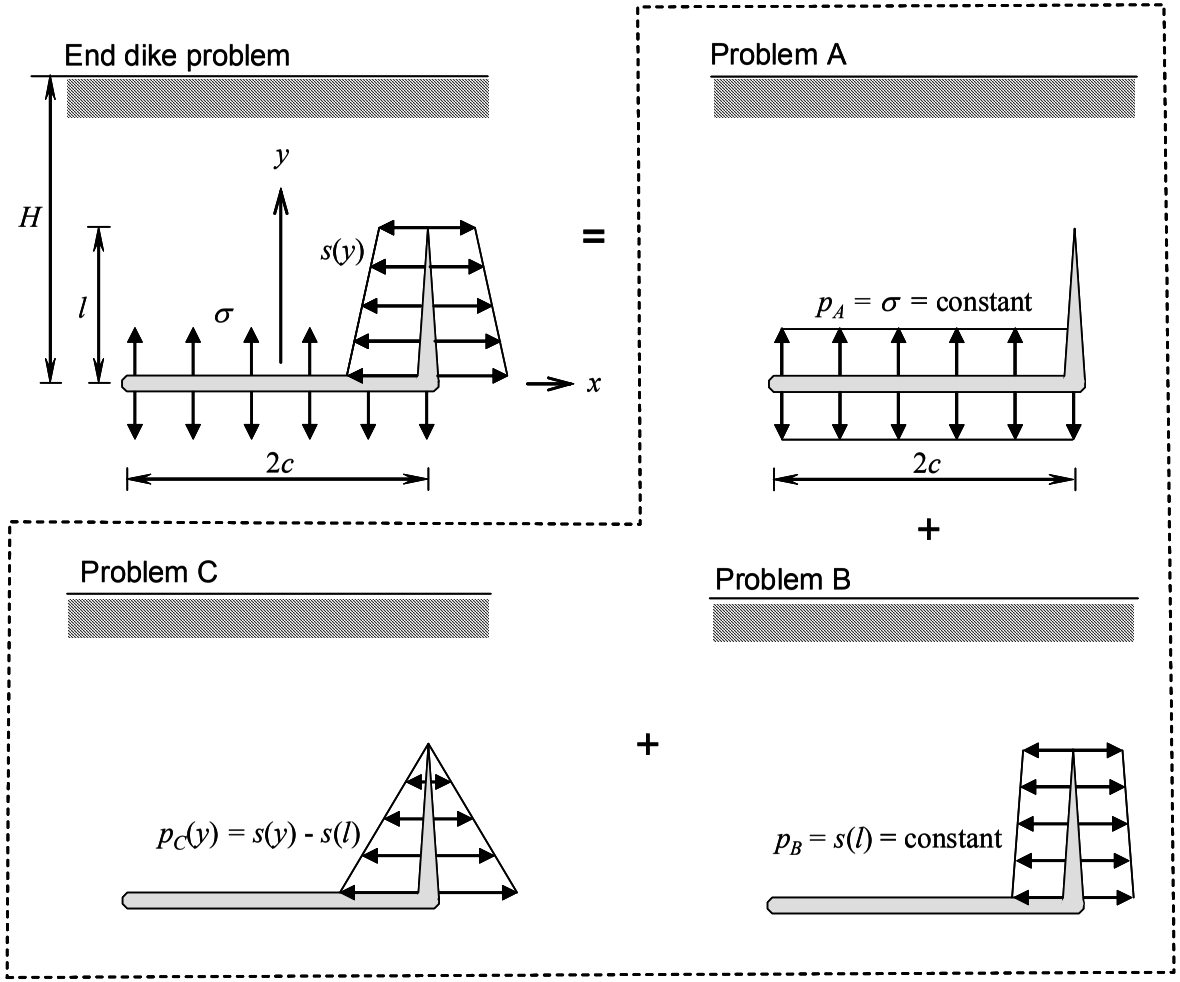

Figure 4.33 Decomposition of the end dike problem into three sub-problems.

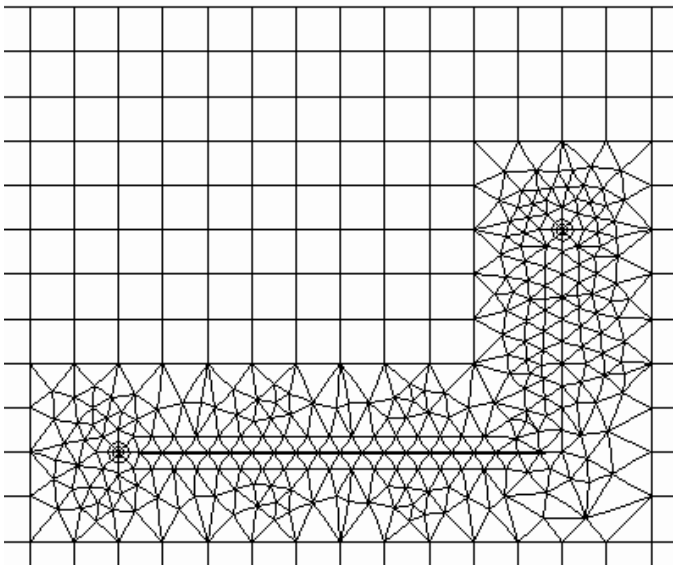

Figure 4.34 Example of typical FRANC2D mesh for the dike propagation from the lens tip (H = 1 km, $2c$ = 1 km, and l = 0.5 km).

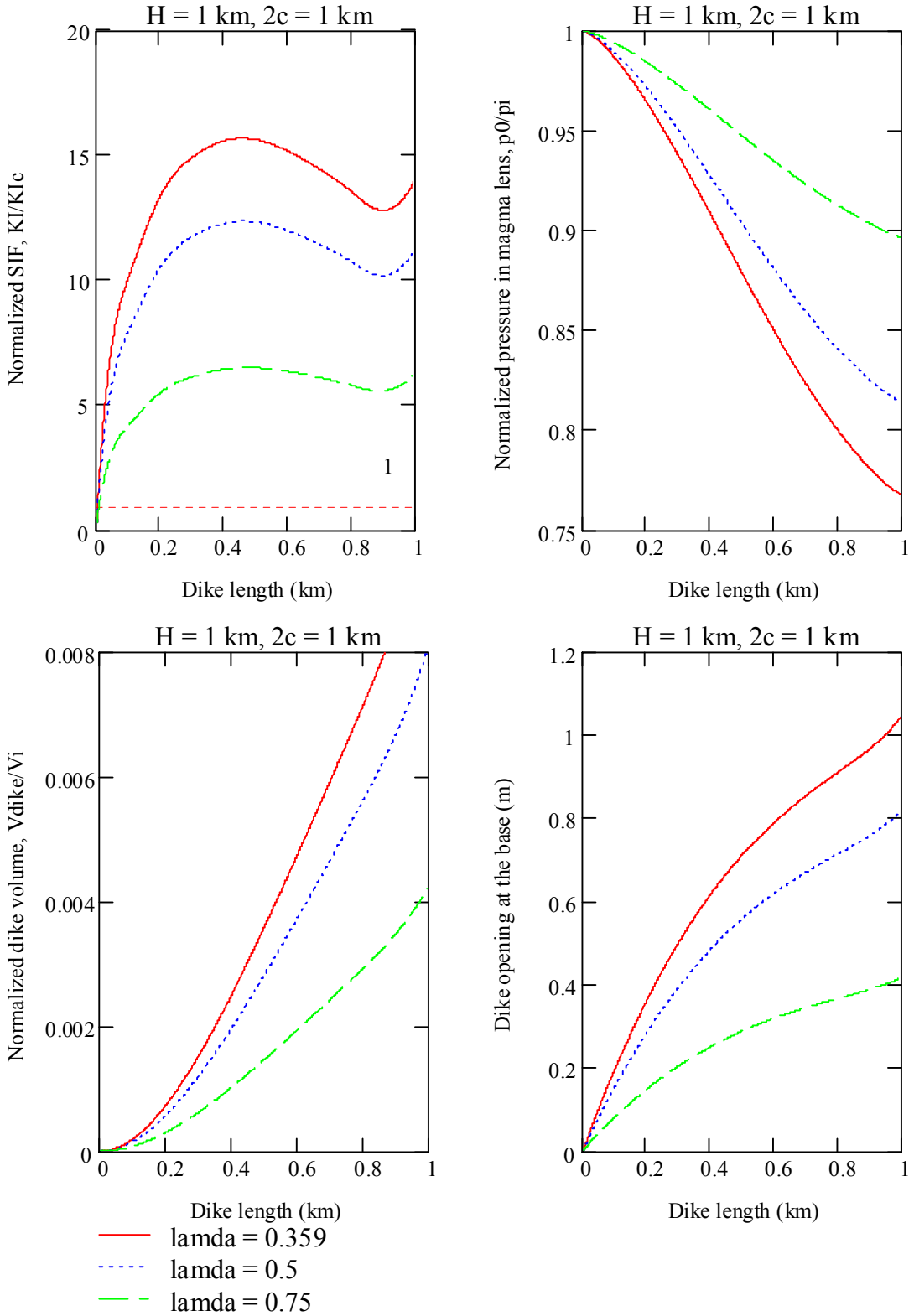

Figure 4.35 Results for the dike propagation from lens tip in the upper bound estimate (H =1 km and $2c$ = 1 km).

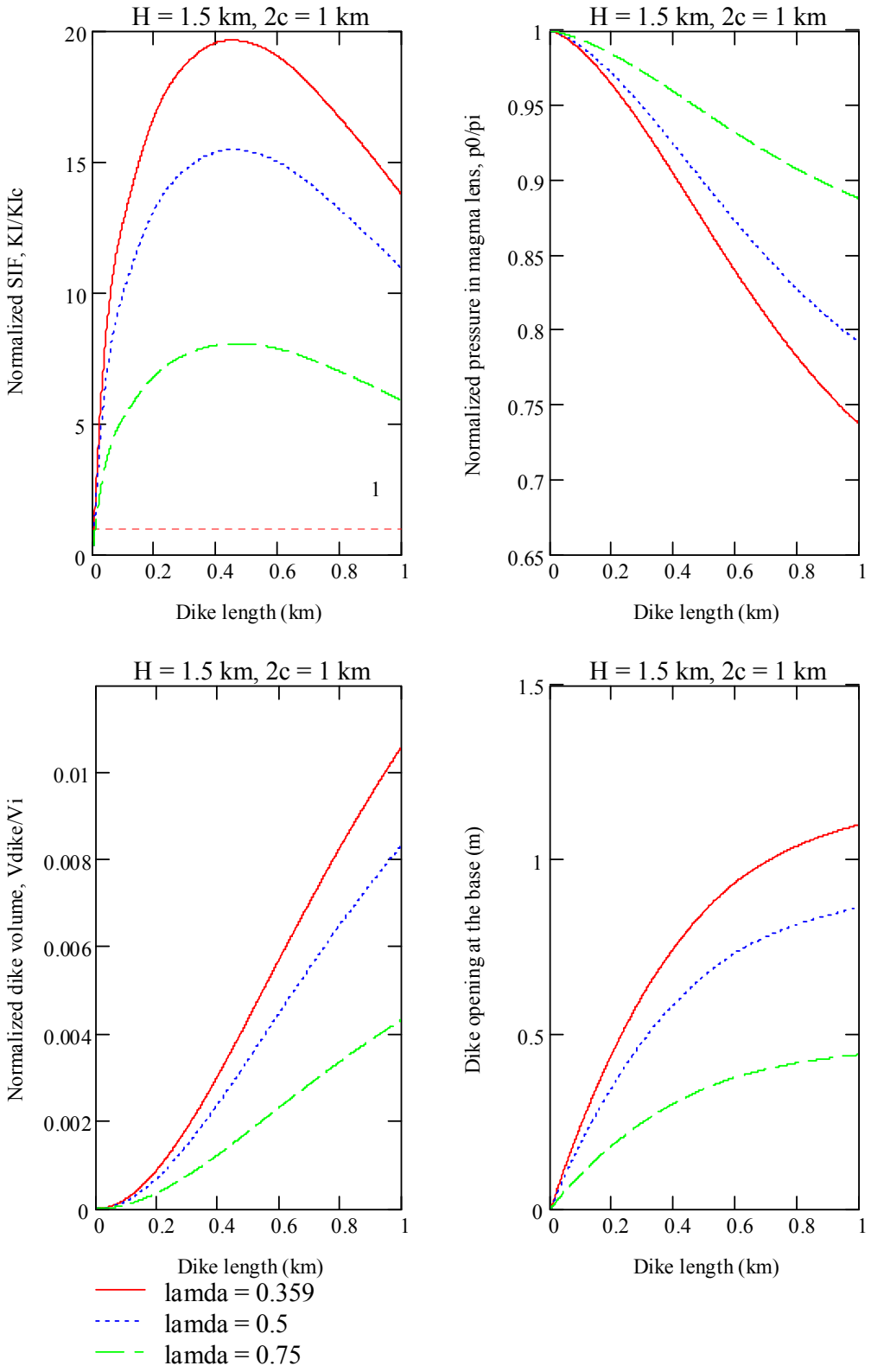

Figure 4.36 Results for the dike propagation from lens tip in the upper bound estimate (H =1.5 km and $2c$ = 1 km).

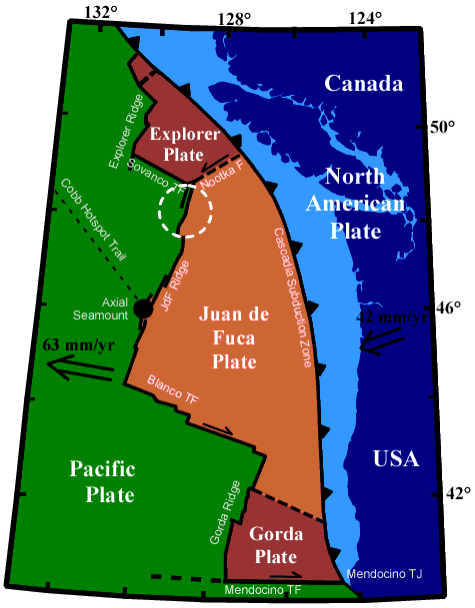

(a)

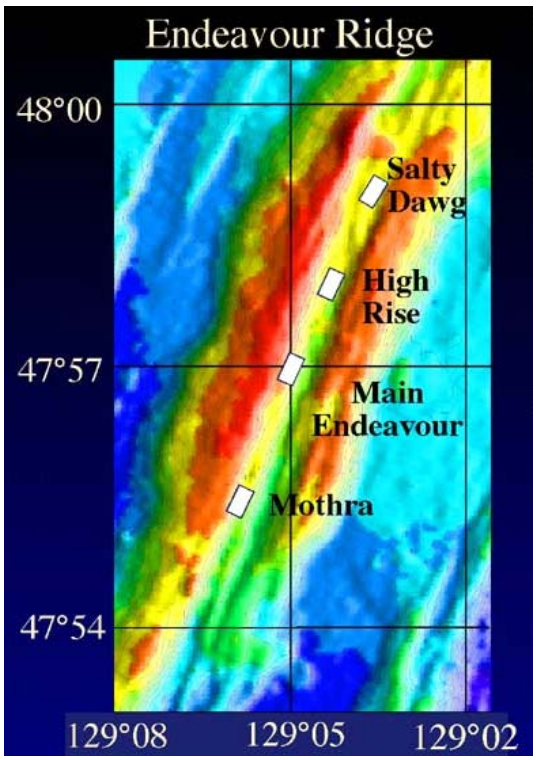

(b)

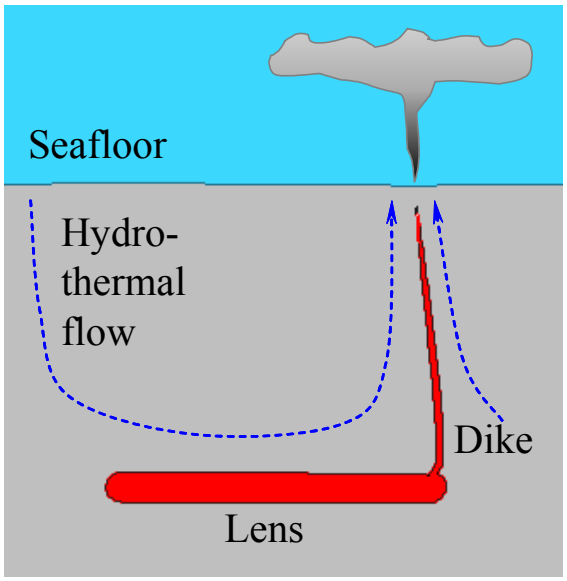

(c)

Figure 4.37 Examples of tip dike propagation: (a) location of the JdFR [*Wilcock*, 2000], dashed line indicates Endeavor segment; (b) hydrothermal site on Endeavor segment [*Delaney et al*., 2000], and (c) hydrothermal venting activity at the location above the tips away from the ridge axis.

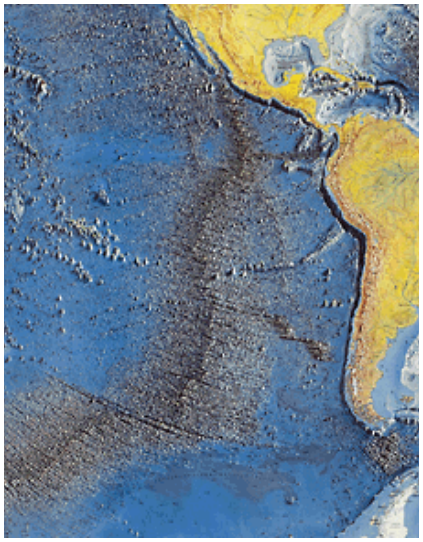

(a)

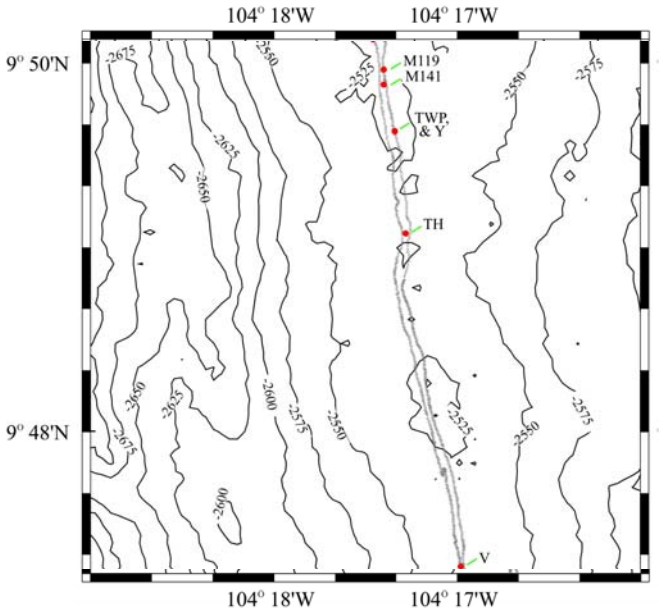

(b)

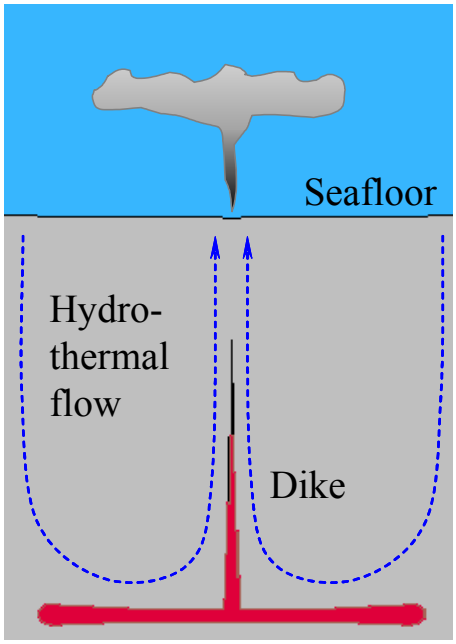

(c)

Figure 4.38 Examples of central dike propagation: (a) location of the EPR [*Heezen and Tharp*, 1977], (b) hydrothermal vents at EPR [EPR 9°-10° N Archive website], and (c) hydrothermal venting activity at the center of ridge axis.

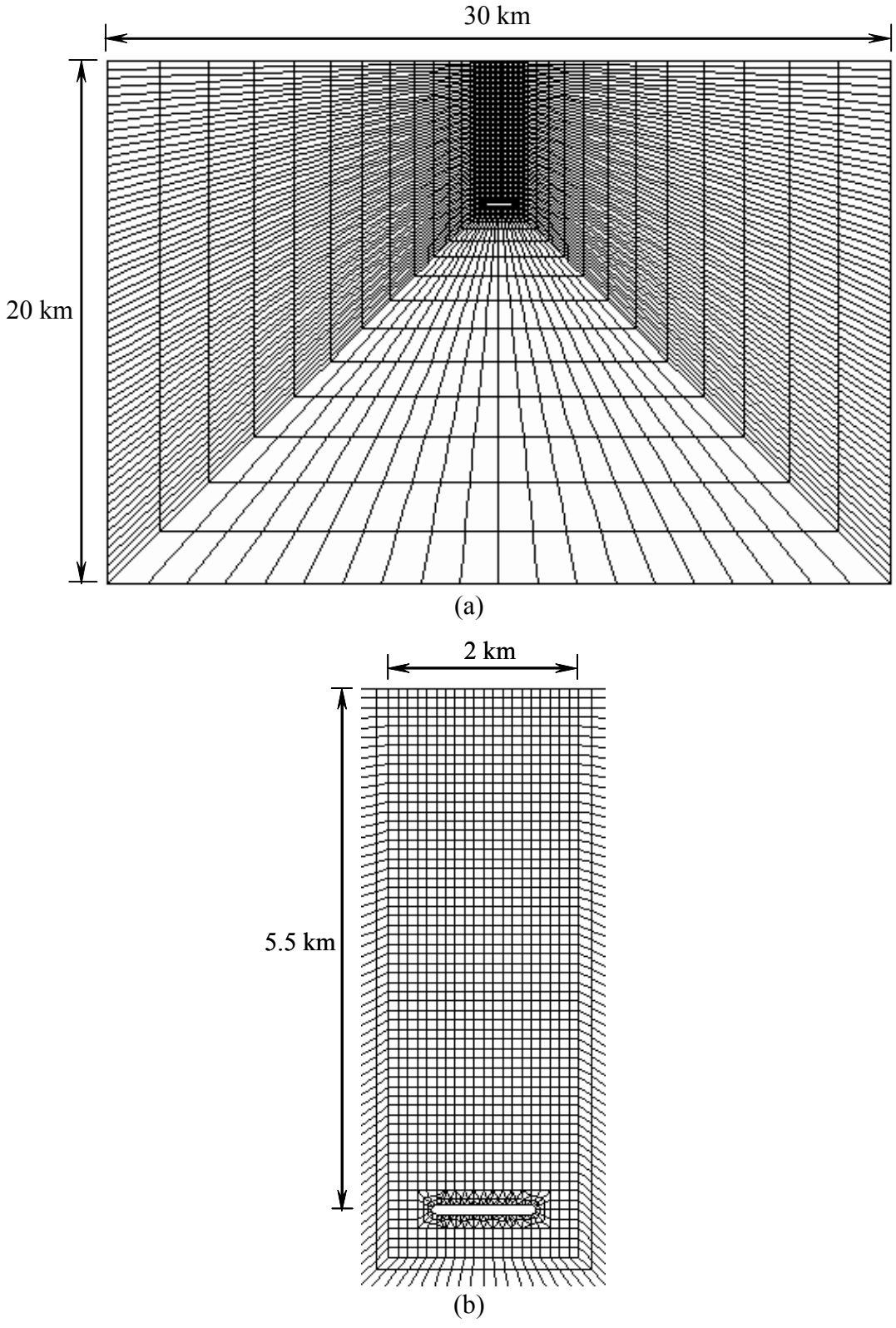

Figure 4.39 Example of typical FRANC2D mesh for the simulation of the deep magma lens (H = 5.5 km and $2c$ = 1 km): (a) full mesh, and (b) magnification of mesh around deep lens.

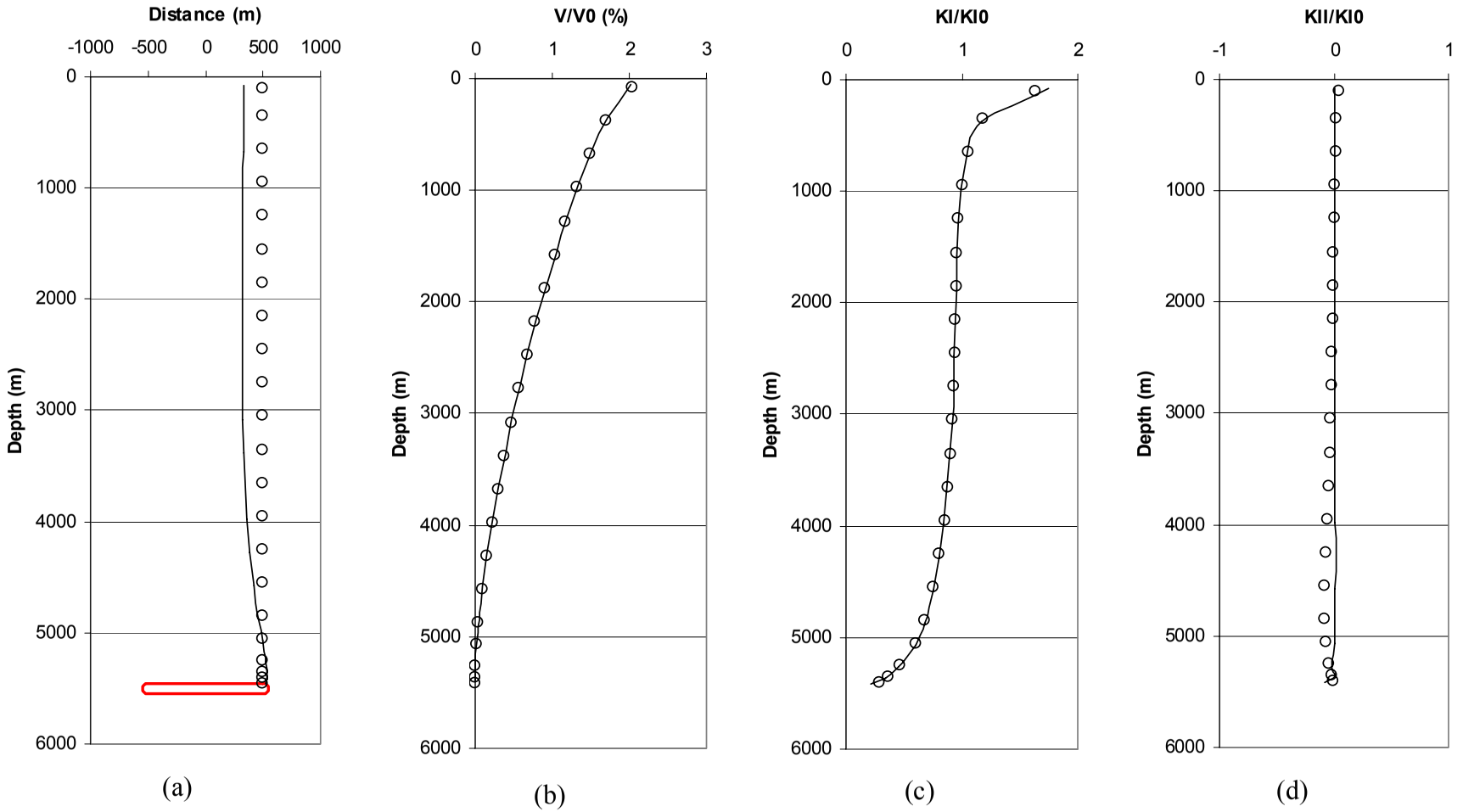

Figure 4.40 Comparison between numerical simulations of the vertical propagation of the dike originating from the tip of the deep magma lens in a homogeneous crust for a depth of H = 5.5 km and a lens width of $2c$ = 1 km – simulated propagation path (solid line) versus simplified propagation path that is forced to be straight and completely vertical (circles): (a) dike trajectories, (b) normalized volume, (c) normalized K_I, and (d) normalized K_{II}.

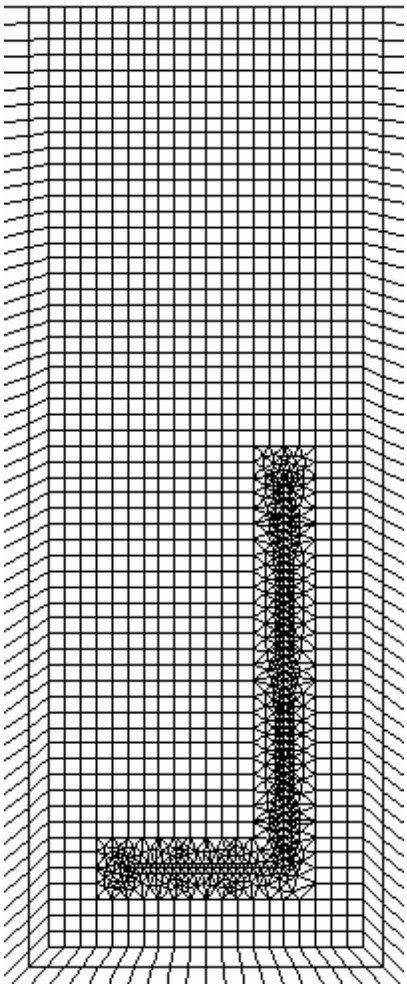

Figure 4.41 Example of typical FRANC2D mesh for the dike propagation from deep magma lens tip (H = 5.5 km, $2c$ = 1 km, and l = 2.5 km).

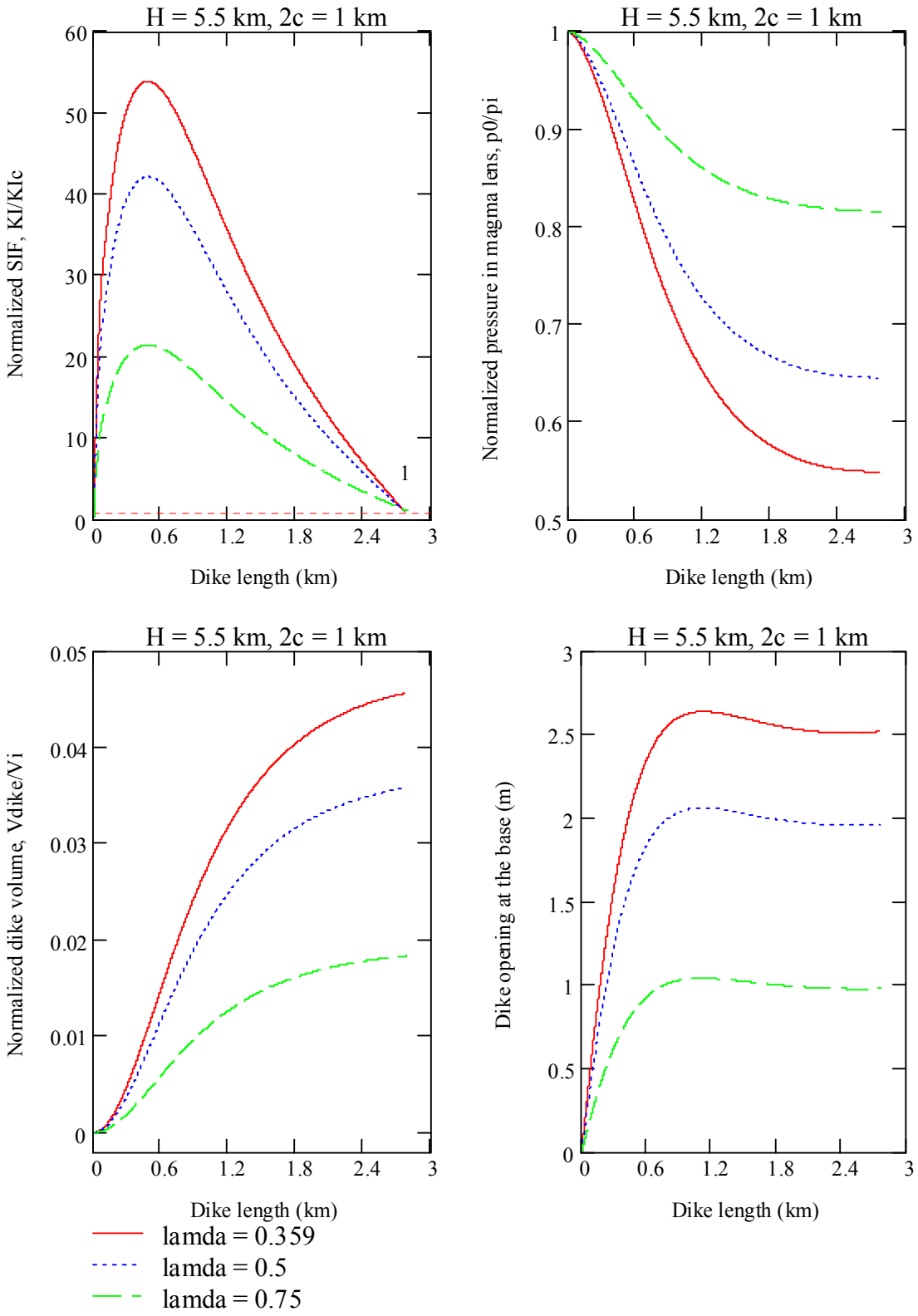

Figure 4.42 Results for the dike propagation from the deep magma lens tip in the upper bound estimate (H =5.5 km and $2c$ = 1 km).

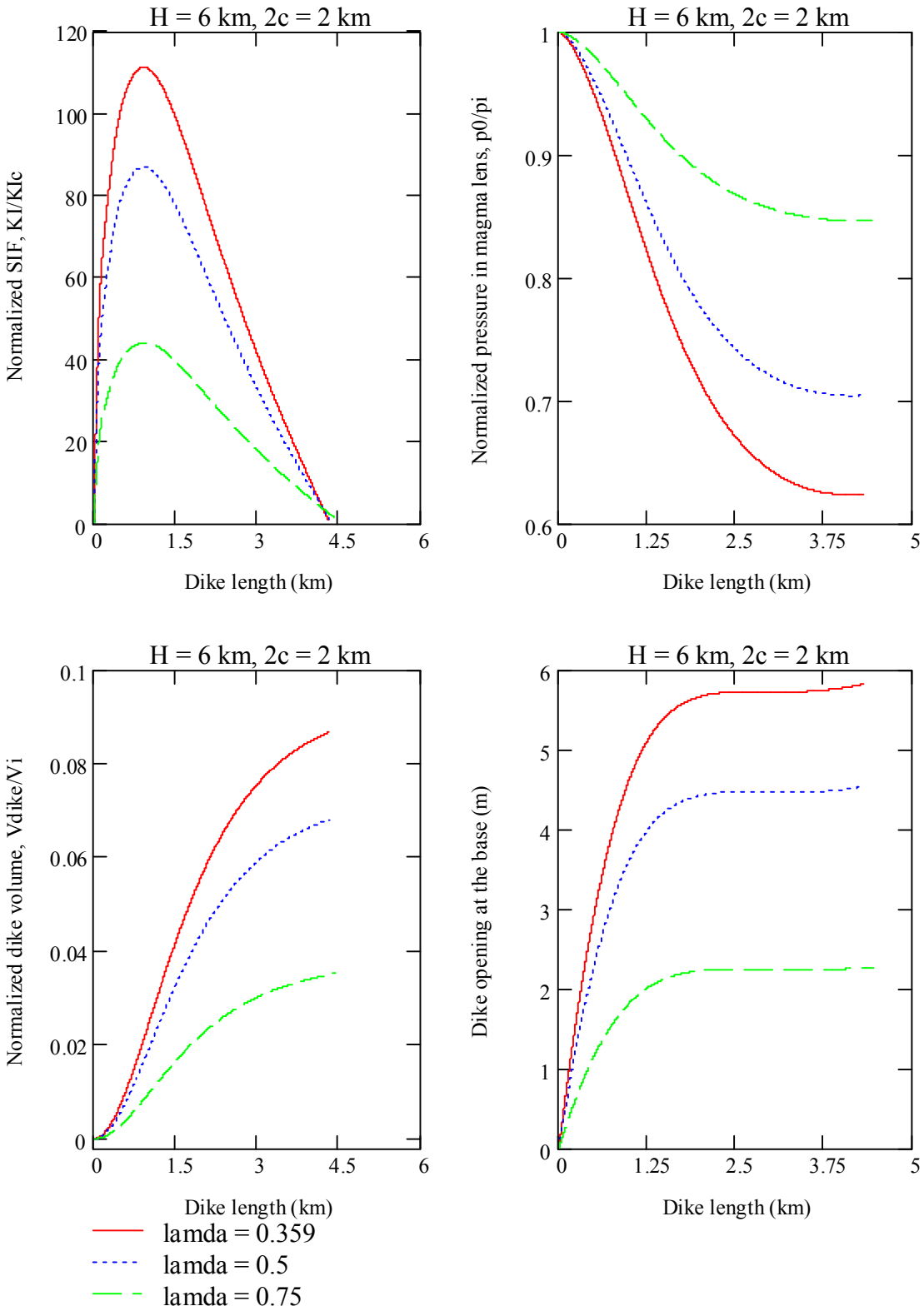

Figure 4.43 Results for the dike propagation from the deep magma lens tip in the upper bound estimate (H =6 km and $2c$ = 2 km).

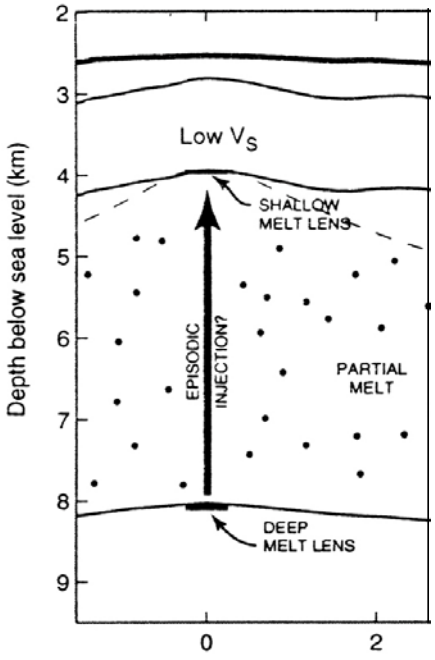

(a)

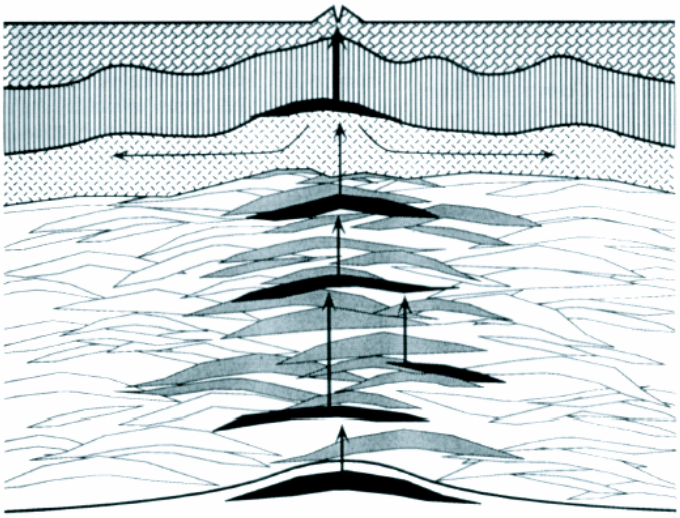

(b)

Figure 4.44 Hypothesized model for dike propagation from the deep melt lens: (a) dike propagation from deep melt lens to shallow lens, [*Crawford et al*., 1999]; and (b) magma lenses with the shape of thin lenses [*Korenaga and Kelemen*, 1997].

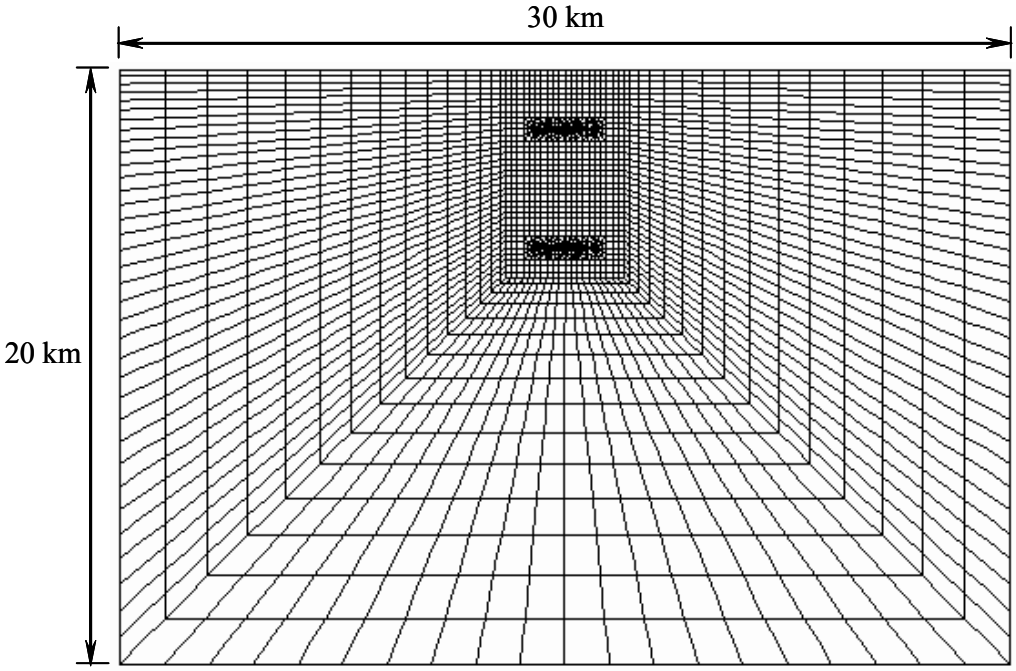

(a)

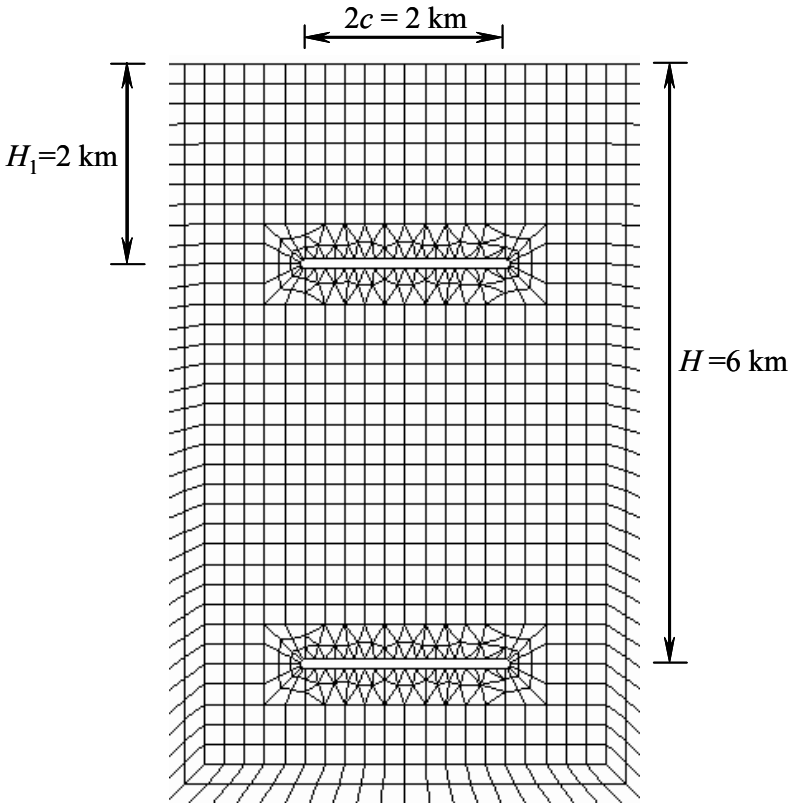

(b)

Figure 4.45 FRANC2D mesh for the simulation of dike propagation from the deep magma lens (H = 6 km and $2c$ = 6 km) to the shallow magma lens (H_1 = 2 km and $2c$ = 2 km): (a) full mesh; and (b) magnification of mesh around two magma lenses.

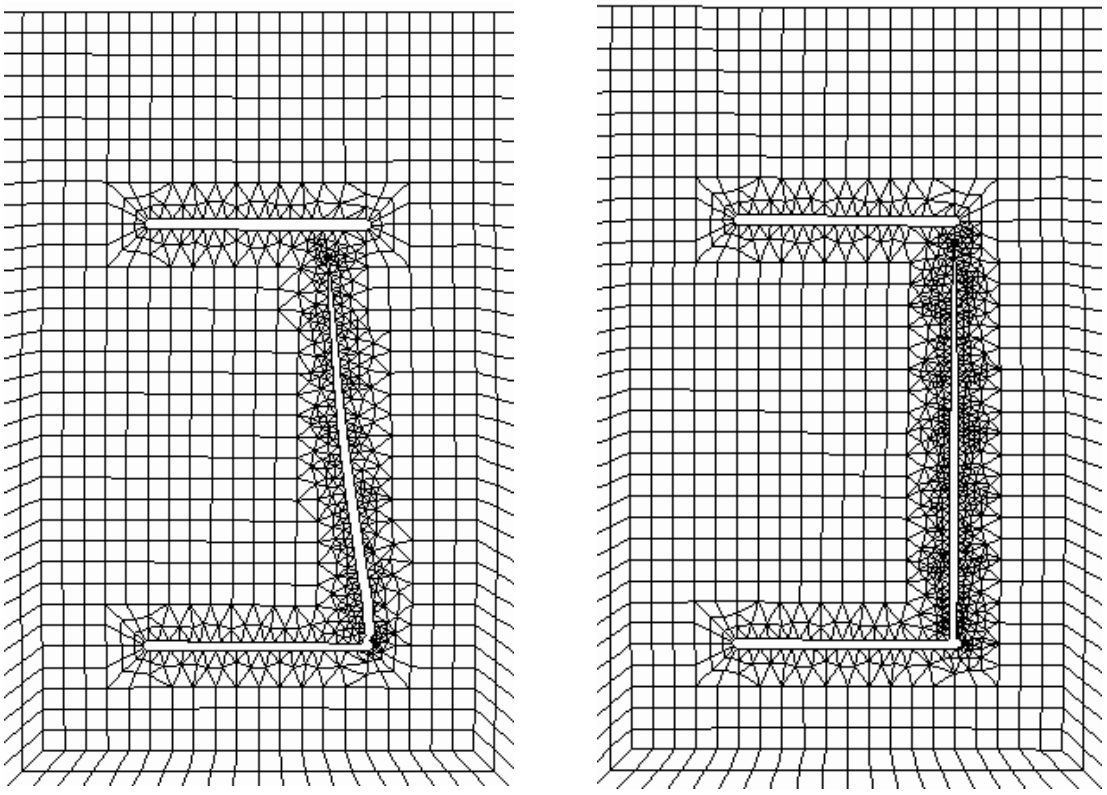

(a) (b)

Figure 4.46 Dike propagation from the deep magma lens tip to the shallow magma lens in FRANC2D: (a) real dike trajectory; and (b) simplified dike trajectory.

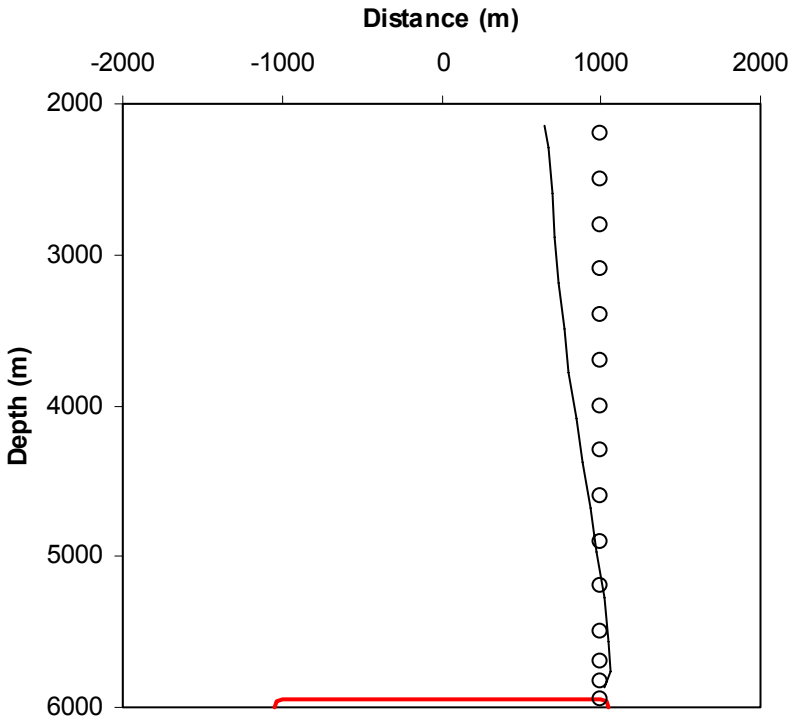

(a)

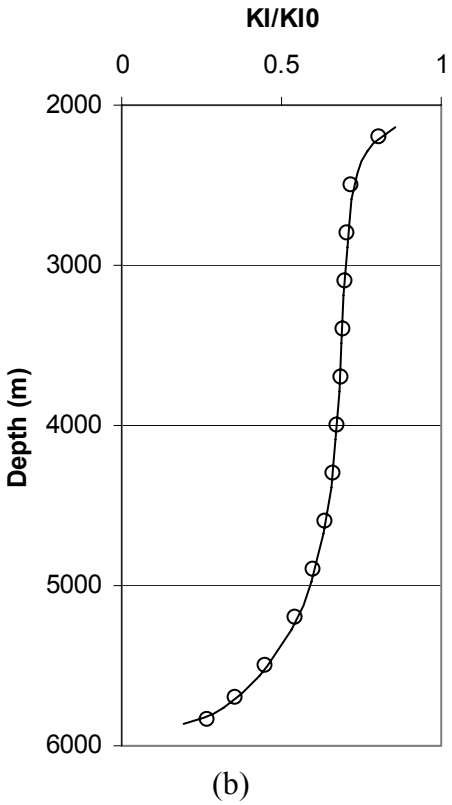

(b)

Figure 4.47 Comparison between numerical simulations of the vertical propagation of the dike originating from the deep magma lens tip – simulated propagation path (solid line) versus simplified propagation path that is forced to be straight and completely vertical (circles): (a) dike trajectories, and (b) normalized K_I.

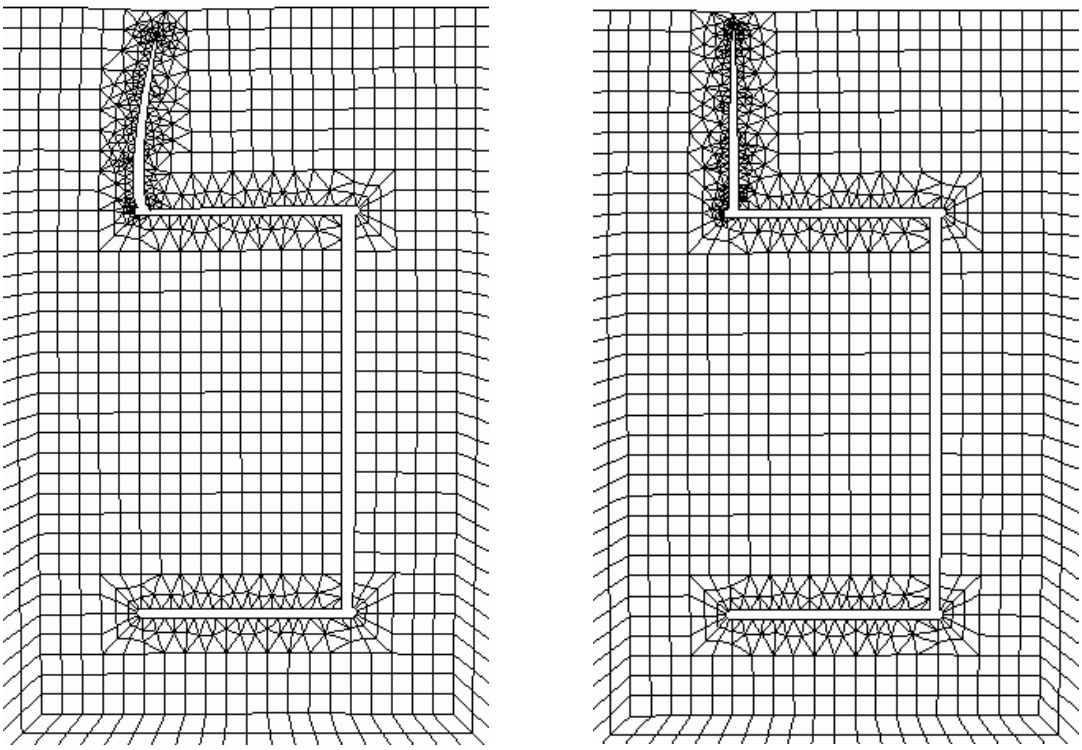

(a) (b)

Figure 4.48 Subsequent dike propagation from shallow magma lens tip in FRANC2D: (a) real dike propagation, and (b) simplified dike trajectory.

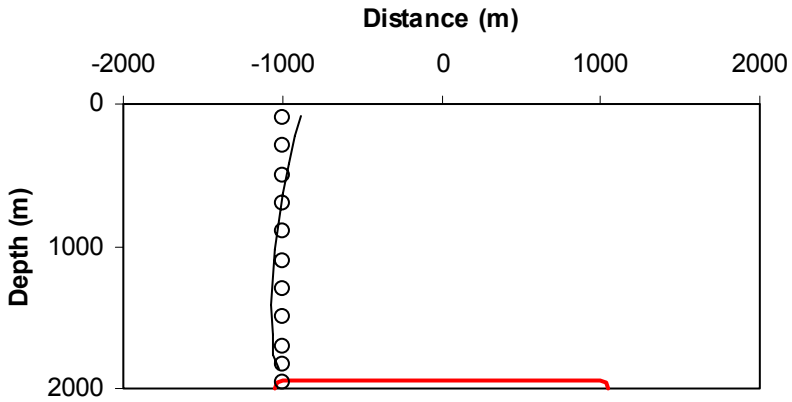

(a)

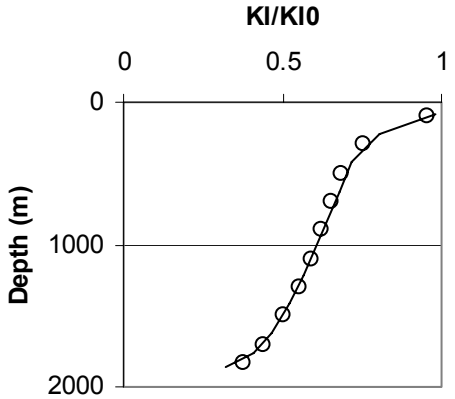

(b)

Figure 4.49 Comparison between numerical simulations of the vertical propagation of the dike originating from the shallow magma lens tip – simulated propagation path (solid line) versus simplified propagation path that is forced to be straight and completely vertical (circles): (a) dike trajectories, and (b) normalized K_I.

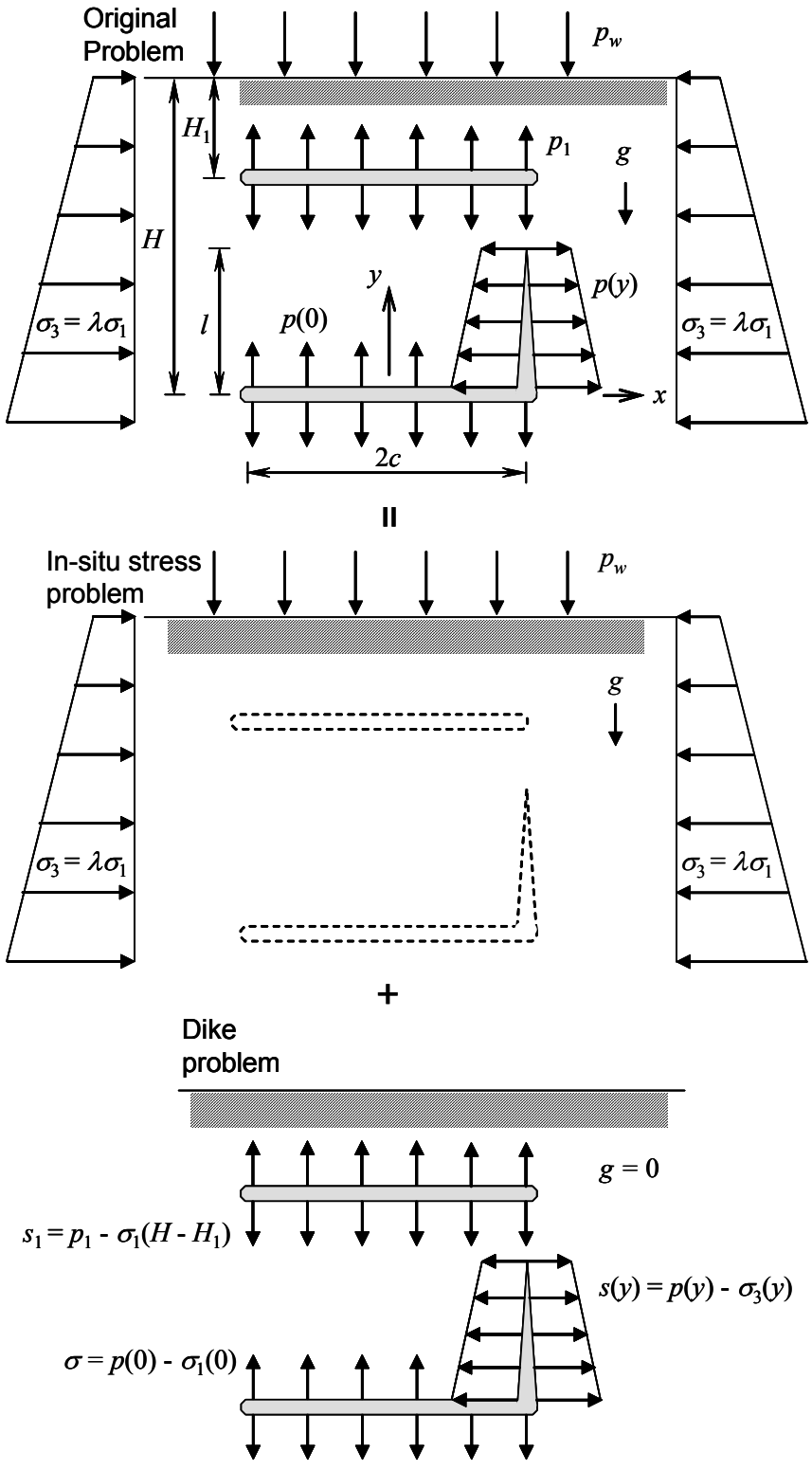

Figure 4.50 Superposition of problem for the dike propagation from the deep lens tip to the shallow magma lens.

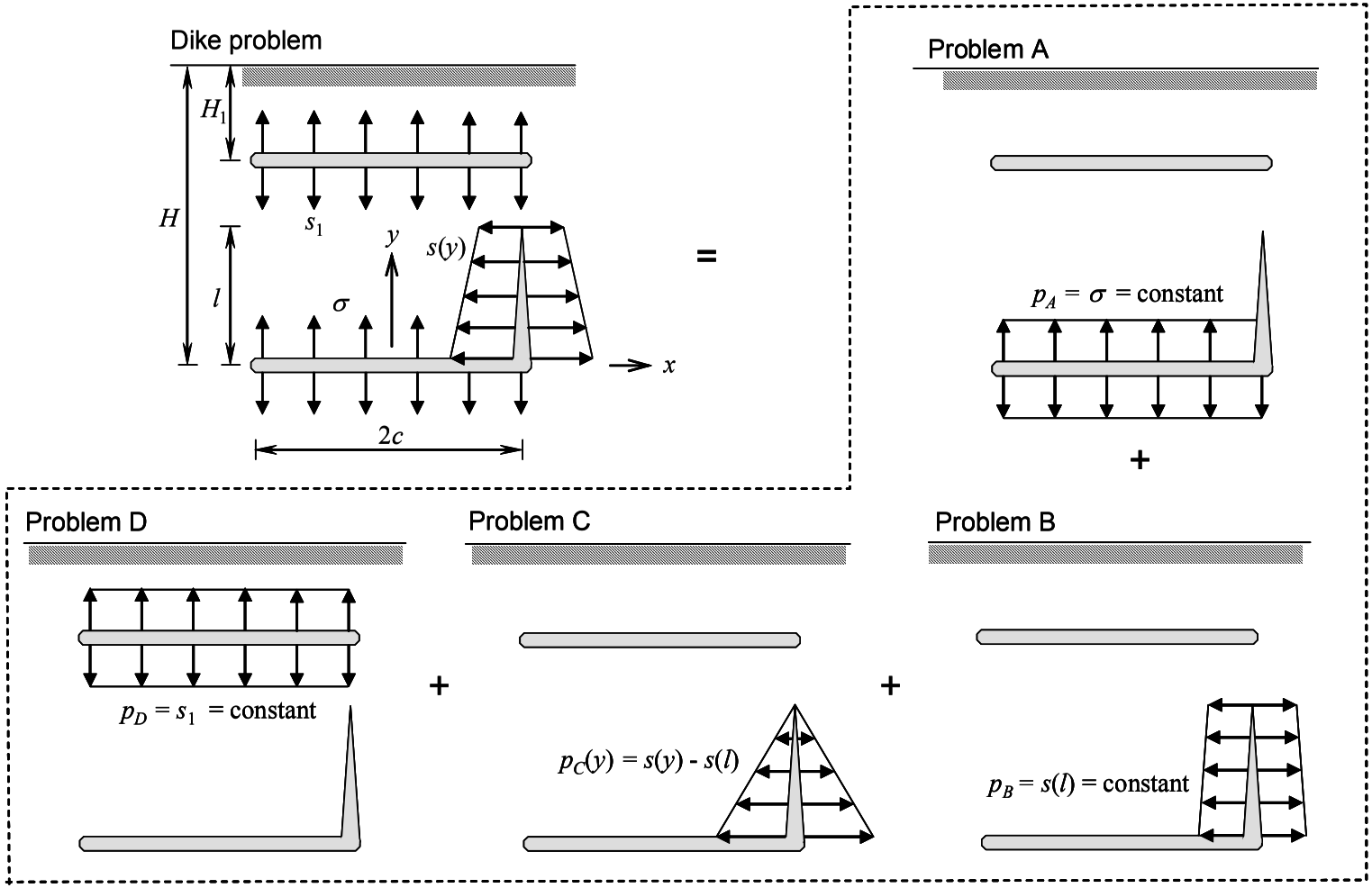

Figure 4.51 Decomposition of the dike problem into four sub-problems.

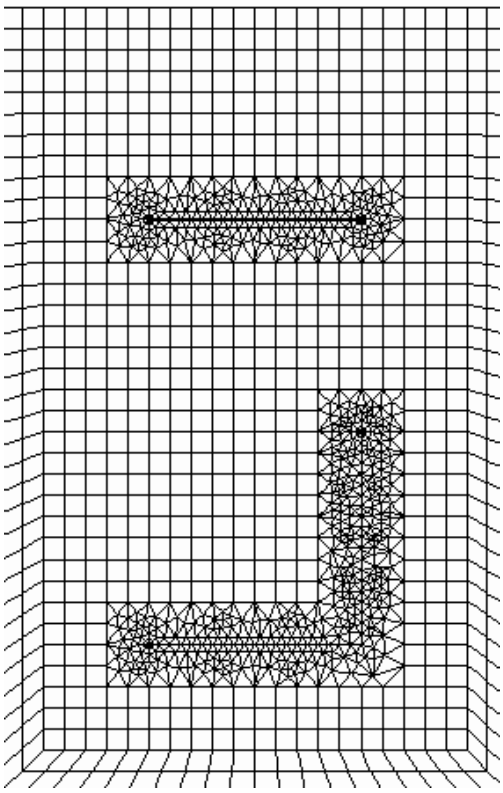

Figure 4.52 Example of typical FRANC2D mesh for the dike propagation from the deep magma lens tip to the shallow magma lens (H = 6 km, $2c$ = 2 km, and l = 2 km).

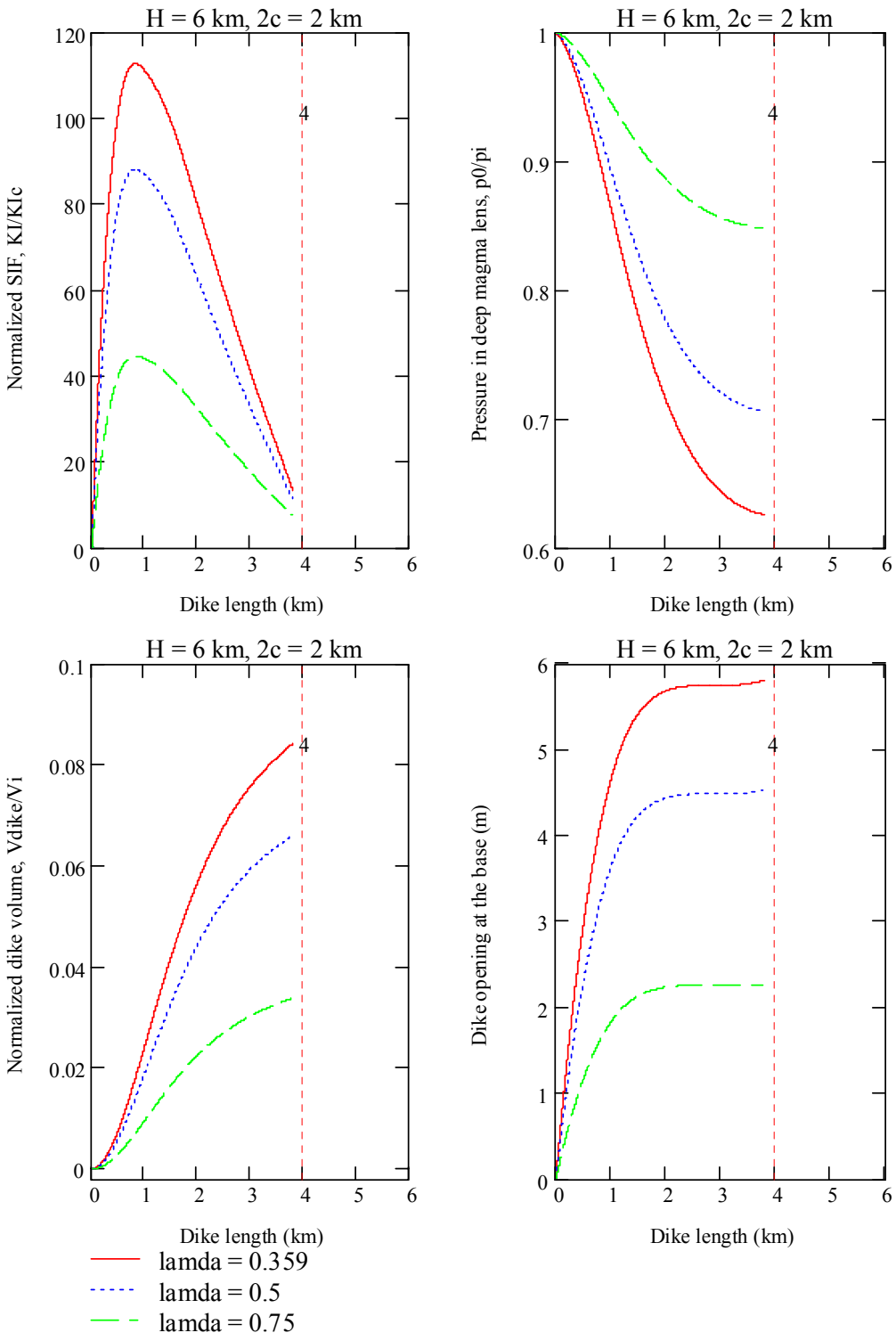

Figure 4.53 Results for the dike propagation from deep lens tip to the shallow lens in the upper bound estimate (H =6 km and $2c$ = 2 km). Vertical dashed line indicates the location of shallow magma lens (H_1 = 4 km).

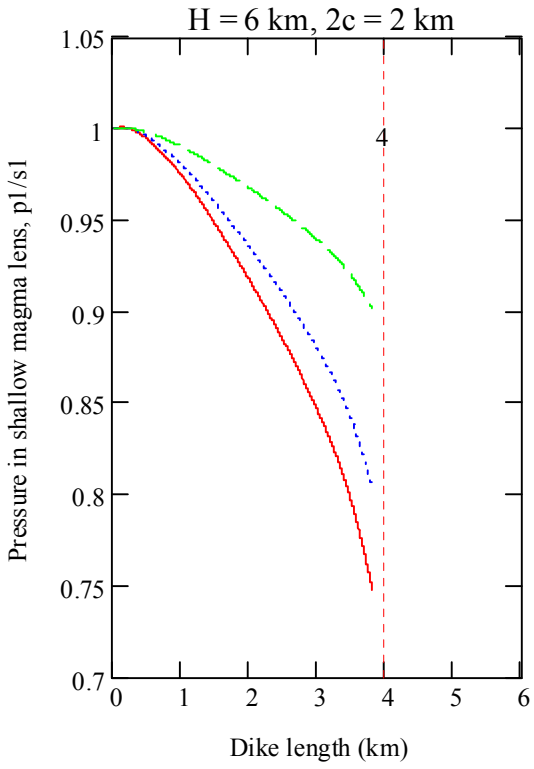

Figure 4.53 (Continued).

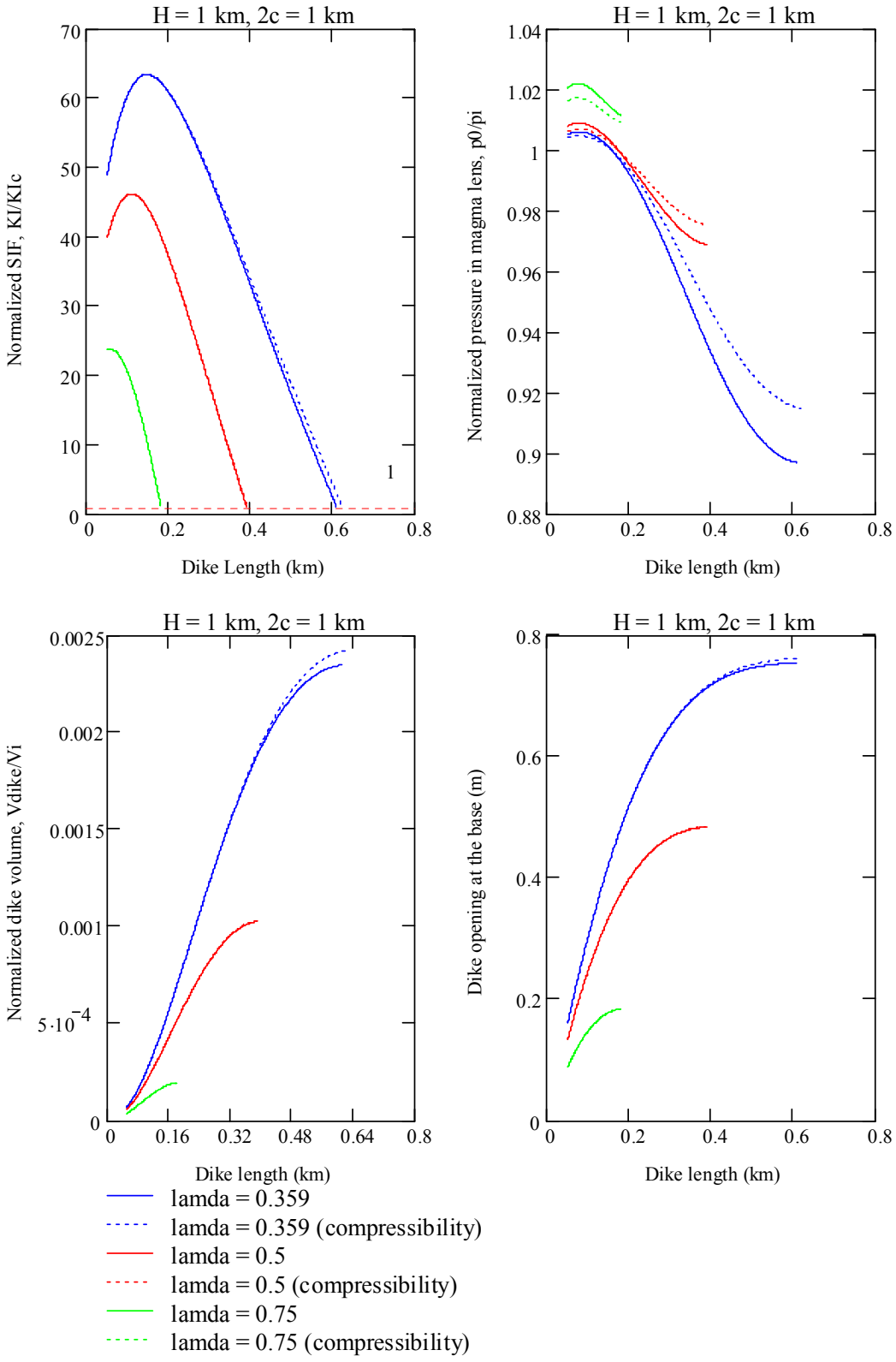

Figure 4.54 Dike propagation from the lens center (H = 1 km and $2c$ = 1 km). Dotted lines shows the results when the compressibility of the magma is considered.

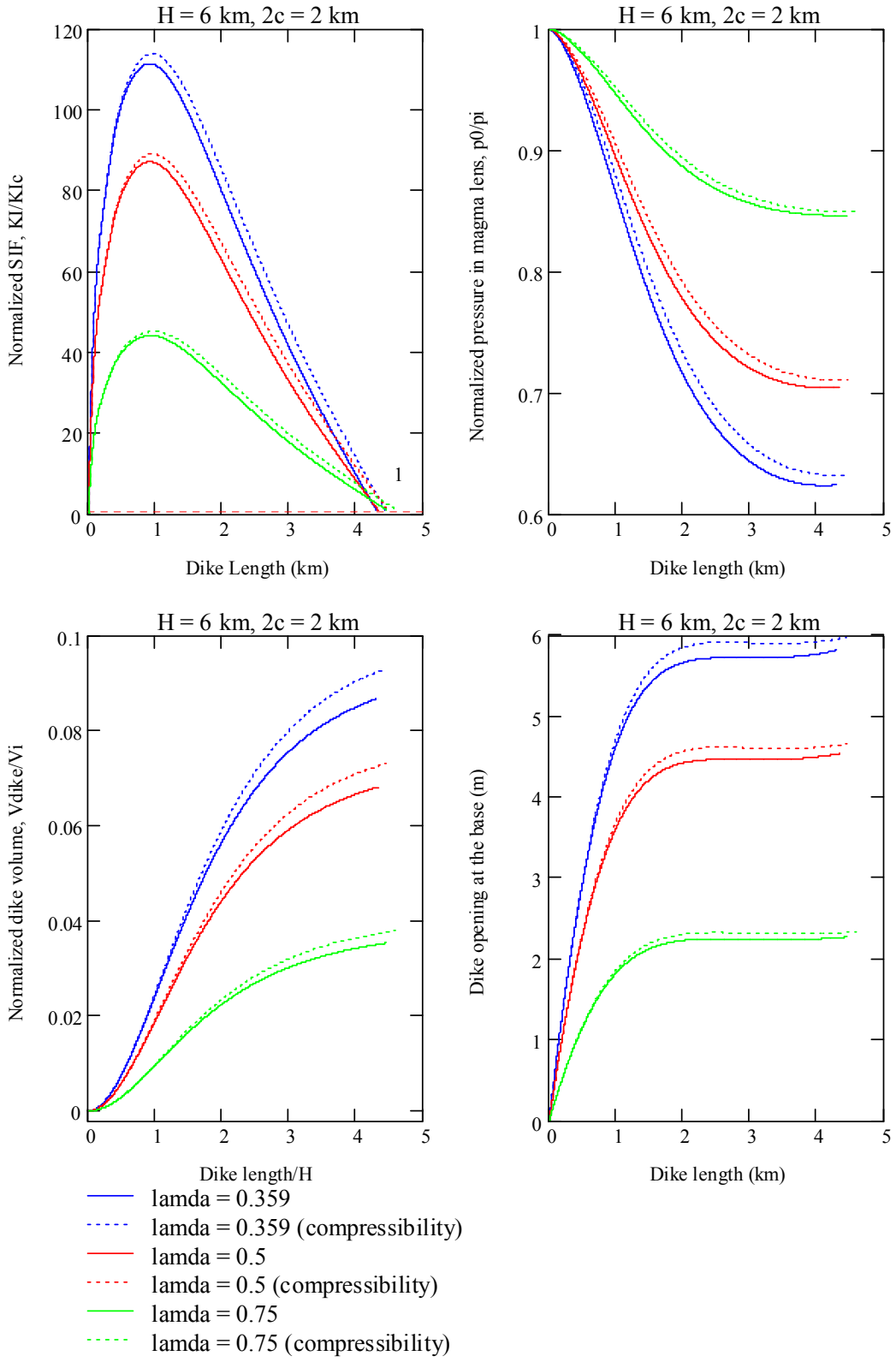

Figure 4.55 Dike propagation from the lens tip (H = 6 km and $2c$ = 2 km). Dotted lines show the results when the compressibility of the magma is considered.

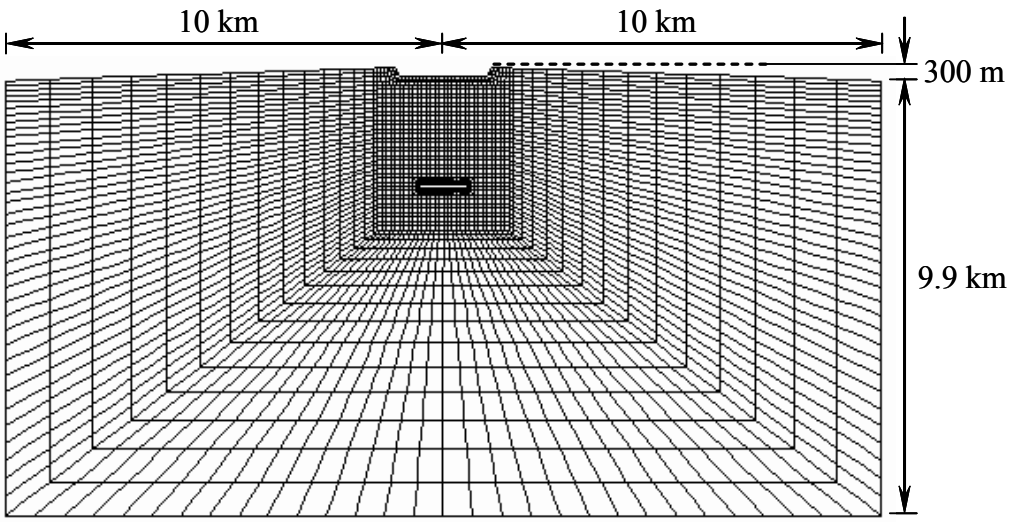

(a)

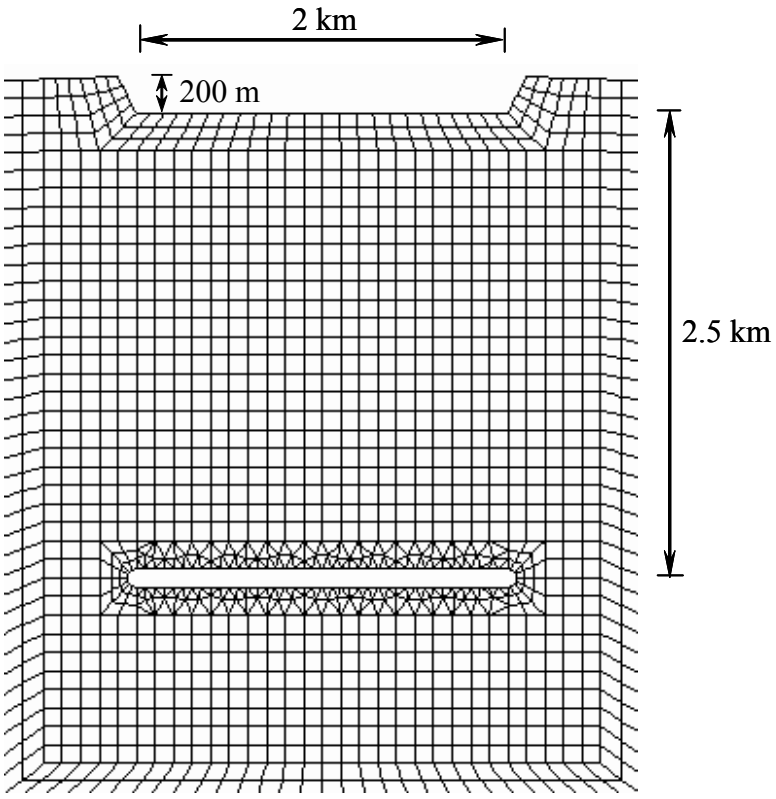

(b)

Figure 4.56 FRANC2D mesh for the numerical model of a magma lens considering topography: (a) whole mesh that has a non-horizontal topography, and (b) magnified non-horizontal topography with $2c$ = 2 km size of melt lens at the depth of H = 2.5 km.

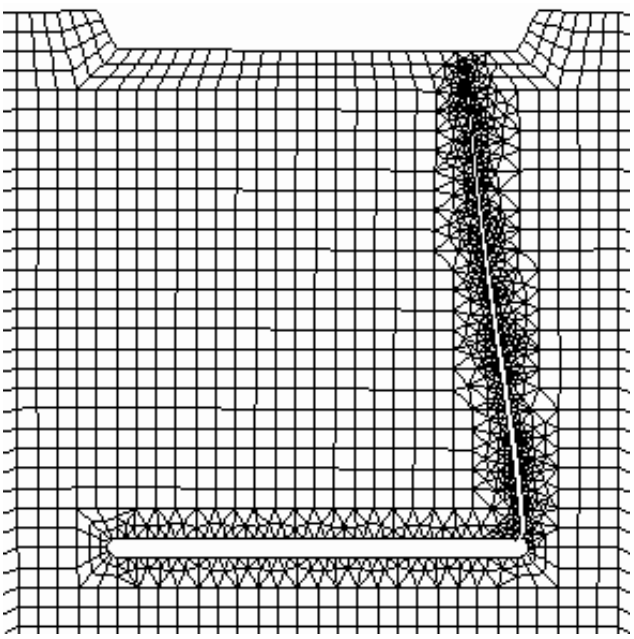

(a)

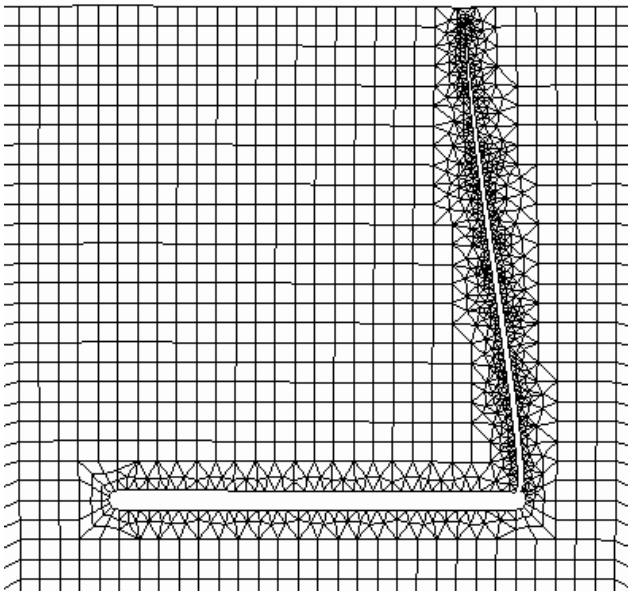

(b)

Figure 4.57 Dike trajectories from the magma lens tip (H = 2.5 km and $2c$ = 2 km): (a) non-horizontal seafloor; and (b) horizontal seafloor.

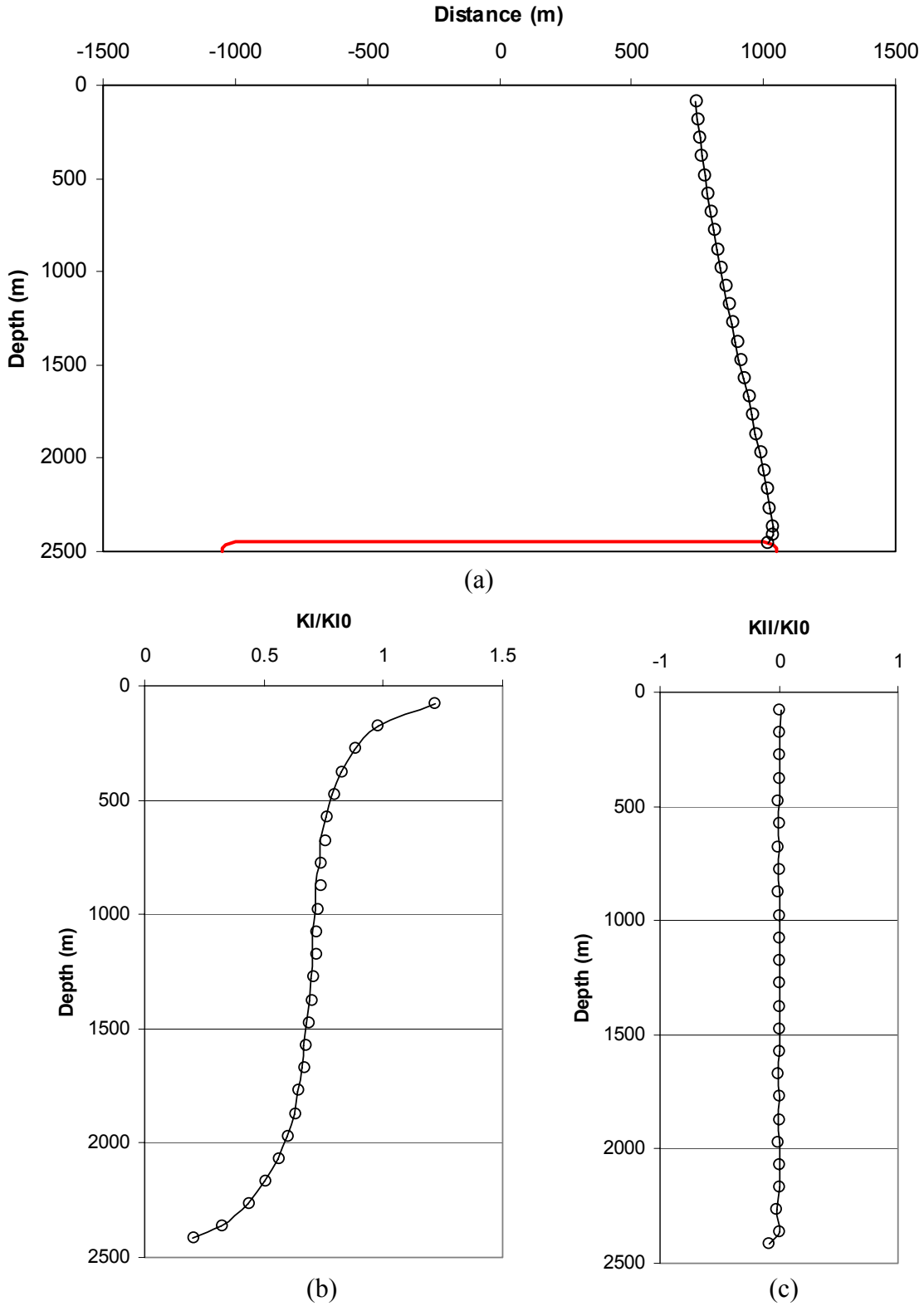

Figure 4.58 Comparison of results between horizontal and non-horizontal seafloor ($2c$ = 2 km): (a) dike trajectory, (b) normalized K_I, and (c) normalized K_{II}. Solid line indicates results in the non-horizontal seafloor, and circles indicate result in horizontal seafloor.

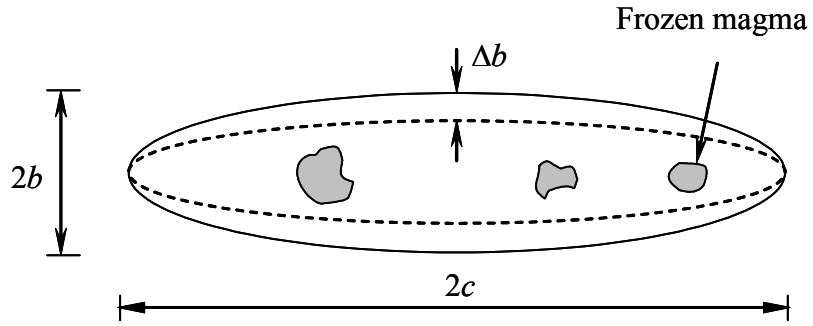

Figure 4.59 Shrinkage of the lens volume as a result of magma crystallization.

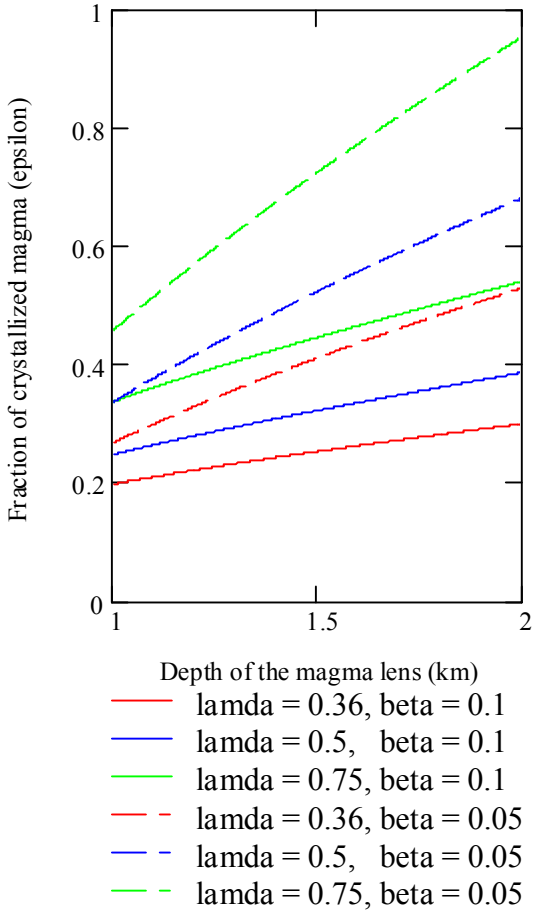

Figure 4.60 Critical fraction of the crystallized magma in the lens required for the dike initiation from the lens center.

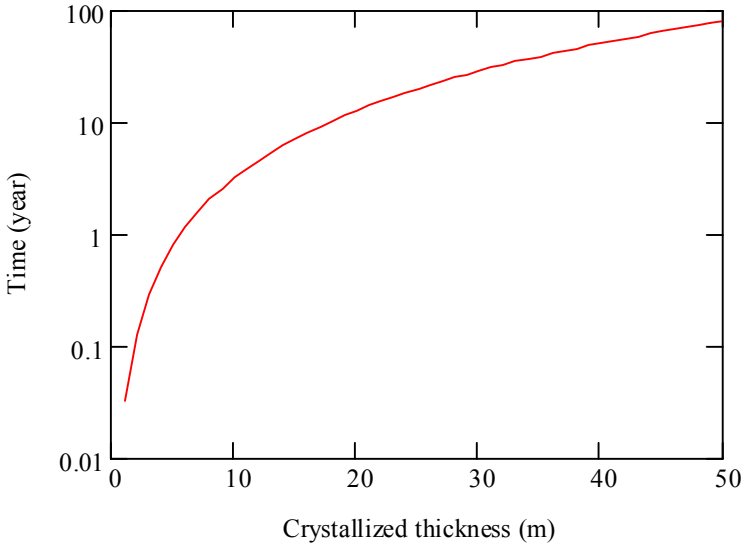

Figure 4.61 Time scale of magma crystallization.

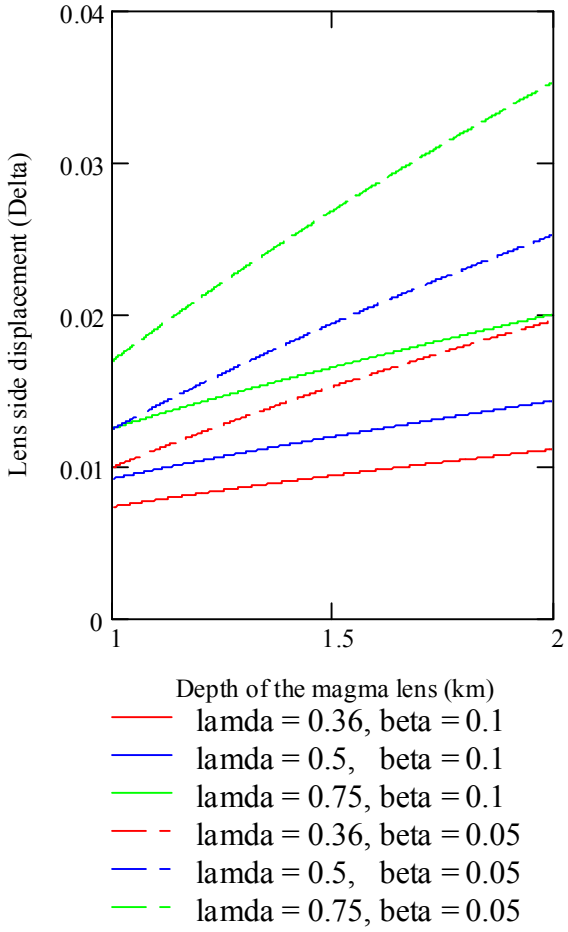

Figure 4.62 Normalized displacement of the lens sides at the center.

CHAPTER V

CONCLUSIONS

Hydraulic fracturing is an important and abundant process in both industrial applications and natural environments. The formation of hydraulic fractures includes nucleation, growth, and termination in numerous rock types and stress regimes, at scales ranging from microns to many kilometers. As a result, the fractures show complicated geometries, which reflect the complexity of the underlying physical mechanisms. Fracture segmentation, commonly observed at all scales and in all materials, contributes to this complexity in many ways. In particular, the mechanical interaction of fracture segments as well as the interaction of a fracture with other fractures, the Earth's surface, and pre-existing geological discontinuities strongly affect almost all hydraulic fracturing processes.

For more than five decades, hydraulic fracturing techniques have been widely used to enhance oil and gas production. Recent observations based on geological evidence, laboratory tests, and mineback experiments confirm that complex multisegmented hydraulic fractures are common phenomena. However, current hydraulic fracture models presume a single fracture, or neglect the interaction between the fracture segments. This is despite the fact that the interaction dramatically changes the simulated dimensions of the hydraulic fractures and their net pressures.

The current work is the first systematic quantitative study of the effects of the mechanical interaction in and between complex hydraulic fractures. A mathematical model, based on the boundary collocation method, has been developed. A typical field

case, a highly segmented vein, is studied and used to understand the effects of segment interaction at different spatial scales. For this well-mapped vein that represents a well constrained case, the simplest constitutive model, based on an ideal elastic material, has been tested for its capability to capture the complex behavior of multisegmented fractures.

The mathematical model is tested by comparing computed segment apertures to the measured apertures at three different spatial scales. By using this simple constitutive model and by including the effect of interaction between the segments, an excellent match was obtained at all considered scales. Only two net pressures were needed to fit 3,339 highly irregular measured apertures. This simulation also suggests that the interaction between the segments strongly affects the apertures of the fractures and their net pressures. In contrast, by neglecting the interaction between the segments, the net pressures can be grossly overestimated, by as much as an order of magnitude or more.

In addition, the concept of the effective fracture, as currently accepted in the literature, has been employed for a simple simulation of fractures with closely spaced and interacting segments. In the studied field case, the effective fracture model provided rather robust and accurate results. In general, however, due to the complex interplay between the parameters of segmentation, this concept may not always be applicable and may lead to unbounded inaccuracy.

Our computations recreate the final stage of the vein evolution. The simulated apertures are such as if they have been opened by the two calculated net pressures. These two distinct pressures indicate that the pressure communication between the two corresponding vein parts is weak or non-existent. Further geological interpretation, based on our results, is required to reconstruct the complete history of the vein (e.g., initiation,

propagation, fluid flow, and precipitation) that is well beyond the scope of this work. Yet, as long as the vein was pressurized, mechanical interaction was always a major mechanism regardless of whether other processes were active or not.

In most cases, very little (if any) directly measured data on fracture and material properties is available. An important example of such a weakly constrained case, involving hydraulic fracturing, is diking beneath the seafloor at mid-oceanic ridges. In this study, it is shown that the conventional scenario of a dike propagating from the center of the pressurized magma chamber to the ocean floor is not consistent with conventional fracture mechanics due to the fact that the chamber has the shape of a thin lens. Even at such a large scale (i.e., a kilometer or more), the mechanical principles of elastic interaction appear to be applicable. The dikes that initiate from the subsurface magma lens, and the magma lens itself, can be considered as mechanically interacting segments in an elastic half-space bounded by the seafloor.

Model calculations show that dike propagation from a thin axial magma lens beneath the seafloor depends primarily on the pressure magnitude within the magma lens. Excess magma pressure due to magma replenishment results in nearly vertical dike propagation originating from the vicinity of the tips of the lens. In contrast, a deficit of magma pressure stemming from hydrothermal cooling and magma crystallization results in vertical dike propagation from the center of the magma lens.

The propagating dike withdraws magma from the magma lens, which decreases the lens pressure. Despite this pressure decrease, the tip dike does propagate to the seafloor, because the dike-seafloor interaction is sufficiently strong to compensate for the

pressure decrease. In contrast, the central dike does not propagate to the seafloor, because of insufficient dike-seafloor interaction.

Since diking is likely to generate a region of high permeability near its margin, in addition to heat, the ongoing hydrothermal activity becomes localized. Our calculations suggest the possible positions of the propagating dikes. Consequently, comparing the observed locations of the hydrothermal sites with respect to that of the magma chamber could be useful for constraining the magma lens modeling.

The occurrence of hydrothermal vents near the tips of the magma lens at the Main Endeavor and Salty Dawg hydrothermal sites of the Juan de Fuca Ridge is consistent with an episode of recent pressurization of the subsurface magma lens and dike propagation from one of its tips. The fact that hydrothermal venting at the East Pacific Rise occurs above the center of the magma lens suggests that rapid hydrothermal cooling and magma crystallization in the lens may be important in controlling the permeability distribution at that site.

As has recently been speculated in the literature, the pressurization of the magma lens may be occurring by the diking originating from the underlying, deep magma chambers (also with a lens shape). Our quantitative results support this hypothesis. Furthermore, not only may these dikes pressurize overlying shallow magma lenses, but this can then also lead to the subsequent dike propagation from the tips of these shallow lenses to the seafloor.

Hence, the mechanical interaction is likely to have a pronounced effect on the behavior of complex natural and industrial hydraulic fractures and needs to be included into the modeling efforts.

APPENDIX A

FORTRAN 90 SOURCE CODE

```
!*********************************************************************
!* This program determines alpha and beta coefficients and           *
!* stress intensity factor for multiple segments.                    *
!*********************************************************************

program interact
use msflib
character(len=35) datfil
integer(kind=4) :: cnt, tcol
integer(kind=4), allocatable :: indx(:),l(:)
real, allocatable :: a(:,:),b(:)
real, allocatable :: x0(:),y0(:),alf(:),c(:),p(:),tau(:)
real, allocatable :: K1il(:),K1ir(:),K2il(:),K2ir(:)
! ax = b       : matrix type to solve
! x0(n), y0(n) : center coordinate
! alf(n)       : inclination angle
! c(n)         : half-length
datfil="ldata.dat"
write(*,*)
write(*,'(a\)') " Input data file name [ldata.dat] "
read(*,'(a)') datfil
if(datfil.EQ."")then
   datfil="ldata.dat"
endif
! n: total number of segments
! l(n): array of collocation points for each segment
! m & l(1): number of collocation points for first segment
open(unit=1,file=datfil)
read(1,*) n
allocate(l(n))
read(1,*) sx,sy,txy
read(1,*) (nd,dx0,dy0,dalf,dc,dp,dtau,l(i), i=1,n)
close(1)
m=l(1)
! tcol : total number of collocation points
! isize: size of linear system of equation
tcol=0
do i=1,n
   tcol=tcol+l(i)
enddo
isize=2*tcol
n=n-1
! Memory allocation for arrays
write(*,*)
write(*,*) "Preparing data."
write(*,*)
allocate(a(isize,isize),b(isize),indx(isize))
allocate(x0(n),y0(n),alf(n),c(n),p(n),tau(n))
allocate(K1il(n),K1ir(n),K2il(n),K2ir(n))
! Subroutine for converting data to reference format and assigning
! the reference segment
call dataconv(n+1,datfil,c_1)
! Read data
open(unit=9,file='$ldata1.dat')
read(9,*) pz,tz
read(9,*) (x0(i),y0(i),alf(i),c(i),p(i),tau(i),l(i),i=1,n)
close(9)
```

```
! Subroutine forming the system of equations to be solved
call form(a,n,l,m,x0,y0,alf,c,isize)
write(*,*)'The main matrix has been formed.'
! Subroutine forming the right-hand side of the equation system
call rside(b,n,l,m,p,tau,isize)
write(*,*)'The right hand side has been formed.'
! Subroutines solving the system of equation
call ludcmp(a,isize,isize,indx,d)
call lubksb(a,isize,isize,indx,b)
! Subroutine calculating SIF's and writing the output files
call res(b,n,l,m,c,K1il,K1ir,K2il,K2ir,c_1,isize)
! Deleting temporal data file created by subroutine dataconv
cnt = delfilesqq("$ldata1.*")
end program interact


!**********************************************************************
!* This subroutine performs the conversion of the input data to the   *
!* internal format and assigns reference segment.                     *
!**********************************************************************
subroutine dataconv(n,datfil,c_1)
integer n,nd
dimension x0(n),y0(n),alf(n),c(n),p(n),tau(n),l(n)
real x1(n),y1(n),alf1(n),c1(n),p1(n),tau1(n),s1(n),t1(n)
real sx,sy,txy,c_1
character*35 datfil
open(unit=9,file=datfil)
read(9,*) dn
read(9,*) sx,sy,txy
read(9,*) (nd,x0(i),y0(i),alf(i),c(i),p(i),tau(i),l(i),i=1,n)
close(9)
pi=acos(-1.0d0)
do i=1,n
   alf(i)=alf(i)/(180.d0/pi)
enddo
do i=1,n
   s1(i)=sy*cos(alf(i))**2+sx*sin(alf(i))**2-txy*sin(2.*alf(i))
   t1(i)=(sy-sx)/2.*sin(2.*alf(i))+txy*cos(2.*alf(i))
enddo
p0=p(1)+s1(1)
t0=tau(1)+t1(1)
c_1=c(1)
do i=1,n-1
   c1(i)=c(i+1)/c(1)
   xtmp=(x0(i+1)-x0(1))*cos(alf(1))+(y0(i+1)-y0(1))*sin(alf(1))
   x1(i)=xtmp/c(1)
   ytmp=-(x0(i+1)-x0(1))*sin(alf(1))+(y0(i+1)-y0(1))*cos(alf(1))
   y1(i)=ytmp/c(1)
   alf1(i)=alf(i+1)-alf(1)
   p1(i)=p(i+1)+s1(i)
   tau1(i)=tau(i+1)+t1(i)
enddo
! Modified input data is saved.
open(unit=9,file='$ldata1.dat')
write(9,*) p0,t0
write(9,'(6e12.4,i5)') (x1(i),y1(i),alf1(i),c1(i),p1(i),tau1(i),&
         l(i+1),i=1,n-1)
```

```
close(9)
end subroutine dataconv


!**********************************************************************
!* This subroutine forms the matrix of the equations system to be     *
!* solved.                                                            *
!**********************************************************************
subroutine form(a,n,l,m,x,y,alf,c,isize)
dimension a(isize,isize)
dimension x(n),y(n),alf(n),c(n),l(n)
! Calculate tractions induced by each segment on all other segments.
! Reference segment is excluded at this point.
pi=acos(-1.0d0)
dx=0.
dy=0.
dalf=0.
lsumt=0
do i5=1,n
   lsumt=lsumt+l(i5)
enddo
do i=1,n          ! i- row number
   write(*,*)'Computing tractions induced by segment', i
   lsumi=0
   do i3=1, i-1
      lsumi=lsumi+l(i3)
   enddo
   do li=1,l(i)
      xli=x(i)+c(i)*cos(alf(i))*cos(pi*(2.*li-1.)/2./l(i))
      yli=y(i)+c(i)*sin(alf(i))*cos(pi*(2.*li-1.)/2./l(i))
      xp=cos(pi*(2.*li-1)/2./l(i))
      do j=1,n    ! j- column number
         lsumj=0
         do i4=1, j-1
            lsumj=lsumj+l(i4)
         enddo
         if(j /= i)then
         do lj=1,l(j)
            dx=(xli-x(j))*cos(alf(j))/c(j)+(yli-y(j))*sin(alf(j))/c(j)
            dy=-(xli-x(j))*sin(alf(j))/c(j)+(yli-y(j))*cos(alf(j))/c(j)
            dalf=alf(i)-alf(j)
         call coef2( a(lsumi+li,lsumj+lj) , &
                     a(lsumi+li,lsumt+lsumj+lj), &
                     a(lsumt+lsumi+li,lsumj+lj), &
                     a(lsumt+lsumi+li,lsumt+lsumj+lj),&
                       dx,dy,dalf,lj)
         enddo
         else
! Calculate tractions induced by each segment on itself.
! The reference segment is excluded.
         do lj=1,l(i)              ! lj- column number
            a(lsumi+li,     lsumj+lj)=Um(xp,lj-1)
            a(lsumi+li,     lsumt+lsumj+lj)=0
            a(lsumt+lsumi+li, lsumj+lj)=0
            a(lsumt+lsumi+li, lsumt+lsumj+lj)=Um(xp,lj-1)
         enddo
         endif
```

```
      enddo
   enddo
enddo
! Calculate tractions induced by each segment on the reference one.
write(*,*)'Computing remaining tractions.'
do i=1,n                                  ! i- row number
   lsumi=0
   do i3=1, i-1
      lsumi=lsumi+l(i3)
   enddo
   do li=1,l(i)
      xli=x(i)+c(i)*cos(alf(i))*cos(pi*(2.*li-1.)/2./l(i))
      yli=y(i)+c(i)*sin(alf(i))*cos(pi*(2.*li-1.)/2./l(i))
      do j=1,m                            ! j- column number
         call coef2(a(lsumi+li,2*lsumt+j) ,&
                    a(lsumi+li,2*lsumt+m+j), &
                    a(lsumt+lsumi+li,2*lsumt+j),&
                    a(lsumt+lsumi+li,2*lsumt+m+j),&
                      xli, yli, alf(i), j)
      enddo
   enddo
enddo
! Calculate tractions induced by the reference segment on all
! other segments.
do i=1,m                                  ! i- row number
   xp=cos(pi*(2.*i-1)/2./m)
   do j=1,n                               ! j- colomn number
      lsumj=0
      do i4=1, j-1
         lsumj=lsumj+l(i4)
      enddo
      do lj=1,l(j)
         dx=(xp-x(j))*cos(alf(j))/c(j)-y(j)*sin(alf(j))/c(j)
         dy=-(xp-x(j))*sin(alf(j))/c(j)-y(j)*cos(alf(j))/c(j)
         dalf=-alf(j)
         call coef2(a(2*lsumt+i,lsumj+lj), &
                    a(2*lsumt+i,lsumt+lsumj+lj),&
                    a(2*lsumt+m+i,lsumj+lj), &
                    a(2*lsumt+m+i,lsumt+lsumj+lj),&
                      dx , dy, dalf, lj)
      enddo
   enddo
enddo
! Calculate tractions induced by the reference segmen on itself.
do i=1,m                                  ! i- row number
   xp=cos(pi*(2.*i-1)/2./m)
   do j=1,m                               ! j- colomn number
      a(2*lsumt+i,2*lsumt+j)=Um(xp,j-1)
      a(2*lsumt+i,2*lsumt+m+j)=0
      a(2*lsumt+m+i,2*lsumt+j)=0
      a(2*lsumt+m+i,2*lsumt+m+j)=Um(xp,j-1)
   enddo
enddo
end subroutine form
```

```
!**********************************************************************
!* This subroutine forms the right-hand side of the equation system   *
!* to be solved.                                                      *
!**********************************************************************
subroutine rside(b,n,l,m,p,tau,isize)
dimension b(isize),p(n),tau(n),l(n)
pi=acos(-1.0d0)
lsumt=0
do i5=1,n
   lsumt=lsumt+l(i5)
enddo
do i=1,n
   lsumi=0
   do i3=1,i-1
      lsumi=lsumi+l(i3)
   enddo
   sigs=tau(i)
   sigt=p(i)
   do li=1,l(i)
      b(lsumi+li)=sigt
      b(lsumt+lsumi+li)=sigs
   enddo
enddo
open(unit=9, file = '$ldata1.dat')
read(9,*) pz,tz
close(9)
p0=pz
tau0=tz
do i=1,m
   sigs=tau0
   sigt=p0
   b(2*lsumt+i)=sigt
   b(2*lsumt+m+i)=sigs
enddo
end subroutine rside
```

```
!*********************************************************************
!* This subroutine (Press et al. p38, 1992) is for the decomposition. *
!* It was slightly changed from original one.                         *
!*********************************************************************
subroutine ludcmp(a,n,np,indx,d)
integer n,np,indx(n),nmax
real d,a(np,np),tiny
parameter (nmax=20000, tiny=1.0d-20)
integer i,imax,j,k
real aamax,dum,sum,vv(nmax)
d=1.
write(*,*) 'Checking matrix.'
do i=1,n
   aamax=0.
   do j=1,n
      if(abs(a(i,j)) > aamax) then
         aamax=abs(a(i,j))
      endif
   enddo
   vv(i)=1./aamax
enddo
write(*,*) 'Decomposition.'
do j=1,n
   if(mod(j,100) == 0)then
   write(*,*)''
   call current_time
   write(*,*) j,' out of',n, ' equations have been processed.'
   endif
   do i=1,j-1
      sum=a(i,j)
      do k=1,i-1
         sum=sum-a(i,k)*a(k,j)
      enddo
      a(i,j)=sum
   enddo
   aamax=0.
   do i=j,n
      sum=a(i,j)
      do k=1,j-1
         sum=sum-a(i,k)*a(k,j)
      enddo
      a(i,j)=sum
      dum=vv(i)*abs(sum)
      IF(dum >= aamax) then
         imax=i
         aamax=dum
      endif
   enddo
      if(j /= imax) then
         do k=1,n
            dum=a(imax,k)
            a(imax,k)=a(j,k)
            a(j,k)=dum
         enddo
         d=-d
         vv(imax)=vv(j)
      endif
```

```
      indx(j)=imax
      if(a(j,j) == 0.) then
         a(j,j) = tiny
      endif
      if(j /= n) then
         dum=1./a(j,j)
         do i=j+1,n
            a(i,j)=a(i,j)*dum
         enddo
      endif
enddo
end subroutine ludcmp


!*********************************************************************
!* This subroutine (Press et al. p38, 1992) performs forward         *
!* substitution and backsubstitution.                                *
!*********************************************************************
subroutine lubksb(a,n,np,indx,b)
integer n, np, indx(n)
real a(np,np), b(n)
integer i, ii, j, ll
real sum
ii=0
write(*,*)
write(*,*) 'Forward substitution.'
do i=1,n
   ll=indx(i)
   sum=b(ll)
   b(ll)=b(i)
   if(ii /= 0) then
      do j=ii,i-1
         sum=sum-a(i,j)*b(j)
      enddo
   else if(sum /= 0.) then
      ii=i
   endif
   b(i)=sum
enddo
write(*,*) 'Back substitution.'
   do i=n,1,-1
      sum=b(i)
      do j=i+1, n
         sum=sum-a(i,j)*b(j)
      enddo
      b(i)=sum/a(i,i)
   enddo
end subroutine lubksb
```

```
!*********************************************************************
!* This subroutine calculates SIFs and writes the output results.     *
!*********************************************************************
subroutine res(b,n,l,m,c,K1il,K1ir,K2il,K2ir,c_1,isize)
character*35 alffil,betfil,intfil
integer l(n)
real b(isize)
real K1l,K2l,K1r,K2r
real c(n),c_1
real K1il(n),K1ir(n),K2il(n),K2ir(n)
pi=acos(-1.0d0)
! In some problems (e.g., interaction
! between a large fracture and a set of small microfractures), it is
! convenient to consider one fracture as a reference one.
! This is done here for the sake of convenience only.
! Introduce the reference segment of 2*c0 length:
c0=1.0d0
c01 = sqrt(pi*c0)
alffil="alpha.txt"
write(*,'(a\)') " File name for alpha coefficients [alpha.txt] "
read(*,'(a)') alffil
if(alffil == "") then
   alffil="alpha.txt"
endif
write(*,'(a\)') " File name for beta coefficients [beta.txt] "
read(*,'(a)') betfil
if(betfil =="") then
   betfil="beta.txt"
endif
open(unit=4, file=alffil)
open(unit=5, file=betfil)
lsumt=0
do i5=1,n
   lsumt=lsumt+l(i5)
enddo
i=0
write(4,'(x,i3,x,e12.4)')(i+1,b(2*lsumt+li),li=1,m)    ! alpha.txt
write(5,'(x,i3,x,e12.4)')(i+1,b(2*lsumt+m+li),li=1,m)  ! beta.txt
do i=1,n
   lsumi=0
   do i3=1,i-1
      lsumi=lsumi+l(i3)
   enddo
   K1il(i)=0.
   K1ir(i)=0.
   K2il(i)=0.
   K2ir(i)=0.
   do li=1,l(i)
      K1il(i)=K1il(i)+sqrt(pi*c(i))*(-1)**(li+1)*b(lsumi+li)
      K2il(i)=K2il(i)+sqrt(pi*c(i))*(-1)**(li+1)*b(lsumt+lsumi+li)
      K1ir(i)=K1ir(i)+sqrt(pi*c(i))*b(lsumi+li)
      K2ir(i)=K2ir(i)+sqrt(pi*c(i))*b(lsumt+lsumi+li)
   enddo
   write(4,'(x,i3,x,e12.4)')(i+1, b(lsumi+li),li=1,l(i))
   write(5,'(x,i3,x,e12.4)')(i+1, b(lsumt+lsumi+li),li=1,l(i))
enddo
close(4)
```

```
close(5)
K1l=0.
K2l=0.
K1r=0.
K2r=0.
do i=1,m
   K1l=K1l+c01*(-1)**(i+1)*b(2*lsumt+i)
   K2l=K2l+c01*(-1)**(i+1)*b(2*lsumt+m+i)
   K1r=K1r+c01*b(2*lsumt+i)
   K2r=K2r+c01*b(2*lsumt+m+i)
enddo
write(*,'(a\)')" File name for SIFs [inten.txt] "
read(*,'(a)') intfil
if(intfil == "")then
   intfil="inten.txt"
endif
cc=sqrt(c_1)
open(unit=4,file=intfil)
write(4,*)'-------------------------------------------------------'
write(4,*)'  n     KI_left      KI_right     KII_left    KII_right'
write(4,*)'-------------------------------------------------------'
i=0
write(4,'(x,i3,x,e12.4,x,e12.4,x,e12.4,x,e12.4)') i+1, cc*k1l,&
          cc*k1r, cc*k2l, cc*k2r
do i=1,n
   write(4,'(x,i3,x,e12.4,x,e12.4,x,e12.4,x,e12.4)') i+1, cc*k1il(i),&
              cc*k1ir(i),cc*k2il(i),cc*k2ir(i)
enddo
close(4)
end subroutine res


!**********************************************************************
!* This is an auxiliary subroutine for calculating functions a0,b0,c0,*
!* d0 characterizing tractions generated by a segment on the place of *
!* another segment. This subroutine will be used by subroutine form   *
!* forming the main matrix of the equations set to be solved.         *
!**********************************************************************
subroutine coef2(a0,b0,c0,d0,x,y,alf,m)
complex rm, gm1, gm2
complex crm, cgm1
real Im, Jm, Lm, Km
real cIm, cJm
complex ed, z0, z0c
pi=acos(-1.0)
ed=(0.,1.)
tet=atan2(y,x)
tet1=atan2(y,x-1)
tet2=atan2(y,x+1)
r=sqrt(x*x+y*y)
r1=sqrt((x-1)*(x-1)+y*y)
r2=sqrt((x+1)*(x+1)+y*y)
z0=r*cdexp(ed*tet)
rm=(z0-sqrt(r1*r2)*cdexp(ed*(tet1+tet2)/2.))**m
gm1=-rm/sqrt(r1*r2)/cdexp(ed*(tet1+tet2)/2.)
Im=real(gm1)
Jm=-aimag(gm1)
```

```
gm2=(m/sqrt(r1*r2)/cdexp(ed*(tet1+tet2)/2.)+z0/(z0*z0-1))*gm1
Lm=-real(gm2)
Km=aimag(gm2)
! Calculate Im(x,-y) and Jm(x ,-y).
tetm=atan2(-y,x)
tetm1=atan2(-y,x-1)
tetm2=atan2(-y,x+1)
r=sqrt(x*x+y*y)
r1=sqrt((x-1)*(x-1)+y*y)
r2=sqrt((x+1)*(x+1)+y*y)
z0c=r*cdexp(ed*tetm)
crm=(z0c-sqrt(r1*r2)*cdexp(ed*(tetm1+tetm2)/2.))**m
cgm1=-crm/sqrt(r1*r2)/cdexp(ed*(tetm1+tetm2)/2.)
cIm=real(cgm1)
cJm=-aimag(cgm1)
a0=1./2.*(2.*Im+(cIm-Im-2.*y*Km)*cos(2*alf)-(cJm+Jm-2.*y*Lm)&
   *sin(2*alf))
b0=-1./2.*(2.*Jm+(cJm-Jm+2.*y*Lm)*cos(2*alf)+(cIm+Im+2.*y*Km)&
   *sin(2*alf))
c0=1./2.*((cJm+Jm-2.*y*Lm)*cos(2*alf)+(cIm-Im-2.*y*Km)&
   *sin(2*alf))
d0=-1./2.*(-(cIm+Im+2.*y*Km)*cos(2*alf)+(cJm-Jm+2.*y*Lm)&
   *sin(2*alf))
end subroutine coef2


!**********************************************************************
!* Function for creating Chebyshev polynomial of second kind          *
!**********************************************************************
function Um(x,m)
Um=sin((m+1)*acos(x))/sin(acos(x))
end function Um


!**********************************************************************
!* Subroutine showing current time and date                           *
!**********************************************************************
subroutine current_time()
integer(2)  tmpday,tmpmonth,tmpyear
integer(2)  tmphour,tmpminute,tmpsecond,tmphund
character(1) mer
call getdat(tmpyear,tmpmonth,tmpday)
call gettim(tmphour,tmpminute,tmpsecond,tmphund)

if(tmphour > 12)then
   mer = 'p'
   tmphour = tmphour - 12
   else
   mer = 'a'
   endif
   write(*,'(10x,i2,"/",i2.2,"/",i4.4,",",x,i2,":",i2.2,":",i2.2,x,a,&
        "m")') tmpmonth,tmpday,tmpyear,tmphour,tmpminute,tmpsecond,mer
end subroutine current_time
```

APPENDIX B

CONVERGENCE STUDY FOR ALL INTERACTING CASES AT THE MICROSCALE

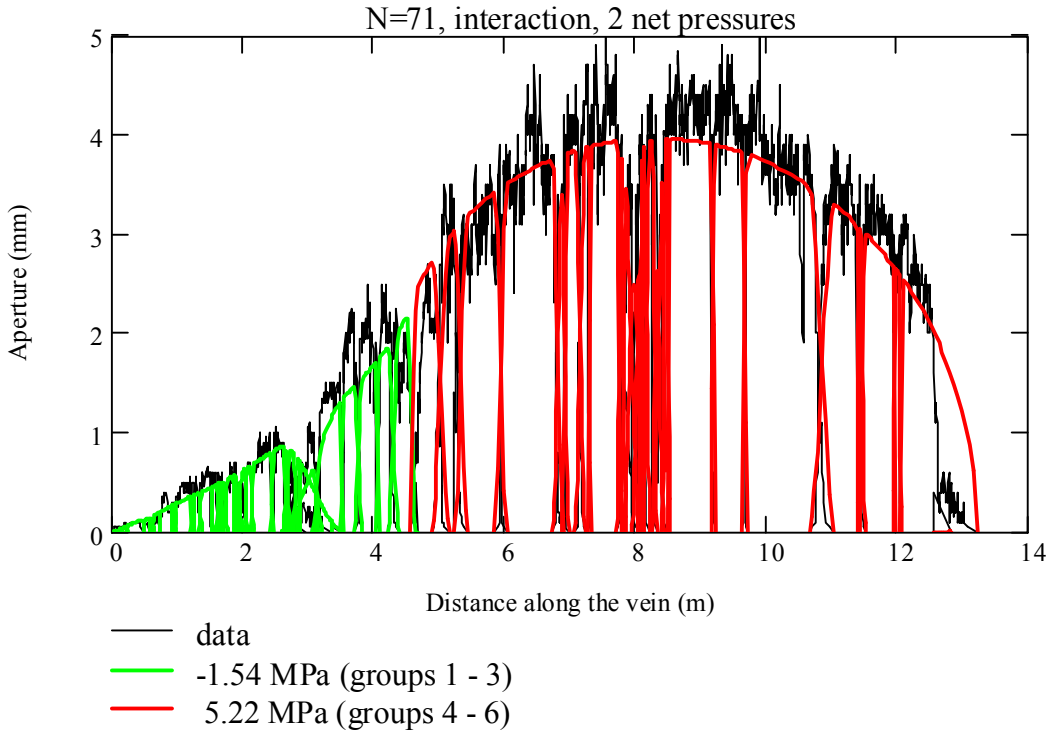

(a)

Figure B.1 Application of two pressures for interacting segments at the microscale after an increase in the number of collocation points: (a) 50% increase, and (b) 75% increase (values in the legend indicate the computed net pressure magnitudes).

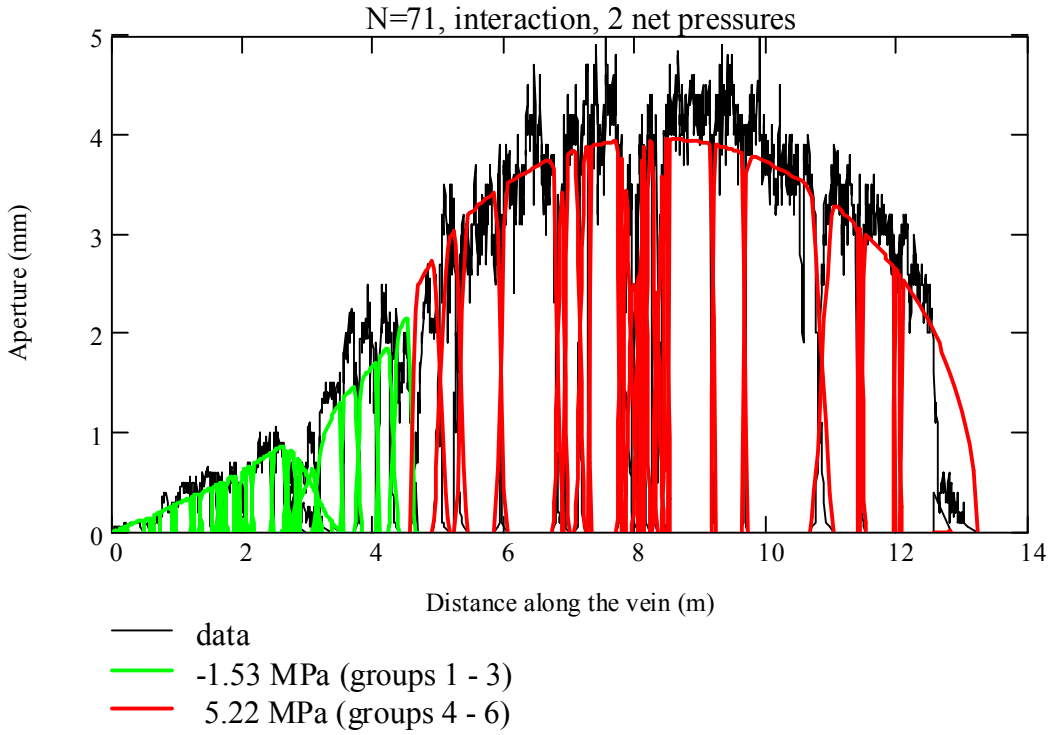

(b)

Figure B.1 (Continued)

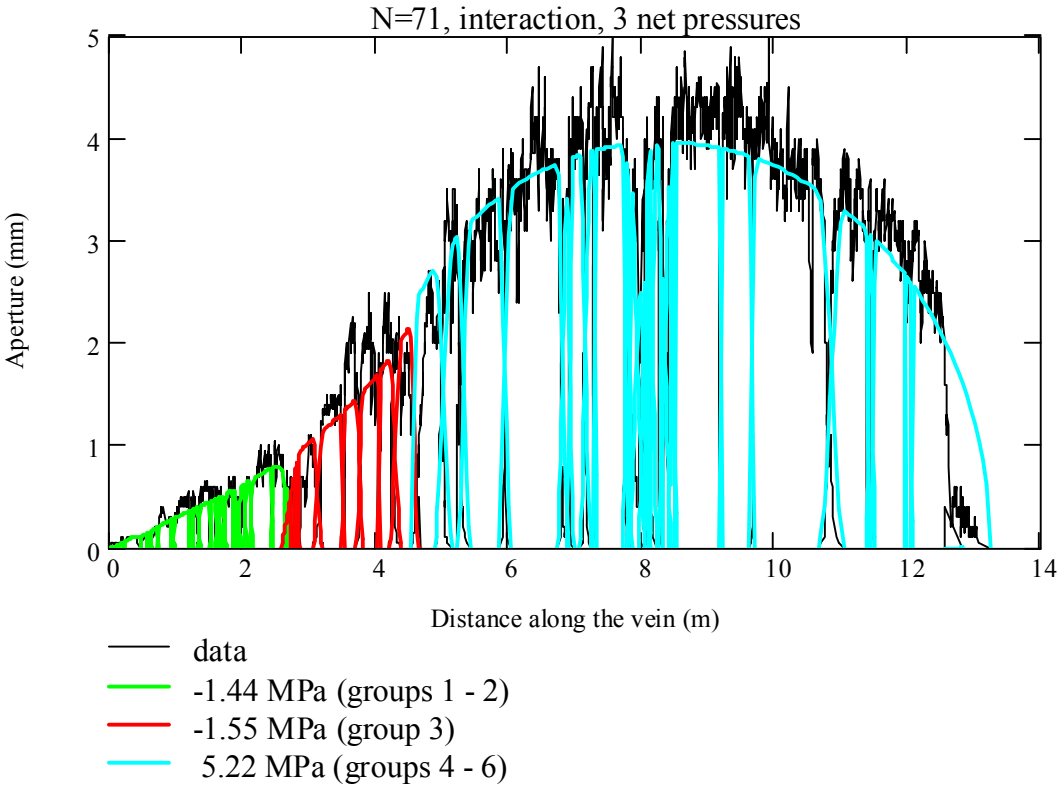

(a)

Figure B.2 Application of three pressures for interacting segments at the microscale after an increase in the number of collocation points: (a) 50% increase, and (b) 100% increase (values in the legend indicate the computed net pressure magnitudes).

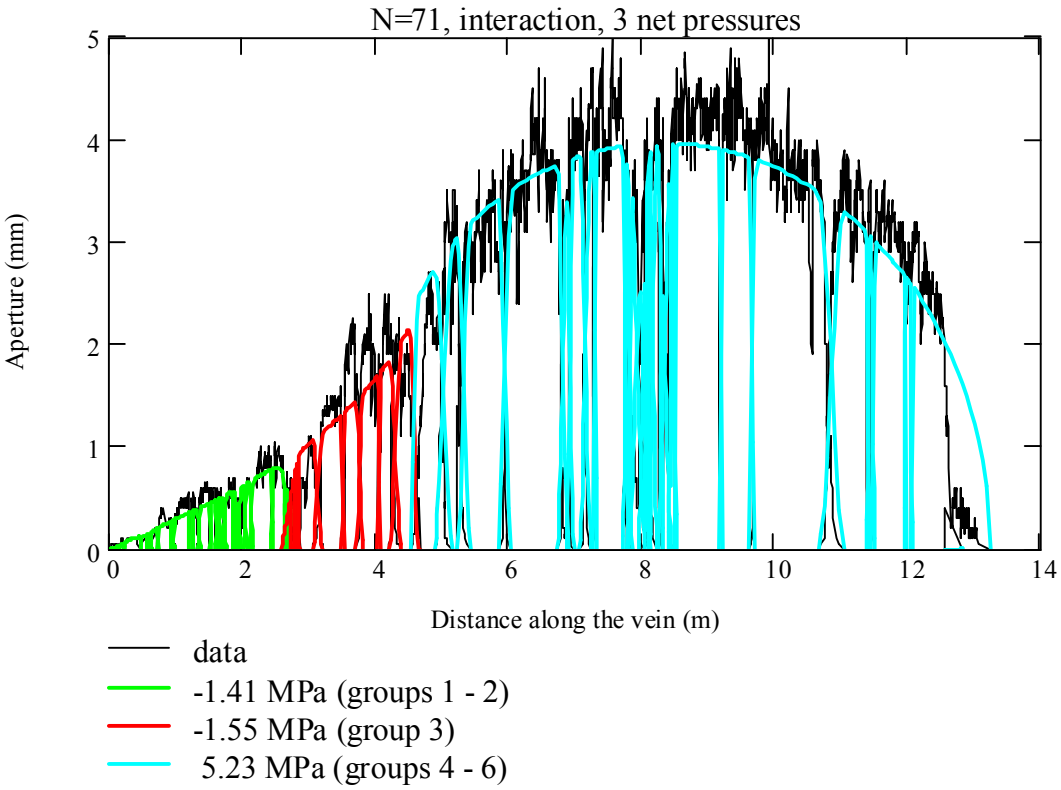

(b)

Figure B.2 (Continued).

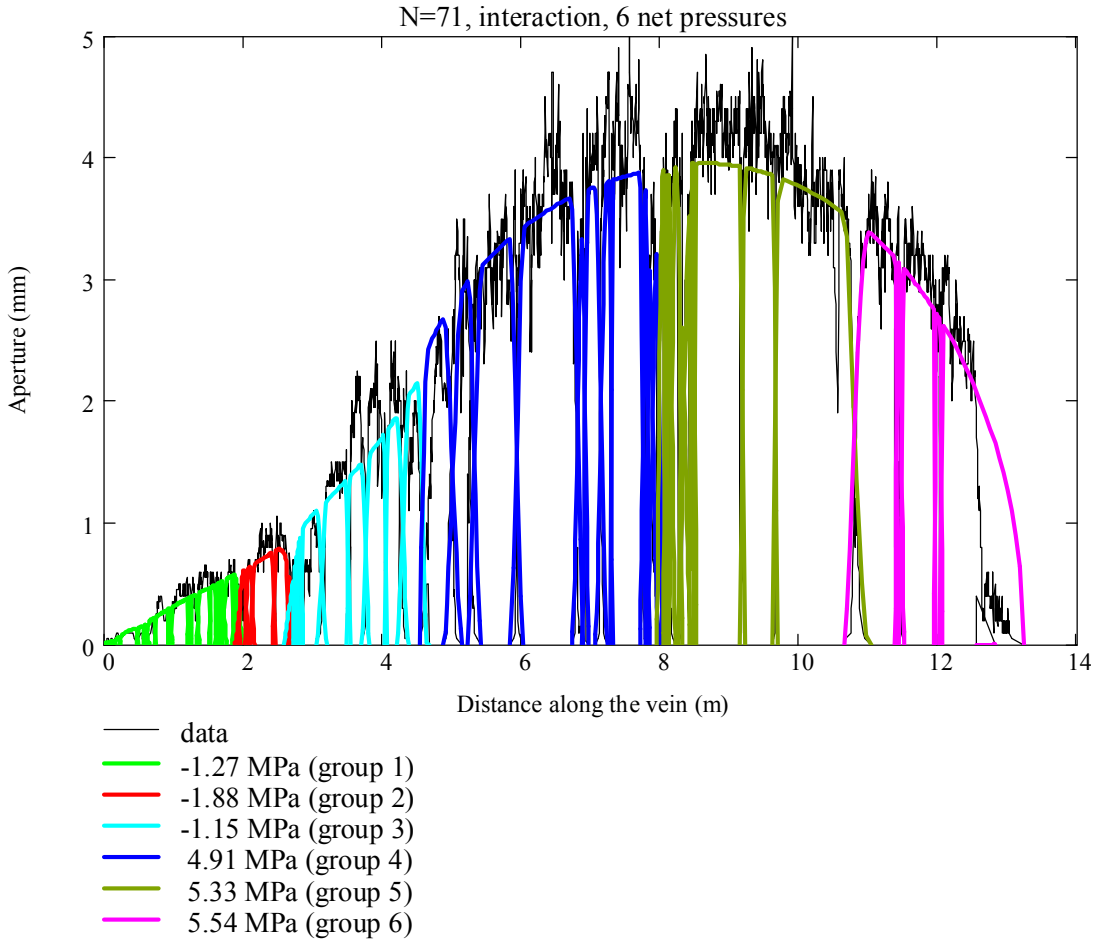

(a)

Figure B.3 Application of six pressures for interacting segments at the microscale after an increase in the number of collocation points: (a) 50% increase, and (b) 100% increase (values in the legend indicate the computed net pressure magnitudes).

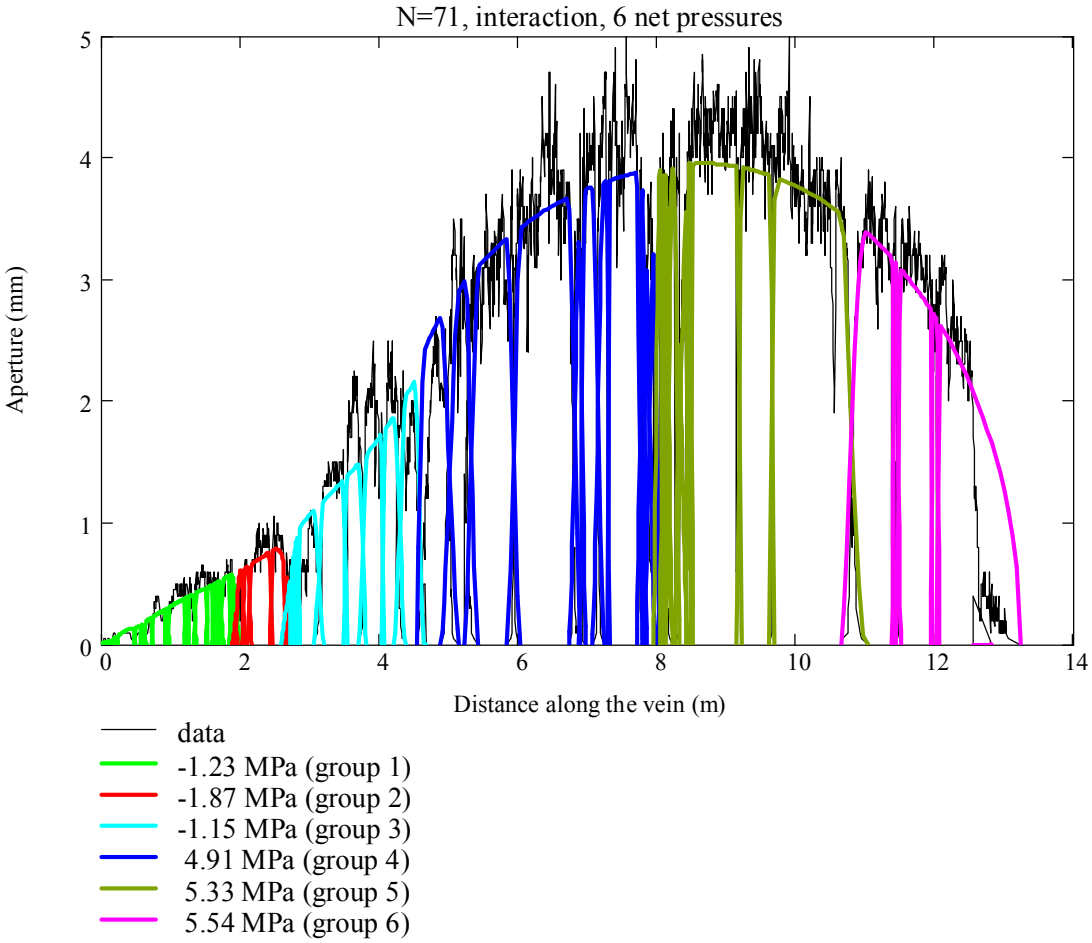

(b)

Figure B.3 (Continued).

Table B.1 Change of net pressures for all interacting cases at the microscale after an increase in the number of collocation points for the convergence study.

Number of net pressures		2			3			6		
Number of collocation points		11,515	17,273	20,166	9,775	14,663	19,550	9,775	14,663	19,550
Number of solved equations		23,030	34,546	40,332	19,550	29,326	39,100	19,550	29,326	39,100
Increase of collocation points		-	50%	75%	-	50%	100%	-	50%	100%
Net pressure, MPa	Group 1	-1.52	-1.54	-1.53	-1.38	-1.44	-1.41	-1.17	-1.27	-1.23
	Group 2							-1.89	-1.88	-1.87
	Group 3				-1.59	-1.55	-1.55	-1.15	-1.15	-1.15
	Group 4	5.23	5.22	5.22	5.24	5.22	5.23	4.90	4.91	4.91
	Group 5							5.34	5.33	5.33
	Group 6							5.55	5.54	5.54

APPENDIX C

MODELING 35 ECHELON MINETTE DIKE SEGMENTS NEAR SHIP ROCK, NEW MEXICO

The apertures of the 35 minette dike segments near Ship Rock, New Mexico are modeled by using the boundary collocation method and compared to the results by *Delaney and Pollard* [1981]. The dike consists of 35 discrete segments arranged in en echelon, with an outcrop length of approximately 2,900 m, an average thickness of 2.3 m, and a maximum thickness of 7.2 m. All data used for our simulation was obtained from the work of *Delaney and Pollard* [1981].

Figure C.1 shows the map view and opening of the dike segments. Figure C.2 shows the comparison of computed and measured apertures following the same procedure that was used by *Delaney and Pollard* [1981]. Based on the subsurface consideration, they suggested that some of the 35 segments are merged so that mechanically, the entire dike behaves as having only 10 segments. We obtained the pressure-to-modulus ratio of 0.0017 for the dike with 10 segments, which is similar to the value of 0.0018 that was found by *Delaney and Pollard* [1981].

Figure C.3 shows the mode I stress intensity factors K_I normalized by that for the non-interacting segments for the boundary collocation method (used in this work) as compared to the method of successive approximations (implemented by *Delaney and Pollard* [1981]). The results are similar and show the good accuracy of the computations by *Delaney and Pollard* [1981].

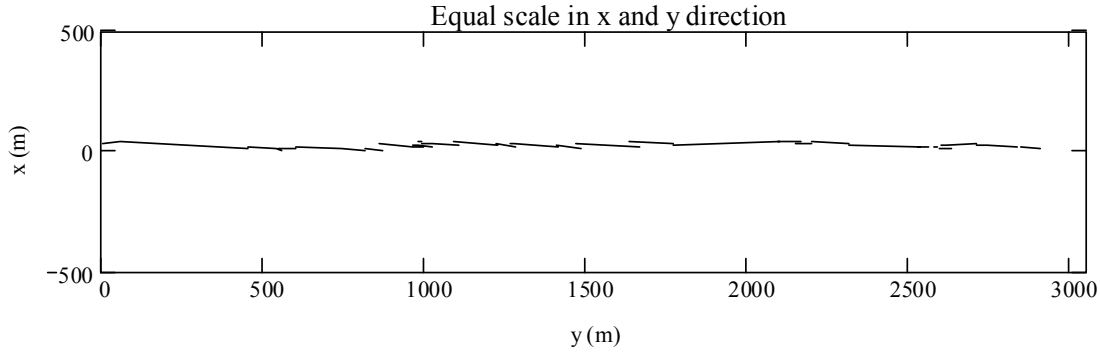

(a)

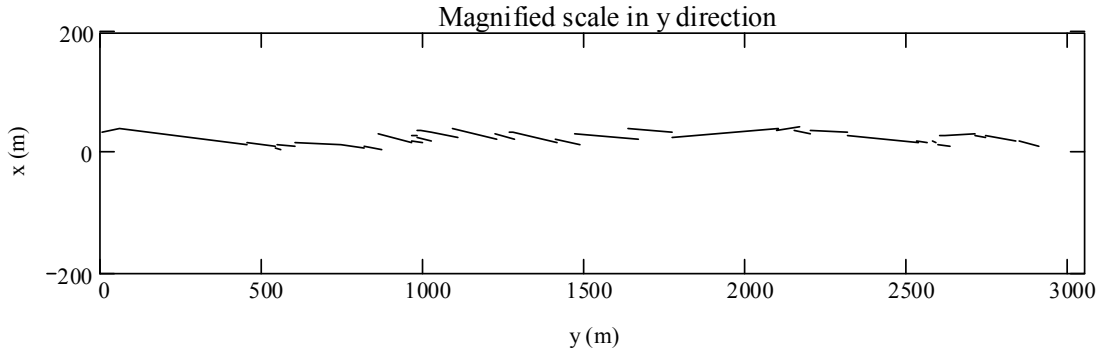

(b)

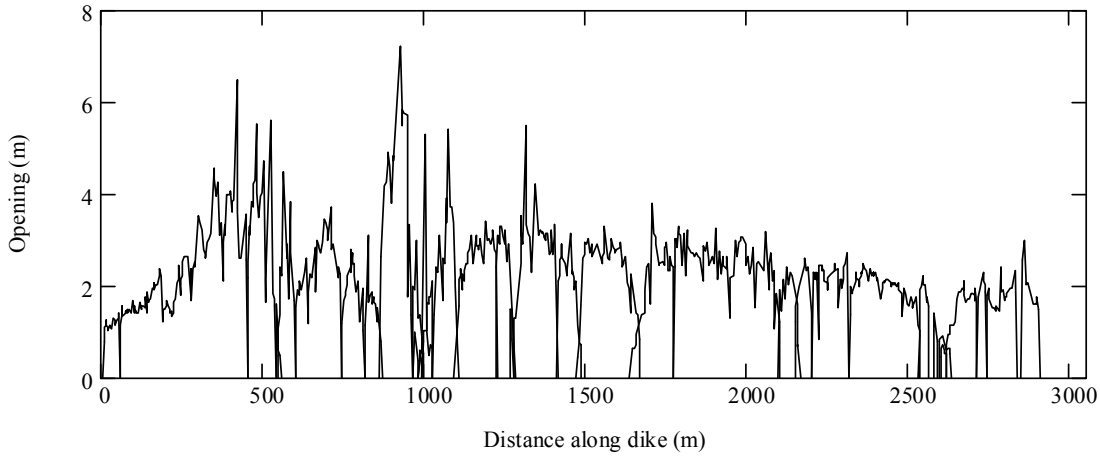

(c)

Figure C.1 Map view and opening of the 35 echelon dike segments, Ship Rock, New Mexico [*Delaney and Pollard*, 1981]: (a) map view for equal scale, (b) map view at magnified scale in *y* direction, and (c) opening versus distance along the dike segments.

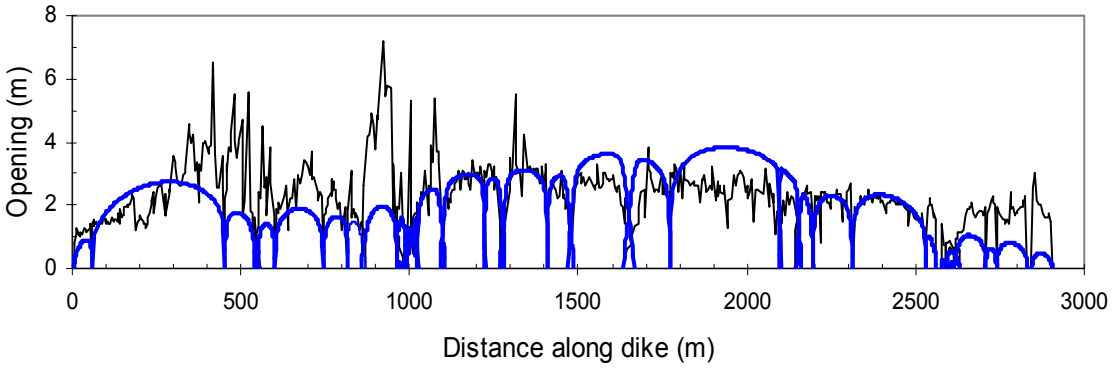

(a)

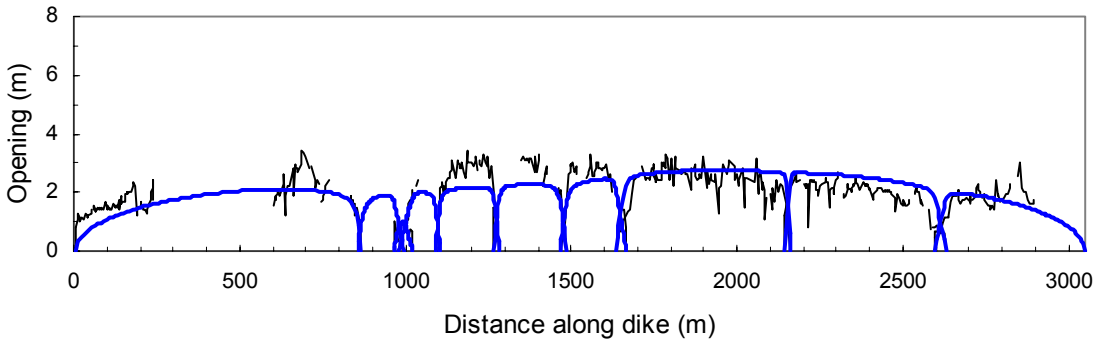

(b)

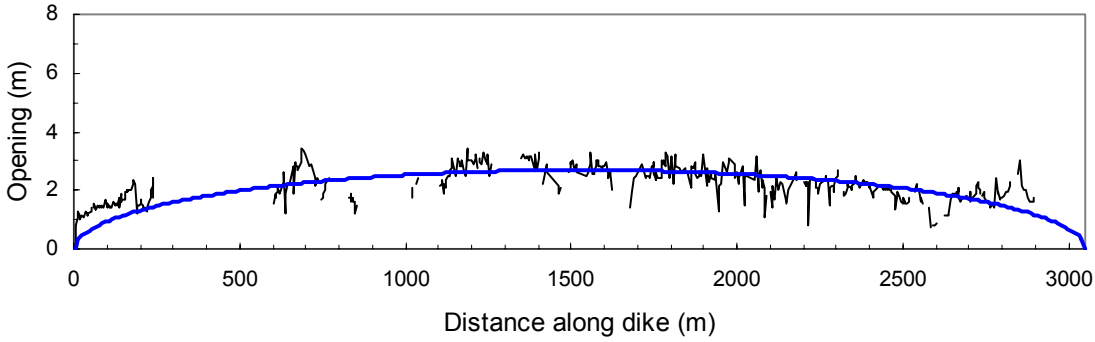

(c)

Figure C.2 Comparison of computed and measured openings for a single uniform pressure by using boundary collocation method: (a) 35 dike segments model, (b) 10 dike segments model obtained after removing data for brecciated parts of dike wall, joining together closely spaced segments, and removing data near adjacent ends of jointed segments, and (c) single dike model obtained by joining all segments together and removing data near segment ends.

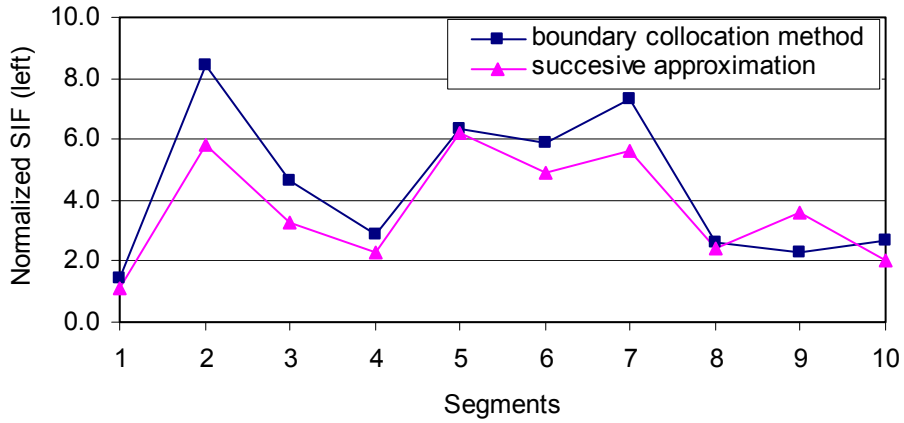

(a)

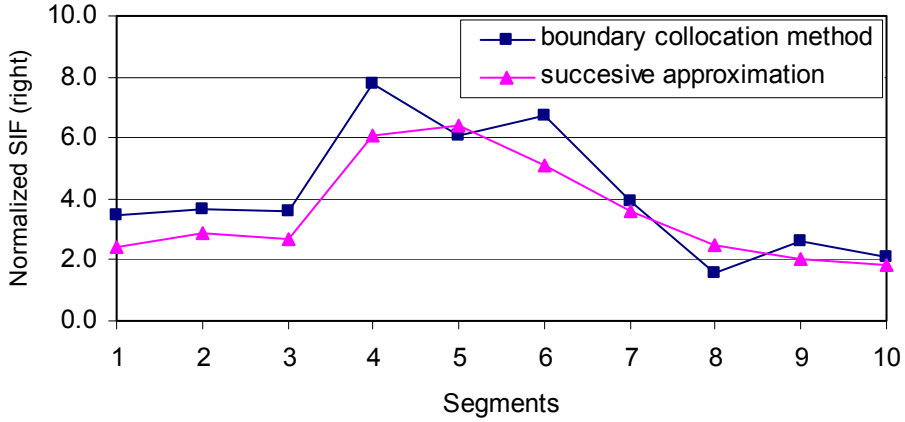

(b)

Figure C.3 Comparison of K_I SIFs between boundary collocation method and successive approximation for 10 dike segments model: (a) normalized SIF (left), and (b) normalized SIF (right).

APPENDIX D

TESTING PROBLEMS FOR DIKE PROPAGATION FROM THE CENTER AND THE TIP OF THE MAGMA LENS

D.1 Testing problems for dike propagation from the lens center

It is necessary to verify the dimensionless functions (f_Z^{dike}, $f_Z^{chamber}$, and k_{IZ}^{dike}) and displacements obtained from numerical simulations of the vertical propagation of a fracture (dike) from the center of a horizontal fracture (i.e., magma lens) in a half-space (Figure 4.26) to avoid significant errors and to verify the results. Although there is no analytical solution for comparison in a half-space, some specific cases can be compared approximately.

In Problem A of Figure 4.26, the dimensionless function $f_A^{chamber}(50)$ (Table 4.3) can be compared to the dimensionless function, $f_A(0)$ of (4.78), that is derived analytically for the magma volume before the dike propagation. Repeating (4.78) here gives

$$f_A(0) = 2\pi(1-\nu^2)\left[1+\frac{3c^2}{4H^2}\right] \tag{D.1}$$

Table D.1 shows a comparison of the dimensionless functions $f_A(0)$ and $f_A^{chamber}(50)$. It is expected that $f_A(0)$ is always less than $f_A^{chamber}(50)$. However, for H = 1 km case, $f_A(0)$ is greater than $f_A^{chamber}(50)$, because the chamber crack is close to the half-space boundary, which may result in a slight deviation.

Table D.1 Comparison of dimensionless functions $f_A(0)$ and $f_A^{chamber}(50)$, for dike propagation from the lens center.

Function	H = 1 km and $2c$ = 1 km	H = 1.5 km and $2c$ = 1 km
$f_A(0)$	6.941	6.332
$f_A^{chamber}(50)$	6.929	6.465

In problem B of Figure 4.26, the dimensionless functions for small propagation in a half-space (e.g., l = 50 m or 100 m) can be compared with those in the semi-infinite space (Figure D.1a). Analytical expressions for the dimensionless functions, f_B^{dike} and k_{IB}^{dike}, in a semi-infinite space are [*Tada et al*., 1985]

$$f_B^{dike} = 1.258\pi(1-\nu^2)\frac{l^2}{c^2} \tag{D.2}$$

$$k_{IB}^{dike} = 1.1215\sqrt{\frac{l}{c}} \tag{D.3}$$

Compared to the analytical solutions, the computed dimensionless functions are in good agreement (Tables D.2 and D.3). Additionally, the half-opening profile of a dike in a semi-infinite space is available [*Tada et al*., 1985]:

$$\delta(y) = \frac{2p_Z(1-\nu^2)}{E}\sqrt{l^2-y^2}\left[1.454 - 0.727\left(\frac{y}{l}\right) + 0.618\left(\frac{y}{l}\right)^2 - 0.224\left(\frac{y}{l}\right)^3\right] \tag{D.4}$$

Compared to the analytical solutions, they are in good agreement (Figure D.2).

Table D.2 Comparison of dimensionless function, f_B^{dike}, for dike propagation from the lens center.

Function	H = 1 km and 2c = 1 km		H = 1.5 km and 2c = 1 km	
	l = 50 m	l = 100 m	l = 50 m	l = 100 m
Tada et al. [1985]	0.037	0.147	0.037	0.147
This work	0.036	0.143	0.036	0.144

Table D.3 Comparison of dimensionless function, k_{IB}^{dike}, for dike propagation from the lens center.

Function	H = 1 km and 2c = 1 km		H = 1.5 km and 2c = 1 km	
	l = 50 m	l = 100 m	l = 50 m	l = 100 m
Tada et al. [1985]	0.355	0.502	0.355	0.502
This work	0.350	0.491	0.350	0.492

In problem C of Figure 4.26, the dimensionless functions of small propagation in a half-space can be compared with those in the semi-infinite space (Figure D.1b). Analytical expressions for dimensionless functions, f_C^{dike} and k_{IC}^{dike}, in a semi-infinite space are [*Tada et al*., 1985]:

$$f_C^{dike} = 2.349(1-\nu^2)\frac{l^2}{c^2} \tag{D.5}$$

$$k_{IC}^{dike} = 0.439\sqrt{\frac{l}{c}} \tag{D.6}$$

Compared to the analytical solutions, the computed dimensionless functions are also in good agreement (Table D.4 and D.5). The dimensionless function, k_{IC}^{dike}, for H = 1 km case shows a slight deviation from the analytical solution because the chamber crack is

close to the half-space boundary. Additionally, the analytical expression for dike opening at the base in a semi-infinite space is [*Tada et al*., 1985]

$$\delta(0) = 4.174(1-\nu^2)\frac{l}{c} \tag{D.7}$$

Compared to the analytical solutions, the computed dike openings at the base are in good agreement (Table D.6).

Table D.4 Comparison of dimensionless function, f_C^{dike}, for dike propagation from the lens center.

Function	H = 1 km and 2c = 1 km		H = 1.5 km and 2c = 1 km	
	l = 50 m	l = 100 m	l = 50 m	l = 100 m
Tada et al. [1985]	0.022	0.087	0.022	0.087
This work	0.022	0.086	0.022	0.086

Table D.5 Comparison of dimensionless function, k_{IC}^{dike}, for dike propagation from the lens center.

Function	H = 1 km and 2c = 1 km		H = 1.5 km and 2c = 1 km	
	l = 50 m	l = 100 m	l = 50 m	l = 100 m
Tada et al. [1985]	0.139	0.196	0.139	0.196
This work	0.094	0.133	0.132	0.188

Table D.6 Comparison of normalized dike opening at the base for dike propagation from the lens center.

Function	H = 1 km and 2c = 1 km		H = 1.5 km and 2c = 1 km	
	l = 50 m	l = 100 m	l = 50 m	l = 100 m
Tada et al. [1985]	0.388	0.777	0.388	0.777
This work	0.366	0.735	0.367	0.735

D.2 Testing problems for dike propagation from the lens tip

In Problem A of Figure 4.35, the dimensionless function $f_A^{chamber}(50)$ (Tables 4.4 and 4.5) can be also compared with the analytically derived dimensionless function, $f_A(0)$ of (4.78). Compared to the analytical solutions, the computed dimensionless functions are in good agreement (Table D.7).

Table D.7 Comparison of dimensionless functions, $f_A(0)$ and $f_A^{chamber}(50)$, for dike propagation from the lens tip.

Function	H = 1 km	H = 1.5 km	H = 5.5 km
$f_A(0)$	6.941	6.332	5.882
$f_A^{chamber}(50)$	7.126	6.516	5.971

The stress intensity factor of a propagating fracture in Problem A can be compared approximately with other available solutions obtained in an infinite space. As expected, if the fracture is located at a greater distance from the half-space boundary (e.g. H = 5.5 km), the normalized K_I and K_{II} are in good agreement (Figures D.3 – D.5).

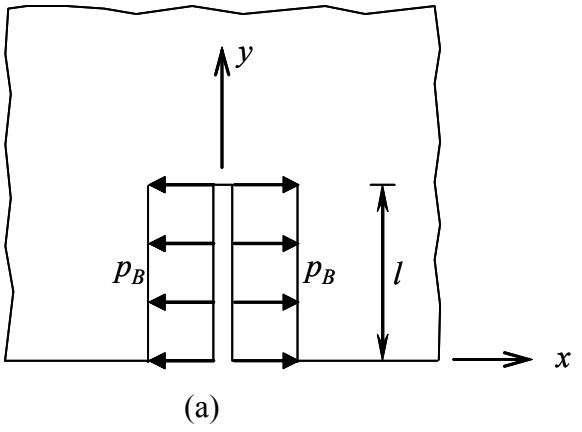

(a)

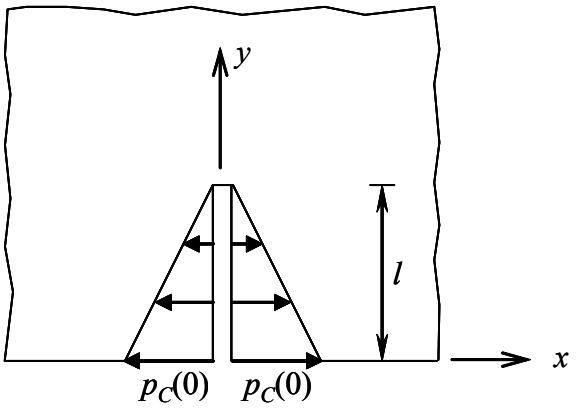

(b)

Figure D.1 Dike propagation in a semi-infinite space: (a) constant pressure, and (b) linear pressure.

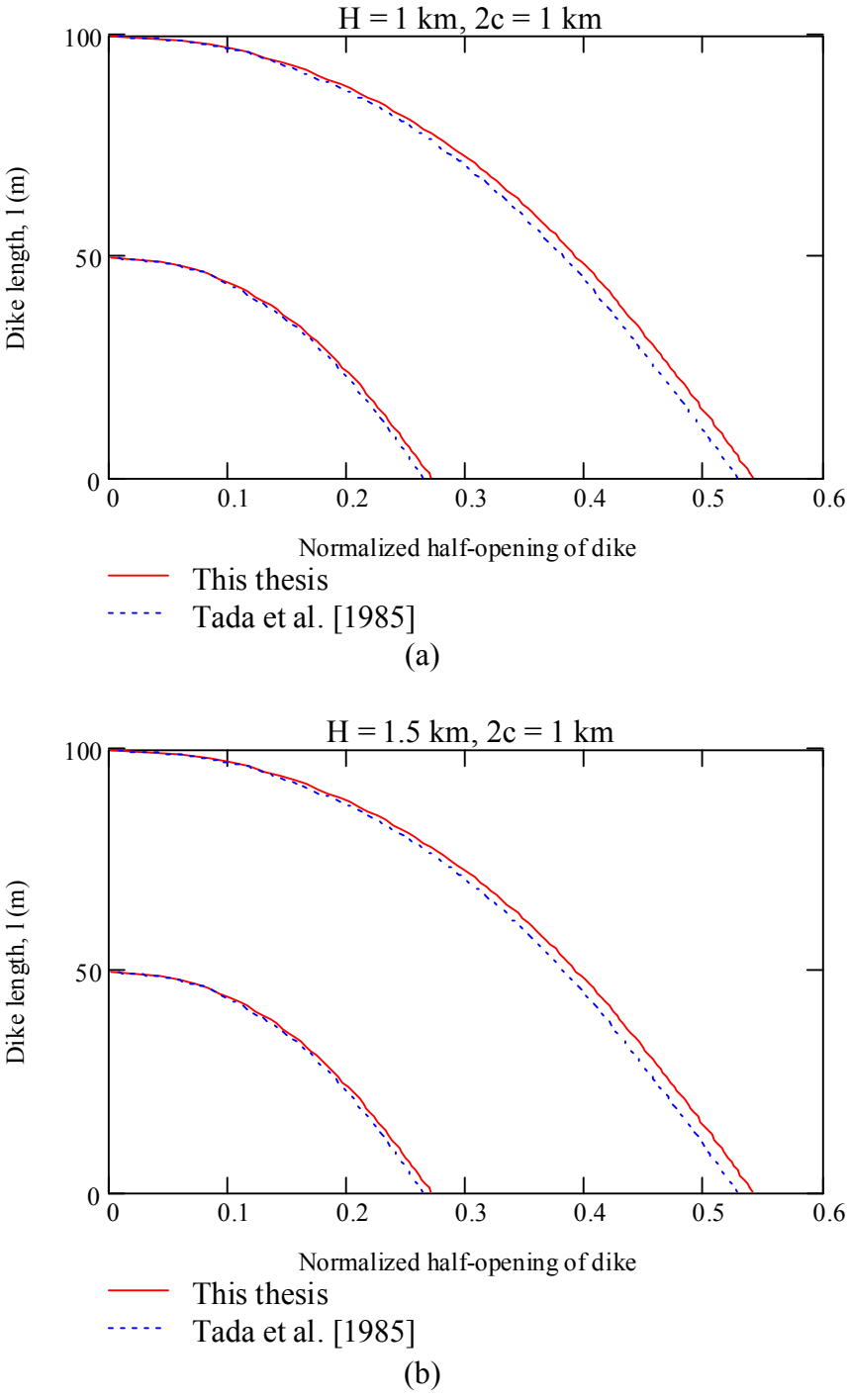

Figure D.2 Comparison of half-opening of dike for dike propagation from the lens center: (a) H = 1 km and $2c$ = 1 km, and (b) H = 1.5 km and $2c$ = 1 km.

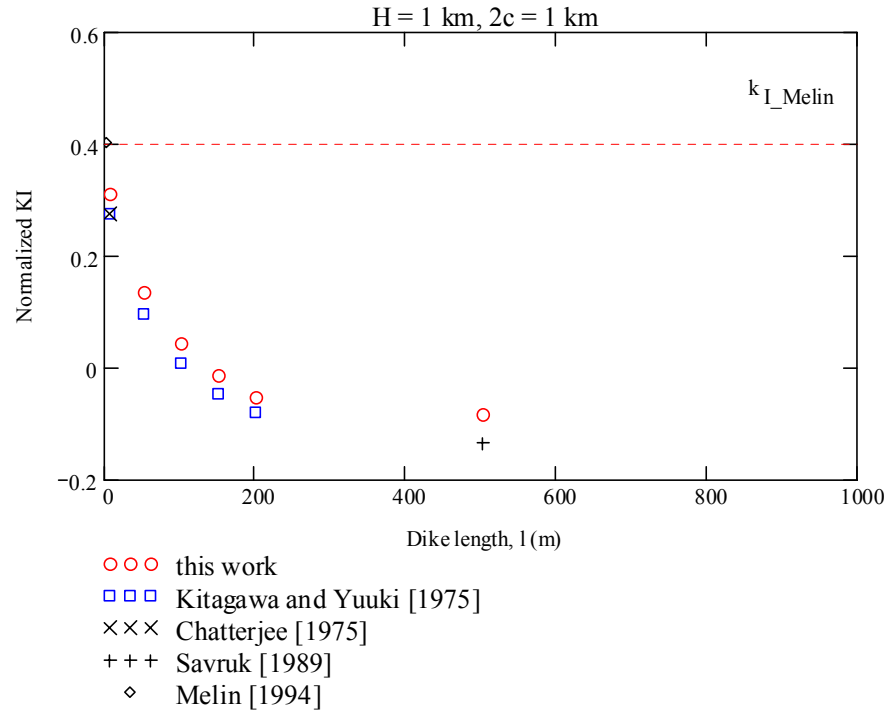

(a)

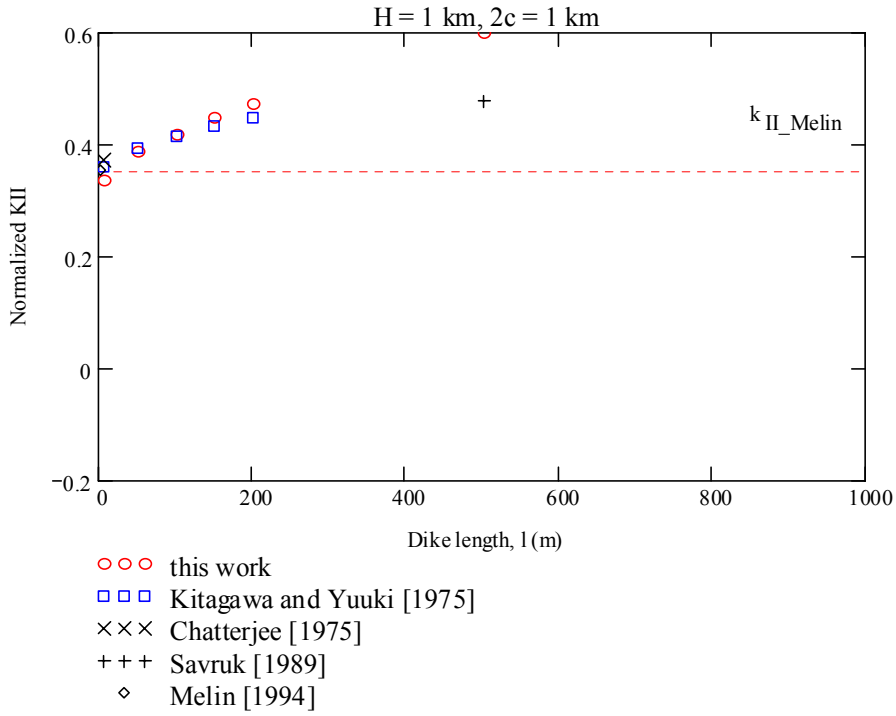

(b)

Figure D.3 Comparison of SIFs with available solutions for dike propagation from the lens tip (H =1 km and 2c = 1 km): (a) normalized K_I, and (b) normalized K_{II}.

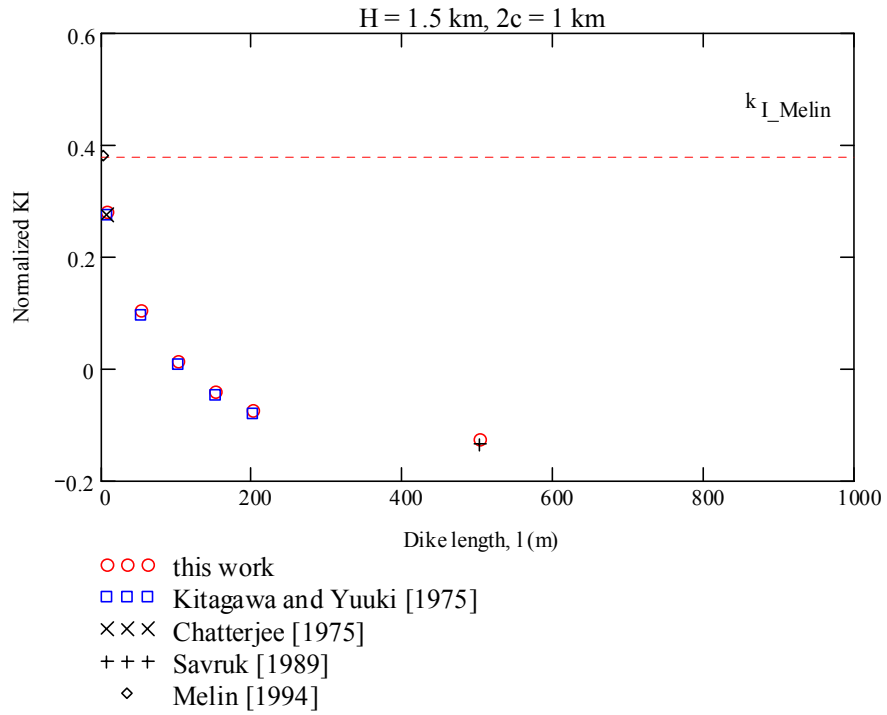

(a)

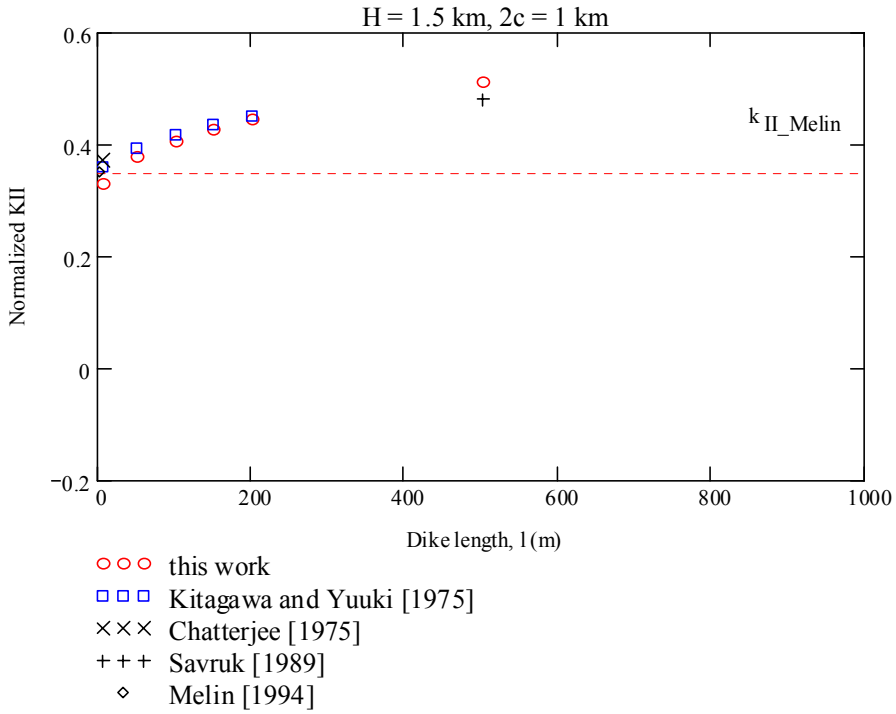

(b)

Figure D.4 Comparison of SIFs with available solutions for dike propagation from the lens tip (H =1.5 km and 2c = 1 km): (a) normalized K_I, and (b) normalized K_{II}.

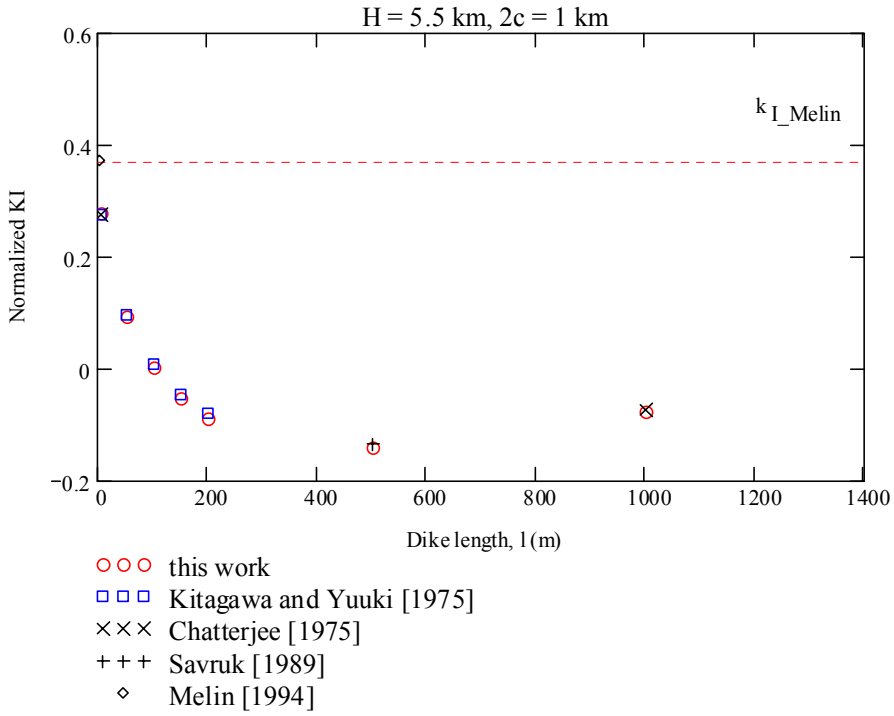

(a)

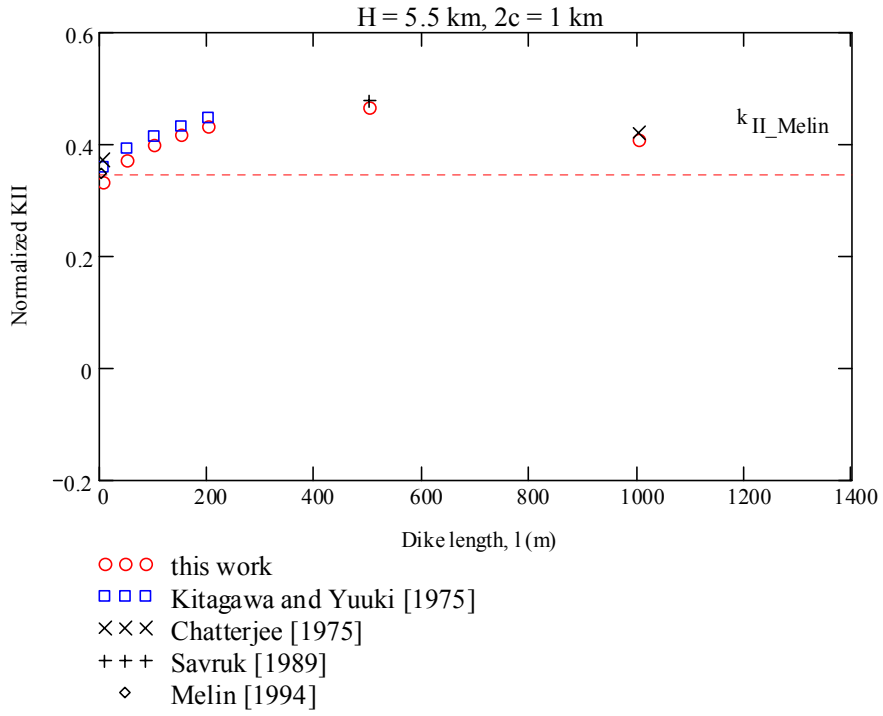

(b)

Figure D.5 Comparison of SIFs with available solutions for dike propagation from the lens tip (H =5.5 km and 2c = 1 km): (a) normalized K_I, and (b) normalized K_{II}.

REFERENCES

Abass, H.H., S. Hedayati, and D.L. Meadows, Nonplanar fracture propagation from a horizontal wellbore: Experimental study, *SPE Production & Facilities*, 133-137, August 1996.

Alexander, R.T. and K.C. Macdonald, Small off-axis volcanoes on the East Pacific Rise, *Earth and Planetary Science Letters*, 139, 387-394, 1996.

Anderson, E.M., The dynamics of sheet intrusion, *Proceedings of Royal Society of Edinburgh*, *Section B*, 58(3), 242-251, 1938.

Anderson, G.A., Effects of friction on hydraulic fracture growth near unbounded interfaces in rocks, *Society of Petroleum Engineers Journal*, 21-29, February 1981.

Astakhov, D.K., Permeability evolution as a result of fluid rock interaction, *Ph.D. Dissertation*, Civil and Environmental Engineering, Georgia Institute of Technology, 2000.

Babcock, J.M., A.J. Harding, G.M. Kent, and J.A. Orcutt, An examination of along-axis variation of magma chamber width and crustal structure on the East Pacific Rise between 13°30'N and 12°20'N, *Journal of Geophysical Research*, 103(B12), 30451-30467, December 1998.

Baer, G., Mechanisms of dike propagation in layered rocks and in massive, porous sedimentary rocks, *Journal of Geophysical Research*, 96(B7), 11911-11929, July 10, 1991.

Bai, T., D.D. Pollard, and M.R. Gross, Mechanical Prediction of Fracture Aperture in Layered Rocks, *Journal of Geophysical Research*, 105(B1), 707-721, January 10, 2000.

Bai, T. and D.D. Pollard, Closely Spaced Fractures in Layered Rocks: Initiation Mechanisms and Propagation Kinematics, *Journal of Structural Geology*, 22, 1409-1425, 2000.

Beach, A., Vein arrays, hydraulic fractures and pressure-solution structures in a deformed flysch sequence, S.W. England, *Tectonophysics*, 40, 201-225, 1977.

Beach, A., Numerical models of hydraulic fracturing and the interpretation of syntectonic veins, *Journal of Structural Geology*, 2(4) 425-438, 1980.

Blanton, T.L., An experimental study of interaction between hydraulically induced and pre-existing fractures, *SPE/DOE* 10847, 1982.

Blair, S.C., R.K. Thorpe, and F.E. Heuze, Propagating of fluid-driven fractures in jointed rock. Part 2-physical tests on blocks with an interface or lens, *International Journal of Rock Mechanics and Mining Sciences and Geomechanics Abstracts*, 27(4), 255-268, 1990.

Bons, P.D., The formation of veins and their microstructures, *Journal of the Virtual Explorer*, 2, 2000

Buck, W.R., S.M. Carbotte, and C. Mutter, Controls on extrusion at mid-ocean ridges, *Geology*, 935-938, October 1997.

Burnett, M.S., D.W. Caress, and J.A. Orcutt, Tomographic image of the magma chamber at 12°50' on the East Pacific Rise, *Nature*, 339, 206-208, 1989.

Canales, J.P., R.S. Detrick, S. Carbotte, J. Diebold, M. Nedimovic, G. Kent, and A. Harding, Crustal structure of the Cleft segment (southern Juan de Fuca Ridge) from multichannel seismic profiling, *Eos*. *Trans*. *AGU*, 84(46), Fall Meet. Suppl., Abstract B12A-0754, 2003.

Cann, J.R., A model for oceanic crustal structure developed, *Geophysical Journal of the Royal Astronomical Society*, 39, 169-187, 1974.

Carbotte, S.M., R. Detrick, G. Kent, J.P. Canales, J. Diebold, A. Harding, M. Nedimovic, D. Epstein, I. Cochran, E. Van Arken, J. Dingler, and A. Jacobs, A multi-channel seismic investigation of ridge crest and flank structure along the Juan de Fuca Ridge, *Eos*. *Trans*. *AGU*, 83(47), Fall meeting, Suppl., Abstract T72C-07, 2002a.

Carbotte, S., B. Detrick, G. Kent, J. Diebold, P. Canales, and A. Harding, Cruise Report, R/V Maurice Ewing, EW0207, July – August 2002b.

Caress, D.W., M.S. Burnett, and J.A. Orcutt, Tomographic image of the axial low-velocity zone at 12°50'N on the East Pacific Rise, *Journal of Geophysical Research*, 97(B6), 9243-9263, June 1992.

Carslaw, H.S. and J.C. Jaeger, Conduction of heat in solids. 2nd edition, 510 pp., Clarendon, Oxford, 1959.

Chang, H., L.N. Germanovich, R. Wu, J.C. Santamarina, and P.E. Dijk, Hydraulic fracturing in cohesionless particulate materials, *Eos Trans*. *AGU*, 84(46), Fall Meet. Suppl., Abstract H51B-03, 2003.

Chatterjee, S.N., The stress field in the neighborhood of a branched crack in an infinite elastic sheet, *International Journal of Solids and Structures*, 11(5), 521-538, 1975.

Cochran, J.R. and W.R. Buck, Near-axis subsidence rates, hydrothermal circulation, and thermal structure of mid-ocean ridge crests, *Journal of Geophysical Research*, 106(B9), 19233-19258, September 2001.

Collier, J. and M. Sinha, Seismic images of a magma chamber beneath the Lau Basin back-arc spreading centre, *Nature*, 346, 646-648, 1990.

Cooke, M.L. and D.D. Pollard, Fracture propagation paths under mixed mode loading within rectangular blocks of polymethyl methacrylate, *Journal of Geophysical Research*, 101(B2), 3387-3400, February 10, 1996.

Crawford, W.C., S.C. Webb, and J.A. Hildebrand, Constraints on melt in the lower crust and Moho at the East Pacific Rise, 9°48'N, using seafloor compliance measurements, *Journal of Geophysical Research*, 104(B2), 2923-2939, February 1999.

Curewitz, D. and J.A. Karson, Geological consequences of dike intrusion at mid-oceanic ridge spreading centers, in faulting and magnetism at mid-oceanic ridges, Edited by W.R. Roger, P.T. Delaney, J.A. Karson, and Y. Lagabrielle, 348 pp, American Geophysical Union, 1998.

Currie, K.L. and J. Ferguson, The mechanisms of intrusion of lamprophyre dikes indicated by "offsetting" of dikes, *Tectonophysics*, 9, 525-535, 1970.

Daneshy, D.D., Hydraulic fracture propagation in layered foundations, *Society of Petroleum Engineers Journal*, 33-41, February 1978.

Davidson, B.M., B.F. Saunders, B.M. Robinson, and S.A. Holditch, Analysis of abnormally high fracture treating pressures caused by complex fracture growth, *SPE* 26154, 1993.

Delaney, J.R., D.S. Kelley, J.D. Baross, W.S. Wilcock, M.D. Lilley, D. Butterfield, R.E.McDuff, and J. Deming, 2000.
http://www.ocean.washington.edu/hydrothermalvents/

Delaney, P.T. and D.D. Pollard, Deformation of host rocks and flow of magma during growth of minette dikes and breccia-bearing intrusions near Ship Rock, New Mexico, *Geological Survey Professional Paper* 1202, 1981.

De Pater, C.J., L. Weijers, M. Savic, K.H.A.A. Wolf, P.J. van den Hoek, and D.T. Barr, Experimental study of nonlinear effects in hydraulic fracture propagation, *SPE Production & Facilities*, 239-246, November 1994.

Detrick, R.S, A.J. Harding, G.M. Kent, J.A. Orcutt, J.C. Mutter, and P. Buhl, Seismic structure of the southern East Pacific Rise, *Science*, 259, 499-503, January 1993.

Detrick, R.S., P. Buhl, E. Vera, J. Mutter, J. Orcutt, J. Madsen and T. Brocher, Multi-channel seismic imaging of a crustal magma chamber along the east pacific rise, *Nature*, 326(5), 35-41, March 1987.

Detrick, R.S., S. Carbotte, E. Van Arken, J.P. Canales, G. Kent, A. Harding, J. Diebold, and M. Nedimovic, New multichannel seismic constraints on the crustal structure of the Endeavor Segment, Juan de Fuca Ridge: evidence for a crustal magma chamber, *Eos Trans*, *AGU*, 83(47), Fall Meeting, Suppl., Abstract T12B-1316, 2002.

Diamond, W.P. and D.C. Oyler, Effects of stimulation treatments on coalbeds and surrounding Strata, Evidence from underground observations, *Report of Investigations 9083*, U.S. Department of the Interior, 1987.

Dijk, P.E., H. Chang, L.N. Germanovich, and J.C. Santamarina, Experiments on hydraulic fracturing in weakly cemented sediments, *Eos Trans*. *AGU*, 84(46), Fall Meet. Suppl., Abstract H42F-1131, 2003

Dudley, J.W., J. Shlyapobersky, R.B. Stanbery, A. Chudnovsky, M. Gorelik, Z. Wen, S. Glaser, M.K. Hand, and G. Weiss, Laboratory investigation of fracture processes in hydraulic fracturing, *GRI*, Annual Report, December 1995.

Dunn, R.A., D.R. Toomey, and S.C. Solomon, Three-dimensional seismic structure and physical properties of the crust and shallow mantle beneath the East Pacific Rise at 9°30'N, *Journal of Geophysical Research*, 105(B10), 23537-23555, October 2000.

Dyskin, A.V., L.N. Germanovich, and K.B. Ustinov, Asymptotic analysis of crack interaction with free boundary, *International Journal of Solids and Structures*, 37, 857-886, 2000.

Economides, M.J. and K.G. Nolte, Reservoir stimulation, 3rd Edition, *John Wiley & Sons, LTD*, 2000.

Erdogan, F. and G.D. Gupta, On the numerical solution of singular integral equations, *The Quarterly Journal of Pure and Applied mathematics*, 29, 525-534, 1972.

Fast, R.E., A.S. Murer, R.S. Timmer, Description and Analysis of Cored Hydraulic Fractures-Lost Hills Field, Kern County, California, SPE Production & Facilities, 107-114, May 1994.

Fialko, Y., On origin of near-axis volcanism and faulting at fast spreading mid-ocean ridges, *Earth and Planetary Science Letters*, 190, 31-39, 2001.

Ficher, D.M. and S.L. Brantley, Models of quartz overgrowth and vein formation: deformation and episodic fluid flow in an ancient subduction zone, *Journal of Geophysical research*, 97(B13), 20043-20061, December 1992.

Fornari, D.J., R.M. Haymon, M.R. Perfit, T.K. Gregg, and M.H. Edwards, Axial summit trough of the East Pacific Rise 9°-10°N: Geological characteristics and evolution of the axial zone on fast spreading mid-ocean ridges, *Journal of Geophysical Research*, 103(B5), 9827-9855, May 1998.

Garrido, C.J., P.B. Kelemen, and G. Hirth, Variation of rate with depth in lower crust formed at an oceanic spreading ridge: Plagioclase crystal size distributions in gabbros from the Oman ophiloite, *Geochemistry Geophysics Geosystems*, 2, October 2001.

Genge, M.J., G.D. Price, A.P. Jones, Molecular dynamics simulations of CaCo3 melts to mantle pressures and temperature: implications for carbonatite magmas, *Earth and Planetary Science Letters*, 131, 225-238, 1995.

Gere, J.M. and S.P. Timoshenko, Mechanics of materials, Third SI Edition, *Chapman & Hall*, London, 1991.

Germanovich, L.N., D.K. Astakhov, M.J. Mayerhofer, J. Shlyapobersky, and L.M. Ring, Hydraulic fracture with multiple segments, Part I, observations and model formulation, *International Journal of Rock Mechanics and Mining Sciences*, 34(3-4), 1997a.

Germanovich, L. N., L.M. Ring, D.K. Astakhov, J. Shlyapobersky, and M.J. Mayerhofer, Hydraulic fracture with multiple segments, Part II, effect of interaction, *International Journal of Rock Mechanics and Mining Sciences*, 34(3-4), 1997b.

Germanovich, L. N., D.K. Astakhov, J. Shlyapobersky, M.J. Mayerhofer, C. Dupont, and L.M. Ring, Modeling Multisegmented hydraulic fracture in two extreme cases: no leakoff and dominating leakoff, *International Journal of Rock Mechanics and Mining Sciences*, 35(4-5), 1998a.

Germanovich, L. N., D.K. Astakhov, J. Shlyapobersky, and L.M. Ring, A model of hydraulic fracture with parallel segments, Modeling and Simulation Based Engineering, Vol. II, Edited by Atluri, S. N. and O'Donoghue, P. E., *Tech Science Press*, 1261-1268, 1998b.

Germanovich, L.N. and D.K. Astakhov, Fracture closure in extension and mechanical interaction of parallel joints, *Journal of Geophysical Research*, 109(B2), February 24, 2004.

Gidley, J.L, S.A. Holditch, D.E. Nierode, R.W., and Veatch Jr. Recent advances in hydraulic fracturing, Monograph Volume, 12, *SPE*, Henry L. Doherty Series, 1989.

Gladwell, G.M.L. and A.H. England, Orthogonal polynomial solutions to some mixed boundary-value problems in elasticity theory, *Quarterly Journal of Mechanics and Applied Mathematics*, 30, 175-185, 1977

Haimson, B.C., The hydrofracturing stress measuring method and recent field results, *International Journal of Rock Mechanics and Mining Sciences & Geomechanical Abstracts*, 15, 167-178, 1978.

Hainey, B.W. and X. Weng, Mitigation of multiple fractures from deviated wellbores, *SPE* 30482, 1995.

Hanson, M.E., R.J. Shaffer, and G.D. Anderson, Effects of various parameters on hydraulic fracturing geometry, *Society of Petroleum Engineers Journal*, 435-443, August 1981.

Hallam, S.D. and N.C. Last, Geometry of hydraulic fractures from modestly deviated wellbores, *Journal of Petroleum Technology*, 43, 742-748, June 1991.

Harding, A.J., J.A. Orcutt, M.E. Kappus, E.E. Vera, J.C. Mutter, P. Buhl, R.S. Detrick, and T.M. Brocher, Structure of young oceanic crust at 13°N on the East Pacific Rise from expanding spread profiles, *Journal of Geophysical Research*, 94(B9), 12163-12196, September 1989.

Hayashi, K., A. Sato, and T. Ito, *In situ* stress measurements by hydraulic fracturing for a rock mass with many planes of weakness, *International Journal of Rock Mechanics and Mining sciences*, 34(1), 45-58, 1997.

Heezen, B.C. and M. Tharp, World ocean floor, *US Navy*, 1977.

Helgeson, D.E. and A. Aydin, Characteristics of joint propagation across layer interfaces in sedimentary rocks, *Journal of Structural Geology*, 13(8), 897-911, 1991.

Hocking, G. and S. Wells, Design, construction and installation verification of a 1200 long iron permeable reactive barrier, 8th *Annual Florida Remediation Conference*, November 2002.

Hoek, H., Mafic dykes of the Vestfold Hills, East Antarctica: an analysis of the emplacement mechanism of tholeiitic dyke swarms and of the role of dyke emplacement during crustal extension, *Ph.D. Dissertation*, University of Utrecht, 1994.

Horri, H., and S. Nemat-Nasser, Elastic fields of interacting inhomogenieties, *International Journal of Solids and Structures*, 21(7), 731-745, 1985.

Hubbert, M.K. and D.G. Willis, Mechanics of hydraulic fracturing, *Petroleum Transactions*, AIME, 210, 153-166, 1957.

Hufenbach, W. and B. Zhou, Solutions for an anisotropic, finite plate with an elastic inclusion and a loaded boundary, *Composite Structures*, 52, 161-166, 2001.

Hussenoeder, S.A., J.A. Collins, G.M. Kent, R.S. Detrick, and the Tera Group, Seismic analysis of the axial magma chamber reflector along the southern East Pacific Rise from conventional reflection profiling, *Journal of Geophysical Research*, 101(B10), 22087-22105, October 1996.

Isida, M., Analysis of stress intensity factors for plate containing random array of cracks, *Bulletin of the JSME*, 13(59), 635-642, 1970.

Jeffrey, R.G., L. Vandamme and J.-C. Roegiers, Mechanical interactions in branched or subparallel hydraulic fractures, *SPE* 16422, 1987.

Jeffrey, R.G., C.R. Weber, W. Vlahovic, and J.R. Enever, Hydraulic fracturing experiments in the Great Northern coal seam, *SPE* 28779, 1994.

Jeffrey, R.G., A. Settari, and N.P. Smith, A comparison of hydraulic fracture field experiments, including mineback geometry data, with numerical fracture model simulations, *SPE* 30508, 1995.

Jeffrey, R.G., Asymmetrically Propped Hydraulic Fractures, *SPE Production & Facilities*, 244-249, November 1996.

Jeffrey, R.G. and A. Settari, An instrumented hydraulic fracture experiment in coal, *SPE* 39908, April 1998.

Junium, C.K., J.W. Niemitz, and J.M. Elick, Hydrothermal alteration of the balls bluff siltstone, Culpeper basin, Virginia, The *Geological Society America*, *Abstracts with Programs*, 35th Northeastern Section, 2000.

Keck, R.G., P.A. Fletcher, and R.J. Withers, A field demonstration of hydraulic fracturing for solids waste disposal, Part one: injection operations and engineering data analysis, *Deep Injection Disposal of Hazardous and Industrial Waste, Scientific and Engineering Aspects*, edited by J.A. Apps and C.-F. Tsang, Academic Press, San Diego, pp 775, 1996.

Kelemen, P.B., K. Koga, and N. Shimizu, Geochemistry of gabbro sills in the crust–mantle transition zone of the Oman ophiolite: implications for the origin of the oceanic lower crust, *Earth and Planetary Science Letters*, 146, 475-488, 1997.

Kemp, L.F., Study of Nordgren's Equation of hydraulic fracturing, SPE Production Engineering, 311-314, August 1990.

Kent, G.M., A.J. Harding, and J.A. Orcutt, Evidence for a smaller magma chamber beneath the East Pacific Rise at 9°30'N, *Nature*, 344, 650-653, 614-618, April 1990.

Kent, G., A.J. Harding, and J.A. Orcutt, Distribution of magma beneath the East Pacific Rise between the Clipperton transform and the 9°17'N Deval from forward modeling of common depth point data, *Journal of Geophysical Research*, 98(B8), 13945-13969, August 1993a.

Kent, G., A.J. Harding, and J.A. Orcutt, Distribution of magma beneath the East Pacific Rise near the 9°03'N overlapping spreading center from forward modeling of common depth point data, *Journal of Geophysical Research*, 98(B8), 13971-13995, August 1993b.

Kent, G.M., A.J. Harding, and J.A. Orcutt, R.S. Detrick, J.C. Mutter, and P. Buhl, Uniform accretion of oceanic crust south of the Garrett transform at 14°15'S on the East Pacific Rise, *Journal of Geophysical Research*, 99(B5), 9097-9116, May 1994.

Kitagawa H. and R. Yuuki, Stress intensity factors for branched cracks in an infinite body in the two dimensional stress state, *Transactions of the Japan Society of Mechanical Engineers*, 41(346), 1641-1649, June 1975.

Knauss, W.G., An observation of crack propagation in anti-plane shear, *International Journal of Fracture Mechanics*, 6(2), 183-187, June 1970.

Korenaga, J. and P.B. Kelemen, Melt migration through the oceanic lower crust: a constraint from melt percolation modeling with finite solid diffusion, *Earth and Planetary Science Letters*, 156, 1-11, 1998.

Lamont, N. and F.W. Jessen, The effects of existing fractures in rocks on the extension of hydraulic fractures, *Journal of Petroleum Technology*, February 1963.

Langmuir, C.H., J.F. Bender, and R. Batiza, Petrological and tectonic segmentation of the East Pacific Rise, 5°30'-14°30'N, *Nature*, 322, 422-429, July 1986.

Laubach, S.E., Practical approaches to identifying sealed and open fractures, *American Association of Petroleum Geologists Bulletin*, 87(4), 561-579, April 2003.

Lawn, B.R., Fracture of brittle solids, 2nd edition, *Cambridge University Press*, 1993.

Lee, K.Y. and A.J. Froelich, Triassic-Jurassic stratigraphy of the Culpeper and Barboursville Basins, Virginia and Maryland, *U.S. Geological Survey Professional Paper 1472*, 52 pp, 1989.

Lehman, L.V. and J.L. Brumley, Etiology of multiple fractures, *SPE* 37406, March 1997.

Lonsdale, P., Segmentation of the Pacific-Nazca spreading center, 1°N-20°S, *Journal of Geophysical Research*, 94(B9), 12197-12225, September 1989.

Lowell, R.P., Thermoelasticity and the formation of black smokers, *Geophysical Research Letters*, 17(6), 709-712, May 1990.

Lowell, R.P., P.A. Rona, and R.P. Von Herzen, Seafloor hydrothermal systems, *Journal of Geophysical Research*, 100(B1), 327-352, January 1995.

Lowell, R.P. and L.N. Germanovich, Dike injection and the formation of megaplumes at ocean ridges, *Science*, 267, 1804-1807, March 1995.

Macdonald, K.C. and P.J. Fox, Overlapping spreading centers: new accretion geometry on the east pacific rise, *Nature*, 302, 55-58, 1983.

Macdonald, K.C., J-C Sempere, and P.J. Fox, Reply: The debate concerning overlapping spreading centers and mid-ocean ridge process, *Journal of Geophysical Research*, 91(B10) 10501-10511, September 1986.

Macdonald, K.C., D.S. Scheirer, and S.M. Carbotte, Mid-ocean ridges: discontinuities, segments and giant cracks, *Science*, 253, 986-994, August 1991.

Madensi, E., B. Sergeev, and S. Shkarayev, Boundary collocation method for multiple defect interactions in an anisotropic finite region, *International Journal of Fracture*, 94, 339-355, 1998.

Mahrer, K.D., A Review and Perspective on far-field hydraulic fracture geometry studies, *Journal of Petroleum Science and Engineering*, 24, 13-28, 1999.

McCartney, L.N. and T.A.E. Gorley, Complex variable method of calculating stress intensity factors for cracks in plates, *Numerical Methods in Fracture Mechanics, Proceeding of the 4th International Conference*, San Antonio, 55-72, 1987.

Medlin, W.L. and J.L. Fitch, Abnormal treating pressures in MHF treatments, *SPE* 12108, 1983.

Medlin, W.L. and L. Massé, Laboratory experiments in fracture propagation, *Society of Petroleum Engineers Journal*, 256-268, June 1984.

Melin, S., Accurate data for stress intensity factors at infinitesimal kinks, *Journal of Applied Mechanics*, 61, 467-470, June 1994.

Murase, T. and A.R. McBirney, Properties of some common igneous rocks and their melts at high temperatures, *Geological Society of America Bulletin*, 84, 3563-3592, 1973.

Murdoch, L.C., Hydraulic fracturing of soil during laboratory experiments: part 1. methods and observations, *Geotechnique*, 43(2), 255-265, 1992.

Murdoch, L.C., Hydraulic fracturing of soil during laboratory experiments: part 2. propagation, *Geotechnique*, 43(2), 267-276, 1993a.

Murdoch, L.C. and W.W. Slack, Forms of hydraulic fractures in shallow fine-grained formations, *Journal of Geotechnical and Geoenvironmental Engineering*, 128(6), 479-487, June 2002.

Murphy, H., Hot dry rock reservoir development and testing in the USA, *Mechanics of Elastic and Inelastic Solids 5, Hydraulic fracturing and geothermal energy*, edited by S. Namet-Nasser, H. Abé, and S. Hirakawa, Martinus Nijhoff Publishers, pp 528, 1983.

Muskhelishvili, N. I., *Some basic problems of the mathematical theory of elasticity*, Noordhoff, Groningen, 1953.

Naceur, K.B. and J.-C. Roegiers, Design of fracturing treatments in multilayered formations, *SPE Production Engineering, 21-26*, February 1990.

Narendran, V.M., and M.P. Cleary, Analysis of growth and interaction of multiple hydraulic fractures, *SPE* 12272, 1983.

Navin, D.A., C. Peirce, and M.C. Sinha, The RAMESSES experiment-II. Evidence for accumulated melt beneath a slow spreading ridge from wide-angle refraction and multichannel reflection seismic profiles, *Geophysical Journal international*, 135, 746-772, 1998.

Nemat-Nasser, S., Thermally induced cracks and heat extraction from hot dry rocks, *Mechanics of Elastic and Inelastic Solids* 5, Hydraulic fracturing and geothermal energy, edited by S. Namet-Nasser, H. Abé, and S. Hirakawa, Martinus Nijhoff Publishers, pp528, 1983.

Nicolas, A., The mid-oceanic ridges, Mountains below sea level, *Springer*, 1995.

Nolte, K.G., Discussion of influence of geologic discontinuities on hydraulic fracture propagation, *Journal of Petroleum Technology*, 998, August 1987.

Nordgren, R.P., Propagation of a vertical hydraulic fracture, *Society of Petroleum Engineers Journal*, 306-314, August 1972.

Olson, J. and D.D. Pollard, Inferring paleostresses from natural fracture patterns: A new method, *Geology*, 17, 345-348, April 1989.

Olson, J.E. and D.D. Pollard, The initiation and growth of en échelon veins, *Journal of Structural Geology*, 13(5), 595-608, 1991.

Olson, J.E., Sublinear scaling of fracture aperture versus length: an exception or the rule? *Journal of Geophysical Research*, 108(B9), 2413, doi:10.1029/2001JB000419, 2003.

Pallister, J.S. and C.A. Hopson, Samail ophiolite plutonic suite: field relations, phase variation, cryptic variation and layering, and a model of a spreading ridge magma chamber, *Journal of Geophysical Research*, 86(B4), 2593-2644, April, 1981.

Palmer, I.D. and D.P. Sparks, Measurement of induced fractures by downhole TV camera in black warrior basin coalbeds, *Journal of Petroleum Technology*, 270-275, 326-328, March 1991.

Panah, A.K. and E. Yanagisawa, Laboratory studies on hydraulic fracturing criteria in soil, *Soils and Foundations*, 29(4), 14-22, December 1989.

Panasyuk, V.V., M.P. Savruk and A.P. Datsyshyn, A general method of solution of two-dimensional problems in the theory of cracks, *Engineering Fracture Mechanics*, 9,481-497, 1977.

Perfit, M.R., D.J. Fornari, M.C. Smith, J.F. Bender, C.H. Langmuir, and R.M. Haymon, Small-scale spatial and temporal variations in mid-oceanic ridge crest magmatic processes, *Geology*, 22, 375-379, April 1994.

Pollard, D.D. and O.H. Muller, The effect of gradients in regional stress and magma pressure on the form of sheet intrusions in cross-section, *Journal of Geophysical Research*, 81(5), 975-984, February 10, 1976.

Pollard, D.D., Forms of hydraulic fractures as deduced from field studies of sheet intrusions, *Proceedings of 19th U.S. Rock Mechanics Symposium*, Stateline, Nevada, May 1978.

Pollard, D.D. and A. Aydin, Propagation and linkage of oceanic ridge segments, *Journal of Geophysical Research*, 89(B12), 10017-10028, November, 10, 1984.

Pollard, D.D. and A. Aydin, Progress in understanding jointing over the past century, *Geological Society of America Bulletin*, 100, 1181-1204, August 1988.

Pollard, D.D., P. Segall, and P.T. Delaney, Formation and interpretation of dilatant echelon cracks, *Geological Society of American Bulletin*, 93, 1291-1303, December 1982.

Press, W.H., S.A. Teukolsky, W.T. Vetterling, and B.P. Flannery, Numerical recipes in FORTRAN: The art of scientific computing, 2nd edition, *Cambridge University Press*, 1992.

Ramsay, J.G., The crack-seal mechanism of rock deformation, *Nature*, 284, 135-139, 1980.

Renshaw, C.E. and D.D. Pollard, An experimentally verified criterion for propagation across unbounded frictional interfaces in brittle, linear elastic materials, *International Journal of Rock Mechanics and Mining Sciences & Geomechanics Abstracts*, 32(3), 237-249, 1995.

Renshaw, C.E. and J.C. Park, Effect of mechanical interactions on the scaling of fracture length and aperture, *Nature*, 386, 482-484, April 1997.

Rohr, K.M.M., B. Milkereit, and C.J. Yorath, Asymmetric deep crustal structure across the Juan de Fuca Ridge, *Geology*, 16, 533-537, June 1988.

Sagy, A., Z. Reches, and I. Roman, Dynamic fracturing: field and experimental observations, *Journal of Structural Geology*, 23, 1223-1239, 2001.

Sato, K., C.A. Wright, and I. Makoto, Post-frac analyses indicating multiple fractures created in a volcanic formation, *SPE Production & Facilities*, 14(4), 284-291, November 1999.

Savruk, M.P. and A.P. Datsyshin, On the limiting state of equilibrium of a plate weakened by two arbitrarily-oriented cracks, *Physico-Mechanical Institute, Academy of Sciences of the Ukrainian SSR*, L'vov. Translated from Prikladnaya Mechanika, 9(7), 49-56, July 1973.

Savruk, M.P., P.N. Osvis, and I.V. Prokopchuk, Numerical analysis in two dimensional problems of crack theory, *Naukova Dumka*, Kiev, 246 pages, 1989.

Secor, D.T. and D.D. Pollard, On the stability of open hydraulic fractures in the earth's crust, *Geophysical Research Letters*, 2(11), 510-513, November 1975.

Secor, D.T., Role of fluid pressure in jointing, *American Journal of Science*, 263, 633-646, October 1965.

Sempere, J.-C. and K.C. Macdonald, Overlapping spreading centers: implications from crack growth simulation by the displacement discontinuity method, *Tectonics*, 5(1), 151-163, February 1986a.

Sempere, J.-C. and K.C. Macdonald, Deep-tow studies of the overlapping spreading centers at 9°03′N on the East Pacific Rise, *Tectonics*, 5(6), 881-900, October 1986b.

Shah, A.K. and W. Roger Buck, Causes for axial high topography at mid-ocean ridges and the role of crustal thermal structure, *Journal of Geophysical Research*, 106(12), 30865-30879, September 2001.

Shin, K., K. Sugawara and S. Okubo, Application of Weibull's theory to estimating in situ maximum stress σ_H by hydrofracturing, *International Journal of Rock Mechanics & Mining Sciences*, 38, 423-420, 2001.

Singh, S.C., G.M. Kent, J.S. Collier, A.J. Harding, and J.A. Orcutt, Melt to mush variations in crustal magma properties along the ridge crust at the sourthern East Pacific Rise, *Nature*, 394, 874-878, August 1998.

Sinha, M.C., S.C. Contable, C. Peirce, A. White, G. Heinson, L.M. MacGregor and D.A. Navin, Magmatic processes at slow spreading ridges: implications of the RAMESSES experiment at 57°45'N on the Mid-Atlantic Ridge, *Geophysical Journal International*, 135, 731-745, 1998.

Sinton J.M. and R. Detrick, Mid-ocean ridge magma chambers, *Journal of Geophysical Research*, 97(B1), 197-216, January 1992.

Stadulis, J.M., Development of a completion design to control screenouts caused by multiple near-wellbore fractures, *SPE* 29549, 1995.

Tada, H., P.C. Paris, and G.R. Irwin, The stress analysis of cracks handbook, *Paris Productions Incorporated*, St. Louis, Mo., 1985.

Takada, A., Experimental Study on Propagation of Liquid-Filled Crack in Gelatin: Shape and Velocity in Hydrostatic stress Condition, *Journal of Geophysical Research*, 95(B6), 8471-8482, June 10, 1990.

Teufel, L.W. and J.A. Clark, Hydraulic fracture propagation in layered rock: experimental studies of fracture containment, *Society of Petroleum Engineers Journal*, 19-32, 1984.

Toomey, D.R., G.M. Purdy, S.C. Solomon, and W.S.D. Wilcock, The three-dimensional seismic velocity structure of the East Pacific Rise near latitude 9°30'N, *Nature*, 347, 639-645, October 1990.

Tsamasphyros, G. and D.A. Eftaxiopoulos, Energy considerations in the boundary collocation method applied in fracture, *Engineering Fracture Mechanics*, 54(5), 639-652, 1996.

Ukadgaonker, V.G. and B. Murali, Stress intensity factors for finite plate by boundary collocation, *International Journal of Fracture*, 52, R17-R24, 1991.

Van Ark, E.M., R.S. Detrick, J.P. Canales, S.M. Carbotte, J.B. Diebold, A. Harding, G. Kent, M.R. Nedimovic, and W.S.D. Wilcock, *Eos. Trans. AGU*, 84(46), Fall Meet. Suppl., Abrtract B12A-0752, 2003.

Vandamme, L., R.G. Jeffrey, and J.H. Curran, Pressure distribution in three dimensional hydraulic fractures, *SPE Production Engineering*, 181-186, May 1988.

Van Eekelen, H.A.M., Hydraulic fracture geometry: Fracture containment in layered formations, *Society of Petroleum Engineers Journal*, 341-349, June 1982.

Veatch, R.W., Overview of current hydraulic fracturing design and treatment technology-part 1, *Journal of Petroleum Technology*, 677-687, April 1983a.

Veatch, R.W., Overview of current hydraulic fracturing design and treatment technology-part 2, *Journal of Petroleum Technology*, 853-863, April 1983b.

Veeken, C.A.M., D.R. Davies, and J.V. Walters, Limited communication between hydraulic fracture and (deviated) wellbore, *SPE* 18982, March 1989.

Vera, E.E., J.C. Mutter, P. Buhl, J.A. Orcutt, A.J. Harding, M.E. Kappus, R.S. Detrick, and T.M. Brocher, The structure of 0- to 0.2-m.y.-old oceanic crust at 9°N on the East Pacific Rise from expanded spreading profiles, *Journal of Geophysical Research*, 95(B10), 15529-15556, September 1990.

Vermilye, J.M. and C.H. Scholz, Relation between vein length and aperture, *Journal of Structural Geology*, 17(3), 423-434, 1995.

Vermilye, J.M., The growth of natural fracture systems: A fracture mechanics approach, *Ph.D. Dissertation*, Columbia University, 1996.

Von Damm, K.L., Personal Communication, 2004.

Warpinski, N.R., Measurement of width and pressure in a propagating hydraulic fracture, *Society of Petroleum Engineers Journal*, 46-54, February 1985.

Warpinski, N.R., J.C. Lorenz, P.T. Branagan, F.R. Myal, and B.L. Gall, Examination of a cored hydraulic fracture in a deep gas well, *SPE Production & Facilities*, 150-158, August 1993a.

Warpinski, N.R., J.C. Lorenz, P.T. Branagan, F.R. Myal, and B.L. Gall, Author's reply to discussion of examination of a cored hydraulic fracture in a deep gas well, *SPE Production & Facilities*, 164, August 1993b.

Warpinski, N.R. and L.W. Teufel, Influence of geologic discontinuities on hydraulic fracture propagation, *Journal of Petroleum Technology*, 209-220, February 1987.

Wawrzynek, P.A. and A.R. Ingraffea, Interactive finite element analysis of fracture processes: an integrated approach. *Theoretical and Applied Fracture Mechanics*, 8, 137-150, 1987.

Weijers, L., C.J. de Pater, K.A. Owens, and H.H. Kogsboll, Geometry of hydraulic fractures induced from horizontal wellbores, *SPE Production & Facilities*, 87-92, May 1994.

Weiland, C.M., K.C. Macdonald, and N.R. Grindlay, Ridge segmentation and the magnetic structure of the southern Mid-Atlantic Ridge 26S and 31-35S: implications for magmatic processes at slow spreading centers, *Journal of Geophysical Research*, 101(B4), 8055-8073, April 10, 1996.

Wilcock, W.S.D., S.C. Solomon, G.M. Purdy, and D.R. Toomey, The seismic attenuation of fast-spreading mid-ocean ridge, *Science*, 258, 1470-1474, November 1992.

Wilcock, W.S.D., *NEPTUNE Working Group White Paper*, Opportunities for Seismology and Geodynamics in NEPTUNE, 2000.
http://gore.ocean.washington.edu/reportsmeetings/neptune_seismology/

Wilcock, W.S.D., *Course note*, 2001.
http://gore.ocean.washington.edu/classpages/ocean410/notes/unit06.htm

Withers, R.J., T.K. Perkins, and R.G. Keck, A field demonstration of hydraulic fracturing for solids waste disposal, Part Two: Real-time passive seismic monitoring system and data anaylsis, *Deep Injection Disposal of Hazardous and Industrial Waste, Scientific and Engineering Aspects*, edited by J.A. Apps and C.-F. Tsang, Academic Press, pp 775, 1996.

Wright. C.A., J.J.Tanigawa, M. Shixin, and L. Zhigang, Enhanced hydraulic fracture technology for a coal seam reservoir in central China, *SPE* 29989, November 1995.

Wu, R. and L.N. Germanovich, Hydraulic fracturing branching and segmentation, *The 11th Annual David S. Snipes/Clemson Hydrogeology Symposium*, Clemson, South Carolina, April 2003.

Zhan, S., Z. Wang, and X. Han, Effective elastic moduli of two-dimensional solids with multiple cracks, *Science in China* (*Series* A), 41(10), 1114-1120, October 1998.

VITA

Youngjong Sim was born in Jangsung, a small town in Korea on January 20, 1970. He is the son of Sangmyung Sim and Youngbai Kim. He graduated from Hwakok High School in Seoul, Korea in 1988. He earned his Bachelor's degree in Civil Engineering from Hongik University, Seoul in 1995. During the B.S. period, he served his military duty in the Air Force in Seoul between 1992 and 1993. He entered graduate school in 1995 and received his Master's degree in Civil Engineering with specialization in Geotechnical Engineering from Hongik University in 1997. He then worked for one year at Hong-Ik University as a research scientist. Before he came to the United States to pursue his Ph.D., he married Eunju Joung in 1998. He began his doctoral studies in Civil and Environmental Engineering at the Georgia Institute of Technology in Atlanta in 1998. He received his Ph.D. degree in 2004. His first daughter, Jaehee, was born in Atlanta on July 13, 2001. The second daughter, Seohee, was born in Atlanta on January 6, 2004.